An Investigation of Precision and Scaling Issues in Nuclear Spin and Trapped-Ion Quantum Simulators

by

Robert J. Clark

B.S. Physics and Chemistry
Ohio Northern University, 2003

Submitted to the Department of Physics
in partial fulfillment of the requirements for the degree of

Doctor of Philosophy in Physics

at the

MASSACHUSETTS INSTITUTE OF TECHNOLOGY

June 2009

Author ....
Department of Physics
April 28, 2009

Certified by ....
Isaac L. Chuang
Associate Professor of Electrical Engineering and Computer Science
and Associate Professor of Physics
Thesis Supervisor

Accepted by ....
Thomas J. Greytak
Lester Wolfe Professor of Physics, Associate Department Head for Education

An Investigation of Precision and Scaling Issues in Nuclear Spin and Trapped-Ion Quantum Simulators

by

Robert J. Clark

Submitted to the Department of Physics
on April 28, 2009, in partial fulfillment of the
requirements for the degree of
Doctor of Philosophy in Physics

Abstract

Quantum simulation offers the possibility of using a controllable quantum-mechanical system to implement the dynamics of another quantum system, performing calculations that are intractable on classical computers for all but the smallest systems. This great possibility carries with it great challenges, two of which motivate the experiments with nuclear spins and trapped ions presented in this thesis.

The first challenge is determining the bounds on the precision of quantities that are calculated using a digital quantum simulator. As a specific example, we use a three-qubit nuclear spin system to calculate the low-lying spectrum of a pairing Hamiltonian. We find that the simulation time scales poorly with the precision, and increases further if error correction is employed. In addition, control errors lead to yet more stringent limits on the precision. These results indicate that quantum simulation is more efficient than classical computation only when a limited precision is acceptable and when no efficient classical approximation is known.

The second challenge is the scaling-up of small quantum simulators to incorporate tens or hundreds of qubits. With a specific goal of analog quantum simulation of spin models in two dimensions, we present novel ion trap designs, a lattice ion trap and a surface-electrode elliptical ion trap. We experimentally confirm a theoretical model of each trap, and evaluate the suitability of each design for quantum simulation. We find that the relevant interaction rates are much higher in the elliptical trap, at the cost of additional systematic control errors.

We also explore the interaction of ions over a wire, a potentially more scalable system than the elliptical trap. We calculate the expected coupling rate and decoherence rates, and find that an extremely low capacitance ($\mathcal{O}$(fF)) between the coupling wire and ground is required, as well as ion-wire distances of $\mathcal{O}(50\ \mu m)$ to realize a motional coupling of $\mathcal{O}$(1 kHz). In pursuit of this situation, we measure the effect on a single ion of a floating wire's static and induced ac voltages as a function of the ion-wire distance.

Thesis Supervisor: Isaac L. Chuang
Title: Associate Professor of Electrical Engineering and Computer Science
and Associate Professor of Physics

Acknowledgments

What a long, strange trip it's been.

I'd first like to thank my advisor, Prof. Isaac Chuang. Ike has certainly taught me most of what I can claim to know about doing research. Working here was an intense but rewarding experience, in part because Ike grants his students a large amount of independence, which affords one the opportunity to lead a research project, from design, construction, and theory, all the way to writing up the results. This gave me a chance to do my own work, including making my own mistakes, and in the process I learned a great deal. Ike also has high standards regarding the communication of scientific information, and I greatly appreciate the training I've received in writing and speaking about physics.

Thanks are also due to Profs. Wolfgang Ketterle and Leonid Levitov for sitting on my thesis committee, and giving good suggestions and feedback before and after the writing of this thesis. I enjoyed my semi-annual advising sessions with Wolfgang, especially once I was taking 8.THG every single semester, and we could chat about science instead of coursework.

Before coming to MIT, I had the privilege of learning from several excellent teachers. I'd like, most especially, to thank David French and Jeffrey Radloff, who got me started in chemistry and physics as a high school student. It was they who inspired me to study these subjects in college, and thus they have had a huge influence on the direction of my life. At Ohio Northern, I benefitted from many excellent teachers. I would most particularly like to thank my undergraduate research advisor, Prof. Jeff Gray, without whose encouragement and instruction I would not have gone on to MIT.

I arrived at MIT the same day as Ken Brown, who immediately became my collaborator, and very shortly thereafter my good friend as well. A good part of the credit for helping me get up to speed here at MIT is due to Ken's patient instruction. He is also responsible for some great parties, and for introducing me to some excellent new music. I'd also like to thank Matthias Steffen for taking the time to show Ken and me how to run the NMR machine. Further instruction in the lab and good conversation outside of it came from Andrew Houck, with whom I had the pleasure of rooming for a while. The first two undergraduates that I worked with at MIT, Waseem Bakr and Susanna Thon, were excellent students who made coming to lab more fun.

In due course, the days of NMR gave way to the days of ion traps, and I acquired a new team of coworkers and friends. Jarek Labaziewicz and Dave Leibrandt joined the group and they and I, together with Ken, built the first atomic ion traps in the lab. Their technical skills and work ethic continue to impress me, but more impressive than this is the fact that they're somehow also awesome guys to hang out with. New projects brought new undergraduate collaborators, and it was a pleasure to work on laser stabilization with Christalee Bieber, PCB traps with Phil Richerme, and lattice ion traps with Ziliang (Carter) Lin. Carter, even though things were a bit rough with me being several thousand kilometers away for part of the time, I hope it was a good learning experience for you. I thank you, from the bottom of my heart, that I did not end up in the oven. I would also like to thank two collaborators on the lattice trap project, Yufei Ge and Tongyan Lin. Yufei, the undisputed master of trap fabrication at MIT, did a lot of fabrication and trap assembly for me, and Tongyan was a great collaborator throughout the arduous process of writing the lattice paper. I would also like to thank some folks at MIT who really helped us get started in the ion trap business, including Marko Cetina and Andrew Grier, who were building their first ion trap at about the same time we were; Dave Kielpinski, who helped fill in a lot of the gaps in our basic ion trap knowledge; and Prof. Vladan Vuletic, who imparted to us a small but sufficient fraction of his vast knowledge of lasers and AMO physics.

Ich möchte auch meinen Kollegen, die ich in Innsbruck getroffen habe, herzlich danken. Es war ja eine besondere Gelegenheit, eine kurze Zeit mit euch zu arbeiten und zu wohnen. Hartmut - vielen Dank für deine Hilfe und Lehren, und auch für einige schöne kurze Reisen in die Berge um Innsbruck herum. Ich danke auch Rainer Blatt, der so nett war, mich in seinem Labor willkommen zu heissen. Ich habe viel über Ionenfallen von ihm und seiner Arbeitsgruppe gelernt. Meine Frau und ich werden uns auch immer an den schönen Abend bei Herrn und Frau Draxl und ihren köstlichen Schnaps erinnern. Ich danke auch Christian Roos, Volckmar Nebendahl, und Piet Schmidt für die guten Diskussionen über Physik, und Wolfgang Hänsel für die guten Diskussionen über Physik *und* Musik. Herzlichen Dank an Jan Benhelm und Gerhard Kirchmair für ihre Hilfe und Geduld mit den PI-Lasern.

Ich habe viele neue Freunde in Innsbruck bekommen. Mit diesen Männern hatte ich, meistens ausserhalb des Labors, viel Spass. Ich danke Max "Captain Schnitzel" Harlander, Börge Hemmerling, und Lukas an der Lan, nicht nur für viele nette Abende, sondern auch für ihren Rat mit den Ionenfallen. Die Weisswurst-Kochgruppe wird immer ein Beispiel von Wie echte Männer Mittags essen sollen sein.

I would like to apologize for my horrible German, and also to thank the non-German-speaking members of the Innsbruck group. My collaborators Tony Lee, Nikos Daniilidis, and Sankar Narayanan were a pleasure to work with. They each brought a new perspective into the lab. I'd like to thank Nikos for some great times outside the lab too, especially our September trip to a little party they were having up in Munich, and for being willing to go for a hike when we were working on a beautiful Saturday. Thanks are due to Tony for showing me the ropes in the CCT lab, for increasing my tolerance of piano music (which I do enjoy in moderate amounts), and for occasionally sharing an offensive joke. Rene Gerritsma was always available for good conversation over a slice of pizza and a Kaiser, and I owe Felicity Splatt thanks for a good deal of discussion about the trials and tribulations of microtraps.

Coming now to the later years of my Ph.D., there are still more colleagues and friends to acknowledge. It was a pleasure to be joined in the lab by Shannon Wang, with whom I've had useful scientific and musical discussions. I appreciate the opportunities I've had to enjoy Shannon's singing voice, from chamber concerts to my own wedding. Shannon - you should totally start a band. I also owe much to Paul Antohi for his assistance with setting up the new cryostat. Kenan Diab, an undergraduate with whom I've worked recently, is a really smart guy, and it was an honor to work with him on something relatively practical, before he goes on to discover the Theory of Everything. Other colleagues with whom I've shared some good discussions and great times are, in no particular order: Liz George, Ruth Shewmon, Arghavan Safavi-Naini, Chris Pearson, Dave Schuster, Josh Folk, Terri Yu, and Peter Herskind. Thanks to all of you!

In addition to the above individuals, there are some friends I've had in Boston without whom it would have been most challenging to hold on to my sanity. I'd like to thank Doug and Bory Eastman for a lot of great times and some unique experiences. I'd also like to thank Simon Myrgren, who was a pleasure to room with and to hang out with. It was a lot of fun to live with and enjoy some scientific, musical, and philosophical discussions with Andrew and Abigail Cross. I know someday my grandchildren will scarcely believe that *I* was at the world premier of "Tonya and Nancy: The Opera." Finally, I'd like to thank two fellow Ohioans, who followed me out to Boston (cough), and were a great source of support all the while, Ryan and Stephanie Alvanos. When I think of all the busking, concerts, hanging out, camping trips, and sundry other activities that helped me to keep my cool during these six years, I am profoundly grateful. I wish you all the best until you follow me to Austin!

This brings me to my family. I can't thank my mother and father, Priscilla and James Clark, enough for their love and support over all these years. Without them, needless to say, I would not exist, much less have made it through graduate school. I'd like to thank Derek Clark for being a great brother, and Sarabeth Wilson for being a good girlfriend to him and friend to me. I appreciate all that Joanne Clark has done for me, as well. I also thank Mary and Paul Leidel for being great in-laws.

It's a bit unbelievable that this is really the end of the long, long period of long, long distance between me and my wife, Christina. Bumi - thank you so much for your patience, your love, and your support, from the moment I got into MIT and we had to part ways, through the moment I sprung that little surprise on you in New York, all the way to Erterreinpratz, our wedding, Ireland, and our house in Texas. It's been a great journey already, even though we're really still just at the beginning. You may tell the kids I'm on my way home.

Finally, I'd like to thank my grandparents, Gertrude and Russell Clark, and Joan Dayton, for all their support and love over the years. Sadly, one of my grandparents departed this world just before the completion of this work, but I believe he would have been as proud of me and as full of encouragement as he was during the rest of my life. This thesis is dedicated to the memory of Robert Jean Dayton.

Contents

List of Figures

List of Tables

Chapter 1

Introduction

The growth of computing technology over the past century has revolutionized how much of the human race lives, works, and interacts with itself. Although the miniaturization of transistors has enabled phenomenal computational feats, the same basic principles apply to modern devices that applied to Babbage's difference engine, and to the model system of Turing. These principles are those of classical physics, in which any given physical system exists in one and only one state at one time, evolves under the laws of Newton and Maxwell, and can remain in the same state upon being measured. What this means is that classical mechanics can be efficiently simulated on a computer: you need keep track only of the degrees of freedom of each subsystem separately. For instance, in a system of 100 two-level systems, you need only to keep track of the state (say, 0 or 1) of each individual system to completely specify the state of the entire system.

The discovery of quantum mechanics has led to a more correct, but rather more unintuitive view of the workings of the universe. In the quantum world, systems can be thought to exist in many possible configurations at once, evolve under a different dynamics, and are irreversibly altered when measured. This quantum strangeness of the world has posed a difficult problem for classical computers: given the laws of quantum mechanics, the number of numbers needed to specify a given system scales not linearly, but exponentially with the number of interacting subsystems. Our example of 100 systems is suddenly intractable, because now not 100 but roughly 2^{100} numbers (and complex ones at that) are required to specify the state of the system. Thus, even *printing* the complete state of the system cannot be done efficiently with respect to the number of particles. A host of problems that are described by quantum mechanics are thus intractable, from chemistry to solid-state physics and many others. Although the clever use of approximations, symmetries, and probabilistic algorithms yields satisfactory solutions to many problems, the full quantum dynamics of most systems cannot be simulated.

The first sign that this hopeless situation could be rectified came in 1982, when Richard Feynman suggested that perhaps one quantum mechanical system could be used to calculate the behavior of another. This visionary conjecture was confirmed by Seth Lloyd in

1996, right on the heels of Peter Shor's 1994 factoring algorithm. Factoring and quantum simulation were the first two practical (and classically intractable) problems that quantum computers were shown to be able to efficiently solve. Since that time, numerous proposals have been set forth to do quantum simulation of physical systems. And, slowly but surely, experiments have started to catch up. Throughout this thesis, we will encounter several small-scale implementations of quantum simulation.

There remain difficult problems to be solved, however, before a quantum simulator that can outperform classical computation is realized. In this thesis we address some of these problems. Our journey takes us across two different physical systems, nuclear spins and trapped ions, as we explore two of the most important problems facing quantum simulation: precision and scalability. The question of precision asks, for a given quantum simulation algorithm, how many digits of precision can be obtained, in principle, and how does this number scale with the space and time resources required? Also, in practice, how do the real-world effects of decoherence and control errors impact this precision? The exploration of this question in the context of solution-state nuclear magnetic resonance (NMR) forms the first part of this thesis.

Quantum systems are generally hard for classical computers to simulate, although there do exist classical techniques for solving some large quantum systems either exactly or approximately. To solve the exact dynamics of a general quantum system, however, requires a quantum simulator of the same number of interacting subsystems as the model being simulated. Moreover, each small quantum system is subject to the effects of decoherence and control errors. The question of scalability is: how do you build a reliable large-scale quantum simulator out of faulty small-scale quantum simulators? This is a highly nontrivial question, but trying to answer it for the case of trapped ions occupies the second and third parts of this work.

This chapter is organized as follows. In Sec. 1.1, we present a brief overview of the concepts of quantum information processing, including motivations and experiments. Sec. 1.2 is an introduction to quantum simulation, including its history, most important literature, and most enticing applications. In Sec. 1.3, we discuss two different approaches to quantum simulation, termed digital and analog, both of which are of importance to this thesis. Some of the outstanding challenges in quantum simulation, focusing on the issues of precision and scaling mentioned above, are then discussed in Sec. 1.4, which in turn motivate the main results and content of the thesis, presented in Sec. 1.5. The final section, Sec. 1.6, enumerates the contributions of the author and coworkers to this thesis, as well as resulting publications.

1.1 Quantum information

The concept of using the information contained in quantum states has led to the discovery of many new technologies, including computation, cryptography, communication, precision measurement, and simulation.

The possibility of exponential speedups for tasks such as factoring and discrete logarithms [Sho94], in addition to the square-root (but nonetheless attractive) speed-up of the quantum search algorithm [Gro97], has spurred a huge effort from theoretical and experimental research groups toward developing a practical quantum information processor. Many experimental successes using NMR, trapped-ion, and other physical systems have demonstrated all the basic protocols of quantum computation and quantum communication. The theoretical breakthrough of the discovery of quantum error correction [CS96, Ste96], and with it fault-tolerant quantum computation [Sho96, DS96, Got97], has provided a way to overcome the unavoidable errors that will afflict the delicate information encoded in quantum states. With error correction, however, comes a large overhead in the number of qubits (quantum bits) that must be employed.

The discovery of these algorithms has been accompanied by other interesting possibilities that make use of the tools of quantum information. One of these is *quantum cryptography*, which is a provably secure protocol for private key distribution [BB84]. A series of qubits is used in this scheme to transmit a key which can be used to decode a message; attempting to intercept the quantum message leads to a loss of the coherence of the message, and this can be detected and the key discarded in the event of eavesdropping. It is remarkable that the laws of physics guarantee privacy that no one may breech. This is to date the most technologically advanced application of quantum information, in that commercial quantum cryptography systems are already available [1].

Another exciting application of quantum information has been to precision measurement. There are two main approaches: the first has shown that phase measurement on a set of N entangled qubits has an error that scales as $1/N$, whereas the best that is possible classically is $1/\sqrt{N}$. Another more recent technique uses a two-qubit quantum logic gate in an ion trap to probe the structure of an ion that itself has no "cycling transition" and thus cannot be directly probed [SRL$^+$05]. Such techniques have improved our measurement of time and frequency, and perhaps also enable more-precise measurements of physical constants such as the fine structure constant.

The field of quantum communication is integral to many of the applications above, and is also interesting in its own right. The most noteworthy protocol for transmission of quantum information is *quantum teleportation*, in which a quantum state may be sent between two arbitrarily distant persons if they share a single entangled state in advance, and use two bits of classical communication per quantum bit [BBC$^+$93]. A related technique, *superdense coding*, permits the transmission of two classical bits using one qubit of a two-qubit entangled

---

[1] For example, see MagiQ: http://www.magiqtech.com

state [BW92]. Quantum communication also enables unconditional exponential gains in communication complexity for certain problems, e.g. as discussed in Refs. [HBW98, Raz99, BCWdW01, GKK$^+$08].

The application of quantum information processing that is of most interest to many physicists, and that motivates the work of this thesis, is quantum simulation. It is presented in its own section below.

Quantum information primitives have been implemented in a number of different physical systems, including trapped ions ([LBMW03], and many others cited in this thesis), nuclear spins ([VSB$^+$01, VC05], and many others cited in this thesis), superconducting circuits [MNAU02, MOL$^+$99, NPT99, HSG$^+$07], neutral atoms [ALB$^+$07, BCJD99, MGW$^+$03], and quantum dots [LD98, KBT$^+$06, PJT$^+$05]. Each of these systems carries certain advantages and disadvantages. Solution-state NMR was the first system in which small algorithms, including the simplest nontrivial case of Shor's algorithm, were implemented [VSB$^+$01]. The long coherence times of nuclear spins combined with the superb control techniques already developed (and developed further still by quantum information researchers [VC05]) enabled this system to get off the ground fairly quickly. However, NMR cannot scale to large numbers of qubits. Trapped ions have now emerged instead as the leading technology, because they combine coherence times even longer than nuclear spins in solution with a now highly-developed control apparatus, superior measurement accuracy, and several promising avenues to scalability.

Of course, no technology has yet been scaled up to even more than ten qubits, meaning that a quantum computer or simulator that can outperform classical computation has not yet come close to being realized.

1.2 What is quantum simulation?

We now begin to explore the overarching theme of this thesis, quantum simulation. Quantum simulation is the use of one controllable quantum system, referred to in this thesis as the *model system*, to calculate properties of some other quantum system that is more difficult to control, which we call the *target system*. For instance, one may map a Hamiltonian that describes a set of interacting fermions to a set of spin-1/2 systems which an experimenter can control well, such as (in this thesis) nuclear spins in molecules or the electronic states of trapped ions. If controls are available to apply the same effective dynamics on the model system that is thought to govern the target system, then predictions regarding the target system can be inferred by performing experiments on the model system. Although deceptively simple as stated here, in practice it is difficult to discover good methods for performing quantum simulation. Of course, the person carrying out the quantum simulation also must make the assumption that the target system obeys a specific Hamiltonian. This could be stated in a positive light, in that simulation by model systems may inform us whether the target system obeys a given Hamiltonian at all!

The concept of quantum simulation was first conjectured by Feynman in 1982 [Fey82], and subsequently rigorously proven by Lloyd in 1996 [Llo96]. Following this, a number of significant papers presented in detail methods for simulating a variety of physical systems. Abrams and Lloyd discovered algorithms for calculating the eigenvalues and eigenvectors of a Hamiltonian on a quantum computer [AL97] and for simulating the dynamics of fermionic many-body systems [AL99]. Following this, a 2001 paper presented a method for efficiently simulating quantum chaos and localization [GS01]. In 2002, a paper of great importance to our work was published by Wu *et al.*, which proposed a method for simulating pairing models on an NMR-type quantum computer [WBL02]. Jumping ahead a bit, in 2005 an interesting report was published, detailing classical simulations of a quantum computer calculating molecular energies [AGDLHG05]. This paper suggested that, using only tens of qubits, a quantum computer might indeed be able to solve certain problems in chemistry more efficiently than a classical computer can. This paper was followed-up by an article detailing a general polynomial-time algorithm for the simulation of chemical dynamics [KJL$^+$08].

The above partial listing of the important literature is meant to illustrate the breadth of interest in quantum simulations, but also an important caveat: it is not trivial to design a quantum simulation algorithm for a given quantum system. There is no "general purpose" quantum algorithm that can solve any problem in quantum mechanics efficiently. Although it may be efficient to implement a given simulated Hamiltonian, it is not, in general, straightforward to design an efficient *measurement.* It is fairly easy to see why: the length of the state vector for n qubits is of length 2^n. Even if the state could be measured without collapse, inquiring as to the state of the whole system is intractable. Part of the art of designing quantum simulations is asking the *right questions.*

We would like to note a common theme throughout this thesis and a dominant one in the current effort of researchers worldwide. Some of the most interesting and classically-intractable models occur within the realm of solid-state physics, especially with regard to superconductivity. The BCS Hamiltonian is a model for which some good approximate methods (such as the density matrix renormalization group) exist, but which eludes a full quantum-mechanical description on a classical computer. The paper of Wu *et al.* [WBL02] provides a way for a quantum simulator to calculate the low-lying spectrum of this Hamiltonian in polynomial time.

This is only the beginning, though. BCS theory works well for Type-I superconductors, and the main advantage of quantum simulation of this model would be in calculating the spectra to greater precision. However, the mechanism behind Type-II superconductivity is still poorly understood. It has been conjectured that the phenomenon of spin frustration in a 2-D lattice of antiferromagnetically interacting spins may hold some insight into the dynamics of high-temperature superconductors [GP00, NGB92, BDZ08]. Research is active into using both neutral atoms and trapped ions to realize such spin Hamiltonians [DDL03, PC04b]. In both cases, the idea differs from those mentioned above, in that rather than employing a sequence of discrete control pulses, they instead propose the creation of model Hamiltonians using a limited set of continuously-varying controls. Similar ideas have been set forth for the simulation of Bose-Hubbard models, also using trapped ions or neutral atoms [GME$^+$02, PC04a]. In these examples, the opportunity arises to observe whether the target system behaves qualitatively like the model system being studied for similar sets of parameters.

1.3 Models of quantum simulation

The quantum simulations introduced above may be divided into two distinct types, or models: in the first, of which the paper of Wu *et al.* [WBL02] is a fine example, a quantum simulator is prepared in some initial state and then manipulated with a set of *discrete* pulses, a situation akin to a digital computer. In fact, this type of simulation bears other resemblances to classical digital computation, such as the fact that error correction codes may be used [CS96, Ste96, Sho96, DS96, Got97]. We refer to this type of simulation as *digital quantum simulation*. The second type, which the neutral atom community has recently excelled at, involves creating an effective Hamiltonian that is controlled by *continuously* adjusting the relevant parameters. This type is akin to classical analog computation, and we refer to it as *analog quantum simulation*. This approach lends itself to more qualitative questions, such as what phase (superfluid, insulator, etc.) the particles occupy within some region of parameter space. Let us dig a bit more deeply into this distinction, because both types are of interest in this work.

1.3.1 "Digital" quantum simulation

Digital quantum simulations are characterized by the use of discrete quantum gates to implement the desired Hamiltonian. To clarify the terminology, a quantum gate is a (usually) unitary operation that is applied to some set of qubits for a finite amount of time; any gate involving more than two qubits may be decomposed into a sequence of one- and two-qubit gates. Measurement is also considered a quantum gate, and is typically assumed to be of the strong, projective variety. The weak measurements used in nuclear magnetic resonance (NMR) are a notable exception.

This approach has some very appealing advantages: for one, any region of parameter space may be probed, since the interactions are entirely engineered by control pulses from the experimenter. The other very big advantage is that quantum error correction techniques may be applied, and indeed will be necessary when the system grows to a large enough size. However, quantum error correction schemes generally require a substantial increase in the required number of control pulses, increasing the likelihood that systematic control errors will reduce the accuracy of the simulation.

Nevertheless, there are a number of interesting problems in quantum simulation that will require the ultimate digital quantum simulator, a universal quantum computer. A quantum computer (or simulator) is universal if it employs a set of gates that can approximate any unitary transform to arbitrary precision. It was shown in Ref. [FKW02] that quantum computers can efficiently simulate topological field theories. Intimately related to such theories is the Jones polynomial, which is a *knot invariant* of knots in R^3 which is invariant under transformations of the knot. A quantum algorithm for approximately evaluating certain instances of this polynomial is presented in Ref. [AJL08], whereas no efficient classical algorithm is known to solve the same problem. Together, these results imply the possibility of using quantum computers to model some of the most fundamental aspects of nature.

1.3.2 "Analog" quantum simulation

Analog quantum simulation consists of preparing a system in some initial state (which may indeed involve discrete gates), and then applying some global effective Hamiltonian, perhaps adiabatically, that permits one to mimic the exact dynamics of the target system. The key difference from digital quantum simulation is that the control variables are varied continuously. Such approach enables, for instance, the observation of the phases that the target system exhibits in various regions of parameter space, for a given Hamiltonian. In some sense, given the Ising-type interaction between spins in NMR, that system could already be considered to be an effective Hamiltonian system. However, this doesn't give one any control over what exactly the effective Hamiltonian is; refocusing pulses that modify this interaction fall more under the blanket of circuit model simulation, in that they are discrete control pulses.

The analog approach has shown much promise for trapped ion and neutral atom systems, leading to a number of stimulating papers. Two 2004 papers, Refs. [PC04b] and [PC04a], have stimulated much research on analog quantum simulators. The former describes a method for simulating quantum spin models using trapped ions; they propose the creation of effective Ising or Heisenberg interactions between ions by using state-dependent optical forces. In the latter, the quantized motional states of trapped ions are made to simulate bosons obeying a Bose-Hubbard Hamiltonian. It is predicted that in such a system, among other phenomena, Bose-Einstein condensation of phonons could be observed.

Neutral atom systems have already had some remarkable experimental success with this type of quantum simulation, in that several groups have simulated fermionic and bosonic lattice models in an optical lattice. For example, the superfluid-Mott insulator phase transition has been observed in ultracold ^{87}Rb atoms in an optical lattice [GME$^+$02]. Other notable papers include the simulation of the Mott insulator phase of interacting fermions [JSG$^+$08] and imaging of the Mott insulator shells in a Bose gas [CMB$^+$06]. Remarkably, a recent analog quantum simulation settled a long-standing question regarding the phase diagram of an ultracold Fermi gas with respect to temperature and spin polarization [SSSK08]. It is even possible in theory to simulate quantum magnetism in a neutral atom system by tuning the optical lattice strength [DDL03]. However, such a system has not yet been realized, in part due to the very low temperatures required to observe it [BDZ08].

Analog simulations offer distinct advantages. In the case of optical lattices, one may find that the Hamiltonian governing the particles is also an interesting Hamiltonian to simulate, e.g. a Bose-Hubbard model. This is not true in every case, and sometimes other forces are added, i.e. in Ref. [JSG+08]. Nevertheless, analog simulations provide a route to studying many-body phenomena without requiring the degree of control available in a digital quantum simulator.

The advantages of analog simulation also differ from system to system. One difference between the neutral atom and ion trap implementations of the Bose-Hubbard model is the individual control over ions that ion traps offer. For instance, in the proposal of Porras and Cirac [PC04a], it is possible to adjust the trapping potentials to create site-specific interactions. Although still analog, such control permits a wider variety of simulated Hamiltonians than neutral atom BEC's. The advantage, by contrast, of the optical lattice experiments is the ability to rapidly incorporate many bosons in many ($\mathcal{O}(10^5)$) sites [GME+02], a situation that has not yet been realized in ion traps.

The analog approach also has some drawbacks. For one, the ability of an experimenter to control the Hamiltonian is generally more constrained than it is for digital simulations. For instance, in the above optical lattice experiments, both the "onsite" terms, which describe repulsion between atoms at the same site, and the "hopping" terms, which describe motion of atoms from site to site, depend on the depth of the optical lattice U. Changing this depth changes the *ratio* of onsite to hopping interaction strengths, which is what permits observation of interesting phenomena, e.g. phase transitions. However, the accessible regions of parameter space are also constrained by U. Another drawback of analog quantum simulation is that quantum error correction (if needed) is not possible. Digital quantum simulations, by contrast, are seen to be both more general and more robust, but also significantly more difficult to implement.

1.3.3 Comparison of digital and analog quantum simulation

We would now like to compare the digital and analog approaches for both classical and quantum simulation of quantum mechanical systems. The main question is the resource requirements, in both space and time, required to perform a given simulation. In the examples below, we will consider a simulation of the dynamics of a system of n spin-1/2 systems (qubits). In this section, we also focus entirely on the *dynamics* of the system, neglecting for the time being the resources needed to extract the answer.

We begin with classical simulation. What resources are required to simulate n qubits on a classical computer? In the digital case, the dimension of the state vector is 2^n, which is

	Classical	Quantum
Digital	Space: 2^n Time: $T2^{2n}$	Space: n Time: Tn^2
Analog	Space: 2^n Time: T	Space: n Time: T

Table 1.1: A comparison of the resources required to implement the dynamics of digital and analog simulation of quantum systems, using both classical and quantum simulation. We consider a system of n qubits simulated for a total time T.

the spatial resource requirement. In general, the time needed to simulate the system is also exponential, since an exponentiation of a 2^{2n}-element matrix is required to propagate the state vector forward in time. Further, the total simulation time T adds a constant factor to the total time required. For the analog case, suppose that the implementation is done using a set of voltages which specify the real and complex parts of the state vector amplitudes to the maximum possible precision. In this case, 2^n individual voltages will be required to specify the state, meaning that the spatial resource requirement is 2^n, the same as the digital case. However, the time required to perform the evolution is specified only by the total time T.

Let us now consider the quantum-mechanical case. For digital quantum simulation, the space required scales as n, since each qubit in the model system may represent one qubit in the target system (and error correction adds only a polynomial number of qubits). The time required to implement the unitary evolution is proportional to n^2, but only for Hamiltonians that can be modularly exponentiated efficiently [NC00]. The restrictions on simulable Hamiltonians are described in detail in Ref. [Llo96]. In the analog case, n model qubits again map to n target qubits, but the total simulation time is proportional only to T, as in the classical case.

We summarize these results in Table 1.1, which describes the space and time resources required for implementation of the quantum dynamics, but does not include the error in the result. Although at first glance, it may seem that quantum methods are always superior to classical, and analog methods always superior to digital, this is not the case when the effects of errors are considered, or when probabilistic approaches are considered.

1.4 Challenges for quantum simulation

Quantum simulation is a tantalizing prospect, but there are good reasons why we don't already have a large-scale quantum simulator. The three main reasons can be classified broadly as decoherence, precision limitations, and scalability. We discuss all of these in this section.

1.4.1 Decoherence

Decoherence is the irreversible loss of information from a quantum system to its environment. It arises from interactions between a quantum system and a "reservoir" of states too numerous to keep track of. Thus, although the full evolution of the system and reservoir together is unitary, the evolution of the system alone exhibits non-unitary dynamics. Decoherence is present in any quantum-mechanical system, but the question always is the *degree* to which the evolution is altered by decoherence. The main questions studied by researchers are the sources of decoherence and the methods of reducing it. Since nuclear spins and ion traps are the quantum systems used in this thesis, we discuss here the main sources of decoherence for each.

The two primary types of decoherence relevant to nuclear spins are *amplitude damping* and *dephasing*. Each affects a different part of the density matrix of the quantum system. Amplitude damping affects the on-diagonal elements, or "populations," causing population transfer from one state to another, typically from an excited state to a lower-energy (or the ground) state. However, due to the low spin polarization of a room-temperature nuclear spin system, the thermal state is a nearly equal mixture of the ground and excited spin states. In NMR, the rate at which this occurs is given by the inverse of the T_1 time. Dephasing affects the off-diagonal elements, or "coherences," effectively changing the relative phases between different terms of the quantum state, and thus destroying coherence. The rate of this process is characterized in NMR as $1/T_2$. The T_2 time arises from a number of both macroscopic and microscopic sources.

An important macroscopic source of dephasing in NMR is inhomogeneities in the static and oscillating magnetic fields used to control the nuclei. Such inhomogeneities can be corrected in one of two ways: first, by measuring and improving the field homogeneity, and second by using spin-echo techniques to correct for the inhomogeneities that remain. Still, a number of microscopic and uncontrollable processes contribute to limiting the coherence time, including the fundamental cause of the T_1 time: spin transitions induced by thermal excitation of spins.

Decoherence of the quantum states of trapped ions, by contrast, includes processes that affect either the internal (electronic) or external (motional) degrees of freedom. Both the electronic and motional quantum states are important for the storage and processing of quantum information. Decoherence of electronic states can be attributed to two primary sources: scattering events and control errors. For instance, the excited state lifetime in a qubit separated by optical wavelengths is fundamentally limited by spontaneous emission. For hyperfine qubits manipulated with a laser Raman transition, however, the spontaneous scattering rate defines this limit [OLJ$^+$95]. Some common control errors include fluctuations in the laser intensity or polarization, as well as fluctuations of ambient magnetic fields, and in practice these fluctuating controls limit the coherence times [BKRB08]. Motional states, by contrast, decohere largely due to heating caused by fluctuating potentials on the trap electrodes [TKK$^+$99]. This heating has been observed to scale roughly as $1/d^4$, where d is the distance from the ion to the nearest electrode [DOS$^+$06].

Several steps have been taken to reduce these sources of decoherence in ion trap systems. Decoherence due to fluctuating magnetic fields has been suppressed by the encoding of qubits in a decoherence-free subspace [LOJ$^+$05, HSKH$^+$05], and also, for hyperfine qubits, by using a magnetic field-insensitive transition [LOJ$^+$05]. Errors due to spontaneous scattering can theoretically be eliminated by performing gates using magnetic fields and radiofrequency pulses rather than laser light [CW08, OLA$^+$08, JBT$^+$08]. Although decoherence of internal (electronic) states of the ions is of considerable importance, our efforts to develop ion trap architectures are mainly driven by the need to minimize motional state decoherence, or heating. The problem of motional decoherence has been partially and practically addressed by the demonstration of suppression of heating rates by several orders of magnitude through cryogenic cooling [LGA$^+$08, DOS$^+$06]. Recently, the temperature-dependence of this heating rate has been more systematically characterized [LGL$^+$08]. However, the sources of this noise are still not completely understood.

Considerations of the effects of decoherence have a major impact on the next two limitations of quantum simulation presented.

1.4.2 Limitations to Precision

In quantum simulation, one seeks to calculate some specific property of a quantum system, for instance an eigenvalue of a Hamiltonian. The precision to which a given quantity can be calculated depends on any inherent limitations in the algorithm used, as well as on factors such as imperfect controls and decoherence. Therefore, we may frame our investigations by two questions:

1. For a given quantum simulation algorithm for calculating some quantity Δ, what is, in principle, the expected error ϵ in the measurement of Δ, as a function of the space and time resources required?

2. How does ϵ change as a certain systematic or random error in the control pulses applied to the system is introduced?

We begin the discussion of the first question with an example. Suppose that one wished to calculate the difference Δ between the energy eigenvalues of two states $|1\rangle$ and $|2\rangle$. One way to do this is to prepare a superposition of the two states, then evolve under some simulated Hamiltonian for a set of discrete times t_n, for N total timesteps. Measurements of a suitable operator on the system at each time will oscillate at a rate Δ. Determination of Δ can then be done by classically Fourier-transforming the measurement results. With how much *precision* can Δ, in principle, be measured? Certainly, in the above scheme, the sampling rate plays a role: more points will lead to more precision. Therefore, we expect that the error ϵ scales as $1/N$. Noting that the precision of the final result is proportional to $1/\epsilon$, we find that each additional digit of precision requires an exponential increase in N, and therefore the time required to complete the simulation scales exponentially with the precision. We expect also that the finite coherence time, in the absence of error correction, leads to a hard limit on the achievable ϵ. Note that this is a separate issue from the number of experimental averages required, due to shot noise, to obtain each experimental data point with a given signal-to-noise ratio (SNR). In this case, SNR $\propto 1/\sqrt{\mathcal{N}}$, where $\mathcal{N}$ is the number of averaged experiments.

How general is this scaling behavior of the precision? Does it apply only to the above method, or to others as well? Actually, it applies also to algorithms that employ the quantum Fourier transform, such as those proposed by Lloyd for calculation of eigenvalues and eigenvectors of a Hamiltonian [AL99], and for quantum simulation of the dynamics of fermions [AL97]. Why should the precision $1/\epsilon$, in general, scale as the number of gates N? Suppose one wished to measure the quantum state itself. The Hilbert space of a system of n qubits is 2^n-dimensional. If one wished to read out the state exactly, 2^n measurements would be required. Each time, the system would collapse into eigenstates of the measurement operator, and averaging would reveal the amplitude of each basis state. Measurement of the eigenvalues of a Hamiltonian also requires measurement of a specific quantum state with some suitable measurement operator, and this measured value is also obtained with a precision that scales inversely with the number of measurements. Therefore, an efficient quantum simulation necessarily returns an approximate answer. The strength of quantum simulation comes from the ability to implement the *dynamics* efficiently. A large quantum system with n qubits cannot be efficiently represented on a classical computer, even if only approximate values are used for the amplitudes of each basis state. An exact replication of the quantum dynamics requires a quantum simulator.

We now move on to the second question above, concerning the effect of control errors. We expect that a systematic control error will alter the final answer because it causes a systematic deviation in the simulated Hamiltonian. Numerous techniques exist for compensating for such errors; however, this compensation increases the number of required pulses (e.g. see Ref. [BHC04]), which is a disadvantage in light of a finite coherence time. We expect that additional pulses will require more time to obtain a certain level of precision. For analog quantum simulation, by contrast, such composite pulse techniques are not possible. Instead, some constant error in the applied Hamiltonian induces a constant error in the final result. Fluctuating control errors, by contrast, generally lead to decoherence, due the the fact that they effect evolution under an uncontrolled and unknown Hamiltonian. The precision limitations due to control errors can be expected to depend on the physical implementation of the quantum simulator, and must be studied in detail for each.

How does this scaling with precision compare to classical simulation? For digital classical simulation, additional bits of precision may be obtained by adding only one bit for

	Classical	Quantum
Digital	Space: $2^n\mathcal{O}(\log 1/\epsilon)$ Time: $T2^{2n}$	Space: n Time: $Tn^2\mathcal{O}(1/\epsilon)$
Analog	Space: 2^n Time: T Precision: $\mathcal{O}(\log 1/\epsilon_{fix})$	Space: n Time: $T\mathcal{O}(1/\epsilon)$

Table 1.2: A comparison of the resources required for digital and analog simulation of quantum systems, using both classical and quantum systems, and taking into account the precision obtained. We consider a system of n qubits simulated for a total time T. The error due to projection noise is denoted ϵ, while the fixed error of a classical analog computer is denoted ϵ_{fix}.

each additional decimal place of precision. Therefore, a factor of $\log(1/\epsilon)$ multiplies the space requirement of 2^n qubits. It is interesting that the cost of increasing the precision differs so greatly between classical and quantum simulation: for classical, digital systems, one requires additional *space* that is polynomial in the precision, while for quantum simulation one requires additional *time* that is exponential in the precision! For a classical analog simulation, by contrast, in which each state amplitude is represented as a continuous variable, there will ultimately be some level of noise that limits the precision with which each value may be represented. This may be quantified as a fixed error ϵ_{fix}. For classical analog simulation, the precision is ultimately limited by this fixed error, scaling as $\log(1/\epsilon_{fix})$. We summarize the resource requirements for simulation in light of the obtainable precision in Table 1.2.

So far we have considered numerically exact classical simulations, which attempt to mimic the full quantum dynamics of a quantum system, which is always inefficient with respect to the system size. However, there do exist classical algorithms that can solve certain problems exactly or approximately, and for many problems such methods are entirely sufficient. Three well-known numerical (and approximate) methods are the numerical renormalization group (NRG) [Wil75], density matrix renormalization group (DMRG) [Whi04], and quantum Monte Carlo methods. Although each method is applicable to many problems, each also has inherent limitations to the types of problems that may be simulated. The NRG and DMRG algorithms work only in cases for which the original system Hamiltonian may be mapped to a local Hamiltonian defined on a one-dimensional chain [VMC08]. Monte Carlo methods, by contrast, fail to efficiently simulate fermionic systems, due to the so-called "negative-sign problem" [TW05]. Nevertheless, new methods are still being found for simulating additional classes of quantum systems. Notable examples are a method for simulation of 1-D quantum spin chains [Vid04] and the recently-discovered projected entangled-pair state [VC08] and time-evolving block decimation [Vid07] algorithms, which have been applied to the simulation of 2-D quantum spin lattices [JOV$^+$08] for the case of translational invariance, when an infinite lattice is assumed.

To conclude our discussion of precision, we note that even as the number of classically simulable quantum systems grows through the discovery of new algorithms, it is generally believed that classical computation is not able to approximate any general quantum-mechanical system. If it could, then there would be no speedup of quantum computation over classical; a classical method would then exist for factoring, searching, and all other quantum algorithms, by classical simulation of a quantum simulator. For the quantum systems for which no classical approximation is known, quantum simulation is an attractive possibility, despite the inherent precision limitations.

1.4.3 Scalability

Scalability is the study of how to take a small number of faulty systems and connect them to form one arbitrarily large, reliable system. This is an important subject in quantum computation; the solution of computationally hard problems requires such a network of qubits. To begin with, we note that a digital quantum simulator is a quantum computer that may not have a universal set of gates; that is, it may not require sufficient controls to simulate any Hamiltonian, but rather just the Hamiltonian of the problem of interest. A quantum simulator may not need the same degree of control, but the problem of scalability is the same. Analog systems will also be composed of many distinct subsystems, but the form of the scaled-up architecture may be different. For example, an optical lattice presents a framework for simulating the Bose-Hubbard model on a large scale, but one does not need the ability to control the internal states of individual atoms, or to implement deterministic two-atom gates, that would be necessary for digital quantum simulation.

There is still the question of how large a quantum system will need to be to implement quantum dynamics that are intractable on a classical computer. A recent benchmark [RMR$^+$07] sets the record, to our knowledge, of exactly simulating 36 interacting spin-1/2 systems on a supercomputer. The importance of this number is that even if a given idea for scalability does not lead to *arbitrarily* large systems, it may still be of great use as a quantum simulator, and be able to exactly simulate quantum dynamics that classical computers cannot. To scale to this or a larger number of subsystems, however, requires a system that satisfies certain conditions. These are important for creating a system in which sufficient control is available to execute a given simulation, and to measure the result.

DiVincenzo criteria

To begin the discussion of scalability, we present the five basic DiVincenzo criteria [DiV00], which are the generally agreed-upon requirements for a scalable quantum computer. Although these were originally proposed for quantum computation, they still hold for less-general quantum simulations, albeit in a modified form, and we review them here.

1. A scalable physical system with well-defined qubits.

2. Initialization to a simple fiducial state such as $|000...0\rangle$.

3. Decoherence times much longer than the gate times.

4. A universal set of quantum gates.

5. High efficiency, qubit-specific measurements.

We now briefly summarize how these criteria differ for quantum simulation. The first criterion certainly holds, although the form of the large-scale quantum simulator may be different for analog, as opposed to digital, quantum simulation (as discussed above). The second and third also hold, but the initial state will depend greatly on the problem being simulated. It may be necessary to create a state such as $|000...0\rangle$, which may then be transformed into the correct initial state through single-qubit rotations. An example of this is in Ref. [WBL02]. However, it is also possible that the relevant degrees of freedom may be described by continuous variables. In the example of cold atoms in an optical lattice, it is typically necessary for the translational degrees of freedom of the atoms to be cold; however, the simulation itself may not depend on the internal states. This is one way in which analog quantum simulation enables simulation with less control than digital; in the digital case, the momenta of the atoms would be discretized and then programmed into a set of qubits at the beginning of the simulation.

The fourth criterion must also be modified for quantum simulation, and again varies between the digital and analog types. Depending on the problem being implemented, a set of controls less powerful than those of a universal quantum computer may be required. The optical lattices are again a good example. In this analog simulation, sufficient control is present to simulate a Bose-Hubbard model. By contrast, a universal quantum simulator is equally as powerful as a universal quantum computer, because for either any arbitrary Hamiltonian (and corresponding unitary gate) may be approximated to arbitrary accuracy. It is also true, however, that for certain digital quantum simulations, only a subset of a universal gate set will be required. Finally, high measurement fidelity is important in both analog and digital quantum simulation, but for the analog variety, it may be a measurement of a continuous variable, and "qubit-specific" may not have meaning. Measuring the density of atoms in space is an example of this.

Scaling up quantum simulators is a major research question no matter what physical system forms the qubit. The two physical systems that are studied in this thesis are solution-state NMR and trapped ions; however, solution-state NMR is intrinsically unscalable. Ion traps, by contrast, do satisfy all the DiVincenzo criteria. The only caveat is that although ion traps are scalable in principle, we do not yet know which method for scaling them up will prove most effective. We therefore focus here on the scalability of ion traps.

Proposals for scaling up ion trap quantum simulators

Quantum control of up to eight ions in linear Paul traps has now been demonstrated [HHR$^+$05, LKS$^+$05]. The challenge in controlling that number and larger numbers has many sources. For one, the number of motional normal modes that must be effectively cooled depends linearly on the number of ions in the trap. This is a difficulty mainly for schemes that require ground state cooling. Also, the ion-ion distance, and therefore coupling rate, is not constant in a chain of more than three ions. These issues encourage one to come up with ways of networking ions that are stored in different traps, or finding single-trap designs in which quantum simulations may be implemented. We present below some of the proposals for scaling up ion trap quantum simulators.

- Store a small number of ions in each of a large number of separate Paul traps, Move ions from trap to trap to allow them to interact [KMW02].

  The traps for shuttling ions require microfabrication, mainly because dc control electrodes need to be close to the ions to perform shuttling. There are two broad classes of microfabricated traps, 3-D and 2-D. 3-D traps have electrodes in more than one plane, allowing for a deeper trap (all else being equal) [MHS$^+$04, SHO$^+$06, BWG$^+$05]. 2-D traps, also called "surface-electrode" traps, have all electrodes fabricated in a single plane. These are shallower, but simpler to fabricate [CBB$^+$05, SCR$^+$06]. The Wineland group at NIST in Boulder uses a segmented trap for their quantum operations, and already incorporates ion movement into their protocols, e.g. in [BCS$^+$04]. Ion movement has also been demonstrated in a T-junction [HOS$^+$06], and in a wider variety of planar geometries, albeit with charged microspheres rather than atomic ions [PLB$^+$06].

- Connect ions using photons.

  Some encouraging early progress has also been made in networking ions using photons. For instance, in Ref. [MMO$^+$07], entanglement of ions at a distance was demonstrated. This approach has the advantage that the motional states of the ions do not have a role in storing or processing quantum information, implying that the motional state of the ion can be neglected, as long as the ions are confined to a region of space much smaller than the photon wavelength (Lamb-Dicke limit). Accordingly, the cooling requirements are less stringent than those for other quantum operations, such as the Cirac-Zoller gate [CZ95].

- Connect ions using wires.

  The idea is that the image charges due to the oscillations of one ion are transmitted over a conductive wire to another ion. In this scheme, the ion-ion coupling arises from the motional state of the ions, even though the ions are located in different traps. This was discussed in Ref. [TBZ05] in the context of connecting ions to superconducting qubits, and in Ref. [SGA$^+$05] in the context of connecting individual ions in Penning traps. Theoretical calculations of this situation are presented in Ref. [HW90]. To date, this approach has been explored less than ion movement or photonic coupling. However, it may allow for switchable interactions between ions, as with photonic coupling, but with a simpler experimental setup. The coupling wires could, perhaps, be integrated into the trap structure itself.

- Do quantum operations on a large planar crystal of trapped ions.

  This has been discussed theoretically in Ref. [PC06], and may be used to implement in two dimensions the proposals of Refs. [PC04b, PC04a]. Despite the need for complex networking of trapped ions for digital quantum simulation, such simpler structures may be appropriate for certain analog simulation protocols, or for "one-way" quantum computation [RB01]. For example, a quantum simulation of 2-D spin models [PC04b] could be done using such an architecture.

1.5 Main results and organization of this thesis

In this thesis, we explore experimentally and theoretically the three challenges discussed above: decoherence, precision limitations, and scalability. The thesis is divided into three parts.

Part I

In this part we ask the question: with what degree of precision can one (in principle, and in practice) calculate the eigenvalues of a Hamiltonian using a quantum simulator? We examine the theoretical bound on the precision, and also study the effect of control errors on the fidelity of the simulation. To this end, we report on the quantum simulation of the BCS pairing Hamiltonian using a three-qubit nuclear spin system. Although a small and non-scalable system, NMR offers the possibility to illustrate key features of quantum simulation that should be applicable also to much larger systems. Our primary question is the amount of precision that can be obtained using digital quantum simulation, both in general, and in the specific case of an NMR implementation of the digital quantum simulation presented in Ref. [WBL02].

Chapter 2 explains how NMR quantum simulation works, starting with the NMR Hamiltonian and continuing with the state of the art prior to our work. We discuss the limitations to the precision of a simple NMR quantum simulation reviewed within the chapter.

In **Chapter 3**, we present our implementation of the quantum simulation, including the algorithm and specific parameters used, experimental apparatus, results, and analysis. We find that digital quantum simulations are *inefficient* with respect to the number of digits of precision in the final result. We also note that the inefficiency increases if error correction techniques need to be used, such that the time required scales as $\mathcal{O}(1/\epsilon^r)$, where $r \geq 2$. Errors in the final answer are also induced by systematic control errors; we find that evolution during single-qubit pulses due to the "always-on" NMR interaction Hamiltonian is the main source of these errors. The time resources needed for error correction and to compensate control errors may be compared to Table 1.2, which presents the required resources accounting only for the error in the final measurement estimates.

Our results do not rule out the usefulness of digital quantum simulations. They merely point out that quantum simulation outperforms classical only for specific problems and numbers of qubits. It remains exponentially more efficient than classical simulation for quantum systems for which no good approximate classical simulation is known, as long as only fixed precision is required.

Part II

In the second part, we ask: how can one build a scalable two-dimensional array of trapped ions that is suitable for analog quantum simulation? We will be focused, in particular, on the goal of analog simulation of quantum spin models, particularly spin frustration. In pursuing the answer to this question, we design, test, and evaluate two types of ion trap that may be suitable for this purpose, a lattice ion trap and an elliptical surface-electrode ion trap. It is essential not only to design, model, build, and test these traps, but also to examine how analog quantum simulation might actually be performed in such traps. It will be important to estimate the expected simulated coupling rates in each type of trap, including all rf and dc fields that act on the ion. This requires us to ask, for example, how the motional frequencies and simulated coupling rates scale with the size of the trap, how the potentials that produce an effective Hamiltonian might be applied, and how rf-induced micromotion might affect the fidelity of analog quantum simulations.

In **Chapter 4**, we begin with an introduction to quantum simulation with trapped ions, including ion trap Hamiltonians, control techniques, and proposals for analog quantum simulation. We particularly focus on the proposal of Porras and Cirac for the study of 2-D spin models [PC04b]. The goal of building a 2-D simulator of antiferromagnetic spin lattices, in which phenomena such as spin frustration could be observed, is the prime motivation for the rest of the work in this part.

In **Chapter 5**, we examine the lattice ion trap architecture, in which ions are confined in a 2-D array of individual potential wells, enabling the trapping of ions in virtually any configuration (since sites can be loaded selectively) with a well-defined spacing between ions. Such a trap could provide the stable array of trapped ions that is required for scalable analog quantum simulation. We experimentally test certain predictions about the trapping potentials, most importantly the motional frequencies of the ions, and find that the traps agree well with our theoretical predictions. However, despite the apparent advantages of the lattice architecture, we discover a serious flaw in this idea: the physics of ion traps requires an increase in the motional frequencies of the ions as the trap scale, and with it the ion-ion spacing, decreases. This means that the coupling between ions a distance d apart is actually much less than it would be if the ions were in the same trapping region, with the same d. We find that this lattice trap design is not promising for simulation of 2-D spin models.

Chapter 6 introduces surface-electrode ion traps, in which all trapping electrodes reside in a single plane. The specific type of trap used in this chapter is based on printed circuit board technology, which is useful for prototyping a wide variety of ion traps, including those that could be used for analog quantum simulation. Surface-electrode traps have some particular challenges, though: they are shallower than comparable three-dimensional traps, and are more sensitive to the buildup of stray charges on the dielectrics that isolate the electrodes from one another. How to efficiently load such traps with minimal accumulation of stray charge is thus an important technical question. In this chapter, we compare and contrast the advantages of electron-gun loading in the presence of a buffer gas and laser ablation loading of these ion traps. These are compared to the photoionization technique used in Chs. 5 and 7. We find that among the three loading methods, photoionization is superior to electron impact and ablation loading for our purposes, in that it succeeds in loading shallow traps comparably to ablation loading, but without as much stray charge buildup on nearby dielectrics. However, we point out certain situations in which ablation or e-gun loading may be more useful. Most importantly, we demonstrate the PCB ion trap technology that we use for prototyping new designs for analog ion trap quantum simulators.

In **Chapter 7**, we turn to an alternative method for realizing a 2-D array of ions for analog quantum simulation, a surface-electrode elliptical ion trap, in which ions in a single trap region align into a 2-D crystal through mutual Coulomb repulsion. Although the coupling rates are much higher than in a lattice trap with the same ion-ion spacing, this scheme suffers from two limitations: the structure of ion crystals leads to a non-uniform spacing between neighboring ions, and rf-driven micromotion is present that cannot be removed. We present calculations of the pertinent properties of the trap, including motional frequencies and ion crystal structure, and test them with experimental measurements. In an effort to reduce motional state decoherence, these traps are tested in a cryogenic system. We also demonstrate theoretically how quantum simulations may be done even in the presence of micromotion, showing that micromotion leads to a *systematic* shift in the simulated coupling rate between each pair of ions. Finally, we discuss the possibility of producing this force with a magnetic field gradient rather than an optical force, and discuss scaling down of the system to increase the interaction rates.

Our results indicate that lattice-style ion traps suffer from poor simulated interaction rates, but that elliptical traps offer potentially much higher interaction rates, at the cost of unavoidable micromotion. However, we show that certain two-body interactions may be implemented with a precision that scales favorably with the number of experiments. We also explore ways of actually implementing quantum simulations in such traps, and in doing so make progress toward the goal of a 2-D analog quantum simulator based on trapped ions.

Part III

In the third part, we ask: can ion-ion coupling over wires be used to scale up digital and analog ion-trap quantum simulators? Coupling over wires could provide a scalable and switchable connection between the motional states of many trapped ions, leading in principle to a more scalable architecture than the traps discussed in Part II. However, some questions must first be addressed. In this part, we focus on the theoretical problems of calculating the expected coupling rate and decoherence rates, and the experimental problem of measuring how the dc and rf electric fields experienced by a single ion vary with the ion-wire distance. These are essential questions when evaluating the potential of this novel method for scaling up ion trap quantum simulators.

In **Chapter 8**, we present a system consisting of two ions confined in a linear surface-electrode Paul trap, near which a thin conducting wire is positioned. We theoretically analyze the ion-ion coupling mediated by the wire, and determine the coupling rate and some important decoherence rates for certain sets of experimental parameters. This work is also important for establishing constraints on the experiment, such as the fact that the wire must be very well-isolated from both dc and rf paths to ground.

In **Chapter 9**, we present the experimental setup and measurements. We study some aspects of connecting ions over a wire by first understanding the effect that a wire has on a single ion. We examine how the presence of the wire alters the trapping potentials, including both ac contributions from the rf trapping potentials and dc contributions from the static charge on the (electrically floating) wire. These results demonstrate the ability to measure electrical properties of a macroscopic object using an ultrasensitive detector: a single trapped ion. We also discuss progress towards understanding how the motional heating rates of the ion vary with the distance from the ion to the wire. Although for the ion-wire distances achieved in our work to date, the heating rate does not vary systematically with the ion-wire distance, this "negative result" is useful for calculating an upper bound on the ion-wire distance such that the heating rate due to the trap electrodes themselves is not greatly increased by the presence of the wire.

The results presented in this part show that the wire-mediated coupling between two ions stored in Paul traps is observable in principle, but that the electrically floating wire strongly affects the potentials that act upon the ion. Ion-ion coupling over a wire is a promising method for scaling up ion trap simulators, but more experimental measurements are required at smaller ion-wire distances, of both the effects of the wire on the trap potentials and of the motional heating rate due to the wire.

Following Part III, **Chapter 10** contains our conclusions and outlook.

1.6 Contributions to this work

In this section we present the main contributions of the author and his coworkers to this thesis, and then list the publications that have resulted from this work.

1.6.1 Personal contributions

In Part I, I participated in all aspects of the experiment and theoretical modeling. I wrote many of the pulse sequences and experimental automation, as well as analyzing the experimental results. I also wrote many of the simulation programs that predicted the results of the quantum simulation, and helped to pinpoint the sources of divergence between them, including the systematic error. A great deal of work that does not appear in this thesis, such as quantum state tomography to diagnose the sources of decoherence, was also done by me.

In Part II, I contributed a variety of work. In the experimental work of Ch. 5, I led the investigation of atomic ions in the lattice trap. I built the vacuum chamber and ion trap in which measurements were taken. I also discovered the poor scaling properties of the lattice trap. I worked with my coauthors to analyze the data, particularly the macroion repulsion data. In the experiments which are described in Ch. 6, my primary contribution was the collection of a large quantity of data for both of the resulting publications. I also helped build the vacuum apparatus and prepare the traps for the ablation experiment and set up the ablation targets and laser. For the work of Ch. 7, I designed and had manufactured the elliptical ion traps, set up a new cryogenic vacuum system for testing them, performed all the measurements on them, and drove the theoretical side of the project as well by suggesting problems I thought important to my undergraduate coworkers. I also contributed to writing and debugging many of the simulation codes.

Part III represents a collaboration between the Chuang group at MIT and the Blatt group at the Institut für Quantenoptik und Quanteninformation (IQOQI), located at the University of Innsbruck, Austria. I worked about eight months in total at the IQOQI on the experiment. While I was there, some specific things I accomplished were: completing the setup of the vacuum system, including feedthroughs and calcium oven; the first trapping of ions using a trap brought from MIT; electronics including filter boxes, the rf resonator, and putting together the pulse programmer; preparing the Doppler recooling technique and using it to measure the heating rate of a single ion; and making the first systematic observations of the variation in trap frequency and compensation voltages as a function of the ion-wire distance. While back at MIT, I also contributed much to the analysis of new data.

1.6.2 Contributions of coworkers

The results of Part I would not have existed without Kenneth Brown, who worked with me on the experiment and taught me a lot about quantum mechanics along the way. He did many of the same tasks that I did, and as I was just beginning graduate school at the time, taught me what I needed to know to then do them myself. A coworker for a very brief time, Matthias Steffen, introduced us to the NMR system.

In Part II, when the Chuang group moved to ion trapping, the atomic ion trapping team included Kenneth Brown, Jaroslaw Labaziewicz, and David Leibrandt. These people were instrumental in the construction of the laser systems (especially Jaroslaw and Kenneth) and some of the vacuum apparatus (especially David and Kenneth) presented in Ch. 6. We owe the design of the first planar trap in that chapter to Christopher Pearson, and of the second to Jaroslaw. The work of Ch. 5 was done in conjunction with Kenneth and Tongyan Lin, who made the macroion measurements and worked with me on the analysis of that data. The cryostat apparatus in Ch. 7 was assembled with a lot of help from Paul Antohi, and the theory presented in the section was developed in detail by two undergraduates, Ziliang Lin and Kenan Diab, who I mentored in those efforts. Each also made some contributions to the experimental apparatus; Ziliang designed and built the optics delivery system that survived in modified form for the experiments of that chapter, while Kenan built some fine rf resonant circuits for driving the trap.

The work in Part III relies heavily on the contributions of coworkers in Innsbruck. Tony Lee set up the laser systems, constructed the bulk of the vacuum chamber, and prepared sundry other experimental tools. We worked together to trap ions for the first time in that system, using a trap from our group at MIT. Subsequent experimental refurbishing and data collection was done by Nikos Daniilidis and Sankara Narayanan. In particular, Nikos fabricated the gold surface traps used in Chapter 9, in collaboration with Andreas Wallraff at ETH Zürich. After I departed, Sönke Möller joined the experimental effort, helping to obtain the data presented in this thesis.

1.6.3 Publications included in this thesis

Below is a list of articles that have already been published or submitted on the basis of this work. All but number 8 deal with work presented in this thesis.

1) **Ref. [BCC06]** Limitations of quantum simulation examined by simulating a pairing Hamiltonian using nuclear magnetic resonance

2) **Ref. [BCL$^+$07]** Loading and characterization of a printed-circuit-board atomic ion trap

3) **Ref. [LCL$^+$07]** Laser ablation loading of a surface-electrode ion trap

4) **Ref. [CLBC09]** A two-dimensional lattice ion trap for quantum simulation

5) **Ref. [DLC$^+$09b]** Wiring up trapped ions to study fundamental aspects of quantum information

6) **Ref. [CDLC09]** Surface-electrode elliptical ion traps for quantum simulation

7) **Ref. [DLC$^+$09a]** Measurement of electrical properties of a conductor with a single trapped ion

8) **Ref. [LLC$^+$09]** Demonstration of a scalable, multiplexed ion trap for quantum information processing

In addition, the undergraduate thesis of Ziliang Lin (Ref. [Lin08]) overlaps with Chs. 5 and 7 of this thesis.

Part I

Digital quantum simulation with nuclear spins

Chapter 2

Quantum simulation using nuclear magnetic resonance

Nuclear magnetic resonance (NMR) is a well-known technique for manipulating and measuring the spins of nuclei in molecules. It found its first widespread use in the identification of chemical compounds and the elucidation of their chemical structures. Subsequently, NMR came to form the basis of magnetic resonance imaging (MRI), a leading medical diagnostic technique. The success of NMR depends on the exquisite degree of control over the quantum dynamics of the nuclei, combined with their long ($\mathcal{O}$(seconds)) coherence times. These same features allow NMR to serve as an ideal test-bed for quantum algorithms and quantum simulation. In a 1997, two groups independently proposed implementing quantum algorithms in bulk solution-state NMR: Gershenfeld and Chuang in Ref. [GC97], and Cory, Havel, and Fahmy in Ref. [CFH97].

Following this stimulus, nuclear magnetic resonance (NMR) was the first system in which a wide variety of quantum algorithms were implemented. NMR demonstrations of the Deutsch-Josza [CVZ$^+$98], Grover [VSS$^+$99], and Shor [VSB$^+$01] algorithms were the first to be realized in any technology. It offers an extremely convenient test-bed for quantum algorithms: a customized off-the-shelf experimental system in which many quantum computation protocols can be applied to a closed quantum system. In addition, implementing quantum algorithms with NMR can lead to insights about quantum control that are applicable to other systems as well, e.g. ion traps [GRL$^+$03]. Several detailed treatments of solution-state NMR quantum computation have been written, including Ref. [VC05] and the theses of Vandersypen [Van01] and Steffen [Ste03].

In this chapter, we show how an NMR system can be used as a quantum simulator. We first discuss, in Sec. 2.1, the basic properties of an NMR system, including the Hamiltonian under which atomic nuclei evolve and the techniques for controlling the nuclei. Then, in Sec. 2.2, we examine prior experiments that have proven the capacity of NMR to act as a quantum simulator for small numbers of qubits. The question of the limitations to the precision of a quantum simulation is then discussed, in light of these experiments, in Sec. 2.3. In Sec. 2.4, we summarize the chapter and then enumerate some outstanding questions that remain to be addressed.

2.1 Hamiltonian and control techniques

In this section we present a simple description of the NMR system, and with it the Hamiltonian that governs the nuclear spins. We then show how this Hamiltonian enables quantum control of the nuclear spins. In so doing, we explain how a NMR system satisfies most of the DiVincenzo criteria for quantum computation (Sec. 1.4.3).

We begin with a comment on the first criterion. Although suitable for small systems, NMR is not a scalable architecture for quantum computation (or universal quantum simulation) because there is no way to do operations *fault-tolerantly.* It is not possible to perform operations on the system conditioned on fast measurements, as would be required in the diagnosis and correction of errors. This stems from the nature of measurement in solution-state NMR, which is based on a slow recording of the bulk magnetization of the system (see Sec. 2.1.6).

The other criteria are state initialization, a universal set of gates, high-efficiency measurement, and a sufficiently long coherence time; the satisfaction of these by NMR will be explained in the remainder of this section. Throughout we will use "nucleus," "spin," and "qubit" interchangeably, since the exclusive topic of this section is spin-1/2 nuclei.

2.1.1 The static Hamiltonian

The NMR system consists of a sample of dissolved molecules, the nuclear spins of which, in thermal equilibrium, are aligned (or antialigned) with a strong external magnetic field of magnitude B_0, which by convention points along the $\hat{z}$ direction. Oscillating magnetic fields of peak magnitude B_1, and oriented along $\hat{x}$ and $\hat{y}$, are applied to the nuclei to rotate their spin states. Finally, the bulk magnetization of the sample may be read out inductively, giving an ensemble measurement of the spin states. Details of this setup for a real experimental system are given in Sec. 3.4. In this chapter, we focus on the Hamiltonian and control techniques.

The static portion of the NMR Hamiltonian is composed of two terms: one describes rotations of the nuclei about the $\hat{z}$ axis due to the the static magnetic field, and the other describes the spin-spin coupling between nuclei. Using i to index the individual nuclear spins, the term due to B_0 is written

$$H_0 = \sum_i \hbar\omega_0 Z_i \, , \tag{2.1}$$

where the Larmor frequency ω_0 is given by $\omega_0 = g_N \mu_n B_0/\hbar$, and g_N is the nuclear g-factor,

μ_N the nuclear magneton, and B_0 the magnitude of the magnetic field along $\hat{z}$. Z_i is the Pauli Z matrix operating on qubit i. Here, and throughout, we use the most common phase convention for the Pauli matrices:

$$X = \begin{bmatrix} 0 & 1 \\ 1 & 0 \end{bmatrix} \quad ; \quad Y = \begin{bmatrix} 0 & -i \\ i & 0 \end{bmatrix} \quad ; \quad Z = \begin{bmatrix} 1 & 0 \\ 0 & -1 \end{bmatrix} \quad . \tag{2.2}$$

where the spin states, unless otherwise noted, are written in the $\hat{z}$ basis, with vector representations

$$|\uparrow\rangle = \begin{bmatrix} 1 \\ 0 \end{bmatrix} \quad \text{and} \quad |\downarrow\rangle = \begin{bmatrix} 0 \\ 1 \end{bmatrix} . \tag{2.3}$$

The other important term in the static Hamiltonian arises from couplings between individual nuclei that are mediated by the electron clouds surrounding them, which form the chemical bond in the molecule. Although, in general, there are also direct dipole-dipole couplings, in a dilute solution this interaction averages to zero. The through-bond coupling is called *scalar coupling*, or just *J-coupling*. This interaction takes the form of a ZZ interaction:

$$H_I = \frac{\hbar}{4} \sum_{i,j<i}^{N} J_{ij} Z_i Z_j \ , \tag{2.4}$$

where i and j label nearest-neighbor nuclei. Although in general J is a tensor quantity, it can be treated as a scalar in liquids (when the orientation of molecules relative to each other is randomized), when the couplings are weak compared to the static field, or when the Larmor frequencies of the interacting nuclei are very different [NC00]. The first two always apply to solution-state NMR, and very often the third does as well.

2.1.2 Effective pure states

The state of the nuclear spins in thermal equilibrium is a highly-mixed one, a probabilistic sum of pure states. To see why this is the case, let us write the density matrix in thermal equilibrium:

$$\rho_{th} = \frac{e^{-\beta H_0}}{\mathrm{Tr}(e^{-\beta H_0})} \ . \tag{2.5}$$

Here $\beta = 1/(k_B T)$; the denominator is the usual partition function normalization. We have neglected H_I since its magnitude is several orders of magnitude smaller than that of H_0. The highly-mixed nature of ρ_{th} comes from the smallness of the exponential: $\hbar\omega_0\beta \approx 10^{-5}$

for B_0 strengths on the order of 10 T.[1] Due to this fact, we can approximate the thermal state as $\rho_{th} = 2^{-n}(1 - \beta H_0)$. Here n is the number of qubits. The thermal state of one qubit, then, is

$$\rho_{th} = \begin{bmatrix} 1+\epsilon & 0 \\ 0 & 1-\epsilon \end{bmatrix}, \tag{2.6}$$

where $\epsilon = \hbar\omega_0/(2k_BT)$ is the spin polarization. Our convention is that the qubit state is written in the $\hat{z}$ basis, unless otherwise stated.

Although this highly mixed thermal state may seem to prevent the satisfaction of the second DiVincenzo criterion, regarding the preparation of a known and pure initial state, there are several techniques in which one may average over several experiments with different initial density matrices and obtain at the end the same result as if the experiment were done on a single pure state. This is known as an *effective pure state* or *pseudopure state.* The downside is that this generally requires a number of experiments that is exponential in n, but for some purposes a smaller number of experiments may suffice to approximate the pure state. The three primary techniques for producing effective pure states are called *temporal labeling*, *spatial labeling*, and *logical labeling.* Here, we limit our discussion to temporal labeling, since that is the method employed in the experiments of Chapter 3. The reader may find discussions of this and the other techniques in Nielsen and Chuang [NC00], and in the Ph.D. theses of Vandersypen [Van01] and Steffen [Ste03].

In presenting temporal labeling, we shall follow the approach of Nielsen and Chuang's book [NC00]. Let's say we start with an initial state ρ_1:

$$\rho_1 = \begin{bmatrix} a & 0 & 0 & 0 \\ 0 & b & 0 & 0 \\ 0 & 0 & c & 0 \\ 0 & 0 & 0 & d \end{bmatrix}. \tag{2.7}$$

The thermal state ρ_{th} is such a state. By convention, and throughout the thesis, we use the following tensor product basis:

$$|\uparrow\uparrow\rangle = \begin{bmatrix} 1 \\ 0 \\ 0 \\ 0 \end{bmatrix}; \quad |\uparrow\downarrow\rangle = \begin{bmatrix} 0 \\ 1 \\ 0 \\ 0 \end{bmatrix}; \quad |\downarrow\uparrow\rangle = \begin{bmatrix} 0 \\ 0 \\ 1 \\ 0 \end{bmatrix}; \quad |\downarrow\downarrow\rangle = \begin{bmatrix} 0 \\ 0 \\ 0 \\ 1 \end{bmatrix}. \tag{2.8}$$

Now suppose we permute the populations of this state, which can be done using a sequence of CNOT's (Sec. 2.1.4), to produce the states ρ_2 and ρ_3:

---

[1] Magnetic fields are measured throughout in Tesla (T); we will use italic script for the temperature T, to avoid confusion.

$$\rho_2 = \begin{bmatrix} a & 0 & 0 & 0 \\ 0 & c & 0 & 0 \\ 0 & 0 & d & 0 \\ 0 & 0 & 0 & b \end{bmatrix} ; \tag{2.9}$$

$$\rho_3 = \begin{bmatrix} a & 0 & 0 & 0 \\ 0 & d & 0 & 0 \\ 0 & 0 & b & 0 \\ 0 & 0 & 0 & c \end{bmatrix} . \tag{2.10}$$

A quantum computation (or simulation), not including measurement, is a unitary operation, which we will write as U. The sum of the density matrices $P = \sum_{i=1,2,3} \rho_i'$, where $\rho_i' = U^\dagger \rho_i U$, is

$$P = (4a-1)\,U \begin{bmatrix} 1 & 0 & 0 & 0 \\ 0 & 0 & 0 & 0 \\ 0 & 0 & 0 & 0 \\ 0 & 0 & 0 & 0 \end{bmatrix} + (1-a) \begin{bmatrix} 1 & 0 & 0 & 0 \\ 0 & 1 & 0 & 0 \\ 0 & 0 & 1 & 0 \\ 0 & 0 & 0 & 1 \end{bmatrix} . \tag{2.11}$$

The measured NMR signal is given by $\mathrm{Tr}(P) = \sum_{i=1,2,3} \rho_i' M$, where M is the observable in question. The portion of the signal that is proportional to the identity matrix above does not produce any signal when measured, and does not evolve under unitary transforms. Therefore, by performing this experiment three times with the initial states ρ_1, ρ_2, and ρ_3, we obtain a signal that is proportional to what the result would have been on a pure state $\langle\uparrow\uparrow \mid \uparrow\uparrow\rangle$:

$$\sum_{i=1,2,3} \mathrm{Tr}\left(\rho_i' M\right) = (4a-1)\mathrm{Tr}\left(U\langle\uparrow\uparrow \mid \uparrow\uparrow\rangle U^\dagger\right) . \tag{2.12}$$

As can clearly be seen, two qubits produce a four-dimensional Hilbert space, which requires three averaging steps. From the above example, for n qubits one will require, in general, $2^n - 1$ steps. Therefore, this method is inefficient, and nulls the speedup of quantum computation, but is sufficient for the implementation of algorithms involving a small number of qubits.

2.1.3 Single-qubit operations

The rf coils along the $\hat{x}$ and $\hat{y}$ directions generate magnetic fields that oscillate at a frequency ω, whose strength is characterized by a frequency ω_1, which is related to the magnetic field produced by $\omega_1 = \gamma B_1$. Here $\gamma = g_N \mu_N$ is the magnetic moment of the nucleus being addressed, with g_N the nuclear g-factor and μ_N the nuclear magneton. The Hamiltonian for the interaction of this field with a given nucleus is

$$H_{rf}(t) = -\hbar\omega_1 \left(\cos(\omega t + \phi) X/2 + \sin(\omega t + \phi) Y/2\right) \,, \tag{2.13}$$

where ω is the frequency of the applied magnetic field.

For purposes of effecting rotations of the spins, we use the resonance condition $\omega = \omega_0$, where again, ω_0 is the Larmor frequency of the given spin. Then, in the rotating frame at frequency ω_0, we can write this Hamiltonian as

$$H_{rf}^{rot} = -\hbar\omega_1 \left(\cos(\phi) X/2 + \sin(\phi) Y/2\right) \,. \tag{2.14}$$

Because in this frame the rotations occur at a rate ω_1, the total angle of rotation θ is just given by the time t_p over which a resonant pulse is applied times ω_1: $\theta = \omega_1 t_p$. These rotations may be performed in either the $\hat{x}$ or $\hat{y}$ directions, or in both at the same time. We shall use the general form of $R_{\hat{n}}(\theta)$ for describing these rotations, where e.g. $R_{\hat{x}}(\pi)$ is a rotation of π radians (180°) about the x-axis, and $R_{\hat{y}}(-\pi/2)$ is a rotation of $-\pi/2$ radians (−90°) about the y-axis.

There are multiple ways of performing single-qubit rotations along $\hat{z}$. We present three such methods here.

1. Composite $\hat{x}$ and $\hat{y}$ rotations.

   Any rotation about $\hat{z}$ can be composed of other rotations about $\hat{x}$ and $\hat{y}$. The following is an example of this:

   $$R_{\hat{z}}(\pi) = R_{\hat{x}}(\pi/2) R_{\hat{y}}(\pi/2) R_{\hat{x}}(-\pi/2) \,. \tag{2.15}$$

2. Compression of $\hat{z}$ rotations.

   We can also use relations such as Eq. 2.15 to place all $\hat{z}$ rotations at the end of the pulse sequence. An example of this is

   $$R_{\hat{x}}(\pi/2) R_{\hat{z}}(\pi/2) = R_{\hat{x}}(\pi/2) R_{\hat{y}}(\pi/2) R_{\hat{x}}(-\pi/2) R_{\hat{y}}(-\pi/2) = R_{\hat{z}}(\pi/2) R_{\hat{y}}(-\pi/2) \,. \tag{2.16}$$

   Here the rotation about $\hat{x}$ is replaced with one about $\hat{y}$, and the $\hat{z}$ rotation is moved to the end. The advantage of this method is that all the $\hat{z}$ rotations can be grouped into one single pulse, reducing the total number of single-qubit pulses that must be performed. This leads to a reduction of errors due to control errors, i.e. evolution under H_I (Eq. 2.4) that occurs during the pulse duration t_p. For this method to work, the $\hat{z}$ rotations must commute with the free-evolution Hamiltonian, $H_0 + H_I$. Since both of these depend only on Z operators, this is clearly the case.

3. Implicit absorption of $\hat{z}$ rotations.

The same effect as number 2 above is achieved if we regard $\hat{z}$ rotations as merely a shifting of the reference frame by the angle θ in each $R_{\hat{z}}(\theta)$ rotation. The effect of $\hat{z}$ rotations is implemented by shifting the phases of each subsequent single-qubit pulse to account for them. Choosing between this method and number 2 is a practical matter; because it requires less modification to the pulse sequence, this method is generally preferred.

2.1.4 Two-qubit operations

Now that we are armed with the ability to do arbitrary single-qubit rotations and with an interaction Hamiltonian (Eq. 2.4) we can construct two-qubit gates such as the controlled-not (CNOT). The CNOT, along with arbitrary single-qubit rotations, is sufficient to implement universal quantum computation; all the operations needed for quantum simulation are contained within this, and in practice less control is often required. In the computational basis ($\{|00\rangle, |01\rangle, |10\rangle, |11\rangle\}$), the CNOT has this matrix representation:

$$\mathrm{CNOT}_{12} = \begin{bmatrix} 1 & 0 & 0 & 0 \\ 0 & 1 & 0 & 0 \\ 0 & 0 & 0 & 1 \\ 0 & 0 & 1 & 0 \end{bmatrix} . \tag{2.17}$$

Suppose there are two coupled spins. The basic pulse sequence rotates spin 2, the "target qubit," from a $\hat{z}$ eigenstate into the $\hat{x}$-$\hat{y}$ plane of the Bloch sphere. Then, during a period of free evolution under $H_0 + H_I$, the direction of the rotation of this spin (in the rotating frame) depends on the state of spin 1, called the "control qubit." After a time equal to $1/(2J_{12})$, the spin is rotated back into a $\hat{z}$ eigenstate. This effectively flips (or doesn't) spin 2 based on the state of spin 1. Specifically, the pulse sequence looks like:

$$U'_{\mathrm{CNOT}} = R_{\hat{x}}(\pi/2) U_I(1/(2J_{12})) R_{\hat{y}}(\pi/2) = \begin{bmatrix} 1 & 0 & 0 & 0 \\ 0 & i & 0 & 0 \\ 0 & 0 & 0 & -i \\ 0 & 0 & 1 & 0 \end{bmatrix} , \tag{2.18}$$

where $U_I(t) = \exp(-iH_I t/\hbar)$ is the unitary evolution under H_I. Fig. 2-1 shows the operation of the CNOT gate as described here.

This does not exactly produce the CNOT presented in Eq. 2.17, but the gate can be exactly duplicated by applying appropriate single-qubit pulses to spins 1 and 2. Specifically, a $R_{\hat{z}}(-\pi/2)$ is required on qubit 2 and $R_{\hat{z}}(\pi/2)$ on qubit 1.

2.1.5 Refocusing

We briefly present one more invaluable technique for NMR quantum control. In NMR, the ZZ interaction between spins is "always on," in the sense that it's a part of the Hamilto-

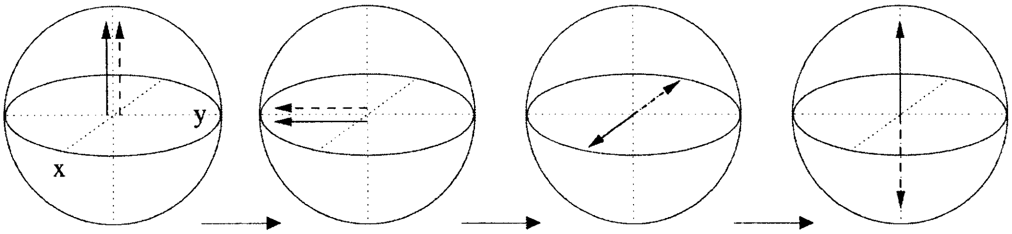

Figure 2-1: Above is a depiction of the CNOT gate in NMR. Spin 1, the control qubit, is not shown but its state alters the precession frequency of spin 2, the target qubit. At first, qubit 2 is in the $|\uparrow\rangle$ $\hat{z}$ eigenstate. A $\pi/2$ rotation about the $\hat{x}$ axis places it into the $\hat{x}$-$\hat{y}$ plane. Depending on the spin state of qubit 1, and in the rotating frame, qubit 2 precesses around the $\hat{z}$ axis in a different direction. The solid arrow evolution is when qubit 1 is in state $|\uparrow\rangle$, while the dotted arrow occurs when qubit 1 is in state $|\downarrow\rangle$. After a free precession time of $t = 1/(2J)$, a single $R_{\hat{y}}(-\pi/2)$ pulse completes the operation: the spin of qubit 2 has been flipped conditioned on the spin of qubit 1. This figure is due to Vandersypen, Ref. [Van01].

nian that is not directly under the experimenter's control. We have seen above how this interaction can be used to generate the CNOT gate. However, sometimes one wishes for some of the spins to not evolve under this Hamiltonian for some period of time. This is used by us, for instance, in Sec. 3.5.

A technique known as *refocusing* can effectively switch off the scalar coupling between one qubit and the others during a period of free evolution. This is done by applying a π-pulse to that qubit halfway through the evolution time, thereby reversing its direction of precession. Suppose one has a three qubit system, and wishes for a time t to implement H_I (Eq. 2.4) on the qubits labeled a and b, while preventing qubit c from coupling to them. One would do the following pulse sequence, where the arrows indicate time-ordered pulses:

$$U_I^{a,b}(t) = U_I^{a,b,c}(t/2) \to R_{\hat{x}}^{c}(\pi) \to U_I^{a,b,c}(t/2) \to R_{\hat{x}}^{c}(\pi)\,. \tag{2.19}$$

This fairly simple technique is of great utility to us.

2.1.6 Measurement

Measurement of the NMR system is done by recording the current induced in a coil of wire surrounding the spins; this coil is the same one that transmits the rf signals to the nuclei, and thus only detects magnetizations in the $\hat{x}$ or $\hat{y}$ directions. The measurement simultaneously records the states of the spins contained in all the many molecules in the sample, but due to the low spin polarization at room temperature, only a the small difference in spin orientations produces the signal. The induced voltage across the rf coil can be written as

$$V(t) = V_0 \mathrm{Tr}\left[e^{-iHt}\rho e^{iHt}\left(-iX_k - Y_k\right)\right]\ , \tag{2.20}$$

where V_0 is the maximum signal strength and ρ is the sample density matrix. The phase of the measurement operator can be chosen so that a given spin state produces a given spectral line shape: for instance, for the above operator $-iX_k - Y_k$, a spin along $-\hat{y}$ produces a positive absorptive spectral line, while one along $\hat{y}$ produces a negative absorptive line. A spin along $\pm\hat{x}$ produces positive or negative dispersive lines. To perform this measurement in the $\hat{z}$ basis, we must first rotate all spins into the $\hat{x}$-$\hat{y}$ plane, since the rf coils are only sensitive to magnetizations in this direction. Thus a $R_{\hat{x}}(\pi/2)$ pulse is first applied to the spins being measured.

The resulting *free-induction decay* (FID) signal oscillates at the frequency of the qubit being measured; a Fourier transform of this signal yields a frequency spectrum, from which one can determine the spin state along $\hat{z}$ of each nucleus (using the chemical shift interaction, Eq. 2.4). The FID decays exponentially at a rate T_2^*, due to decoherence processes which will be discussed shortly. The exponential decay in the time domain leads to a Lorentzian lineshape in the frequency domain:

$$V(t)e^{-t/T_2^*} \mapsto F(\omega) \propto \frac{1}{1/(2T_2^*)^2 + (\omega - \omega_0)^2} - \frac{1}{1/(2T_2^*)^2 + (\omega - \omega_0)^2}, \tag{2.21}$$

where the two parts represent absorptive and dispersive lineshapes. A signal may, in general, be of only one type or a mixture of the two. The full width at half-maximum (FWHM) of the NMR peaks is then given by $\Delta f = 1/(2\pi T_2^*)$.

Although measurements in quantum information are often assumed to be strong, projective measurements, those in NMR are quite weak. The constant T_2^* depends on magnetic field inhomogeneities and other interactions between spins and with the environment; it is noteworthy that the decay of the FID is dominated not by the interaction of the sample with the coil, but by decoherence processes more intrinsic to the sample. This may be contrasted with the classic "strong" measurement, in which the very act of measurement induces sufficient decoherence to immediately effect wavefunction collapse! This weakness of the measurement, combined with the ensemble nature of the experiment, is also the reason why both $\hat{x}$ and $\hat{y}$ components of the magnetization can be simultaneously measured, a feat which is forbidden (for a single quantum system) by the uncertainty principle. What is recorded is the ensemble average of the magnetizations in each direction; each of the 10^{18} or so molecules gives its own answer regarding its spin state, and these are added up.

The result of a measurement is a frequency-domain spectrum, with peaks located at all possible locations for a given nucleus, given the various splittings due to the chemical shifts.

To summarize this section so far, we have assembled all the basic concepts and techniques for performing quantum operations in solution-state NMR. In the next section we show how these principles apply to the simulation of quantum systems. First, though, we address the sources of decoherence in NMR systems.

2.1.7 Decoherence

Decoherence, broadly speaking, is an uncontrolled evolution of a quantum state into a classical mixture of pure states. It is caused by interactions which are outside the control of the experimentalist, and involve noisy or random processes. Decoherence is an ever-present limitation to the amount of time over which quantum operations may be performed, and also to the fidelity of the operation. It is characterized by two time constants, T_1 and T_2, which govern the decay of the populations (T_1) and coherences (T_2) of the system density matrix. Taking ρ as the system density matrix, these decoherence channels can be described using the following density matrix transformation model:

$$\begin{bmatrix} a & b \\ b^* & 1-a \end{bmatrix} \rightarrow \begin{bmatrix} (a-a_0)e^{-t/T_1}+a_0 & be^{-t/T_2} \\ b^*e^{-t/T_2} & (a_0-a)e^{-t/T_1}+1-a_0 \end{bmatrix}, \tag{2.22}$$

where

$$\rho_0 = \begin{bmatrix} a_0 & 0 \\ 0 & 1-a_0 \end{bmatrix} \tag{2.23}$$

is the thermal density matrix. Naturally, it is beneficial to get T_1 and T_2 as large as possible. This can be done by understanding and correcting for some of the sources of decoherence, which form two broad classes: macroscopic and microscopic.

The macroscopic sources of noise normally involve large-scale variations in the electromagnetic fields that interact with the nuclei. Inhomogeneities in B_0 and B_1 lead to a type of decoherence known as *inhomogeneous broadening*, from the fact that the T_2 value is increased, leading to a larger spectral linewidth. The quantity that includes both inhomogeneous broadening and other effects is called T_2^*, and is used above in discussing the lineshape. Other macroscopic sources of noise are electromagnetic fluctuations, which may arise from noisy amplifiers, and radiation damping, which occurs when the magnetic moment of the spins induces a voltage in the rf coils, which then create a magnetic field that itself rotates the spins.

These sources are easier to deal with than the microscopic ones discussed below. Spin-echo techniques can reduce the effect of inhomogeneous broadening, and in fact allow one to measure the field inhomogeneity by comparing T_2 and T_2^*. Also, starting with as uniform a B_0 field as possible allows one to improve T_2^* without spin-echo techniques. A technique called *shimming* allows us to do this (see Sec. 3.4.4). Also, the sample is spun around the $\hat{z}$ axis at about 20 Hz, which averages out inhomogeneities in the $\hat{x}$-$\hat{y}$ plane. With respect to the other two problems, electromagnetic noise can be mitigated by "blanking" the rf amplifiers when pulses are not being applied, and radiation damping can be reduced either by reducing the Q value of the resonant circuit or by making the sample more dilute.

The microscopic sources have been discussed in detail in Ref. [Lev01], and we give some important examples here. One set of decoherence sources is the various dipole-dipole interactions that occur between nuclei in the same or different molecules; the random processes of molecular rotation and translation cause fluctuations in the strength of these interactions. These fluctuating interactions can also occur with electron spins. Another source is anisotropy in the chemical shift or the J-coupling, which are generally assumed to be isotropic in solution-state NMR, but can fluctuate by small amounts as well. Quadrupolar nuclei rapidly relax due to their interaction with electric field gradients, and therefore they are generally avoided. Chemical exchange is a further process in which the dissolved molecules undergo rapid and random change in their chemical structure. Finally, the rotations of the molecules themselves generate tiny magnetic fields, since they are (after all) composed of charged particles themselves.

There is more limitation to what an experimenter can do to correct these. Prevention is indeed the best medicine here. Solvents with a higher viscosity and at a higher temperature have higher molecule tumbling rates, which reduces many of the decoherence sources described above. In addition, one benefits by choosing solvents with non-magnetic nuclei, removing paramagnetic impurities such as molecular oxygen from the sample, and avoiding solvents known to contribute to chemical exchange.

2.2 Quantum simulation using NMR: prior art

Prior to the work of the follwing chapter, several quantum simulations were performed in a solution-state NMR system. Somaroo *et al.* performed the first quantum simulation ever when they simulated a truncated harmonic oscillator with a two-qubit NMR system [STH+98]. Later, they also simulated a (nonphysical) three-body interaction [TSS+00]. Subsequently, Peng *et al.* observed a quantum phase transition of a Heisenberg spin chain simulated in NMR [PDS04], using two qubits. This was followed by Negreveve *et al.*, using three qubits to simulate a Fano-Anderson model [NSO+04]. Clearly, prior to our work, there was a great deal of interest in applying NMR techniques to the simulation of many-body physics.

In this section we summarize the truncated oscillator experiment as an example of an NMR implementation of quantum simulation. This was the earliest NMR quantum simulation experiment, and also one of the simplest. Our goal in this section is to impart a sense of how the principles of NMR outlined above can be used for quantum simulation. We will use these tools to tackle a more difficult problem in the next chapter. Here, we focus on these aspects that are common to all NMR quantum simulations:

1. Mapping the problem Hamiltonian to the NMR Hamiltonian.

2. Implementation of the simulated problem Hamiltonian in NMR.

3. Measurement and analysis

Simulation of a truncated harmonic oscillator

Here we explore the basic features of the truncated oscillator quantum simulation experiment [STH+98], as a guide to understanding some of the issues in NMR quantum simulation.

The Hamiltonian of the quantum harmonic oscillator is

$$H_{HO} = \hbar\Omega \left(N + 1/2\right) \ , \tag{2.24}$$

where $N = a^\dagger a$ is the operator for number of vibrational quanta. The solution is an infinite "ladder" of energy eigenstates $|n\rangle$, with energy $E_{HO} = \hbar\Omega\,(n + 1/2)$ and n ranging from 0 to ∞. The Hilbert space of the set of nuclei in NMR has a tensor product structure. In the $\hat{z}$ basis, the eigenstates that span the Hilbert space are $\{|\uparrow\uparrow\rangle\,, |\uparrow\downarrow\rangle\,, |\downarrow\uparrow\rangle\,, |\downarrow\downarrow\rangle\}$, where the arrows represent the spin state of nuclei 1 and 2. The first step is to find a mapping from this structure to the oscillator eigenstates. They make the following unitary mapping:

$$|n=0\rangle \quad \mapsto \quad |\uparrow\uparrow\rangle \ ; \tag{2.25}$$

$$|n=1\rangle \quad \mapsto \quad |\uparrow\downarrow\rangle \ ; \tag{2.26}$$

$$|n=2\rangle \quad \mapsto \quad |\downarrow\downarrow\rangle \ ; \tag{2.27}$$

$$|n=3\rangle \quad \mapsto \quad |\downarrow\uparrow\rangle \ . \tag{2.28}$$

Since there are four available basis states when using two qubits, the simulation will necessarily be of a *truncated* harmonic oscillator. Higher levels could be simulated by additional qubits; in fact, the number of oscillator levels doubles for each additional qubit. However, doing this in NMR depends on the couplings between all individual qubits being strong enough.

The Hamiltonian, mapped to the NMR system, has the following form:

$$H_{sim} = \hbar\omega_{HO}\left(\frac{1}{2}|\uparrow\rangle\langle\uparrow| + \frac{3}{2}|\uparrow\rangle\langle\downarrow| + \frac{5}{2}|\downarrow\rangle\langle\uparrow| + \frac{7}{2}|\downarrow\rangle\langle\uparrow|\right) \ . \tag{2.29}$$

This Hamiltonian is implemented by using appropriate refocusing pulses (Sec. 2.1.5).

The state preparation is done using logical labeling, rather than the temporal labeling covered previously. Suppose we begin with a superposition state such as $|\Psi_i\rangle = |\uparrow\uparrow\rangle + i\,|\downarrow\downarrow\rangle$. What would we then expect to observe from the above quantum circuit? Eigenstates of the Hamiltonian given by Eq. 2.29 will not evolve, but we do expect a quantum superposition state to evolve at a rate corresponding to the energy difference between the states that form it.

The experiment was done using the two hydrogen nuclei in the 2,3-dibromothiophene molecule (Fig. 2-2). Each of these nuclei is a single proton, and the proton Larmor frequency in their spectrometer is 400 MHz. Other pertinent quantities are $(\omega_2 - \omega_1)/(2\pi) = 226$ MHz and $J = 5.7$ Hz. The experimental results are shown in Fig. 2-3. The simulation is a

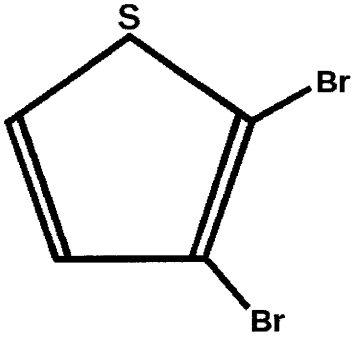

Figure 2-2: The 2,3-dibromothiophene molecule. The two unlabeled vertices represent hydrogen atoms, whose nuclei were used in this experiment.

success; the frequencies at which the signal evolves for each initial state depend on the energy difference between the two states.

In the same paper, they also implement a simulation of a truncated, driven, anharmonic oscillator, but the above is sufficient for our purposes of illustrating the basic methods of quantum simulation with NMR. In what follows, we begin to address the question of precision using this experiment as a model.

2.3 The question of precision

Having seen qualitative evidence for the success of quantum simulation, we move to discussing the quantitative issue of how much precision may be obtained in a measured result. For instance, we might ask in the case of the truncated oscillator experiment, how could one extract the harmonic oscillator frequency from the simulation results? These peaks could be Fourier-transformed to yield an energy (or frequency) spectrum; depending on the initial states used, the spectra would show peaks at Ω, 2Ω, or 3Ω. How well can Ω be measured, and how does this precision depend on the number of pulses used, or the total simulation time?

We wish to give a general idea for how the limitation to the precision may be estimated. To begin with, the precision of the final result is limited by the width of the peak in frequency space; thus, it depends on the Fourier sampling rate. Also, the minimum time step determines the maximum energy that can be measured. Therefore, we may suppose that the error in the final result ϵ scales as Ω/Q, where Q is the maximum number of time steps. Since the total number of gates N_G is proportional to Q, $N_G \propto \Omega/\epsilon$. A bound on the precision may then be obtained by calculating the total simulation time $N_G t_g$, where t_g is the time to perform a single iteration of the simulated Hamiltonian, and setting this equal to the decoherence time.

Admittedly, the above example is somewhat artificial, in that one is attempting to calcu-

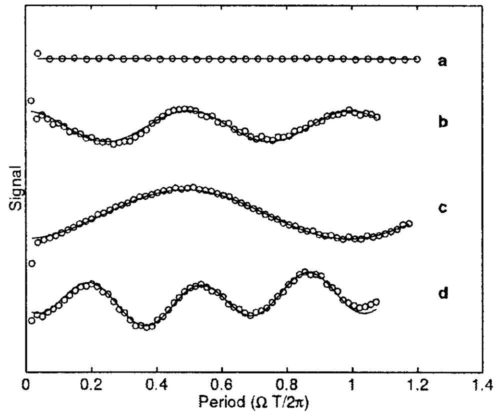

Figure 2-3: The four traces here are NMR peak signals as a function of simulated time T. The temporal variation of the signal depends on the initial state. The top trace, (a), corresponds to the state $|0\rangle$, which is an eigenstate and does not oscillate. In (b), the state $|0\rangle + i\,|2\rangle$ is simulated, and accordingly, it oscillates at 2Ω. In (c) and (d), the state $|0\rangle + |1\rangle + |2\rangle + |3\rangle$ is used, and oscillations at both Ω and 3Ω are observed. Image taken from Ref. [STH$^+$98].

late values that were directly programmed into the system. However, this relatively simple experiment demonstrates the type of reasoning that will be used with a more complicated system in the next chapter. We have seen, generally, how one can bound the error on a quantum simulation due to a classical Fourier transform, if such a method is used. But is this the only error?

We expect that errors due to faulty controls will also affect the precision of the final answer. Since the number of gates needed grows with the desired precision in the result, we would expect control errors to become more and more important as greater precision is required. Furthermore, the simulated Hamiltonian in Sec. 2.2 consists entirely of mutually-commuting terms. This allows for a fairly simple implementation, since approximating non-commuting terms using composite pulses is not necessary.

In Ch. 3, we explore the additional errors that arise when such approximations are needed. We shall see that control errors and natural decoherence (due to the larger number of required pulses) take on increased importance. Most noteworthy is that such errors may introduce a systematic *shift* in the answer, rather than only a broadening of the line.

2.4 Conclusions and further questions

In this chapter, we have seen how an NMR system can be used to implement small quantum simulations. The necessary controls are present to implement a universal set of quantum gates, and we have also seen an example of mapping a target system Hamiltonian to a model system Hamiltonian, in this case an NMR Hamiltonian. We have shown in some detail how this was done with a simulation of a truncated harmonic oscillator. Combined with the techniques discussed above for preparing pseudopure states and measuring the nuclear spin states, we are armed with a technique for implementing a wide variety of quantum simulations in NMR.

But, on the other hand, the potential and the limits of quantum simulation with NMR are still rather unexplored. We have seen already that there is a physical limit to the precision of a quantum simulation using DFT techniques. How does this limit change for a system with more qubits, implementing a more difficult Hamiltonian using a different algorithm? How might we suppose the limitation changes when error correction is used? Finally, what types of control errors occur in the NMR system, and how do they affect the final answer? These questions are the subject of the next chapter.

Chapter 3

Quantum simulation of the BCS Hamiltonian

Quantum simulation has great potential for calculating properties of quantum-mechanical systems that are intractable on classical computers, as we discussed in Ch. 1. However, when considering the power of a quantum simulator relative to a classical one, it is necessary to also consider the precision in the final answer that can possibly be obtained, an issue we began to explore at the close of Ch. 2. In the problem we consider here, the number of gates needed to compute the answer is indeed polynomial in the size of the problem Hilbert space, but is nevertheless exponential in the number of digits of precision one may obtain. Therefore, although the quantum algorithm is in some sense "more tractable," it is not straightforward to determine (or guess), for a given problem, whether a classical or quantum algorithm will actually produce a result with a given precision using a smaller number of gates.

In addition to the question of ultimate precision, there is the fact that all implementations of quantum simulation rely on classical controls that are never perfect; these affect the final result either by inducing decoherence or by leading to systematic errors in the final result. Indeed, even though systematic control errors can in principle be perfectly compensated (Ref. [BHC04]), the number of gates required to do this scales (in general) exponentially with the residual error. This implies that even if a general quantum algorithm may be efficient, the final precision may depend on the specific technology used to implement it. Therefore, implementations of small quantum simulations using various quantum technologies (NMR, ion traps, etc.) are worthwhile, in that the effects of faulty controls for each may be understood.

In this chapter, we report an experiment to test the limitations on the precision of a three-qubit algorithm to compute the low-lying spectrum of a class of pairing Hamiltonians [WBL02]. Our work is somewhat more ambitious than that summarized in the last chapter, for two reasons. First, we implement a Hamiltonian that contains non-commuting parts, and thus requires invocation of the Trotter product formula, dramatically increasing the number of necessary pulses. Second, we attempt to calculate a property of some physical system, an eigenvalue of its Hamiltonian, and in doing so explore the limitations to the precision with which such a quantity can in principle be calculated. In this sense, we test the limits of digital quantum simulation. We not only calculate the bounds on the precision that are inherent in the quantum protocol itself, but also those which are a result of the control techniques used to implement it.

Specifically, we wish to use a digital quantum simulator to calculate Δ, the energy gap between the ground state and first excited state of a pairing Hamiltonian. Algorithms such as WBL, which require a polynomial number of gates in the problem size, are generally not efficient with respect to the precision in the final answer. This was true in Lloyd's proposals [Llo96, AL97, AL99], and in the specific case we consider here.

We ask the following questions: What are the theoretical bounds on precision for the algorithm studied here? Can an NMR implementation saturate the theoretical bounds on precision? What control errors are most important, and what effect do they have on the final result? Do simple methods of compensation for these errors have a predictable effect?

The chapter is organized as follows: in Sec. 3.1, we briefly review the BCS pairing theory; in Sec. 3.2, we present the proposal of Wu *et al.* for the simulation of this Hamiltonian using NMR; in Sec. 3.3, we discuss the bounds on precision in the expected result ; in Sec. 3.4, we discuss our experimental setup; in Sec. 3.5, we present our implementation of the algorithm; finally, in Sec. 3.6, we evaluate this work, including the inherent limitations of digital quantum simulations in general and NMR quantum simulations in particular.

3.1 The BCS theory

The motivation for this work lies in the quantum simulation of superconducting systems. Superconductivity, first discovered in 1911 by H. K. Onnes, is characterized by an abrupt drop to zero of the electrical resistivity of a metal. Although this phenomenon defied theoretical explanation for some time, a phenomenological theory promulgated by Ginzburg and Landau in 1950 explained most of the features of superconductivity, including the Meissner effect (exclusion of magnetic flux) [GL50]. In 1957, Bardeen, Cooper, and Scrieffer (BCS) published the first complete microscopic theory, realizing that the phenomenon of superconductivity was due to the superfluidity of *pairs* of electrons in the conductor [BCS57]. In the BCS theory, electrons form the pairs through very weak interactions that are mediated by phonons in the lattice (made up of the nuclei of atoms in the solid metal). The weakness of these interactions is why superconductivity only occurs at very low temperatures; above the superconducting transition temperature T_c for a given material, thermal energy is enough to break the bonds that hold electron-electron pairs together.

Superconductors are grouped into two types based on their magnetic properties. *Type I* superconductors exhibit the Meissner effect, meaning that in the superconducting state the bulk material excludes magnetic flux. *Type II* superconductors, on the other hand, permit magnetic flux penetration, for a range of magnetic fields, in quantized units of $hc/(2e_c)$ (written in gaussian units, where e_c is the positive fundamental charge). The behavior of Type II superconductors, unlike that of Type I, still lacks a complete microscopic theory.

Well-explained as Type-I superconductors are, it is still not trivial to calculate specific properties of such a system. Indeed, the Hilbert space has the dimension of the number of lattice sites (which we call N). Thus calculating the energy spectrum in general is intractable on a classical computer, with in general 2^N steps being required to diagonalize the Hamiltonian. This Hamiltonian, which governs the electrons in the superconducting state, is given by

$$H_{\rm BCS} = \sum_{m=1}^{N} \frac{\epsilon_m}{2} (n_m + n_{-m}) + \sum_{m,l=1}^{N} V_{ml} c_m^\dagger c_{-m}^\dagger c_l c_{-l} \,, \tag{3.1}$$

where ϵ_m is the *onsite* energy for a pair with quantum number m, $n_\pm = c_{\pm m}^\dagger c_{\pm m}$ is the number operator for an electron in mode $\pm m$, and the matrix elements $V_{ml} = |\langle m, -m| V |l, -l\rangle|$ can be calculated using methods such as those found in Ref. [Mah00]. In a Cooper pair, the two electrons have opposite momenta and spins; here, the quantum numbers m signify the motional and spin states of the electrons: $m \mapsto (\mathbf{p}, \uparrow)$, $-m \mapsto (-\mathbf{p}, \downarrow)$. We shall refer to these distinct quantum numbers m as *modes.*

Physically, the onsite energies signify the energy of one pair, while the hopping terms specify the energy needed to transition from a mode l to a mode m. BCS dynamics is regulated by a competition between these two energies, similar to the physics of the Hubbard model. In general, the BCS ground state is a superposition of modes of different m.

Although the number of states m is clearly staggering in a superconductor of macroscopic size, superconductivity has also been observed in ultrasmall ($\mathcal{O}$(nm)) superconducting metallic grains. The number of states in these systems within the Debye cutoff from the Fermi energy is estimated to be ≈100 [WBL02]. Although the BCS ansatz is expected to hold in the thermodynamic limit, it would be desirable to test its predictions for these small systems.

To test the predictions of the BCS Hamiltonian, we require solutions of its energy spectrum. The BCS Hamiltonian is a member of a class of pairing Hamiltonians, which are of interest in both condensed matter and nuclear physics. There are certain methods of classical simulation that can provide exact solutions for *certain instances* of pairing Hamiltonians. Exact solutions are possible for an integrable subset of general pairing models. The number of free parameters that define an integrable model, for a given number of modes N, is $6N+3$, whereas the set of free parameters of general Hamiltonians is equal to $2N^2 - N$ [DRS03]. Therefore, the fraction of models that are integrable approaches zero as the system size increases. The most successful approximate method is the Density Matrix

Renormalization Group (DMRG), with which, for example, a pairing model with $N \approx 400$ has been solved to five digits of precision [DS99]. However, DMRG is still a fundamentally approximate method. In this chapter we explore an alternative quantum algorithm that is, in principle, numerically exact.

3.2 The Wu-Byrd-Lidar proposal

In 2002, Wu, Byrd, and Lidar (WBL) proposed a method for simulating the BCS Hamiltonian on a NMR-type quantum computer [WBL02]. In this section we will, following their paper, explain how to use a digital NMR-type quantum simulator to calculate the *low-lying* spectrum of the pairing Hamiltonian. We are concerned with finding the energy gap Δ between the ground and excited states for a specified Hamiltonian. Wu *et al.* prove that Δ can be computed using $\mathcal{O}(N^4)$ steps, where N is the number of qubits, and also the number of quantum states included in the simulation, equivalent to the number of modes N above.

They begin by mapping the Fermionic creation and annihilation operators to qubit operators. A computational $|1\rangle$ state signifies the existence of a Cooper pair in one of the possible modes, while $|0\rangle$ is the vacuum state for that mode. Thus, the total number of qubits in the $|1\rangle$ state signifies the number of Cooper pairs, and the total number of qubits translates into the total number of modes that might be occupied. Accordingly, a measurement of the number operator $n_m = (Z_m + 1)/2$ yields 1 if the mode m is excited, and 0 otherwise. The operator σ_m^+ (σ_m^-) signifies the creation (annihilation) of a Cooper pair in mode m: $\sigma_m^+ \mapsto c_{-m}c_m$ and $\sigma_m^- \mapsto c_m^\dagger c_{-m}^\dagger$

The above identification holds for pairing Hamiltonians that simulate Fermionic particle-particle interactions; thus, it is appropriate for the BCS Hamiltonian. Two other cases are given in their paper, but for simplicity, we will restrict our discussion to the case that we actually implemented experimentally (the BCS Hamiltonian). From the above point, it is simple to write H_{BCS} in terms of qubit operators, using the identities $\sigma^+ = (X + iY)/2$ and $\sigma^- = (X - iY)/2$. The final Hamiltonian that we use in our NMR implementation is

$$H_{\text{BCS}} = \sum_{m=1}^{n} \frac{\nu_m}{2}(-Z_m) + \sum_{m<l} \frac{V_{ml}}{2}(X_m X_l + Y_m Y_l) \,. \tag{3.2}$$

Their simulation scheme then follows these steps:

1. Prepare a state $|\Psi_0\rangle$ that contains a fixed number of qubits in state $|1\rangle$; all other qubits will be in $|0\rangle$.

2. Evolve the system *quasi-adiabatically* from the state $|\Psi_0\rangle$ into the state $|\Psi_I\rangle = c_G |G\rangle + c_E |E\rangle$, where $|G\rangle$ and $|E\rangle$ are, respectively, the ground and first excited states of some simulated BCS Hamiltonian. Under truly adiabatic evolution, the system would move from the ground state of the first Hamiltonian into that of the second; by speeding

up the evolution a bit, it is possible to produce excitation to $|E\rangle$ without placing significant population into the higher-energy excited states.

3. Apply the unitary transformation $U_{\mathrm{BCS}}(t_q) = \exp(-iH_{\mathrm{BCS}}t_q/\hbar)$ for t_q ranging from 0 to the total time t_Q, where a total of Q steps are used. Each time, measure one qubit in the Z basis. Any operator M for which $\langle G| M |E\rangle \neq 0$ may be measured.

4. Perform a (classical) discrete Fourier transform (DFT) on the measured spectra; frequency peaks will be present at Δ, the energy gap between $|G\rangle$ and $|E\rangle$.

We now explain how each piece is implemented in an NMR system.

Step 1 is a very common and well-understood operation in NMR quantum computing. Starting in the ground state $|00...0\rangle$, the spins may be initialized by simply applying single-qubit rotations $R_x(\pi)$ to the desired qubits.

Step 2, the quasi-adiabatic evolution, is implemented in the following way. The system is evolved under a Hamiltonian that gradually changes from the NMR Hamiltonian $H_0 + H_I$ (c.f. Sec. 2.1) into H_{BCS}. Specifically, the Hamiltonian used at each step is $H = (1 - s/S)H_0 + (s/S)H_{BCS}$. The unitary corresponding to each is $U = \exp(-iH(s)\tau/\hbar)$, where the timestep τ and total number of steps S together control the rate of quasiadiabatic evolution. This procedure is discussed further in [SvDH$^+$03]. The construction of H_{BCS} is discussed presently.

Step 3, evolution under H_{BCS}, is done by a pulse sequence designed as follows. We require an approximation of the unitary evolution under H_{BCS}, $U_{BCS}(qt_0) = \exp(-iH_{BCS}qt_0)$. An ideal NMR implementation accomplishes this by a repeatable pulse sequence $V_{\mathrm{BCS}}(t_0)$, where $U_{\mathrm{BCS}}(qt_0) \approx (V_{\mathrm{BCS}}(t_0))^q$. The Hamiltonian H_{BCS} (Eq. 3.2) contains three noncommuting parts: $H_0 = \sum_m \frac{\epsilon_m}{2}(-Z_m)$, $H_{XX} = \sum_{m<l} \frac{V_{ml}}{2} X_m X_l$, and $H_{YY} = \sum_{m<l} \frac{V_{ml}}{2} Y_m Y_l$. Assuming for the moment that the corresponding unitary operators $U_0(t), U_{XX}(t)$, and $U_{YY}(t)$ can be implemented, $V_{\mathrm{BCS}}(t_0)$ can be constructed using the third order Trotter-Suzuki formula [Tro58, Suz92],

$$V_{\mathrm{BCS}}(t_0) = [U_0(t_0/2k)U_{XX}(t_0/2k)U_{YY}(t_0/k) \times U_{XX}(t_0/2k)U_0(t_0/2k)]^k + \epsilon_{TS}\,, \qquad (3.3)$$

where the expected error $\epsilon_{TS} \equiv \|U_{\mathrm{BCS}}(t_0) - V_{\mathrm{BCS}}(t_0)\| = \mathcal{O}(t_0^3/k^2)$.

The specific method for implementing $U_0(t), U_{XX}(t)$, and $U_{YY}(t)$ depends on the chosen simulated Hamiltonian. This is presented in Sec. 3.5.

Step 4 is performed on a classical computer using the experimental results of Step 3. For each time step, the signal of one chosen nucleus is measured. As was shown with the experiment described in Sec. 2.2, a correctly prepared superposition state will oscillate at the desired frequency Δ with respect to the simulated time. In practice, the NMR peak with the best signal-to-noise ratio is used for this step.

3.3 The bounds on precision

In this section we consider two possible limitations on the precision of the final result. The first comes from the sampling rate in time used in Step 3 above, and the second from control errors. We define ε to be the average error in the final result: $\varepsilon = |\Delta - \Delta_{exp}|/\Delta$, where Δ_{exp} is the experimentally determined value. The number of digits of precision in the final answer p_ε scales broadly as $\log(1/\varepsilon)$. As discussed in Ch. 1, this implies that $\approx 1/\varepsilon$ operations are required to obtain this precision.

The WBL algorithm requires simulating H_{BCS} for times $t_q = \{0, t_q, ..., t_Q - t_0, t_Q\}$, where Q is the total number of steps, and t_0 the step size. The DFT yields an error of $\varepsilon_{\text{FT}} = 2\pi E_{max}/Q$, where $E_{max} = \hbar/t_0$ is the largest detectable energy. In general, the length of the simulation is proportional to Q; therefore, the number of gates scales inversely with the error. A similar problem in Shor's algorithm overcomes this problem by a clever way of performing the necessary modular exponentiation [Sho94].

The use of the Trotter formula, as noted above, is also a source of error. In the expansion above, the error is $\mathcal{O}(t_0^3/k^2)$. But suppose a first-order Trotter expansion would suffice (as it may for some other quantum simulation). In this general case, when one wishes to simulate the Hamiltonian $H = H_A + H_B$ with $[H_A, H_B] \neq 0$, the expansion to lowest order is

$$\exp\left(-it(H_A + H_B)/\hbar\right) = \left(\exp(-itH_A/(\hbar k)) \times \exp(-itH_B/(\hbar k))\right)^k + \delta\,, \qquad (3.4)$$

where the error $\delta = \mathcal{O}(t^2/k)$ if $\|[H_A, H_B]\|^2 \times t^2/\hbar^2 \ll 1$. The higher-order expansions have an error $\delta = \mathcal{O}(t^{m+1}/(k^m \hbar^{m+1}))$. However, each higher order carries an additional cost of $\mathcal{O}(2^m)$ more gates. Even though the increase in the number of gates is exponential, the total *time* required does not scale so badly. Since the time to implement each gate $U(t/k)$ is $1/k$ the time required to implement $U(t)$, the use of the Trotter formula to implement U requires only $2t$ total time, regardless of k. It would seem that "Trotterization" does not increase the inefficiency of the simulation with respect to the precision.

However, we note that future larger-scale quantum simulations will almost certainly require error correction. The fault-tolerant implementation of $U(t/k)$ actually takes about the same time as $U(t)$ [Pre98, Got97], whether one uses methods based on teleportation [GC99] or the Solovay-Kitaev theorem [KSV02]. Consequently, fault-tolerant simulations using the DFT and the Trotter formula require a number of gates that scales as $1/\varepsilon^r$, where $r \geq 2$.

Although the above argument urges caution for future quantum simulations, we will restrict ourselves in the rest of this section to the bounds on precision without error correction. The authors of Ref. [WBL02] predict that the number of gates scales as $3n^4\Delta/\varepsilon$, where n is the number of qubits. Can we arrive at an intuition for why this should be the case? The total number of gates is proportional to the number of gates needed to simulate U_{BCS}, which scales as n^4, which is proved in their paper. This is multiplied both by the order k

in the Trotter approximation used, as well as total number of steps Q. The fractional error due to the DFT, as stated above, is $\varepsilon \propto 1/(Qt_0)$. We require then that the error due to the Trotter formula is small compared to this, and may choose $k/t_0 = 0.1\Delta$. Upon substitution, we see that $\varepsilon_{\mathrm{FT}} \propto \Delta/(kQ)$, and this proves the WBL bound (up to constant factors).

Arriving at a practical bound on the precision requires taking into account decoherence processes, because the number of gates that can be performed without error correction N_g is given by the ratio of the gate time t_g to the fastest decoherence time τ. This time, in practice, is equal to T_2^* (Sec. 2.1). WBL assume a best-case scenario of $N_g = 10^5$. Therefore calculating Δ to a precision of $\Delta = \varepsilon_{\mathrm{FT}}$ is possible for a maximum number of $n = \sqrt[3]{10^5/3} \approx 10$ qubits. However, given the specific scalar couplings ($t_g \geq 60$ ms) and decoherence rates of our system ($T_2 \approx 10$ s), we should be able to saturate this bound for $n \leq 4$ qubits.

Of course, the above considerations assume perfect control pulses, which in reality do not exist. We now take a look at how control errors can affect the precision. In the static field of the NMR magnet, $B_0\hat{z}$, and in the absence of rf pulses, the unitary evolution is given by

$$U_{ZZ} = \exp\left(-i\hbar\sum_{ij}\frac{\pi}{2}J_{ij}Z_iZ_jt\right). \tag{3.5}$$

Normally, we make the approximation that the time required to rotate a spin by π radians is much smaller than the delay times during which no rf is applied, and the system evolves freely according to Eq. 3.5, that is, $t_\pi \ll t_d \approx 1/J_{ij}$. This is justified since t_π is $\mathcal{O}(\mathrm{ms})$, and $1/J_{ij}$ is $\mathcal{O}(10\ \mathrm{ms})$. When this approximation holds, the rf pulses are treated as δ-functions in time, implying that evolution under the ZZ interaction is assumed not to occur during this time. As t_π approaches t_d, these control errors can be mitigated to some extent, but as the number of pulses becomes greater and greater, this effect also becomes more pronounced.

In the experiment, we will explore whether we can saturate the theoretical bounds on the precision, even given faulty controls. First, though, we discuss the actual hardware that was used in our experiment.

3.4 The NMR system

We now turn to a description of the experimental system used to implement the WBL algorithm. This section contains a description of all the key components of the NMR system used in our work. Here we describe the hardware that implements all the operations discussed in Sec. 2.1.

The NMR system consists of an 11.7 T magnetic field, oriented vertically, which provides the quantization $\hat{z}$ axis for the nuclear spins contained therein. Coils of wire surrounding the

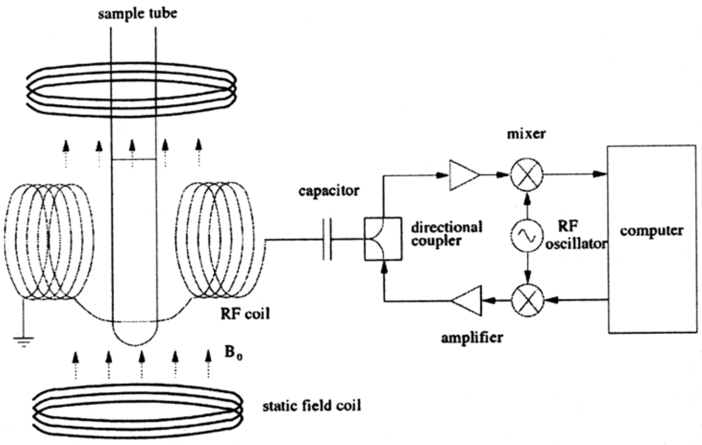

Figure 3-1: A schematic of a generic NMR system.

sample carry carefully-controlled ac currents to provide the rotations of the magnetizations of the atomic nuclei. Fig. 3-1 is a diagram of a basic NMR system. Here we briefly discuss each part, providing some specific details about our experimental system. The information in this section is a somewhat abbreviated treatment of the extensive discussion presented in the Ph.D. theses of Vandersypen [Van01] and Steffen [Ste03].

3.4.1 Sample

The system under study consists of a set of spin-1/2 nuclei that are contained within molecules. Because the signal from a single molecule is difficult to detect, a large ensemble of molecules is used. These are dissolved in a liquid solution. Although "liquid-state" NMR is commonly used for such a system, we prefer the somewhat more accurate term "solution-state." If the sample molecule is dilute enough, this effectively eliminates intermolecular couplings. What one has then is a sample of identical quantum systems. For these experiments, on the order of 10^{18} molecules are used.

The sample is contained in a glass tube with a 5 mm outer diameter and 4.2 mm inner diameter. These sample tubes have very straight sides and a uniform thickness; this minimizes the effects of a varying magnetic susceptibility on the sample. Our tubes were supplied mostly by Wilmad. The solution must be purged of impurities such as paramagnetic oxygen through a freeze-thaw process before being flame-sealed. This process involves freezing the sample, subjecting it to vacuum, then thawing it. With each step, oxygen is removed. The sample is finally placed in a device called a "spinner," which, true to its name, enables the tube to be rotated around the magnetic field axis ($\hat{z}$) at 20 revolutions per second. This helps to cancel inhomogeneities in the $\hat{x}$-$\hat{y}$ magnetic field.

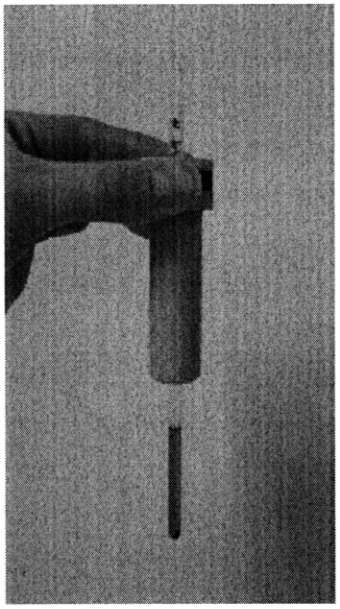

Figure 3-2: A typical sample tube filled with molecules in solution that are used for NMR quantum computation and simulation.

3.4.2 Magnet

The static magnetic field is provided by a superconducting magnet manufactured by Oxford Instruments. A superconducting coil cryogenically cooled with liquid helium to 4.2 K creates a magnetic field of $B_0 = 11.7$ T using about 100 A of current. It features an active vibration isolation system, and is actively shielded so that the 5 gauss line is about 3 m away from the outer shell of the magnet. The cryogenic environment is maintained by surrounding the liquid helium reservoir with a vacuum shell, which in turn is surrounded by a 77 K liquid nitrogen reservoir, which itself is shielded by another vacuum shell. The hold time for liquid nitrogen is about 10 days, while that for liquid helium is about three months.

The magnetic field due to this coil is not perfectly homogeneous. In practice, this leads to a loss of coherence as variations in the field effect a "spread" in the chemical shifts of the nuclei in the sample, and thus errors in the frequency at which the nuclei are being addressed. Homogeneity is fine-tuned by a set of "shim" coils that surround the sample. One set of coils is also superconducting, and is adjusted during magnet installation, not to be changed by the user. The other set is not superconducting, and produces smaller spatially-varying fields that are to be adjusted by the experimenter. The field homogeneity is maximized by observing the linewidth of one nuclear resonance as a function of the currents in each of these coils. This is an iterative process that can take some time. Automated routines do exist, but we find that the best results generally come from manually tweaking the shim currents. The shim settings depend strongly on the sample and probe being used, but for each pair of these, there is a good "baseline" set of shim currents that is saved and re-used.

Figure 3-3: The 11.7 T, 500 MHz superconducting magnet. The rf probe is inserted from the bottom, and the sample from the top. Liquid nitrogen and helium fill ports are also located on the top. Photo courtesy of M. Steffen [Ste03].

After loading these settings, the homogeneity can normally be fine-tuned in a matter of minutes.

A final aspect of the magnet is that the static field B_0 does slowly drift in time due to the tiny amount of power dissipation present in the superconducting coil. The order of magnitude for this drift is about 1 Hz/hour. Although this is tiny in relation to ω_0, this small change can have a negative impact on precision techniques such as quantum operations. To correct this problem, there is one further room-temperature coil that adjusts the static field. The current through this coil is locked to the resonance frequency of the deuterium nuclei in the solvent of the sample. Although this locking method is not the only way to approach the problem, it is quite convenient, since the process runs in the background after some initial setup.

3.4.3 Probe

The probe is a multi-purpose device that supplies the rf fields that manipulate the nuclei, reads out the magnetization signal from the sample, and also regulates the temperature of the sample using air at a specific temperature. The rf coils are about 1.5 cm in diameter and address a region within the sample that is about 2 cm long, called the "active region." The coils are made of a low-resistivity metal (such as copper) and have from 1 to 3 windings.

The coils are part of a resonant circuit with a Q factor on the order of 100. A circuit that contains two adjustable capacitors is used; the first varies the resonant frequency of the circuit, enabling one to tune to a specific nuclear resonance, while the second permits impedance matching. The transmission lines, which are coaxial cables, have an impedance of 50 Ω; thus, the circuit is matched to that impedance to avoid reflection of power from the sample, maximizing the effectiveness of the rf signals, and to permit maximum transfer of the signal from the nuclei to the receiver, maximizing the signal-to-noise ratio.

The probe actually contains two separate pairs of rf coils; the first is for higher-frequency nuclei such as ^{1}H and ^{19}F, both of which have resonances above 200 MHz. The second is for lower-frequency nuclei such as ^{13}C, which has a frequency below 200 MHz. The reason for this is that it is hard to design resonant circuits that have a high Q factor over a very wide bandwidth. The high-band and low-band coils are mounted at right angles to minimize cross-talk. We used a commercial HFX probe from Nalorac. The "H" and "F" refer to the high-band coils, which are tuned for hydrogen or fluorine. The "X" means that the low-band coils are tunable over a wide range. In our experiments, we tuned this coil for ^{13}C.

Finally, the probe is responsible for regulating the temperature of the sample. Thermocouples measure the temperature of the sample, and air at a specific temperature is flowed through the probe in accordance with the temperature measurement. Thus the temperature is actively stabilized. The probe may also contain coils for generating magnetic field gradients in space, but this does not play a role in our work here.

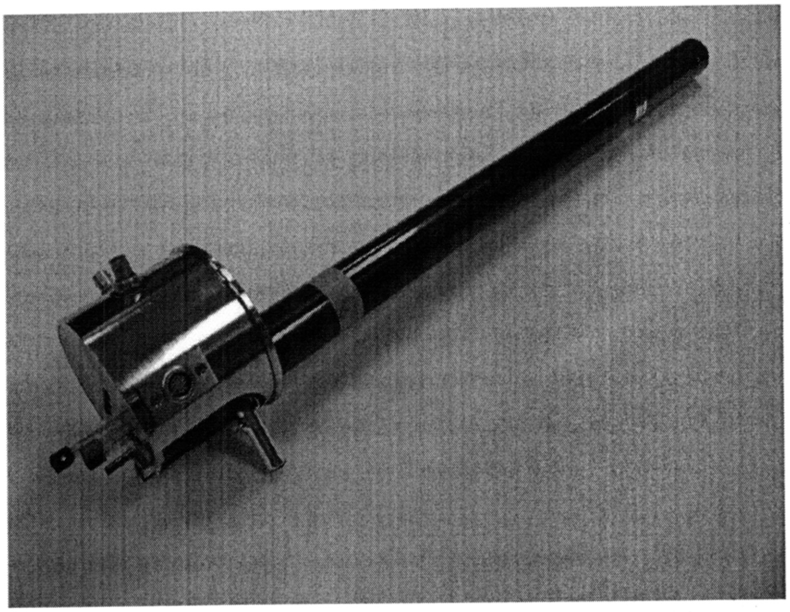

Figure 3-4: The above probe is a Nalorac HFX probe, where X was tuned to ^{13}C

.

3.4.4 RF electronics

The rf electronics discussed in this section consist of the transmitter and the receiver. The spectrometer we used is a custom-modified Varian $^{\text{UNITY}}$*Inova* unit with four transmitter channels.

The transmitter consists of four frequency sources (PTS 620 RKN2X-62/X-116) that are supplied with a 10 MHz reference signal by a temperature-controlled crystal oscillator. These frequency sources then supply rf signals of up to 1 V_{rms} in the range of 1-620 MHz, with frequency resolution of 0.01 Hz. These signals are sent to *transmitter boards* that create pulses of the duration programmed by the experimenter. These have a resolution of 50 ns with a minimum pulse length of 100 ns. In addition, the phase may be set with a ressolution of 0.5°. A set of fast memory boards, the *waveform generator boards*, is then used to shape the pulses as desired.

The power of the pulses is then set by passing through a set of coarse attenuators. These can attenuate the signals by up to 79 dB in steps of 1 dB. The relative powers of each pulse are set here, and finally the pulses pass through a set of linear amplifiers. There are two dual amplifiers that each contain two units, a *low-band* amplifier that operates from 6-200 MHz with 300 W maximum pulse power and 60 dB gain, and a *high-band* amplifier that operates from 200-500 MHz with 100 W maximum pulse power and 50 dB gain. The amplifiers are fast; rise/fall times are 200 ns, which is more than sufficient for our experiments. Also, there are fast "blanking" circuits which shut off all output from the amplifier to the experiment. Were this not the case, noise from the amplifiers in between pulses would harm the fidelity of the quantum simulation effectively making our classical controls excessively noisy. The on/off time for these blanking circuits is $> 2\ \mu$s. The signal is normally routed automatically from the transmitter boards 1 and 2 to the correct (high/low) band channel of the first amplifier unit, and likewise from boards 3 and 4 to the second unit.

All of the outputs from the amplifiers within each band are combined using high-power combiners before passing through a PIN diode transmit/ receive switch. This switch isolates these high-power signals from the sensitive receiver preamplifier. The signals are finally routed to the correct coils of the probe.

When the PIN diode switches are in receive mode, the signals induced in the probe by the nuclei are passed to high-band and low-band preamplifiers with gain of 35 dB. These signals are sent to receiver boards in the electronics cabinet that mix the signals down to audio frequencies and separate them into two quadratures, after which they are also passed through audio filters (with bandwidth 100 Hz to 256 kHz). The signal is then digitized and uploaded to the computer. The maximum sampling rate is 1 MHz.

3.4.5 Computer control

A Sun Ultra 10 workstation is the control panel of the spectrometer. Pulse instructions are sent to the spectrometer using commercial software from Varian. The pulse sequences themselves are written in C and compiled. One may use a set of low-level commands that adjust parameters such as pulse duration, phase, and channel number.

It is convenient to use a higher-level language to specify a set of experiments to be run and to subsequently process the data. Matlab serves this purpose nicely. This affords a great deal of automation, as a number of experiments can be run for a long period of time (say, overnight) and then automatically processed later on. For instance, a number of experiments may be performed and then the final average density matrix calculated.

3.5 Experiment

We chose as our sample ^{13}C-labeled CHFBr$_2$, the structure of which is shown in Fig. 3-5. The J-couplings between each nucleus are $J_{HC} = 224$ Hz, $J_{HF} = 50$ Hz, and $J_{CF} = -311$ Hz. This three-qubit molecule is appropriate for quantum simulations of three modes and up to three Cooper pairs. We chose to implement two different Hamiltonians, using two Cooper pairs. The Hilbert space is therefore spanned by $|101\rangle$, $|110\rangle$, and $|011\rangle$.

We implemented two different Hamiltonians: H_1, in which $V_{ab} = \pi J_{HC}$, $V_{ac} = \pi J_{HF}$, and $V_{bc} = \pi J_{CF}$, and a harder case, H_2, in which $V_{ab} = \pi J_{HC}$ and $V_{ac} = V_{bc} = 0$. For both Hamiltonians, $\nu_1 = 150\pi$ Hz, $\nu_2 = 100\pi$ Hz, and $\nu_3 = 50\pi$ Hz. Although the choice of Hamiltonians is somewhat arbitrary, they are sufficient to illustrate the impact of control errors, as H_2 requires more refocusing pulses than H_1.

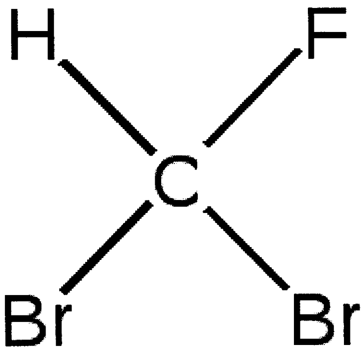

Figure 3-5: The $CHFBr_2$ molecule. Although drawn in a plane here, it is actually tetrahedral.

The method of implementing these Hamiltonians is as follows. The pulse sequences presented here implement the individual parts of the longer pulse sequence discussed in Sec. 3.2. We use composite rotations about the $\hat{x}$ and $\hat{y}$ axes to generate rotations about $\hat{z}$:

$$U_0 = \prod_m R^m_{\hat{y}}(\pi/2) R^m_{\hat{x}}(\pi\nu_m) R^m_{-\hat{y}}(\pi/2)\,, \tag{3.6}$$

where m indexes the individual qubits. U_{XX} and U_{YY} are generated by applying single qubit pulses to rotate the scalar coupling from $\hat{z}$ to $\hat{x}$ or $\hat{y}$. Let us use the same convention as above, that qubit a is ^{1}H, qubit b is ^{13}C, and qubit c is ^{19}F. Written in time order, the pulse sequence to implement H_1 is

$$U_{H_1} = R^a_{\hat{y}}(\pi/2) - R^b_{\hat{y}}(\pi/2) - U_{ZZ}(t) - R^a_{\hat{y}}(-\pi/2) - R^b_{\hat{y}}(-\pi/2)\,, \tag{3.7}$$

where the superscripts of the rotation operators denote the qubit being acted upon, and the U_{ZZ} evolution affects all qubits. The rotation operators for qubits 1 and 2 on either side of $U_{ZZ}(t)$ may be swapped, as these operations commute (and are assumed to take zero time).

To implement H_2, one only needs to remove the coupling of the third nucleus since $V_{ac} = V_{bc} = 0$. This can be done using the refocusing technique presented in Sec. 2.1.5. H_2 is simulated by replacing $U_{ZZ}(t)$, in the above sequence, with

$$U_{ZZ}(t/2) - R^c_{\hat{x}}(\pi) - U_{ZZ}(t/2)\,. \tag{3.8}$$

The initialization of the state $|\Psi_I\rangle = c_G\,|G\rangle + c_E\,|E\rangle$ requires, as mentioned in Sec. 3.1, quasiadiabatic evolution. This discrete-step process was demonstrated in [SvDH$^+$03], but here we speed it up somewhat to populate the first excited state $|E\rangle$. The Hamiltonian at each discrete timestep s is $H_{ad}(s) = (1 - s/S)H_0 + (s/S)H_{\text{BCS}}$. We find $S = 4$ steps, with time steps of $t_{ad} = 1/700$ s, to be sufficient. We do note that, for for $\|H_{XX} + H_{YY}\| \gg \|H_0\|$ there can be a phase transition as s is changed [McK96]; as the gap goes to zero at the

Model	Δ/Hz	Method	$\Delta_{exp}/2\pi\cdot$Hz	τ_e/ms	t_0/ms	Q
H_1	218 $\cdot 2\pi$	$W1$	227 ± 2	180	1	400
		$W1$	220 ± 2	250	2	200
H_2	452 $\cdot 2\pi$	$W1$	554 ± 10	30	.5	200
		$W2$	440 ± 5	80	.5	200

Table 3.1: Experimental results for gaps found for Hamiltonians H_1 and H_2. Estimated gaps (Δ_{exp}) and effective coherence times (τ_e) for given time steps t_0 and number of steps Q are given.

phase transition this can be problematic, since the number of steps required for successful quasiadiabatic evolution grows inversely with the gap.

As mentioned in Sec. 3.3, we chose to study the effect of control errors by using a simple method of error compensation. We refer to this method as $W2$, while the above method without error compensation is referred to as $W1$. $W2$ partially corrects for the ZZ evolution during single-qubit pulses by modifying the delay time during the free evolution periods:

$$R(\theta_1)U_{ZZ}(t)R(\theta_2) \to R(\theta_1)U_{ZZ}(t-\alpha)R(\theta_2)\,, \tag{3.9}$$

where $\alpha = (t_\pi/(2\pi))(\theta_1 + \theta_2)$. Numerical results show that using method $W1$ produces a significant systematic shift in the final result compared to $W2$. This is presented together with the experimental data in Fig. 3-6.

From direct diagonalization of the Hamiltonians, we expect $\Delta = 218 \cdot 2\pi$ Hz for H_1, and $\Delta = 452 \cdot 2\pi$ Hz for H_2. For H_2, Δ is the energy difference between $|G\rangle$ and $|E_2\rangle$, since $|E_1\rangle$ is not connected by usual adiabatic evolution. The experimental result Δ_{exp} was determined by a least-squares fit of the ^{1}H NMR peak to a damped sinusoid with frequency Δ_{exp} and decay rate $1/\tau_e$. The choice of nucleus to measure is also arbitrary, since all peaks oscillate at the same frequency Δ_{exp}, but we have chosen the ^{1}H peak since it has the best signal-to-noise ratio.

Our experimental results are presented in Fig. 3-6 and Table 3.1. For these results, we expect the measured value Δ_{exp} for the energy gap to be given by $\Delta_{exp} = \Delta + \varepsilon_{sys} \pm \varepsilon_{\mathrm{FT}}$, where ε_{sys} is the systematic error (due to control errors). The impact of systematic and random errors was investigated by simulating H_1 with $W1$ for $\varepsilon_{\mathrm{FT}} = 2.5 \times 2\pi$ Hz at two different simulation times, $t_0 = 1$ ms and $t_0 = 2$ ms. (Here we have exploited the fact that many values of Q and t_0 yield the same $\varepsilon_{\mathrm{FT}}$.) The random error in both cases is $\varepsilon_{\mathrm{FT}}$, as expected. The systematic error increases with smaller t_0, indicating that the error due to undesired scalar coupling becomes larger than the errors due to the Trotter approximation. Consequently, a slightly longer t_0 yields a systematic error that is within $\varepsilon_{\mathrm{FT}}$ of the exact answer. We have thus shown that for H_1, we have saturated the theoretical bounds on the precision.

While the results for Hamiltonian H_1 were good even without control error compensa-

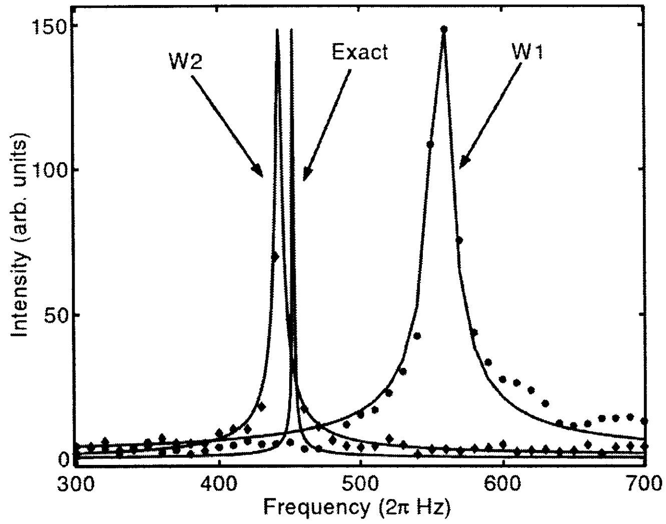

Figure 3-6: Frequency-domain spectra of Hamiltonian H_2 obtained using methods $W1$ (circles) and $W2$ (diamonds). The solid lines are fits to time-dependent data. The width of the exact curve is taken to be the dephasing rate ($1/T_2^*$) of the ^{13}C nucleus, which has the highest dephasing rate.

tion, the effects of control errors were very evident in the results for H_2. Hamiltonian H_2 was implemented using both $W1$ and $W2$ for $\varepsilon_{\rm FT} = 10 \cdot 2\pi$ Hz and $t_0 = 0.5$ ms. The shorter time step was necessary because the larger Δ made the simulation more sensitive to Trotter errors. Comparing the $W2$ and $W1$ results shows that with no control error compensation, a gap Δ_{exp} is found that is $\Delta/5$ away from the actual value. In contrast, with simple error compensation Δ_{exp} is ϵ_{FT} from the actual value. Future implementations should strive to detect and bound control errors by verifying that Δ_{exp} converges as t_0^3 for small values of t_0, as theoretically expected.

3.6 Discussion

To summarize this work, we have simulated the BCS Hamiltonian using the smallest problem instance that requires both adiabatic evolution and the Trotter approximation. We find that our implementation on an NMR quantum computer saturates the bounds on the precision that were predicted by us and by WBL. The most important aspect of this work is understanding the limitations of the precision of the final result, both due to intrinsic aspects of the protocol such as the Fourier transform and the Trotter approximation, and due to system-specific aspects such as control errors and natural decoherence. We summarize our conclusions here.

1. Results obtained using digital quantum simulation are generally inefficient with respect to the precision. Nevertheless, if the dynamics may be implemented efficiently,

	Classical	Quantum
Digital	Space: $2^n \mathcal{O}(\log 1/\epsilon)$ Time: $T 2^{2n}$	Space: n Time: $T n^2 \mathcal{O}(1/\epsilon^r)$
Analog	Space: 2^n Time: T Precision: $\mathcal{O}(\log 1/\epsilon_{fix})$	Space: n Time: $T\mathcal{O}(1/\epsilon)$

Table 3.2: A comparison of the resources required for digital and analog simulation of quantum systems, using both classical and quantum systems, and taking into account the precision obtained. We consider a system of n qubits simulated for a total time T. The error due to projection noise is denoted ϵ, while the fixed error of a classical analog computer is denoted ϵ_{fix}. Here $r \geq 2$ when error correction is required.

the quantum simulation is still *more* efficient than a classical algorithm, provided no efficient classical approximation exists.

2. In general, use of the Trotter formula or some related technique will be necessary in digital quantum simulation, as most non-trivial Hamiltonians have mutually non-commuting terms. We have shown that, when fault tolerance is required, this process increases the number of required gates by a broadly exponential factor. The conclusion here is roughly the same as in item 1: this class of simulations is inefficient with respect to the precision, but moreso when error correction is needed. This result is included in Table 3.2.

3. Control errors are a problem that afflicts any quantum simulator. The type that appear in NMR arise from the "always-on" scalar coupling interaction. Although for small systems it is relatively easy to compensate (to first order) for these errors, and thereby bring the solution to within the theoretical bound, it will not be so straightforward in larger systems. Fortunately, in scalable systems such as ion traps, the two-body interactions are controlled more directly by the experimenter. There will be control errors in that system as well, but of a different sort.

4. All quantum simulations are limited by natural decoherence times. The bound on the number of qubits that may be used to obtain an answer to within a given error depends on the number of gates that may be performed within the coherence time, unless error correction is used. Error correction becomes necessary for larger systems, but then the overall scaling properties become less favorable, as explained in items 1 and 2.

We would like to point out that the above results apply to digital quantum simulation generally, regardless of whether the classical discrete Fourier transform (DFT) or the quantum Fourier transform (QFT) is used. Our results apply to both for the reason that they deal with the implementation of the simulated Hamiltonian; whether the DFT or QFT is used to extract the answer is irrelevant. In fact, the first result was acknowledged by the authors of the papers on QFT-based digital quantum simulation [AL97, AL99]. The second relates only to the application of the simulated Hamiltonian, which is the same in DFT and QFT methods. The third, relating to control errors, will be germane to every quantum control experiment, and again deals with the implementation of the Hamiltonian rather than the extraction of the result. The fourth result, acknowledging the effects of decoherence, is also certainly true in both cases.

These precision limitations being as they are, there is still reason to pursue digital quantum simulation. For instance, in cases for which there is no good classical approximation, the limited precision of a digital quantum simulator will still be superior to classical methods. In addition, analog quantum simulation is promising for systems of an intermediate size, that are too large for classical simulation, but small enough so that error correction is not essential.

Part II

Two-dimensional ion arrays for analog quantum simulation

Chapter 4

Theory and history of quantum simulation using trapped ions

In the previous part, we explored how NMR systems can be used to perform quantum simulations. However, we also saw some drawbacks to the scalability of these systems, as well as to the precision with which results can be calculated. In this chapter, we present an alternative approach based on trapped ions. Trapped ions have a long coherence time (potentially $\mathcal{O}(10\text{ s})$ or longer), which exceeds that of nuclear spins in solution, and offer a potentially scalable system in the sense that the number of ions that can be used is unlimited if proper controls are available and decoherence is sufficiently small (or error correction is used). Networking between ions may be accomplished by moving ions or by linking them with photonic or electronic quantum communication, as discussed in Ch. 1.

We also noted in Ch. 1 that the analog approach to quantum simulation is promising for quantum simulations of systems that do not require error correction, or systems which are fundamentally not amenable to error correction, such as systems with continuous Hilbert spaces. In particular, analog simulations of spin physics may be able to solve problems that classical simulation cannot for as few as 36 interacting particles [RMR+07]. Here, we turn to such analog systems. Our main effort is to design and experimentally characterize an ion trap in which such a simulation could be done, focusing on the problem of simulating a 2-D lattice of interacting spins using trapped ions.

In Sec. 4.1, we present the basic ion trap Hamiltonian and demonstrate how it permits quantum control of the internal and external degrees of freedom of trapped ions using laser radiation. Then, in Sec. 4.2, we outline the method proposed in Ref. [PC04b] for simulating quantum spin models in an ion trap. Sec. 4.3 enumerates the challenges involved with designing ion traps for such quantum simulations, framing the questions explored in the remainder of Part II. We summarize in Sec. 4.4.

4.1 The ion trap system and Hamiltonian

An ion trap is an electromagnetic device for confining a charged particle in space. The charged particle that concerns us is a singly-charged atomic ion, unless otherwise noted. A trapped ion, if left undisturbed, contains two separable quantum systems: a ladder of harmonic oscillator motional states, and an internal electronic state. The key insight of trapped ion quantum computation (and simulation) is that these internal and external states can be made to interact, and even become entangled, using a set of classical control pulses, which usually take the form of laser radiation (but can also be microwaves or magnetic fields). Comparing this situation to solution-state NMR, we note that the same basic ingredients are present, but in a different form. The spin states of nuclei are replaced by the electronic states of ions, while interaction between these states is mediated not by chemical bonds, but by the coupled motion of the ions.

There are two main varieties of ion trap: Paul traps and Penning traps. Paul traps use oscillating radiofrequency (rf) electric fields, possibly in combination with dc electric fields, to confine ions. In these traps, one finds that time-averaging the oscillating field leads to an effective harmonic potential. Penning traps use static magnetic fields and electric fields to confine ions. The ions execute cyclotron motion around the B-field lines, and are simultaneously confined along the axis of the B-field by static voltages applied to endcap electrodes. Both have advantages and disadvantages. Penning traps necessarily have a very large Zeeman shift due to the confining magnetic fields, whereas in Paul traps the internal states are much less sensitive to the trapping fields. However, ions in Paul traps exhibit small oscillations at the rf frequency, called *micromotion*, that can only be removed if the ions are positioned where the confining fields vanish. Because of the independence of the internal states from the trapping fields, but for other reasons as well, Paul traps have been the trap of choice for most quantum information experiments. In this chapter, we shall focus on them exclusively.

In this section we first discuss the ion trap potential and the motion of ions confined therein. We then turn to understanding laser-ion interactions to a sufficient extent that we can study the theory of quantum simulations with trapped ions, and also review the principles of laser cooling of ions, a technique which will be used extensively in the experimental work of this thesis.

4.1.1 Motional states of trapped ions

All Paul traps obey the following basic principle. An electric quadrupole (or "saddle-shaped") potential is formed in space by a set of electrodes, each of which is charged to a certain voltage. In the case of static voltages, the ion would follow the field lines out of the center of the potential. In fact, it is a well-known result, commonly known as *Earnshaw's theorem*, that no static electric field configuration can trap a charged particle. However, if

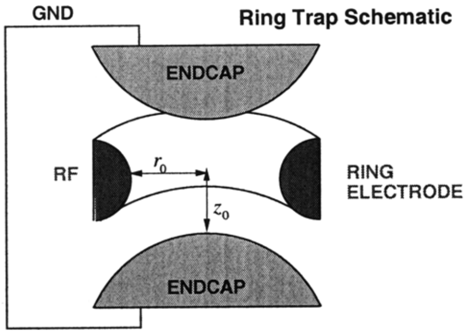

Figure 4-1: A schematic of a ring Paul trap. The ion is located a distance r_0 from the nearest point on the rf electrode, and a distance z_0 from the nearest point on either of the dc endcap electrodes.

the potential is rotated (or, more accurately, "wobbled") at the proper frequency, then a particle can in fact be trapped.

A typical "ring" Paul trap is depicted in Fig. 4-1. It consists of one ring electrode that is oscillating at an rf voltage V_{rf}, along with two "endcap" electrodes that are grounded. These may have a dc voltage applied to them. Near the center of the trap, the electric potential may be written as

$$V(x, y, z) = \alpha x^2 + \beta y^2 + \gamma z^2. \tag{4.1}$$

Since the area in the trap region is free of charge (aside from that of the trapped particle, which is negligible), Laplace's equation, $\nabla^2 V = 0$, must be satisfied. For our potential, this means that $\alpha + \beta + \gamma = 0$. For the case of the ring trap, $\alpha = \beta = -2\gamma$.

To trap an ion, this potential must vary in time. Typically, an oscillating potential of the form

$$V(t) = V_0 \cos(\Omega t + \phi) \tag{4.2}$$

is applied. For the remainder of the thesis, we refer to V_0 as the *rf amplitude* and Ω as the *rf frequency.* In general, the solutions to this equation are solutions to the Mathieu equations, which have the general form

$$\ddot{u}_i = [a_i + 2q_i \cos(\Omega t)] \frac{\Omega^2}{4} u_i = 0, \tag{4.3}$$

where the u_i are the position coordinates of the ion along each direction. The parameters q_i and a_i obey the following equations:

$$
\begin{aligned}
q_i &= \zeta_i \frac{-2e_c V}{m r_0^2 \Omega^2} && (4.4) \\
a_i &= \zeta_i \frac{4 e_c U}{m r_0^2 \Omega^2} && (4.5)
\end{aligned}
$$

where $e_c = 1.6 \times 10^{-19}$ C is used throughout the thesis as the (positive) elementary charge, m is the mass of the ion, and r_0 is defined in Fig. 4-1 as the distance from the trap center to the nearest point of the rf electrode. The constants ζ_i depend on the direction i; $i = 1$ for $\hat{x}$ and $\hat{y}$, while $i = -1$ for $\hat{z}$. U is a voltage that may be applied to the endcaps of the ring trap. Since it is possible to trap with $U = 0$, a is normally zero. In the lattice trap (Ch. 5) and elliptical trap (Ch. 7), no dc voltage is required to trap the ions. In traps based on linear ion traps, however, the rf fields provide confinement along only two directions; a static voltage is required for the third. Even in this case, however, ions may be trapped if U is small compared to V. The parameters a and q determine whether the trap is stable, that is, whether an ion confined in it can remain so. The "stability regions" in a-q space have been calculated, and are given in [Gho95]. In particular, for $a = 0$, $0 \leq q \leq 0.908$ results in a stable trap.

The method of solution of these equations is presented in [LBMW03]. For our purposes, it will be sufficient to invoke the *pseudopotential approximation.* This result assumes that the motion of the ions can be decomposed into two parts: small oscillations at the drive frequency Ω, referred to as *micromotion*, and slower oscillations within an effective harmonic well at a lower frequency, called the *secular motion.* The solution has the form

$$
u_i(t) = A_i \cos(\omega_i t) \left[1 + \frac{q_i}{2} \cos(\Omega t) \right] , \tag{4.6}
$$

where A_i is the amplitude of the ion's motion along direction i. The term that oscillates at Ω represents the micromotion. It is proportional to the term of order unity, and smaller by a factor of $\frac{q_i}{2}$. Since q_i is around 0.3 for many of our experiments, the amplitude of this motion is on the order of one-tenth that of the secular motion, hence the term *micromotion* is apt. When $a = 0$, the relation between the *secular frequency* ω and the drive frequency Ω is

$$
\omega_i = \frac{q_i}{2\sqrt{2}} \Omega, \tag{4.7}
$$

giving rise to our oft-stated "rule of thumb" that the secular frequency is about one-tenth the drive frequency.

The formula for the pseudopotential Ψ is

$$
\Psi(x, y, z) = \frac{Q^2}{4 m \Omega^2} \left| \vec{\nabla} V(x, y, z) \right|^2 , \tag{4.8}
$$

where Q is the charge of the trapped particle (equal to e_c for the atomic ions used in this thesis) and m is its mass. We will use this formula in all our calculations of ion trap potentials, and find that it agrees quite well with our results. Dissecting this formula a bit, we see that Ψ is proportional to $e_c Q/r_0^2$; the $1/r_0^2$ dependence comes from the gradient of the potential squared. This parameter depends on the trap geometry, and in most of our traps is computed numerically. For ion traps that admit approximate analytical solutions, r_0 has a clear physical significance; for example, in the case of the ring trap, it is the distance from the trap center to the nearest point on the rf ring electrode.

For the quadrupole potential above, close to the its minimum, the pseudopotential has the form of a three-dimensional harmonic oscillator:

$$\Psi(x, y, z) = \frac{1}{2} m \sum_i \omega_i^2 u_i^2, \tag{4.9}$$

where the ω_i are the secular frequencies.

The classical solutions for a particle in a harmonic oscillator will not be repeated here. We will briefly present the quantum mechanical solution, since this is essential to the theory of quantum simulation with ion traps. The Hamiltonian of the oscillator in a given direction with frequency ω is

$$H = \hbar\omega \left(a^\dagger a + \frac{1}{2} \right), \tag{4.10}$$

where $[a, a^\dagger] = 1$ (see Ref. [Sak85] for further details). The operators a and $a^\dagger$ are called the *annihilation* and *creation* operators, respectively. Their effect on the state $|n\rangle$ is to remove or add one quantum of vibrational energy to the state $|n\rangle$:

$$a |n\rangle = \sqrt{n} |n - 1\rangle ; \qquad a^\dagger |n\rangle = \sqrt{n+1} |n + 1\rangle . \tag{4.11}$$

The eigenbasis is the set of states $\{|n\rangle\}$ that satisfy, in addition to the above,

$$H |n\rangle = \hbar\omega \left(n + \frac{1}{2} \right) |n\rangle . \tag{4.12}$$

The ground state wave function, for which $a |0\rangle = 0$, is written in coordinate space as

$$\langle 0 | x \rangle = \sqrt{\frac{x_0}{\pi}} e^{-\left(\frac{x}{2x_0}\right)^2}, \tag{4.13}$$

where $x_0 = \sqrt{\frac{\hbar}{2m\omega}}$ is the width of the ground state wavefunction.

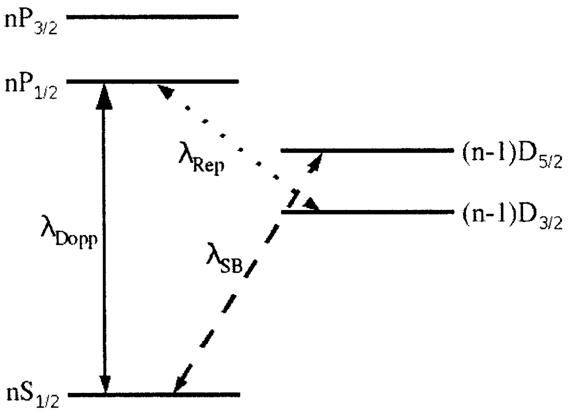

Figure 4-2: Generic level structure for the ions used in the experimental work for this thesis. Here n is the principal quantum number; the D states have one less unit of n, as shown. The three transitions are the ones discussed in this chapter. λ_{Dopp} is the Doppler cooling and detection transition. λ_{Rep} is the repumper for the $\mathrm{P}_{1/2}$ state; it is needed whenever the λ_{Dopp} transition is addressed. λ_{SB} is a narrow quadrupole transition that is used for sideband cooling and state manipulation.

4.1.2 Control of ionic internal states

In this section we will study the basic atomic structure of all the ions used in this work, and describe how lasers can be used to effect transitions between these levels. There are two types of atomic structure that are widely used in trapped ion quantum information processing: the first relies on a ground state connected to a metastable excited state by an optical transition (hundreds of THz), while the second connects two hyperfine levels with a transition that is in the GHz range. Here, we will focus on the former case, since it applies to both ions used in this work, $^{88}\mathrm{Sr}^+$ and $^{40}\mathrm{Ca}^+$.

We begin with a review of the atomic structure of such ions. Both are hydrogenic, meaning that there is only one valence electron. A diagram of the electronic level structure of such an ion is given in Fig. 4-2. Each transition is characterized by two numbers: the transition frequency Ω_{ij}, where i and j label the states, and the excited state lifetime τ, which is related to the spontaneous emission rate Γ by $\tau = 2\pi/\gamma$. The term symbols follow the usual conventions for L-S (Russell-Saunders) coupling, which is valid whenever spin-orbit coupling is weak. This scheme assumes that the orbital angular momentum L and total angular momentum J are good quantum numbers, leading to an atomic state $|nSLJm_J\rangle$. The first number is the principal quantum number n. The superscript 2 is equal to $2S+1$, and is always two for such atoms since there is only one valence electron. The capital letter following it gives the orbital angular momentum, assigning each value a letter (for historical reasons): $(L=0) \mapsto$S, $(L=1) \mapsto$P, and $(L=2) \mapsto$D. The subscript gives the value of the total angular momentum J. J may take values ranging in integer steps from $\|L-S\|$ to $L+S$. The quantum number m_J represents the projection of the total angular momentum along the quantization axis, which is determined by the orientation of the external magnetic field.

We now describe the interaction of the trapped ion with laser radiation, which is essential for understanding how quantum operations may be performed on trapped ions, as well as other techniques such as Doppler cooling and state measurement. We focus on electric dipole transitions, which occur between atomic levels that differ by one unit of orbital angular momentum. For simplicity, we will limit the discussion to the coupling of two discrete levels. The interaction is that of the dipole moment of the electron interacting with the oscillating laser field. The interaction is written as

$$H_{dip} = -\vec{d} \cdot \vec{E} = -\vec{d} \cdot \vec{\epsilon} E_0 \cos\left(-\omega_l t + \vec{k} \cdot \vec{z} + \phi\right), \tag{4.14}$$

where $\vec{d} = e_c \vec{z}$ is the dipole operator, $\vec{z}$ is the displacement vector of the ion from its equilibrium position, $\vec{\epsilon}$ is the polarization of the laser, E_0 is the amplitude of the laser's electric field, ω_l is the frequency of the laser radiation, $\vec{k}$ is the wavevector of the radiation field, and ϕ is a phase that may be chosen by the experimenter. We will assume that the wavevector of the light is in the $\hat{z}$ direction.

We note that the dipole operator is proportional to $\sigma^+ + \sigma^-$, where $\sigma^+ = |\uparrow\rangle\langle\downarrow|$ and $\sigma^- = |\downarrow\rangle\langle\uparrow|$ are the raising and lowering operators for the atomic state, respectively. Making use of the relation of the creation and annihilation operators to the operators x and p, and making a rotating wave approximation, the above Eq. 4.14 takes the form

$$H_I = \hbar\Omega\left(e^{i\eta(a+a^\dagger)}\sigma^+ e^{-i(\omega_l t+\phi)} + h.c.\right), \tag{4.15}$$

where $h.c.$ denotes Hermitian conjugate. The Rabi frequency Ω is the rate at which the atomic state $|\uparrow\rangle$ is flipped to $|\downarrow\rangle$ and vice-versa. For an electric dipole transition, $\Omega = |e_c E_0 \langle\downarrow| z |\uparrow\rangle|$, that is, it depends on the applied electric field and on the expectation value of the dipole operator $e_c z$. The *Lamb-Dicke parameter* η is equal to kz_0, where k is the norm of the wavenumber of the radiation field and z_0 is the width of the ground state wave function along $\hat{z}$: $z_0 = \sqrt{\frac{\hbar}{2m\omega_{\hat{z}}}}$. A small η ($\eta \ll 1$) means that the ion in its ground state is well-localized in space to within the wavelength of the laser light, which implies that the light field will couple well to the harmonic oscillator mode in that direction. This condition is called the Lamb-Dicke limit, and when it is satisfied, the interaction Hamiltonian looks like

$$H_I = \hbar\left(\Omega e^{i\phi}\right)\sigma^+ e^{-i(\omega_l-\omega_0)t}\left(1 + i\eta\left(ae^{-i\omega_{\hat{z}}t} + a^\dagger e^{i\omega_{\hat{z}}t}\right)\right) + h.c., \tag{4.16}$$

where $\omega_{\hat{z}}$ is the ion's secular frequency in the $\hat{z}$ direction.

Eq. 4.16 actually reveals all the physics of how manipulations may be made on both the internal and external states of a single trapped ion using laser radiation. We focus first on the case in which the laser detuning δ_l, defined as $\delta_l \equiv \omega_l - \omega_{\hat{z}}$, is zero. We also neglect coupling to the motional states by setting $\eta = 0$. The Hamiltonian that acts on the internal state of the ion is

$$H_{int} = \hbar\Omega \left(\sigma^+ e^{-i\phi} + \sigma^- e^{i\phi}\right), \tag{4.17}$$

and the unitary transformation done on the ion-qubit is

$$U(t) = \exp\left(-iH_{int}t/\hbar\right). \tag{4.18}$$

The rotations $R_{\hat{x}}(\theta)$ and $R_{\hat{y}}(\theta)$ may be performed by turning on this Hamiltonian for an appropriate period of time and setting the phase ϕ correctly. A rotation along $\hat{z}$ may be composed of $\hat{x}$ and $\hat{y}$ rotations (similar to a method discussed in Sec. 2.1).

We have thus shown that the interaction of a single ion with a laser may be used to perform single-qubit rotations; however, two-qubit operations are also required for the quantum simulations of interest to us. A number of references ([CZ95, MS98, LDM$^+$03]) detail methods for performing two-qubit gates that are sufficient for universal quantum computation. We do not go into detail on these now, since the quantum simulation schemes we study in Sec. 4.2 do not directly make use of these methods.

4.1.3 Control of the ion's external state

We now turn to laser manipulation of the external, i.e. motional states of trapped ions. The interaction Hamiltonian (Eq. 4.16) already contains this physics. It can be shown that by detuning the laser above or below the transition by an amount equal to the motional frequency $\omega_{\hat{z}}$, a quantum of vibrational energy may be added to or subtracted from the ion. That is, for $\delta_l = \omega_{\hat{z}}$, $\Delta n = 1$, and for $\delta_l = -\omega_{\hat{z}}$, $\Delta n = -1$. These transitions are called the *blue sideband* ($\Delta n = 1$) and *red sideband* ($\Delta n = -1$). Repeated cycles of the latter process result in *sideband cooling*, which has been demonstrated by several ion trap groups, e.g. in Ref. [DBIW89].

Sideband cooling requires that the linewidth of the laser Γ_l is much less than $\omega_{\hat{z}}$, for the somewhat that for $\Gamma_l > \omega_{\hat{z}}$ the $\Delta_n = 1$ and $\Delta_n = -1$ transitions are simultaneously addressed. The other case, $\Gamma_l > \omega_{\hat{z}}$, can still be very useful for laser cooling, as we will show below. This process is called *Doppler cooling.* It was first observed in 1978 [WDW78], and formed the basis of the Nobel prize-winning research in laser cooling of neutral atomic ensembles. Because of the prevalence of Doppler cooling over sideband cooling in this thesis, we will focus on that from this point on. However, it is important to know that ground state cooling is *possible*, because many quantum information protocols rely on it to initialize the system.

We will treat the problem of a single two-level atom interacting with a monochromatic radiation field (laser) that is detuned by δ_l from the atomic transition frequency ω_0, as before. The ion is also characterized by "natural" linewidth Γ, which is the rate of spontaneous emission from the excited state $|\downarrow\rangle$. This quantity is given by

$$\Gamma = \frac{e_c^2 \omega_0^3 \left|\langle\downarrow|\,\vec{r}\,|\uparrow\rangle\right|}{3\pi\epsilon_0 \hbar c^3}. \tag{4.19}$$

For the types of atoms discussed in this thesis, Γ is on the order of $2\pi\cdot$ 20 MHz. The operator $e_c\vec{r}$ is the (vector) dipole operator.

The principle of Doppler cooling is as follows: an atom (or ion) excited from $|\uparrow\rangle$ to $|\downarrow\rangle$ absorbs an amount of momentum from the laser equal to $\hbar k$, where k is the laser wavenumber. However, this energy is then spontaneously emitted in a random direction. Doppler cooling works by red-detuning the laser ($\delta_l < 0$) so that the atom is more likely to absorb light when it is moving *toward* the laser than when it is moving away. This, combined with spontaneous emission, serves to cool the atom. When the atom is moving away from the laser, it is further off-resonance, and is not as affected by the beam. For Doppler cooling neutral atoms along a given direction, a total of six lasers are needed (three orthogonal pairs of counterpropagating beams). This is known as the *optical molasses* technique. For a trapped ion, the situation is better, because an ion is already bound in space by the trap. If the cooling laser has a component along $\hat{x}$, $\hat{y}$, and $\hat{z}$, then the back-and-forth motion of the ion allows it to be cooled in all three directions.

Let us make the above description more quantitative. A result we shall need is the steady-state solution to the Optical Bloch equations that describes the average steady-state population $p_\downarrow$ of the excited atomic state. It reads as follows:

$$p_\downarrow = \frac{I/I_0}{1 + I/I_0 + \left(\frac{2\delta_v}{\Gamma}\right)}, \tag{4.20}$$

where $I_0 = \hbar\omega_0^3\Gamma/(6c^2)$ is the *saturation intensity* of the transition. The quantity δ_v is the detuning, including the Doppler shift due to the atom's velocity: $\delta_v = \delta_l - \vec{k}\cdot\vec{v}$. The cooling force on the atom due to the laser light is calculated in the following way: the force is equal to the momentum per photon times the rate of photon emission, which is the spontaneous emission rate times the probability that the atom is in state $|\downarrow\rangle$. Altogether, the light force is

$$F = \hbar k \frac{\Gamma}{2} p_\downarrow. \tag{4.21}$$

When the ion has been cooled to a sufficiently low velocity, one can approximate Eq. 4.21 as being linear in v: this leads to an expression for the cooling rate:

$$\left\langle \dot{E}_{cool} \right\rangle = Fv = \alpha v^2, \tag{4.22}$$

with the constant α given by

$$\alpha = 2\hbar k^2 \frac{4I\delta}{I_0\Gamma\left(1+(2\delta/\Gamma)^2\right)}. \tag{4.23}$$

Although it may at first seem that cooling to zero velocity is possible, it is important to remember that the absorption events are random and themselves add some amount of entropy to the atom's state. The atom thus executes a random walk in momentum space. The rate of heating due to this process is

$$\left\langle \dot{E}_{heat} \right\rangle = \frac{\langle \dot{p} \rangle^2}{2m} = \frac{2\hbar^2 k^2 \Gamma p_\downarrow}{m} = D/m, \tag{4.24}$$

where $\langle \dot{p} \rangle$ is the rate of change of the average value of the ion's momentum, m is the mass of the ion, and the constant D, defined in Eq. 4.24, is the momentum diffusion constant.

Equating $\left\langle \dot{E}_{heat} \right\rangle$ with $-\left\langle \dot{E}_{cool} \right\rangle$, and noting that the temperature of the ion is related to the mean kinetic energy by $m\left\langle v^2 \right\rangle/2 = k_B T/2$, the ultimate temperature attainable by Doppler cooling is

$$T_{Dopp} = \frac{\hbar\Gamma}{2k_B}, \tag{4.25}$$

which is known as the *Doppler cooling limit.* A simple numerical estimate for a $^{88}\mathrm{Sr}^+$ ion in a trap of frequency 1 MHz shows that this limit is about 10 motional quanta. At this point, sideband cooling can take the ion to the motional ground state, if desired.

In practice, the heating rate due to momentum diffusion is often not the limiting factor in ion trap Doppler cooling. Heating of the ions due to electric potentials plays a strong role. In the cloud state, the micromotion of the ions couples into the secular motion, and the rf voltages can directly cause heating of the ions. In a crystal state, this does not occur; the micromotion and secular motion are largely decoupled. Even though micromotion does not directly create heating if the ions are in a crystalline state, the line broadening due to it can raise the ultimate Doppler temperature attainable. This has been treated in Ref. [CGB$^+$94]. However, even in a compensated trap, heating due to fluctuating potentials on the trap electrodes can exceed that due to the spontaneous emission events. This heating process is discussed in Sec. 4.1.5.

4.1.4 State preparation and measurement

Methods for preparing the qubits in some initial state and measuring their state are essential to every quantum information protocol, and are briefly presented here.

The internal state of the ion is prepared not only in the electronic ground state, but also typically in a specific magnetic sublevel of it. A controlled bias usually field breaks the degeneracy of the ground state; this is done to avoid pumping to "dark states," superpositions of S and D states that do not fluoresce. A beam of circularly polarized radiation with selection rule $\Delta m = \pm 1$ is applied to the ions until, with high probability, they are in the desired state. This *optical pumping* technique was first demonstrated by Kastler (although not in an ion trap) [Kas50], and won him a Nobel prize.

Measurement is one of the strongest advantages of ion traps, in that measurement fidelities well over 90% have been demonstrated [MSW$^+$08]. The basic principle is quite simple: the same laser used for Doppler cooling is also used for state measurement. If the ion is in state S, then many photons will be scattered; the rate, as argued above, is $\Gamma p_\downarrow$. This is millions of photons per second, and even given a finite light collection angle and inefficient detectors, the scattering rate tremendous: to take one example, from a single ion in the Innsbruck experiment (Part III), it was not uncommon to observe 30,000 photons per second in our photomultiplier tube. By contrast, if the ion is in state D, no photons will be scattered.

In the proposals for quantum simulation studied in this thesis, it is not necessary to measure the motional state of the ion, nor even to cool it to the ground state, but this could in principle be done in the following way. First assume the ion is in internal state $|\uparrow\rangle$. Suppose you want to determine if the motional state in a given direction is $|0\rangle$ or $|1\rangle$. A pulse on the red sideband will take the state $|\uparrow 1\rangle$ to $|\downarrow 0\rangle$ and subsequent measurement of the internal state will reveal the state is indeed $|\downarrow\rangle$. However, if the state is in $|\uparrow 0\rangle$, there literally *is* no red sideband transition. The ion will remain in $|\uparrow 0\rangle$, and the fluorescence signal will determine that the motional state was $|0\rangle$.

To summarize, we have assembled all the necessary ingredients for quantum simulation with trapped ions, with the exception of two-qubit operations. Following a brief discussion of decoherence in ion traps, we present, in Sec. 4.2, an interesting method for producing two-body interactions between trapped ions.

4.1.5 Decoherence

Decoherence afflicts all quantum simulators, including a set of trapped ions being used as such. It includes amplitude damping and dephasing of both the internal and motional states of the trapped ions. The choice of qubit states is important. Qubits that consist of a ground state and an excited state separated by a quadrupole transition have as their fundamental limitation the spontaneous emission rate of the excited state, which is on the order of a few Hz. However, classical control errors such as fluctuations in the laser intensity and frequency currently limit the amplitude damping rate in many experiments. By contrast, hyperfine qubits can exhibit coherence times on the order of seconds. They are subject, however, to errors due to spontaneous scattering from the excited electronic state used to implement Raman transitions between the levels. Dephasing due to static or slowly-varying sources, such as stray magnetic fields, can be compensated for by using spin-echo techniques, but there always remains some dephasing that cannot be removed. A technique known as the decoherence-free subspace can be used, however, to dramatically increase the dephasing time, using linear superpositions of qubit states that are insensitive to magnetic field fluctuations [HSKH+05].

Equally important is the uncontrolled heating of the motional state of the trapped ions, leading to motional state decoherence. In ion trap quantum computing, the motional states are important since they actually encode quantum information; in fact, the classic way of doing a quantum logic gate is to map the state of one ion to the shared motional mode, then perform an operation on the second ion that changes its internal state only if a given motional mode is excited. This is the basic principle of the Cirac-Zoller gate [CZ95], which has been used with great success by the Innsbruck group (e.g. in Ref. [GRL+03]). Clearly, unwanted excitations of the motional state can ruin this process.

Studies have shown that the heating rate in an ion trap scales roughly as h^{-4}, where h is the distance from the ion to the nearest trap electrode, and is strongly dependent on temperature. The process is often called *anomalous heating*, since it scales more strongly with h than Johnson noise (which would be $1/h^2$) and is of uncertain origin [TKK+99]. The leading hypothesis for the cause of this heating is fluctuating patch potentials on the trap electrodes. However, as stated before, it is now known that this heating can be reduced by orders of magnitude by cryogenic cooling of the trap electrodes [LGA+08]. We will make use of this approach in Ch. 7. Further work from this experiment has narrowed down the possible causes of this noise by studying its temperature dependence [LGL+08]. However, this phenomenon is still not perfectly explained.

Although there are some schemes for quantum simulation that do not require ground state cooling (e.g. the Porras/ Cirac scheme below), it is nevertheless important that the heating rate is minimized. Extra quanta of motion incoherently gained during the simulation decrease the accuracy, and excessive heating could even push the ions out of the Lamb-Dicke regime or cause the ions to transition from a crystal to a cloud state.

4.2 Quantum simulation of quantum spin models

Many proposals have been published for performing quantum simulation with trapped ions. Milburn proposed the simulation of nonlinear spin models using trapped ions [Mil99]. A paper from Porras and Cirac explains how to simulate Bosonic physics such as Bose-Einstein condensation using the vibrational degrees of freedom in a crystal of trapped ions [PC04a]. The group of Wineland, in 2002, proposed and implemented the simulation of a nonlinear interferometer using a single trapped ion [LDM+02]. New and exotic ideas such as the simulation of quantum fields in an expanding universe [ADM05] have also emerged. Although many of these proposals are quite compelling, in this thesis we choose to focus on the physics of quantum spin model simulation.

Spin physics in 2-D is most interesting because of the phenomenon of *spin frustration*. On certain types of lattices, spins that have an antiferromagnetic interaction (meaning that

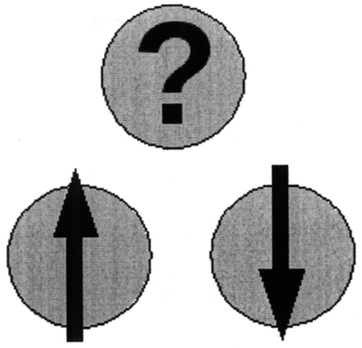

Figure 4-3: Schematic diagram of spin frustration. The blue circles represent lattice sites, while the arrows represent the spin state of the particle on a given site. Suppose the spins are governed by an antiferromagnetic interaction, meaning that it is energetically favorable for pairs of spins to anti-align. If two spins are in well-defined states, the third does not "know" which way to align. Thus, the ground state of the system is a quantum-mechanical superposition of spin states. As the number of particles grows, the system becomes very difficult to simulate on a classical computer.

they are inclined to anti-align) exhibit a state in which the ground state wave function is a superposition of many distinct spin states. This occurs because there is not a single spin configuration which minimizes the energy of the system. A schematic diagram of spin frustration is given in Fig. 4-3.

One of the reasons spin frustration is interesting is that it is believed to hold insight into the phenomenon of high-temperature superconductivity [GP00, NGB92]. We pursue spin frustration because it is hard to simulate classically, and offers an example of an "analog" quantum simulation that may provide a great deal of insight into a perplexing physical system. We consider such simulations to be analog because of the continuously varying controls applied, even though the system Hilbert space is discrete.

In this section, we examine the proposal of Porras and Cirac for simulating spin models with trapped ions [PC04b]. Their scheme is unique in its ability to use a limited set of control techniques to simulate phase transitions in a large system of trapped ions. The benefit of this analog approach is that even with a limited amount of control, one may be able to observe quantum behavior that is not simulable on classical computers, such as quantum phase transitions. Although the ultimate precision in computing quantities such as transition points scales poorly with the number of measurements done, quantum simulation might nevertheless be a powerful tool whenever classical approximations or exact solutions are not known. Here we follow the approach of Porras and Cirac fairly closely. The mathematical steps involved in the derivation are presented in more detail in the S.B. thesis of Ziliang Lin [Lin08]. The challenge of simulating spin physics in two dimensions motivates the work in the rest of this part of the thesis.

4.2.1 The Ising and Heisenberg models

We review here the basic physics and of the Ising and Heisenberg models in preparation for seeing how they could be simulated with trapped ions. These models are Hamiltonians that describe the physics of interacting spins. Although there is a classical Ising model, we are concerned here only with the quantum-mechanical version.

The Ising model has the following general form:

$$H_{Ising} = -\hbar \sum_{i \neq j} J_{ij} \sigma_i \sigma_j \tag{4.26}$$

where the summation is, as noted, over all spins i and j for which $i \neq j$, the J_{ij} are the coupling energies between spins, and σ_i and σ_j are the Pauli matrices for spins i and j. Most often, we shall choose $\hat{z}$ to be the quantization axis, and focus on nearest-neighbor interactions, in which case the Ising Hamiltonian takes the form

$$H_{Ising} = -\hbar \sum_{i,j=i+1} J_{i,j} Z_i Z_j . \tag{4.27}$$

The preceding Hamiltonian is one-dimensional, in that it models spins that are arranged along a line segment. Other configurations are possible, and Eq. 4.27 can readily be generalized to two and three dimensions.

The Heisenberg model is like the Ising model, but involving spin-spin interactions, generally, along more than one direction. For spins arranged in one dimension, the Heisenberg model has this form:

$$H_{Heis} = -\hbar \sum_{i,j} \left(J_{\hat{x}} X_i X_j + J_{\hat{y}} Y_i Y_j + J_{\hat{z}} Z_i Z_j \right) . \tag{4.28}$$

4.2.2 Porras and Cirac's proposal for simulating quantum spin models

We begin with showing how a chain of ions in a linear Paul trap can be used to simulate spin models. In this section we will follow the paper of Porras and Cirac [PC04b] quite closely. Although a linear ion trap was used as a model in their work, the scheme extends quite easily to 2-D, a fact that motivates the rest of our work in this part of the thesis.

We consider a chain of N trapped ions aligned along the $\hat{z}$ direction. We define the index $\hat{\alpha}$ to indicate spatial direction; $\hat{\alpha}$ = 1, 2, and 3 represents $\hat{x}$, $\hat{y}$, and $\hat{z}$, respectively [1]. Accordingly, the Pauli operators are written as $\sigma_{\hat{\alpha}}$ and the corresponding eigenstates as $|\uparrow\rangle_{\hat{\alpha}}$ and $|\downarrow\rangle_{\hat{\alpha}}$. We assume that lasers can be applied to the ions that couple the internal state to the motional state only if the ion is in a specific internal state. This *state-dependent force* is the key ingredient of implementing the simulation. How can one cause a laser force

---

[1] Here, as throughout the thesis, we specify the directionality of a given quantity with a subscripted unit vector, even if only the magnitude (a scalar) is represented by the quantity. We hope that this will clarify symbols with multiple subscripts.

to address an ion in state $|\uparrow\rangle_{\hat{\alpha}}$ but not in state $|\downarrow\rangle_{\hat{\alpha}}$? One way is to set the polarization of this laser such that only one state in a ground state hyperfine or Zeeman manifold is permitted by electric dipole selection rules to couple to a given excited state. Another is to make the laser much closer to resonance with one state than the other, for instance by using an optical qubit. Note that if the laser pushes on *both* $|\uparrow\rangle_{\hat{\alpha}}$ and $|\downarrow\rangle_{\hat{\alpha}}$, but in opposite directions, the derivation will change but the same basic physics will be implemented.

The first step is to write down the Hamiltonian. The full Hamiltonian has three parts: H_v, the vibrational Hamiltonian, H_f, the interaction term due to the state-dependent force, and H_m, a term due to an externally-applied magnetic field that is a key part of the transverse Ising model, and is important for the observation of quantum phase transitions. H_v is written, including the Coulomb repulsion between the ions, as a set of harmonic oscillators at the normal mode frequencies labeled by n:

$$H_v = \sum_n \hbar\omega_n a_n^\dagger a_n. \tag{4.29}$$

Here the magnitudes of the ω_n are determined by the Coulomb interaction.

The state-dependent force term, which is assumed to only act upon state $|\uparrow\rangle_{\hat{\alpha}}$, has the form

$$H_f = -2\sum_{\hat{\alpha},i} F_{\hat{\alpha}} q_{\hat{\alpha},i} |\uparrow\rangle\langle\uparrow|_{\hat{\alpha},i}, \tag{4.30}$$

where $q_{\hat{\alpha},i}$ is the position operator for the i^{th} qubit along direction $\hat{\alpha}$, and $F_{\hat{\alpha}}$ is the magnitude of the state-dependent force along $\hat{\alpha}$. An intuitive picture of the effect of the state-dependent force is depicted in Fig. 4-4.

Finally, the magnetic term is written as

$$H_m = \sum_{\hat{\alpha},i} \mu_{\hat{\alpha}} B_{\hat{\alpha}} \sigma_{\hat{\alpha},i}\,, \tag{4.31}$$

where $B_{\hat{\alpha}}$ and $\mu_{\hat{\alpha}}$ are the magnetic field and atomic magnetic moment, respectively, along the direction $\hat{\alpha}$. The full Hamiltonian H is given by $H = H_v + H_f + H_m$.

Porras and Cirac derive the spin-spin interaction by means of a canonical transformation: $H' = e^{-S} H e^{S}$, where

$$S = \sum_{\alpha,i,n} \eta_{\hat{\alpha},i,n} \left(a_{\hat{\alpha},i}^\dagger - a_{\hat{\alpha},i}\right)(1 + \sigma_{\hat{\alpha},i}) \tag{4.32}$$

and

$$\eta_{\hat{\alpha},i,n} = F_{\hat{\alpha}} \frac{\mathcal{M}_{\hat{\alpha},i,n}}{\hbar\omega_{\hat{\alpha},n}}. \tag{4.33}$$

The $\mathcal{M}_{\hat{\alpha},i,n}$ are the elements of the matrix that diagonalizes the vibrational Hamiltonian,

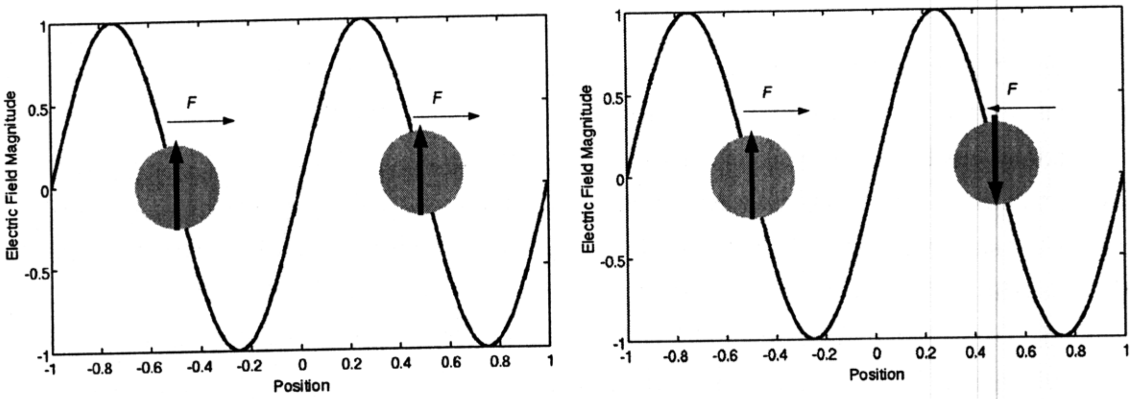

Figure 4-4: Schematic of the action of a state-dependent force on a pair of trapped ions. The force is created by an optical standing wave, and we assume that the frequency and polarization of this laser is such that an ion in one state will be pushed in one direction, and an ion in the opposite state in the opposite direction. On the left, the ions in the same state are pushed in the same direction by the optical force, and thus the system energy is unchanged by the force. On the right, the ions in opposite states are pushed toward one another. This results, through the Coulomb interaction, in an overall increase in the energy of the system. This is equivalent to a ferromagnetic interaction: it is energetically favorable for the ions to be in the same state.

and are defined by the equation

$$q_{\hat{\alpha},i} = \sum_n \frac{\mathcal{M}_{\hat{\alpha},i,n}}{\sqrt{2m\omega_{\hat{\alpha},n}/\hbar}} \left(a^\dagger_{\hat{\alpha},n} + a_{\hat{\alpha},n} \right) . \tag{4.34}$$

It is clear that the nontransformed Hamiltonian already contains the coupling of the internal to the vibrational modes, given the facts that H_f contains $q_{\hat{\alpha},i}$ and that the $a_{\hat{\alpha},n}$ and $a^\dagger_{\hat{\alpha},n}$ depend on these coordinates. The purpose of this transformation is merely to rewrite the Hamiltonian in a form where these interactions are evident.

The transformed Hamiltonian H' is given by

$$H' = \sum_{\hat{\alpha},n} \hbar\omega_{\hat{\alpha},n} a^\dagger_{\hat{\alpha},n} a^\dagger_{\hat{\alpha},n} + \frac{1}{2} \sum_{\alpha,i,j} \hbar J_{\hat{\alpha},i,j} \sigma_{\hat{\alpha},i} \sigma_{\hat{\alpha},j} + \sum_{\alpha,i} \mu_{\hat{\alpha}} B'_{\hat{\alpha}} \sigma_{\hat{\alpha},i} + H_r \tag{4.35}$$

where the effective J-coupling rate is given by

$$-\hbar J_{\hat{\alpha},i,j} = \sum_n \frac{F^2_{\hat{\alpha}}}{m\omega^2_{\hat{\alpha},n}} \mathcal{M}_{\hat{\alpha},i,n} \mathcal{M}_{\hat{\alpha},j,n} = 2\hbar \sum_n \eta_{\hat{\alpha},i,n} \eta_{\hat{\alpha},j,n} \omega_{\hat{\alpha},n} , \tag{4.36}$$

and an additional effective magnetic field is given by $\mu_{\hat{\alpha}} B'_{\hat{\alpha}} = \mu_{\hat{\alpha}} B_{\hat{\alpha}} + \sum_n F^2_{\hat{\alpha}}/(m\omega^2_{\hat{\alpha},n})$. In the case of the transverse Ising model, this induced field will be parallel to the direction of J coupling and perpendicular to the applied external magnetic field.

The term H_r represents a residual coupling between the effective spins and the vibrational modes. Fortunately, this can be neglected in the case of anisotropic traps, or when the vibrational temperature is low. We will make this assumption here; we will either assume that cooling can be efficiently performed in the lattice-style trap (as in Ch. 5), or that the otherwise requisite anisotropy of the trap will suffice to render this term small (as in Ch. 7).

The coupling rate between ions due to the Coulomb interaction, per unit cycle, is characterized by a dimensionless parameter $\beta_{\hat{\alpha}}$, defined as

$$\beta_{\hat{\alpha}} = \frac{e_c^2}{8\pi\epsilon_0 m\omega_{\hat{\alpha}}^2 d^3}. \tag{4.37}$$

When $\beta_{\hat{\alpha}} \ll 1$, the J-coupling rate may be approximated as

$$\hbar J_{\hat{\alpha}} = \frac{c_\alpha e_c^2 F_{\hat{\alpha}}^2}{4\pi\epsilon_0 m^2\omega_{\hat{\alpha}}^4 d^3}, \tag{4.38}$$

where $c_{\hat{\alpha}}$ is a constant of order unity that depends on the trap and laser geometry and d is the average ion-ion distance. For traps in which ions are confined in separate wells, $\beta_{\hat{\alpha}} \ll 1$ for all $\hat{\alpha}$, and this formula holds. This is not necessarily the case when the ions are confined in the same well. As an example, suppose two ions are confined a distance d apart in a linear ion trap, and that the line segment connecting them lies along $\hat{z}$. In this case, $\beta_{\hat{z}} = 0.25$, and the coupling rate $J_{\hat{z}}$ is given by

$$\hbar J_{\hat{z}} = \frac{F_{\hat{z}}^2}{4m\omega_{\hat{z}}^2}\frac{2\beta_{\hat{z}}}{1+2\beta_{\hat{z}}}. \tag{4.39}$$

For a very good discussion of this protocol as applied to two ions, we refer the reader to the thesis of Ziliang Lin [Lin08]. The first experimental realization of this protocol, using two ion-qubits, was published in Ref. [FSG$^+$08].

4.3 Ion trap design for quantum simulation

Performing quantum simulations of phenomena such as spin frustration requires a 2-D array of trapped ions with a lattice structure that is similar to the structure of the target system. This requirement is unique to analog, as opposed to digital, quantum simulation. Creating such a 2-D array, however, is quite nontrivial. Here we present in detail some of the challenges associated with trap design, and then outline our methods for solving them that will comprise the remainder of this part of the thesis.

4.3.1 Challenges for trap design

Recall from Sec. 1.4 that there are three main challenges to quantum simulation: decoherence, precision limitations, and scalability. In this part of the thesis, we focus on the scaling up of analog quantum simulation in 2-D. Despite this focus on only one of the above problems, the others have a strong effect upon our considerations. Estimates of decoherence rates must be calculated for each trap design, and possible control errors must also be considered. Furthermore, although we will focus on the simulation of spin frustration as the ultimate goal, we note that the traps studied in this part may be useful for other simulations as well, such as Bose-Hubbard physics.

The main considerations for a trap design are interaction rates, controls, and decoherence rates. We discuss each of these below. The design must:

1. Provide a regular array of stationary qubits in at least two spatial dimensions.

   The array of ions desired here is an extension to two dimensions of the linear ion crystals used in most quantum information experiments. To do quantum simulations of problems that are unique to configurations of spins in two or more dimensions, such as spin frustration, we need a trap that will produce a two-dimensional array of ions. The word *regular* means here that the ions are stored in some configuration such that the ion-ion distance d between each pair of nearest neighbors is identical. This is important because the simulated coupling rate J depends strongly on the inter-ion distance d (varying as d^{-3} in the $\beta \ll 1$ limit as discussed above). Quantum simulation is also possible in an array for which this distance is not constant, but this adds a constraint to the types of Hamiltonians that can be implemented (the J-coupling will be site-dependent). When applying a global effective Hamiltonian, this site dependence may translate into a control error, limiting the precision of the simulation, but not necessarily rendering it useless. Furthermore, such systematic control errors may be compensated if sufficient controls are available.

2. Enable sufficient control over each qubit to implement the desired simulation.

   A trap design that fulfills the first condition does not guarantee that quantum simulation may be effectively done. Sufficient controls are required to implement the desired effective Hamiltonian. These may include rotations of individual qubits, state-dependent forces arising from an optical or magnetic force, and global or ion-specific measurements. In addition, achieving some desired J-coupling rate requires a sufficient interaction rate between individual ions. Recall that the parameter β is the fractional transfer of the motional energy of one ion to another per secular period; although the dipolar approximation holds for $\beta \ll 1$, the resulting J-coupling rate may prove too small to be observable within the decoherence time of the system. Therefore, in considering the controls required for quantum simulation, one must take into account the pertinent quantities β and J, and calculate each for each trap design.

3. Support a low enough decoherence rate to perform meaningful simulations given certain coupling rates.

   Internal state decoherence depends on the choice of qubit states, ambient field fluctuations, errors in the classical controls, and other factors that are not directly related to the design of the trap itself. Motional state decoherence, by contrast, has a strong dependence on the size of the trap. Decoherence rates for a given trap may be estimated based on previously published measurements, and these estimated values may have a bearing on the choice of experimental conditions, such as the temperature at which the trap is operated.

4.3.2 2-D ion arrays: prior art

Two-dimensional arrays of ions have been realized in both Penning [IBT+98] and Paul [BDL+00] traps; in both cases, an ensemble of ions was trapped and cooled within a single trapping region, and an ion crystal was formed by the mutual Coulomb repulsion of the ions.

Both these approaches have certain advantages and disadvantages. The primary disadvantage of the Penning trap approach is that the ion crystal rotates about the magnetic field axis due to the crossed $\vec{E}$ and $\vec{B}$ fields. This is inconvenient for performing ion-specific operations and measurements. While a Paul trap produces a stationary crystal of ions, each undergoes micromotion at the rf frequency, the amplitude of which increases with the distance of each ion from the center of the trap. The problem of how suitable the Paul trap approach is for quantum simulation was, up until this thesis, unaddressed.

Proposals have also emerged for using arrays of individual ion traps for performing quantum operations, including quantum simulation, in two dimensions. This possibility was noted in the paper on spin model simulation of Porras and Cirac [PC04b], and was discussed in the context of universal quantum simulation in Ref. [CZ00]. A proposal was also published to use ions in microtrap arrays with gates based on microwave or radiofrequency radiation combined with magnetic field gradients to do simulation of quantum spin models [CW08]. However, an array of individual ion traps had not yet been realized prior to this thesis. Furthermore, no analysis had been published of the interaction rates for quantum simulation in such traps.

4.3.3 Methods of trap design, testing, and evaluation

The main goal of this part of the thesis is to ascertain the suitability for analog quantum simulation of two trap paradigms: arrays of individual Paul traps, and 2-D Coulomb crystals within a single Paul trap region. We now describe the methods used for addressing the above challenges. The workflow consists of three steps: design, testing, and evaluation.

Design

At the design stage, we first conceive of a trap design that should, in principle, generate a 2-D array of trapped ions. A method of fabricating the trap must be determined, and then numerical modeling done to calculate the important properties of the trap, both for traps of the scale being tested, and traps of other scales. These properties include the motional frequencies, which are important for calculating β and J, as well as quantities of practical importance such as the trap depth and ion position relative to the trapping electrodes. Results from a trap of one size can typically be scaled to smaller or larger sizes.

Testing

After theoretical calculations of a given trap are done, they must be confirmed by experiment in order to compute the coupling rates and thereby evaluate the trap design. Testing the traps consists of fabricating a trap that is representative of one of the above paradigms, mounting it in a suitable vacuum vessel, and then measuring certain properties of the trap. For both paradigms, the motional frequencies are measured. In the case of an array of ion traps, the lattice geometry is determined by the fabrication of the trap electrodes. However, for ions which form a crystal within the same trap volume, the ion crystal geometry is determined by the trapping potentials, and verifying that this crystal matches theoretical predictions is also important.

Evaluation

Equipped with the ion crystal structure and motional frequencies, the coupling rates may be calculated. A primary goal of this part of the thesis is to determine, for each paradigm, how the coupling rates scale with the trap size (which is typically defined as the distance from the trap center to the nearest electrode). In Ch. 5, we treat the problem of an array of Paul traps, while in Ch. 7 we study ion crystals within one example of a Paul trap that creates a 2-D array of ions: a surface-electrode elliptical ion trap.

Included in the evaluation of a trap design is an estimation of the relevant decoherence rates. Decoherence of internal states depends a great deal on the choice of qubit states, the ambient fields, fluctuations in the control potentials, and other effects. Our primary concern is with motional decoherence rates. In Ch. 7, the quenching of these rates at cryogenic temperatures motivates the construction and use of a 4 K cryostat for ion trap testing. Studying internal and external decoherence is beyond the scope of this thesis, but we cite relevant results from other research efforts where appropriate. Our primary concern is to insure that the coupling rates we determine are much higher than the decoherence rates reported for similar ion traps.

4.4 Summary

We have now explained how the interaction of trapped ions with laser radiation can be used to implement quantum control over both the internal and motional states of the ions. Preparation of the ions' motional state is done effectively by first Doppler cooling the ions into a crystalline state near the Doppler limit, then further cooling them (if necessary) close to the quantum-mechanical ground state using resolved sideband cooling. From this initial motional state, operations can be performed that pump the internal degrees of freedom into some fiducial initial state, then implement unitary transformations on the state vector of the ions that perform some desired quantum simulation. Since simulation of quantum spin models is a focus of this part of the thesis, we have focused on this protocol.

Although in principle sufficient control exists to perform quantum simulations with high fidelity, there are a number of difficult issues when one wishes to do so in practice. In particular, we have pointed out the great challenge associated with scalable or semi-scalable trap designs for quantum simulation. We require traps that can permit a high interaction rate between trapped ions while avoiding decoherence and systematic errors. In the remainder of this part of the thesis, we describe efforts to solve these challenges using the methods described in this chapter: design, test, and evaluate two paradigms for 2-D ion arrays, based on arrays of traps and Coulomb crystals within the same trap.

Chapter 5

Lattice ion traps for quantum simulation

In this chapter we turn to a theoretical and experimental investigation of lattice ion traps for quantum simulation. Many schemes for doing quantum simulation and computation, such as the one presented in Ch. 4, rely on a regular array of trapped ions; a lattice-style architecture, in which single ions are arranged in a regular array of microtraps, is one way of achieving this. If the spatial extent of the array lies in more than one dimension, then interesting physics such as spin frustration becomes accessible, as we noted in the last chapter.

This chapter describes the first implementation of such a trap. We first present a theoretical model describing one method of generating an array of Paul traps. Our experimental work is driven by the question of whether the trap potentials match the predictions of our model, as well as the question of whether interactions between ions in neighboring wells are observable. For these measurements, we trap both both $^{88}\mathrm{Sr}^+$ ions and charged microspheres. Having obtained an answer, we move to the theoretical question of the interaction rates in such a trap. We wish to calculate, based on observations of the trap, how both the motional coupling rate and simulated spin-spin interaction scale with the overall size of the trap. With this calculation done, one may evaluate the utility of this trap design for our ultimate goal: analog quantum simulation of spin frustration. The main results of this work were published as Ref. [CLBC09].

The chapter is organized as follows. In Sec. 5.1, we briefly summarize some theoretical proposals for using lattice ion traps for analog quantum simulation, focusing on physics that can be studied with a 2-D but not with a 1-D array of ions. In Sec. 5.2, we present our theoretical model of the lattice ion trap. In Sec. 5.3, we discuss the experimental setup for trapping atomic ions, including the lasers, vacuum system, and the trap itself. In Sec. 5.4, we report on our results of trapping both ion clouds and single ions, and measuring their motional frequencies. In Sec. 5.5, we report on the measurement of interactions between macroscopic ions across lattice sites. In Sec. 5.6, we evaluate the trap design by computing the interaction rates as a function of trap scale in lattice traps. In Sec. 5.7, we conclude on this work.

5.1 Proposals for quantum simulation in lattice ion traps

Quantum information theorists have put forward several proposals for quantum operations in 2-D arrays of trapped ions. A 2000 paper from Cirac and Zoller suggests using ions in an array of microtraps to form the basis of a scalable quantum computer, in which an ion is moved from site to site within the array to interact with ions contained therein [CZ00]. Later, as we discussed in Ch. 4, the spin model proposal of Porras and Cirac suggested that an array of microtraps could be used to implement quantum simulations of interesting physics such as spin frustration [PC04b].

A subsequent proposal from Chiaverini and Lybarger [CW08] suggested using an array of microtraps to implement a 2-D quantum simulation. In their scheme, microcoils surrounding each lattice site address individual ions contained therein with microwave radiation, effecting single-qubit rotations. In addition, magnetic field gradients may be applied which serve the same purpose as the lasers in the Porras-Cirac scheme, generating state-dependent forces that translate into effective spin-spin interactions.

The commonality between the two is the requirement of a 2-D array of trapped ions. The advantages of a 2-D array of microtraps are that the position of each ion is well-determined by the trap electrodes, and that, conceivably, dc compensation electrodes could be provided for each site. This is in contrast to a trap in which all ions are contained in the same potential well. In such a trap, the ion-ion distance can vary, especially near the edge of the crystal, and micromotion may pose a problem. However, in this chapter, we focus on arrays of Paul traps, or *lattice ion traps.*

5.2 Lattice trap design and theory

The model we study in this chapter is a layered planar rf electrode geometry that creates a 2-D ion lattice. The ion trap consists of a planar electrode with a regular array of holes, held at a radiofrequency (rf) potential, mounted above a grounded planar electrode. A single ion is trapped above each hole in the rf electrode (Fig. 5-1). Ions will be preferentially loaded above the trap electrode at the intersection of the Doppler cooling and photoionization beams, allowing the user to write an arbitrary 2-D lattice structure. We view this design as an archetype of 2-D Paul trap arrays, in the sense that conclusions drawn about some properties of this trap may translate to other, similar, trap designs.

Our lattice trap is an extension of the three-dimensional ring Paul trap [Gho95]. Following this reference, we first review the theory of the ring trap. The ring electrode geometry

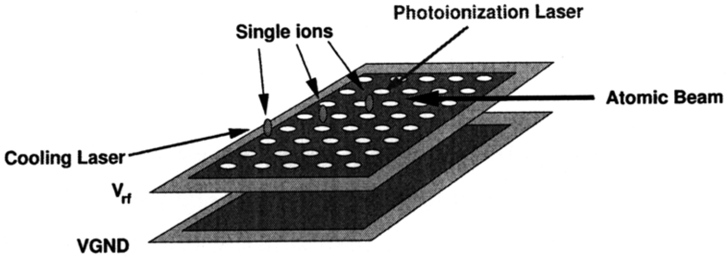

Figure 5-1: Schematic of the lattice trap. An array of traps is produced by a single rf electrode with a regular array of holes, mounted above a grounded electrode. Ions will preferentially be loaded from a broad atomic beam at the intersection of the cooling and photoionization lasers.

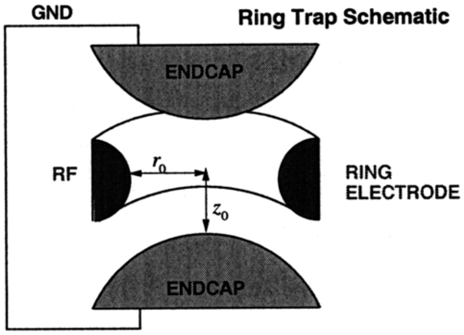

Figure 5-2: Cross section of a ring trap. Ions are confined at the center of the trap. The ring is held at an alternating rf potential relative to the endcaps. Here $r_0 = \sqrt{2}z_0$ and the endcaps and ring electrode are hyperbolically shaped.

is shown in Fig. 5-2. An alternating voltage of the form $V_{rf} = V\cos(\Omega t)$ is applied to the ring electrode and the endcaps are grounded. This situation is discussed in Ch. 4, and we summarize the results here.

The equations of motion for an ion in the ring trap are a set of Mathieu equations which have regions of stability depending on the dimensionless parameters $a = \frac{8QU_0}{mr_0^2\Omega^2}$ and $q = \frac{2QV}{mr_0^2\Omega^2}$. Q and m are charge and mass of the ion, U_0 is any dc voltage applied to both endcaps of the ring trap, and the distance r_0 is the distance from the trap center to the rf electrode (as shown in Fig. 5-2). When $U_0 = 0$ and the system is in vacuum, the condition for stability is $q < .908$. Note that the lattice trap has two "q" parameters, $q_{\hat{z}}$ and $q_{\hat{r}}$, for the vertical and radial directions, respectively. They both must meet this inequality for a stable trap to exist.

We assume the trajectory of a trapped ion is well approximated by a slow secular motion superposed with a rapid oscillation, the micromotion, due to the oscillation in the potential V_{rf}. For $U_0 = 0$, time-averaging the ion motion in the secular approximation ($q \ll 1$) gives the following quasi-static pseudopotential which governs the secular motion:

$$\Psi(\vec{x}) = \frac{Q^2}{4m\Omega^2}|\vec{\nabla}\Phi(\vec{x})|^2. \tag{5.1}$$

Here $\Phi(\vec{x})$ is the electrostatic potential when the drive voltage V is applied to the ring electrode. The quantity $|\vec{\nabla}\Phi(\vec{x})|$ is the magnitude of the electric field.

The lattice trap can be thought of as a planar array of ring traps. Ions are confined in a 2-D lattice of potential wells. At the center of each trap, the electric field associated with the electrostatic potential $\Phi(\vec{x})$ is 0. Assuming approximate rotational symmetry in the plane of the trap, $\Phi(\vec{x})$ has a multipole expansion:

$$\Phi(\vec{x}) = V\frac{r^2 - 2z^2}{r_1^2} + \alpha V\frac{2z^3 - 3zr^2}{r_1^3}\,, \tag{5.2}$$

where r is the radial distance from the central axis of the lattice site and z is the distance along the central axis. This equation is valid only near the center of the trap. Eq. 5.2 contains the two spherical harmonics $Y^{l=2}_{m=0}$ and $Y^{l=3}_{m=0}$; $m = 0$ because of the rotational symmetry. The term that is linear in r (proportional to $Y^{l=1}_{m=0}$) will reflect a dc contribution to the potential, which is not included above. The solution for the ring trap in Fig. 5-2 is obtained by setting $\alpha = 0$, and the term proportional to $Y^{l=3}_{m=0}$ is the lowest-order deviation from the ring trap potential. The above expression is valid for infinite lattices, but for lattice traps containing many ions the potential will be correct near the center lattice site. The $z = 0$ plane is defined such that it coincides with the point of null electric field. Eq. 5.2 defines two constants which depend on the trap geometry: r_1, with dimension of length, and α, which is dimensionless.

The pseudopotential is given by

$$\Psi(\vec{x}) = \frac{QV^2}{m\Omega^2 r_1^4}\left[r^2\left(1 + \frac{3\alpha z}{r_1}\right)^2 + 4z^2\left(1 + \frac{3\alpha z}{2r_1} - \frac{3\alpha r^2}{4zr_1}\right)^2\right].$$

From the pseudopotential we define secular frequencies which characterize the curvature of the pseudopotential in the harmonic region:

$$\omega_{\hat{z}} = 2\sqrt{2}\frac{QV}{m\Omega r_1^2} \quad \text{and} \quad \omega_{\hat{r}} = \sqrt{2}\frac{QV}{m\Omega r_1^2}\,, \tag{5.3}$$

where $\omega_{\hat{r}}$ is the secular frequency in the plane of the trap and $\omega_{\hat{z}}$ is the secular frequency perpendicular to the plane of the trap. Note that $\omega_{\hat{z}}/\Omega \approx q_{\hat{z}}$ so that $\omega_{\hat{z}}/\Omega$ gives a direct measure of the stability of the confined ions.

An additional grounded plate may be added above the ions to shield them from stray charges, and a static potential U may be applied to it. This change can be modeled by adding an extra term $U(z - z_0)/z_1$ to the pseudopotential, where z_1 is a geometric factor with dimensions of length that depends on the height of this plane above the rf electrode

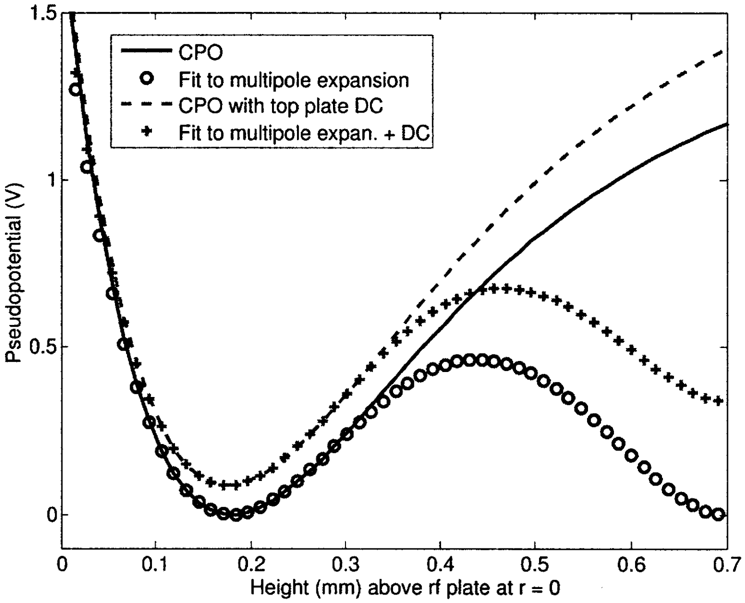

Figure 5-3: Fit to Eq. 5.2 of the CPO computed pseudopotential in the $\hat{z}$ direction at the center of one well. The plot is of potential as a function of height; the $z = 0$ plane is located at the potential minimum, approximately 0.18 mm above the trap electrode. The fit was done only near the center of the well, where the trap is approximately harmonic. Fitting the function at larger z values would require additional terms in the expansion of Eq. 5.2, but since we are most interested in the potential at the trap center, we do not do this. The fit yields $r_1 = 3.1 \pm 0.1$ mm, $\alpha = -4.0 \pm 1.3$, and $z_1 = 19$ mm. Note that the experimental parameters used are those for the macroions (Sec. 5.5), not atomic ions (Sec. 5.4).

and is computed, in practice, using numerical modeling. A consequence of this additional static potential is that $\omega_{\hat{z}}$ is different:

$$\omega_{\hat{z}}^2 = 8\left(\frac{QV}{m\Omega r_1^2}\right)^2\left(1 - \frac{144\alpha m\Omega^2 r_1^3 U}{64QV^2 z_1}\right). \tag{5.4}$$

To obtain the constants r_1, α, and z_1, we use the Charged Particle Optics (CPO) numerical modeling software package to model the trapping potentials. The lattice trap used for our experiments has a hole diameter of $h = 1.14$ mm and a spacing between the centers of the holes of $d = 1.64$ mm. A square section of the rf electrode measuring 10 lattice sites on each side was used for this modeling; for larger sections than this, the effect of adding additional sites on the potentials near the center was negligible. From a simulation of the trap, we obtain the value of the geometric factors: $r_1 = 3.1 \pm 0.1$ mm, $\alpha = -4.0 \pm 1.3$, and $z_1 = 19$ mm for a top plate 15 mm above the rf electrode. Errors arise from the nonlinear least-squares fit used to obtain r_1 and α from the (discrete) simulated potential. In Fig. 5-3, we compare the numerical potential for the lattice trap to the analytical potential from the multipole expansion, indicating that near the minimum of a given potential well the multipole expansion gives an accurate approximation to the simulated pseudopotential. Note that in this plot the trapping parameters are appropriate for the macroion experiment (Sec. 5.5), not the $^{88}\text{Sr}^+$ ion experiment (Sec. 5.4).

5.3 Experimental setup for $^{88}\text{Sr}^+$ trapping

In this section, we present the experimental setup for trapping of $^{88}\text{Sr}^+$ ions in a room-temperature vacuum apparatus. The basic ingredients are:

1. A vacuum chamber containing a mounting place for the ion trap, electrical connections to it, and a resistive oven for producing a beam of neutral strontium.
2. A pair of lasers to perform Doppler cooling and detection of the trapped ions, another pair for photoionization, and optics for detection of the ions' fluorescence signal.
3. Rf electronics for driving the ion trap.

5.3.1 Vacuum chamber and electrical connections

The vacuum chamber used in this work includes a spherical octagon vacuum chamber that houses the ion trap and electrical feedthroughs, two pumps (ion getter pump and titanium sublimation pump), and an ionization gauge to monitor pressure. A photograph of the apparatus is presented in Fig. 5-4, and the components are discussed in detail below.

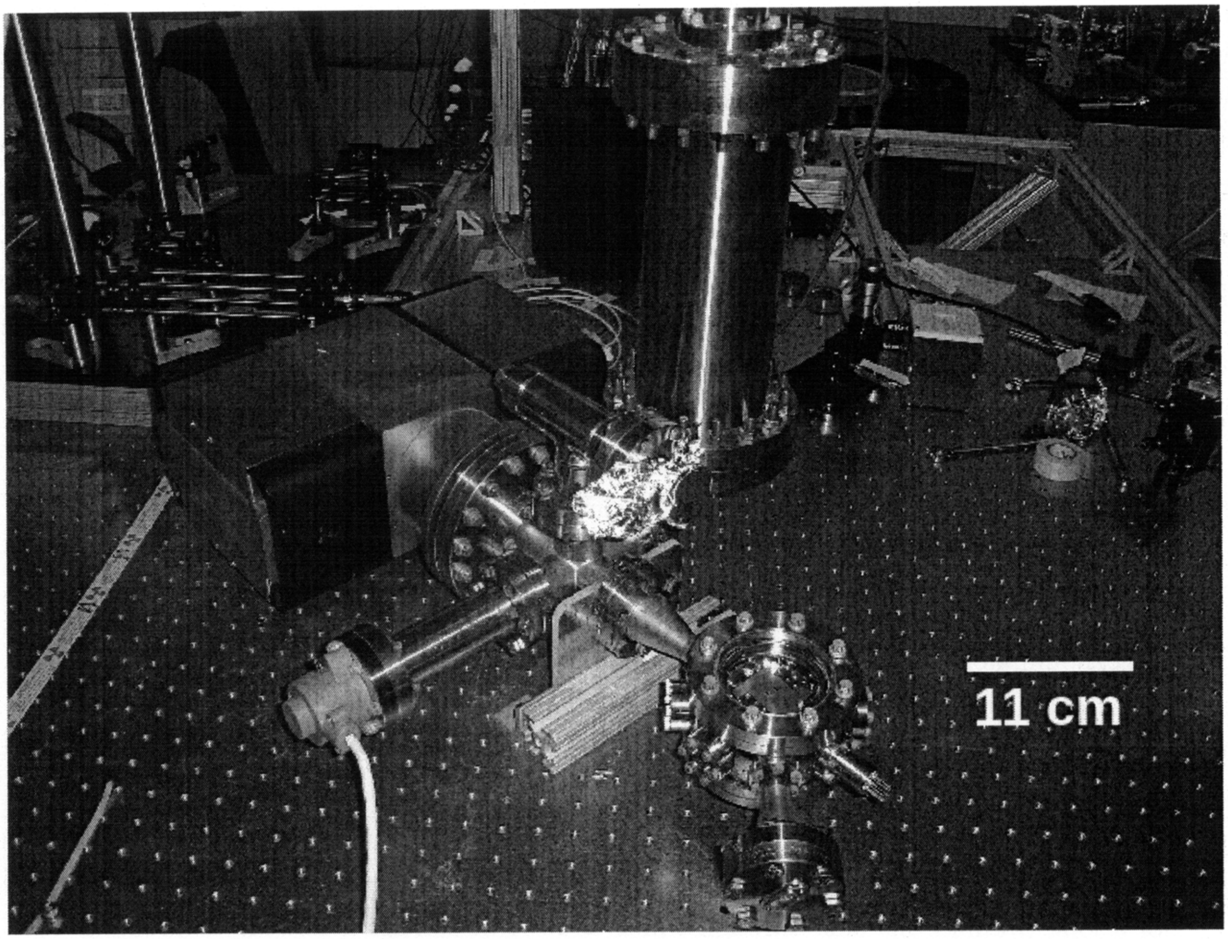

Figure 5-4: The vacuum chamber for the $^{88}\mathrm{Sr}^+$ lattice trap experiments. It contains the spherical octagon with optical access and electrical feedthroughs, ion getter pump, ionization gauge, and titanium sublimation (Ti-sub) pump. The Ti-sub is contained within the tall cylinder mounted at a right angle to the table.

Spherical octagon, feedthroughs, and oven

The spherical octagon is a stainless steel piece manufactured by Kimball physics (Part No. MCF450-SO20008). It has two 4 1/2 in. con-flat (CF) sealing surfaces, and eight 1 1/3 in. CF sealing surfaces. The top 4 1/2 in. surface is used for imaging. A anti-reflective (AR) coated fused silica viewport is used, while on the bottom there is another viewport, although it was not used in this work. The system used a total of three electrical feedthroughs. One provides the high-voltage rf signal to the trap. A separate feedthrough is used for this to limit stray capacitance that can adversely affect the Q factor of the rf resonance. The second feedthrough is a 9-pin sub-d connection that carries any dc voltages that may be needed for the trap. The setup in Ch. 6 is very similar to this one, and does make use of these connections. The final feedthrough holds the strontium oven and is used to supply it with current.

The oven used in the experiments of Ch. 5 and 6 is made of a piece of thin tantalum foil that is folded into a tube. One end of the oven is spot-welded closed and then grains of strontium metal are added to the open end. This end is then spot-welded closed, and both ends of the oven are spot-welded directly to the stainless steel wires of the feedthrough. A hole is poked in the side of the oven that faces the ion trap; it is important that this be the only opening in the oven. A typical resistance for the finished oven, including feedthroughs, is about 0.5 Ω, and currents of 3 A are normally sufficient to load the trap.

Vacuum pumps and pressure gauge

Initial pumpdown of the system to $\mathcal{O}(10^{-6}$ torr) is done with a turbomolecular pump backed by a roughing pump. After reaching this vacuum level, a valve to the turbo pump is closed and two pumps that are an integral part of the vacuum system are used.

The ion pump is a Varian 60 l/s triode pump. The triode configuration pumps noble gases more efficiently than the original diode configuration, which is very useful in Ch. 6, but less essential here. A titanium sublimation pump (Ti-sub) is also used. It consists of a long titanium filament through which ≈ 40 A of current is flowed. Titanium is then deposited on the walls of the vacuum housing. A six-inch-diameter stainless steel nipple serves as this surface; it is significantly wider than the filament to increase the surface area on which titanium is deposited. As shown in Fig. 5-4, the filament is mounted at a right angle to the aperture that leads to the ion trap, reducing the chances of depositing titanium on the trap. The Ti-sub does not need to be fired continuously; typically, it is fired once a week (for 1-5 minutes) as long as some improvement in pressure is observed after firing.

These two pumps are sufficient to reach pressures in the 10^{-10} torr range after bakeout. Bakeout is a process in which the entire vacuum chamber is heated to around 200 °C and pumped on. The higher temperature increases the outgassing rate of material adsorbed on surfaces within the chamber, and essentially speeds up the pumpdown. This is a standard procedure for ultra high vacuum (UHV) apparatus. A typical baking time is around 1-2 weeks. Low pressures depend on choosing materials that have a low vapor pressure at room temperature.

Before assembly, each part within the chamber must be carefully cleaned. We use a four-step process involving four solvents. In order, they are: detergent solution, distilled water, acetone, and methanol. Each step involves sonicating the trap in the solvent for 30 min., typically with heat ($\approx 80^\circ$ C) applied. The process is designed to remove a large variety of impurities on the surface; water and detergent for both polar and non-polar substances, acetone for non-polar molecules that are not soluble in water, and finally methanol, which removes the "residue" that is left over after an acetone clean. Although other vacuum cleaning techniques exist, some involving three methanol steps, some involving only water followed by acetone, we feel that it is better to be "safe than sorry" with the cleanliness of materials put into a UHV chamber. A single dirty component can ruin good vacuum. All components put into the vacuum chamber are subjected to this cleaning process, and so are the tools used inside the chamber.

The pressure is monitored with a Bayard-Alpert ionization gauge, which works by ionizing gas particles in the vacuum chamber and measuring the current induced by them across a pair of charged electrodes. This current is proportional to the density of gas particles in the chamber. Our gauge can measure pressures as low as 10^{-11} torr.

Rf resonator

The trap is driven with a helical resonator that is supplied with voltage from a broadband rf amplifier (MiniCircuits TIA-1000-1R8). The helical resonator is a helically wound transmission line that supports a quarter-wave resonance at a specific frequency that is governed by the capacitance and inductance per unit length of the transmission line, as well as the load impedance (that of the trap and feedthrough). A practical guide for the construction of such resonators is given in Ref. [Fis76].

This paper permits calculation of the *unloaded* frequency of the resonator. However, this frequency changes to a generally lower value when the trap is attached. The frequency drop depends on the electrical characteristics of the trap and feedthrough and is difficult to predict, but it is usually less than a factor of two. Since it is not necessary for the resonance to be at one specific frequency, a small amount of trial and error enables us to get a resonance in the right range. A typical Q factor for the finished resonator is 100, with a voltage step-up between 20 and 40. The circuit was impedance matched by minimizing the power reflected from the circuit along a 50 Ω coaxial cable. The voltage on the trap was measured by securing a wire near the high-voltage end of the resonator and calibrating it at low voltage by simultaneously measuring the actual voltage using a 100X scope probe.

5.3.2 Lasers and imaging

Two lasers are required for Doppler cooling and detection of $^{88}\mathrm{Sr}^+$; these have wavelengths of 422 nm and 1092 nm. The 422 nm laser addresses the $5\mathrm{S}_{1/2} \rightarrow 5\mathrm{P}_{1/2}$ transition and provides the momentum transfer for Doppler cooling. Also, 422 nm photons are detected when imaging ions. The 1092 nm laser is a "repumper" that addresses the $4\mathrm{D}_{3/2} \rightarrow 5\mathrm{P}_{1/2}$ transition and prevents optical pumping to the metastable $4\mathrm{D}_{3/2}$ state. The level structure is depicted in Fig. 5-5.

Both lasers are extended cavity diode lasers. The laser diode is mounted on a temperature-stabilized baseplate, and current (50 - 100 mA) is passed through it to produce laser radiation. An "extended cavity" is formed by using a grating to reflect the radiation back into the diode. This permits additional tuning of the laser frequency.

After leaving the grating, the beam passes through an optical isolator, which is a device that prevents light from the far side of the isolator from being reflected back into the diode. This is essential for preventing any effects due to an unintended cavity being formed by some surface other than the grating; it also prevents overloading of the diode due to excessive feedback. Finally, mode-matching lenses are used to couple the beam into a single-mode fiber patch cord for delivery to the ion trap. Coupling efficiencies of ≈ 50 % are typical.

The beams are outcoupled from the fibers onto fast achromatic lens pairs from Thorlabs for collimation. A telescope and a final focusing lens are used to produce the desired beam waists at the trap site. $1/e^2$ waists of about 50 μm are normally used.

Photoionization (PI) of neutral Sr atoms is done by a two-photon process. The first photon, at 461 nm, pumps the atoms from the $5s5s$ ground state into the $5s5p$ excited state, where the lowercase letters refer to the orbital angular momenta of each of the two valence electrons in the neutral atom. The second photon addresses a broad (≈ 3 nm) transition that pumps the atom from its excited state into an autoionizing state which lies above the dissociation energy. Thus, one electron is removed. This process was described in Ref. [BLW+07].

The 460 nm radiation is produced by doubling the 920 nm output of a titanium sapphire (Ti-Saph) laser (Coherent model no. MBR-110), which is pumped by a 5 W Spectra Physics Millennia Pro solid-state laser. A Spectra-Physics WaveTrain doubler is used. The 405 nm laser is quite a bit simpler; we use the output of an ECDL with a readily-available 405 nm diode. Due to the width of the transition, no further frequency stabilization is needed. Level diagrams for the ionic and PI transitions are presented in Fig. 5-5.

For the atomic ion trap experiments in Ch. 5-7, we used a CCD camera (part no. ST-3200ME) from Santa Barbara Instrument Group. It features a 2184 × 1472 array of 6.8 μm × 6.8 μm pixels, and can be cooled to -10 °C. The quantum efficiency at 422 nm is about 60 %.

Light is imaged onto the CCD using a simple system of two 2 in. diameter achromatic doublets that are mounted vertically above the vacuum chamber. The lens closest to the

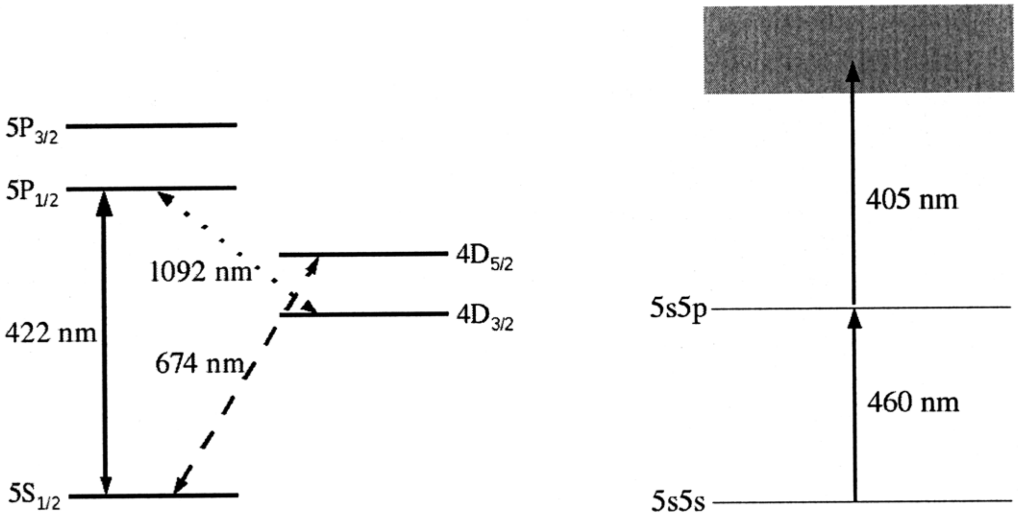

Figure 5-5: Left: Level diagram for the ^{88}Sr^{+} ion, showing the Doppler cooling transition at 422 nm, the repumper at 1092 nm, and the sideband cooling and coherent operations laser at 674 nm. The spontaneous emission rate from the $5P_{1/2}$ state is 20 MHz, with the ion decaying to $4D_{3/2} \approx 1/13$ of the time. The lifetime of the $4D_{5/2}$ state is ≈ 0.4 s. Right: Photoionization transitions for ^{88}Sr. A 460 nm photon pumps the atom from the $5s5s$ state to the excited $5s5p$ state, then a 405 nm photon takes the atom into an autoionizing level, resulting in the loss of a single electron.

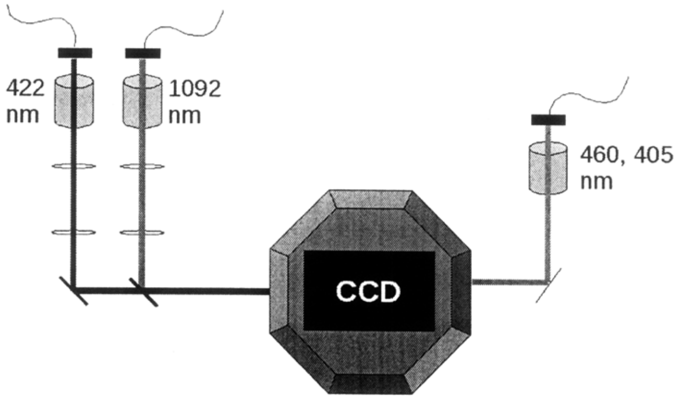

Figure 5-6: Top-view schematic of the optics setup for the atomic ion lattice trap experiment. On the left, the 422 nm and 1092 nm beams are outcoupled from single-mode optical fibers and collimated using fast achromat pairs. The beams are focused to the desired waist at the trap center using telescopes, then coaligned on a dichroic mirror. On the right, the 460 nm and 405 nm photoionization beams arrive in the same single-mode optical fiber and are focused together using a single fast achromat pair, then directed to the trap. The CCD camera is mounted above the vacuum chamber.

trap has a focal length of $f_1 = 150$ mm, while the second has a focal length of $f_2 = 450$ mm. This results in a theoretical magnification of 3 and an f-number of 1.7. A schematic of the optics for this experiment may be found in Fig. 5-6.

5.4 Experimental results for $^{88}\mathrm{Sr}^+$ trapping

In this section, we present our observation of the stable confinement of $^{88}\mathrm{Sr}^+$ ions in a 6×6 lattice trap, and experimental verification of the model of the trap discussed in Sec. 5.2 by measuring the secular frequencies of the ions for one particular lattice site. The rf electrode is cut from a stainless steel mesh from Small Parts, Inc., Part No. PMX-045-A. It is mounted 1 mm above a grounded gold electrode on a ceramic pin grid array (CPGA) chip carrier (Fig. 5-7). An additional planar electrode (the "top plate") is mounted 1 cm above the rf electrode, to help shield the ions from stray charges. Electrical connections to both the rf and ground electrodes were made using a UHV-compatible solder from Accu-Glass (part no. 110796). The vacuum chamber was baked out to a base pressure of 7×10^{-10} torr.

The trap is loaded with $^{88}\mathrm{Sr}^+$ by the photoionization process described above. Typical laser powers used are 10 μW of 422 and 50 μW of 1092, with $1/e^2$ beam waists of 50 μm. For beams of this size, the increase in beam width over the size of the trap (Rayleigh range) is not a concern. Ions were observed as both clouds and crystals (Fig. 5-8). The cloud lifetime is quite short ($O(10\text{ s})$), but a small crystal has been kept in the trap, illuminated with cooling light, for up to 15 minutes. This short lifetime is attributable to the vacuum pressure.

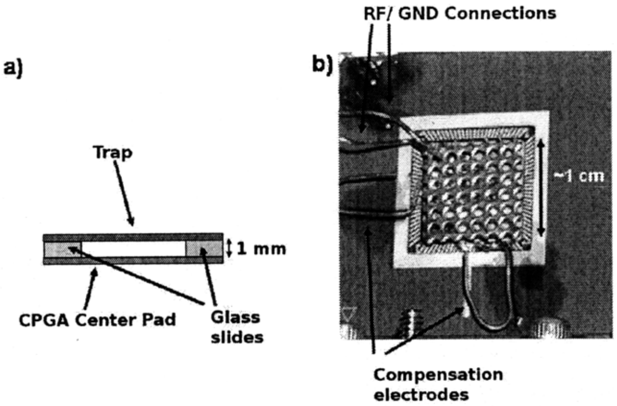

Figure 5-7: (a) Schematic of the cross-section of the trap assembly. The trap electrode is held above the CPGA center pad on top of two 1 mm thick glass slides. (b) Photograph of the trap mounted in the CPGA. Connections for rf and GND (the grounded bottom electrode) are shown, as are the optional control electrodes for the $\hat{x}$ and $\hat{y}$ directions.

A typical voltage of $V = 300$ V at $\Omega/2\pi = 7.7$ MHz was applied to the rf electrode. Numerical modeling of the resulting pseudopotential yields secular frequency values of $\omega_{\hat{r}}/2\pi = 300$ kHz and $\omega_{\hat{z}}/2\pi = 600$ kHz. In order to test the model, we measure both secular frequencies as functions of the applied rf voltage V. We also compute a trap depth of 0.3 eV, which is the energy required for an ion at the potential minimum to escape.

Secular frequencies were measured for one site near the center of the lattice using the standard method of applying a low-amplitude ($\sim$0.02 V) oscillating voltage to the top plate at the motional frequency of the ions. When each vibrational mode of the ions is stimulated, their heating causes measurable drops in the fluorescence intensity. This experiment was performed and compared to the model for several values of the drive voltage (Fig. 5-9). Agreement is very good; measured data points differ from the predicted values by at most 5%, an error that results mainly from the approximation of the trap electrodes as perfect two-dimensional conductors for simulation. Although other sites near the center were also loaded, secular frequency measurements are presented here for only one site of the lattice. To implement a quantum simulation using all 36 sites of such a lattice trap, the potentials at the edges of the trap would also need to be measured, which is outside the scope of this work.

In summary, this experiment verifies the properties of lattice traps derived above. Accordingly, it is with some confidence that we can evaluate this trap design by calculating the simulated coupling rates (Sec. 5.6).

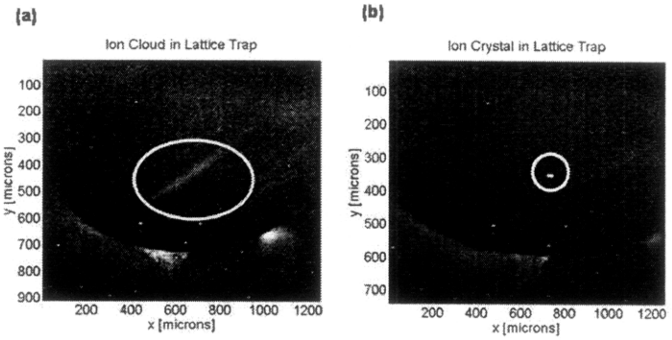

Figure 5-8: (a) A cloud of ions (circled) intersects the detection lasers traversing the trapping region. The bright spots beneath the ions are laser scatter. (b) An ion crystal (circled) with a lifetime of $\mathcal{O}(15\,\text{minutes})$ is observed in the trap. The fact that it's a crystal rather than a cloud can be inferred from the fluorescence per pixel, which is consistent with a crystal but not a cloud, in addition to the fact that the signal vanishes instantly, rather than gradually, when ions are lost from the trap. Resolution in the imaging optics is insufficient to count the number of ions.

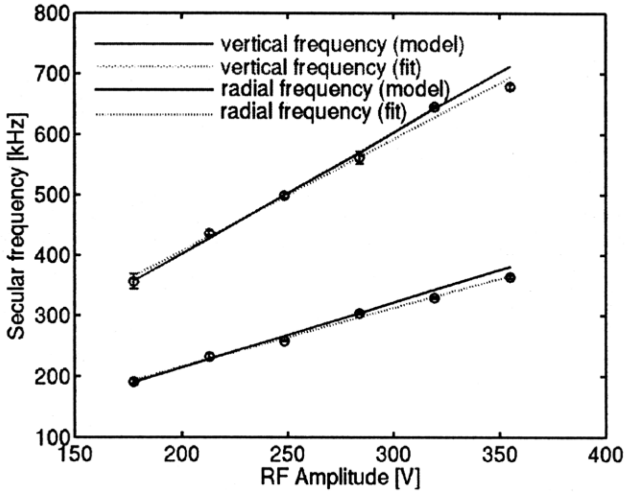

Figure 5-9: Secular frequencies as a function of rf voltage for one site of the lattice trap. Circles represent data points, dotted lines represent linear fits to the data, and the solid lines are the predicted values from the model. The upper (red) data are values of $\omega_{\hat{z}}/2\pi$, and the lower (blue) are values of $\omega_{\hat{r}}/2\pi$.

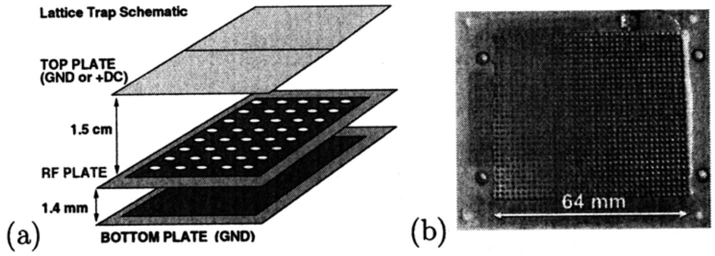

Figure 5-10: Experimental setup for the macroion experiment. (a) 3-D schematic of lattice trap setup. (b) The lattice rf plate, as mounted for the microsphere experiment. The hole diameter is 1.14 mm and the hole spacing is 1.67 mm. The trap is supported by a printed circuit board.

5.5 Measuring interactions between macroscopic ions

Another important test of the applicability of this lattice design to quantum simulations is the strength of interactions between ions in different wells. This section deals with the measurement of repulsion between charged particles in different wells of a lattice ion trap. For this work, we used aminopolystyrene microspheres with diameter 0.44 μm (Spherotech Part No. AP-05-10). This is because the charge to mass ratio of the strontium ions is unsuitable for this measurement in a lattice of this ($d = 1.64$ mm) spacing. The charge-to-mass ratio Q/m of macroions used in the experiment leads to observable repulsions between ions in neighboring wells, although it takes on a relatively wide range of values due to the fact that Q/m is not the same for every macroion. The use of macroions is also experimentally much less demanding than atomic ion trapping, because UHV pressures and laser cooling are not required. In fact, ions can be trapped in atmospheric pressure more easily than under vacuum, since air damping of ion motion increases the range of parameters suitable for stable trapping [PLB$^+$06, WO91, Pea06].

While the measurements of interaction strengths between macroions does not translate directly into interaction strengths expected between atomic ions, the analysis methods involved, particularly with regard to screening effects, is likely to share common points. The measurements made in this section were conducted by Tongyan Lin and Kenneth Brown. The author was involved, along with them, in the analysis of the data.

Fig. 5-11 is a diagram of the experiment, which is an adaptation of the experiment in Ref. [PLB$^+$06]. The main components of our apparatus are the electrospray system and the 4-rod loading trap. To load the ions in the lattice trap, we perform a modification of the method in [CPK$^+$02], skipping the washing step. We prepared a buffer solution of 5 mL pure acetic acid, 26 mL 1M NaOH, and 5% suspension microsphere solution. The buffer solution reduces spread in macroion charge. We sonicated the solution for 10 minutes to

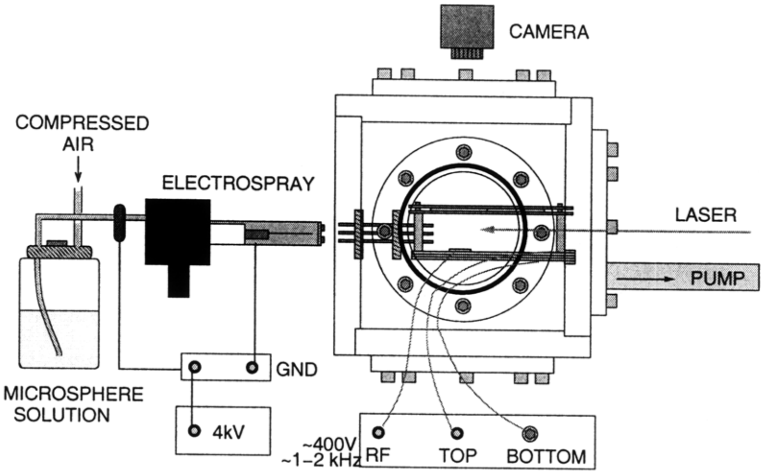

Figure 5-11: Trapping apparatus. The lattice trap is inside a plastic chamber which can be pumped down to ≈ 1 torr. Macroions are loaded via the electrospray and the 4-rod trap, which extends through one side of the chamber over the surface of the lattice trap.

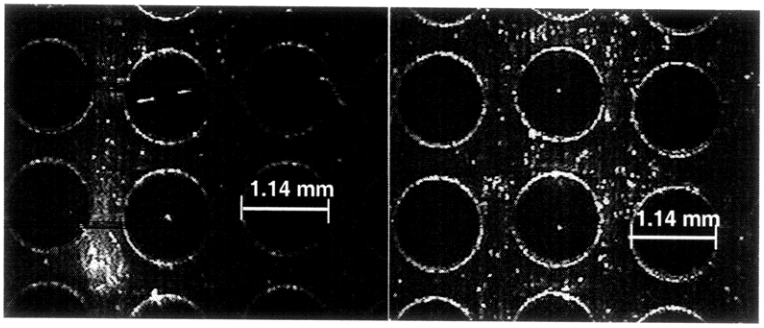

Figure 5-12: Image from above of ions in the lattice. The dark holes are the holes in the rf electrode; the grounded plane is 1.4 mm beneath them. Single macroions appear as white dots that are levitated above the plane of the rf electrode and are illuminated by 532 nm laser radiation at 5 mW. White dots on the surface of the rf electrode are due to stray light scatter. The left image was taken at $V = 300$ V and $\Omega/2\pi = 1200$ Hz and the right image was taken at $V = 300$ V and $\Omega/2\pi = 1960$ Hz. In the left figure, in the top well, two ions are shown repelling each other in the same well.

mix the microspheres evenly in the solution, added 30 mL of methanol, and again sonicated for 10 minutes.

Compressed air, at a pressure of between 3 and 5 Psi, forces the buffer solution first through a 0.45 μm filter and then to the electrospray system. Here a copper wire at a voltage of 4 kV is inserted in the tubing and ionizes the solution as it passes. The ionized solution travels through a thin electrospray tip directed at a perforated, grounded electrospray plate and a 4-rod Paul trap just behind the electrospray plate. The electrospray tips were made from capillary tubes, which are heated and stretched to produce narrow openings of 75-125 μm.

As the solution enters the 4-rod trap, the methanol evaporates and the charged microspheres break into small clusters, the macroions. The 4-rod trap is driven at the drive parameters of the lattice trap and extends through the wall of a plastic chamber over the lattice trap. Inside the chamber, the 4-rod trap extends 0.75 cm over the lattice trap and the bottom rod of the 4-rod trap rests 1 mm above the ground plate.

The lattice trap used for this work is shown in Fig 5-10. The trap is supported by standings inside the chamber, which can be closed on all sides to block air currents and can also be sealed and pumped down to ~1 torr. Glass slides, which are coated with $\mathrm{InTiO_2}$ so that one side is conductive, act as the top plate. They allow a top view of the trap, and are supported approximately 15 mm above the rf plate. The ions are then confined approximately 0.25 mm above the plane of the rf plate. An image of the ions in the trap is given in Fig. 5-12.

Typical initial loading parameters for macroions were $\Omega/2\pi = 1000$ Hz and $V = 250$ V. We also applied a dc voltage of $U = 0 - 10$ V to the top plate to improve the trap depth. Before studying ion-ion repulsion, we estimate the Q/m of the macroions by measuring their secular frequencies ($\omega_{\hat{z}}$). To do this, we apply a low-amplitude tickle to the top plate and observe the resonances directly on a video camera as ions rapidly oscillate back and forth. A measurement of $\omega_{\hat{z}}$ vs. Ω is shown in Fig. 5-13. Using Eq. 5.4, we fit these data to obtain a charge-to-mass ratio of $1.9 \times 10^{-9}\ e_c/\mathrm{amu}$.

We measured the Coulomb interaction of ions in neighboring lattice sites for six pairs of ions. In each pair, we measured the offset of each ion from the center of the well, as shown in Fig. 5-12. Note that while taking data on separation of two ions, we ascertained that wells adjacent to those containing the ions were all empty. The effect of a third ion in an adjacent well is significant.

A simple model of the interaction of two ions across wells is given as follows. An ion is confined by a force $-m\omega_{\hat{r}}^2 x_1$, where x_1 is the ion offset from the center of the well. Since generally $x_1 \ll d$, where d is the lattice spacing, the ion is approximately repelled by a force $Q_1 Q_2/4\pi\epsilon_0 s d^2$. Here s is a screening factor and $Q_{1,2}$ are the charges of the first and second ion, respectively. The screening factor $s < 3$, where $s = 3$ for an ion sitting at a height 0.25 mm above an infinite conducting plane.

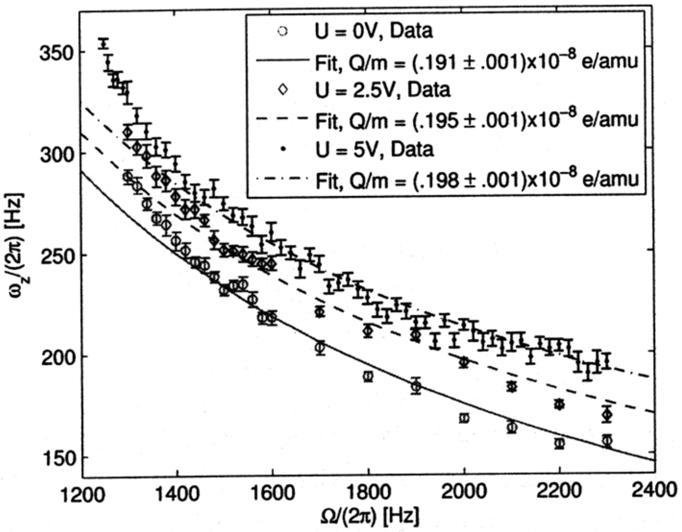

Figure 5-13: $\omega_{\hat{z}}$ vs. Ω for an isolated macroion at a drive voltage of $V = 255$ V. The data for 0 V and 2.5 V come from the same ion. The fit was done only for data above 1500 Hz; data below this frequency begin diverging from this fit because the pseudopotential approximation no longer holds.

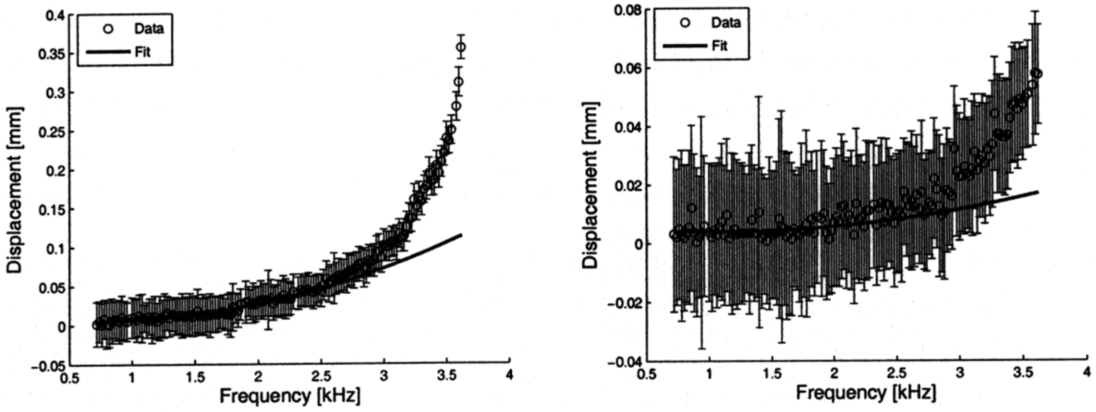

Figure 5-14: Ion displacement from the well center for two ions in neighboring wells, as a function of drive frequency. Due to charge asymmetry, the maximum displacements of the two ions differ by a factor of ten. The drive voltage is 350 V. The model breaks down for large displacements (high trap frequencies); fits only include data below $\Omega/2\pi = 2500$ Hz. Error bars are dominated by the intrinsic error in determining the ion position from the ccd camera image.

Using the expression for $\omega_{\hat{r}}$ derived from Eq. 5.3,

$$x_1 s d^2 \approx \Omega^2 \frac{m r_1^4 Q_2}{8\pi\epsilon_0 V^2 Q_1}. \tag{5.5}$$

When Q_1 is not equal to Q_2, then the confining forces are characterized by different $\omega_{\hat{r}}$ and the two ions have different offsets from equilibrium. The ratio in offsets, if the masses are comparable ($m_1 \approx m_2$), should be $(Q_2/Q_1)^2$. We observed exactly such an asymmetry between the offsets of the two ions, where typically Q_2/Q_1 is between 1 and 5. There may be additional small asymmetries due to edge effects and the presence of the 4-rod trap as well as differences in charge. Fig. 5-14 shows the displacement of a pair of ions as the rf drive frequency is varied, for one experimental run. The spread in charge to mass ratios and accordingly unknown values of Q and m for each ion (as in Ref. [PLB$^+$06]) does not permit us to compare the observed repulsion to a theoretical model. Indeed, if these data were available, this repulsion experiment would be a very useful way to measure the screening factor s for a given trap, perhaps prior to trapping atomic ions.

We conclude that ion-ion interaction in a mm-scale lattice trap is observable by the mutual Coulomb repulsion of macroions. Such an experiment could be used to measure the screening parameter s for a given trap, if knowledge of the charges and masses of the individual particles involved were available. Although we have been able to measure the ion-ion interaction of macroions and fit it to a model (in a certain region of parameter space), it will be necessary to scale the trap down further in order to observe ion-ion interactions between the atomic ions that would be used for quantum simulation.

5.6 Scaling laws for the simulated interactions in lattice traps

The lattice trap discussed in this chapter provides a fairly straightforward method for realizing a two-dimensional array of trapped ions. The first two steps enumerated in Sec. 4.3.3, design and testing of the trap, have now been reported. We turn now to evaluation of the trap design, and ask: how useful could this system be for quantum simulation of two-dimensional spin models [PC04b]? We will need to calculate both the motional coupling rate ω_{ex}, and the simulated coupling rate J.

5.6.1 Motional coupling rate

We begin with the motional coupling rate, which is the rate at which two coupled ions swap motional states (provided they have the same secular frequency). Let us review the basic physics of the system formed by two trapped ions undergoing mutual Coulomb repulsion. The lowest-order term in the Taylor expansion of the Coulomb potential that contains an interaction between the ions is

$$V_{Coup} = \frac{e_c^2}{8\pi\epsilon_0 d^3} x_1 x_2, \tag{5.6}$$

where d is the mean ion-ion distance and x_1 and x_2 are, respectively, the displacements of the first and second ion from their equilibrium positions. Lower-order terms result in either a shift of the overall potential energy or a shift in the ions' motional frequencies. Defining p_1 and p_2 to be the momentum operators for ions 1 and 2 respectively, the Hamiltonian for the motional states of the ions is

$$H_V = \frac{1}{2m}p_1^2 + \frac{1}{2m}p_2^2 + \frac{1}{2}m\omega^2 x_1^2 + \frac{1}{2}m\omega^2 x_2^2 + mg^2 x_1 x_2, \tag{5.7}$$

where we assume that the ions have the same secular frequency ω and mass m, and have defined the coupling constant g as $g^2 = V_{Coup}/(m x_1 x_2)$. This Hamiltonian represents a coupled Harmonic oscillator; the rate ω_{ex} at which energy is exchanged between ions is given by

$$\omega_{ex} = \frac{g^2}{\omega}. \tag{5.8}$$

The factor of ω in the denominator has important implications for the coupling rate in lattice ion traps. The physics of ion traps demands that for constant trap depth and stability parameter q, the drive frequency must increase as the inverse of the trap scale. In a lattice trap, d is directly proportional to the size of the trap, and may be considered one measure of the trap scale. Therefore, since $g^2 \propto 1/d^3$, $\omega_{ex} \propto 1/d^2$ in a lattice-style ion trap. In practice, this means that over reasonable length scales for d, ω_{ex} in a lattice trap is much lower than it would be if the ions occupied the *same* trap region, for instance in a linear ion trap. We plot this comparison in Fig. 5-15.

5.6.2 Simulated J-coupling rate

So far we have remarked only on the motional coupling rate ω_{ex}. A more relevant quantity is the simulated coupling rate J for quantum simulation of spin models. We first give a brief review of the spin model simulation scheme of Ref. [PC04b] described in Sec. 4.2.2. This scheme uses a laser that exerts a state-dependent force on trapped ions that are coupled by their Coulomb interaction. In the limit in which the Coulomb interaction is small compared to the trapping potential (which is the case for lattice traps), the coupling rate between the ions is given by

$$\hbar J = \frac{e_c^2 F^2}{8\pi\epsilon_0 m^2 d^3 \omega^4}, \tag{5.9}$$

where F is the magnitude of the state-dependent force and the other symbols are as defined above. For quantum simulation in a lattice trap, the frequency ω in Eq. 5.9 may be $\omega_{\hat{r}}$ or $\omega_{\hat{z}}$. For the sake of argument here, we assume $\omega = \omega_{\hat{r}}$. F is assumed to be due to a

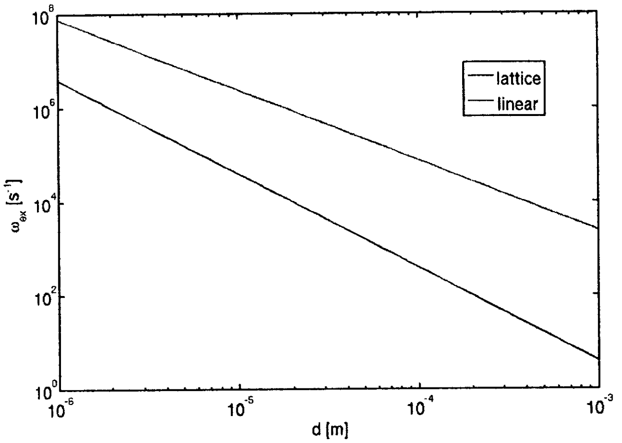

Figure 5-15: Plot of the motional coupling rate ω_{ex} as a function of the ion-ion spacing d in lattice and linear ion traps. For the lattice trap, values at d=1 mm are extrapolated from the lattice trap data in this chapter, while for the linear trap d can readily be calculated given a frequency ω. We see that for any experimentally feasible set of values, including d, ω_{ex} is significantly weaker in the lattice trap than in the linear trap.

tightly-focused laser beam, and arises from a spatially-dependent AC Stark shift. For a 5 W beam of 532 nm radiation that is focused from 50 μm to 3.5 μm over a distance of d = 50 μm, in traps operating at $\omega = 2\pi\cdot250$ kHz, we calculate a J coupling of 10^3 s^{-1}, which should be observable if the dominant decoherence time is significantly greater than $2\pi/J$. Similar values can be obtained by using less powerful lasers closer to the atomic resonance; we use the 532 nm beam as an example only because of the readily-available solid-state lasers at this wavelength.

The motional decoherence rate expected in microfabricated surface-electrode traps becomes small relative to the internal state decoherence time if the trap is cooled to 6 K; rates for the former have been measured at as low as $\dot{n}$ = 5 quanta/s [LGA$^+$08]. Internal state decoherence times depend on the specific ion being used and also on classical controls, but coherence times as long as T = 10 s have been reported [LOJ$^+$05, HSKH$^+$05]. The important point is that both internal and motional decoherence channels are much slower than the J-coupling: $T > 1/\dot{n} \gg 1/J$.

Unfortunately, the scaling properties of lattice traps do not favor such a low secular frequency at small ion-ion spacings. The fact that $\omega \propto 1/d$ is again problematic for the coupling rate. According to Eq. (5.9), J actually increases linearly with d, a result also noted in Ref. [CW08]. In Fig. 5-16, we plot a comparison of the J-coupling rates in lattice and linear traps.

Greatly increasing the trap size is not only impractical, but renders the width of the ground state wave function of each trapped ion comparable to the laser wavelength, leaving the system outside the Lamb-Dicke confinement regime. Fig. 5-16 illustrates how the J

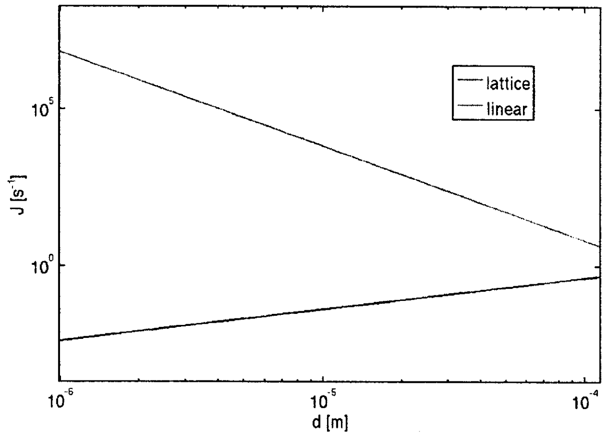

Figure 5-16: Simulated J-coupling rates in lattice and linear ion traps as a function of ion-ion distance d. The maximum value of d given here, 100 μm, is the point at which the Lamb-Dicke parameter is approximately 0.1. The J values for lattice and linear traps intersect at higher d values, when the ion is no longer in the Lamb-Dicke regime.

values obtained in the lattice trap are much weaker than a comparable linear trap within the Lamb-Dicke regime. While some gains might be made from using the stronger field gradients of a standing wave configuration for the "pushing" laser, it is clear that the scaling of ω with $1/d$ is a discouraging feature of lattice traps.

These scaling laws for ω_{ex} and J hold regardless of how a given lattice geometry has been "optimized," whether for trap depth, low motional frequencies, or even ω_{ex} at some length scale. This point bears emphasizing, since recent reports [SWL09] have detailed methods of designing array trap electrodes such that the trap curvature is maximized at each site for a given set of experimental parameters. While this approach is interesting and potentially useful for some applications, it is not clear how the above scaling behavior could be circumvented.

5.6.3 Trap depth

An interesting and still unanswered question is whether it is possible to modify the lattice trap design to allow for low motional frequencies even at small ion-ion spacings, with an adequate trap depth. One simple idea would be to decrease the drive voltage V (and consequently the trap depth) once the trap is loaded with ions and they have been laser-cooled to a temperature much lower than the trap depth. However, the trap depth in this case would be extremely low. To understand why this is the case, consider the following argument. Suppose that one wishes to keep ω constant a the trap scale changes. From the above formulas, we see that the trap depth is proportional to V^2/Ω^2, and also to qV, where $q \propto V/(r_0^2\Omega^2)$. We arrive at the following relation for ω:

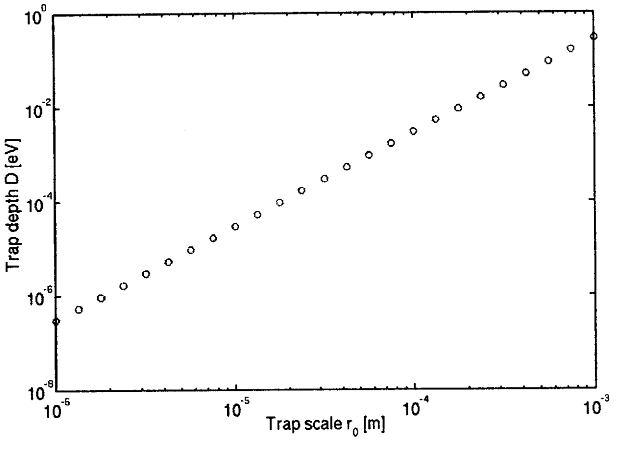

Figure 5-17: Dependence of the trap depth D on the trap scale r_0 for a constant secular frequency ω. The values for $r_0 = 1$ mm, the approximate scale of the lattice trap presented in this chapter, are $D = 0.3$ eV, $\omega = 2\pi\times200$ kHz, and $\Omega = 10\omega$.

$$\omega \propto \frac{e_c V}{m r_0^2 \Omega}. \tag{5.10}$$

We note that in order to hold ω constant as r_0 is varied, the following scaling law must hold: $r_0^2 \propto V/\Omega$. Whether one reduces V or increases Ω, or some combination thereof, the trap depth is reduced in proportion to either V^2 or $1/\Omega^2$. Taking some typical baseline experimental parameters for the lattice trap, we plot in Fig. 5-17 the trap depth as a function of the trap scale. In this particular case, we varied the drive frequency Ω, but according to the above argument, varying V would yield the same trap depth.

The result given in Fig. 5-17 completes our exposition of the scaling behavior of lattice traps. For ion-ion distances for which an appreciable coupling rate might be achieved, as in our above example for $J = 1$ kHz at $d = 50$ μm and $\omega = 2\pi\times200$ kHz, the trap depth is reduced to the order of a mere 100 μeV. While there is no fundamental reason why a laser-cooled ion may not be trapped at such a depth, such trapping has never been reported, to our knowledge, in the literature. In fact, this value is below the Doppler limit for most ions. We again note that even a hypothetical factor of 100 improvement in the ratio of trap depth to secular frequency would result in a trap depth of only ≈ 10 meV, still a very challenging figure.

5.7 Conclusions

In this chapter we have presented the design, testing, and evaluation of a macroscopic lattice ion trap. Our main experimental achievement was verifying that, for two very different systems (atomic and macroion), our theoretical model of the trap is accurate. The principal method of measuring the trap potentials is by measuring the secular frequencies, as was done with both macroions and $^{88}\mathrm{Sr}^+$ ions. The repulsion experiment using macroions is primarily useful for demonstrating the possibility of measuring properties of a trap such as the electrostatic screening factor using a simpler experimental setup than that needed for atomic ions.

Building a prototype trap of a macroscopic scale (mm rather than 10's of μm) is useful because it enables us to very closely examine a given design in less difficult experimental circumstances, for instance without excessive heating due to small ion-electrode distances or laser scatter off the trap. In this case, our investigation of the interaction strength between the macroions led somewhat indirectly to our conclusions about the poor scaling properties of lattice traps from Sec. 5.6.

The poor scaling behavior of lattice traps indicates that other avenues should be sought for creating 2-D lattices of trapped ions. Some possibilities include confining ions within the same trap region in Paul traps, or development of a way to apply global state-dependent forces to ions in Penning traps despite the rapid rotation of the ion crystal. Another possibility would be to modify the electrode design of a lattice trap in such a way that the ratio of trap depth to motional frequency is optimized; perhaps then sufficient coupling rates could be achieved. It remains to be seen which method of preparing 2-D lattices of ions, if any, will succeed in supporting analog quantum simulation.

Chapter 6

Surface-electrode PCB ion traps for trap development

In Ch. 4, we explained how proposals for analog ion-trap quantum simulation of spin frustration rely upon a 2-D lattice of potentials. However, as reported in Ch. 5, we discovered that the interactions between ions held in individual potential wells are quite weak, for a given ion-ion distance, when compared to other designs (e.g. linear ion traps). This motivates us to design ion traps that can confine a 2-D array of trapped ions all in the *same* potential well. In order to design and test such a trap, we have chosen to use printed circuit board (PCB) ion trap technology. These traps are relatively simple to design and manufacture, and can be used to measure all the basic properties of a trap, as was done without the use of PCB's in Ch. 5. The large ($\sim 100\ \mu$m) minimum feature size of PCB's prevents scaling to a "microfabricated" scale trap, should the need arise. Nevertheless, we find them to be a useful tool for trap design and basic testing.

In this chapter, we explore some basic questions regarding the loading of ions into such a trap. With PCB's, the presence of dielectrics in between the trap electrodes presents the problem of stray charge buildup. When using the conventional technique of electron impact ionization, we must ask ourselves how much this trapped charge affects the trap potentials, and even if, in extreme cases, it could prevent trapping at all. We also ask the question of how these effects might be mitigated. In the course of this work, we solve this problem in two ways, first by removing as much dielectric as possible from the trap structure, and then by using a helium buffer gas to cool the ion clouds that suffer greatly from rf heating in the presence of stray fields. We explore whether it's possible, via this technique, to trap a laser-cooled sample of ions at UHV pressures, even in the presence of large stray fields.

In the second experiment presented in this chapter, we study direct laser ablation of ions into surface-electrode traps. In so doing, we again address issues of charge buildup, but the emphasis is on the low trap depths of surface-electrode traps. We ask the question of how shallow a trap may be loaded with this method, and how that result compares to other techniques, including electron impact ionization and photoionization. We also probe some other related practical questions, including how the loading efficiency depends upon the composition of the material that is ablated and upon the ablation laser power, and how the number of ions loaded depends upon the ablation laser power. We also qualitatively discuss the buildup of stray electric charge, relative to other loading methods.

Although we present PCB's here as a step towards development of 2-D arrays, our work on them chronologically precedes the work on the lattice trap of the previous chapter. The traps presented in this work are surface-electrode (purely two-dimensional) versions of the well-known linear ion traps from quantum information research. All the experiments were done in a room-temperature vacuum vessel, and the basic questions on which we focused are how ions might be loaded into such a trap, and what effects the loading methods have on the subsequent trapping potentials. Our work on buffer-gas loading with electron impact ionization into a PCB ion trap was the first demonstration of a PCB ion trap for atomic ions, and was presented in Ref. [BCL+07]. Our work, following this, on laser ablation loading of PCB ion traps, was published as Ref. [LCL+07]. Following our work, the use of planar PCB ion traps has spread around the world, with traps of our design being used in Innsbruck, Austria, and Osaka, Japan. Additionally, work has been published on the construction of a 3-D segmented linear ion trap from PCB components [HDS+08], with the goal of creating an extremely accurate single-ion source.

The chapter is organized as follows: in Sec. 6.1, we discuss the various prior designs and experiments in surface-electrode ion trapping; in Sec. 6.2, we present the design of our first surface-electrode trap, along with the experimental setup used to study it; in Sec. 6.3, we present the buffer gas loading and micromotion compensation techniques for this trap; in Sec. 6.4, we present the second-generation PCB trap; in Sec. 6.5, we discuss past work in the loading of ion traps using laser ablation, and then present our results using this technique; in Sec. 6.6, we summarize and offer an evaluation of the loading methods presented in this chapter.

6.1 Surface-electrode ion traps: history and theory

The "workhorse" of quantum information experiments with trapped ions has been, for the past several years, the linear ion trap. As shown in Fig. 6-1, the trap consists of four long electrodes, on two of which an rf voltage is applied, while the other two are grounded. In this case, "long" means that the length of the electrodes is large compared to the spacing between them. This configuration creates a quadrupole potential; near the center of the trap, this leads to an approximately harmonic time-independent pseudopotential, as discussed in Ch. 4. Confinement along the trap axis, the $\hat{z}$ direction, is created by a static voltage applied to two *endcap* electrodes.

If the secular frequency in the $\hat{z}$ direction is small compared to those along $\hat{x}$ and $\hat{y}$,

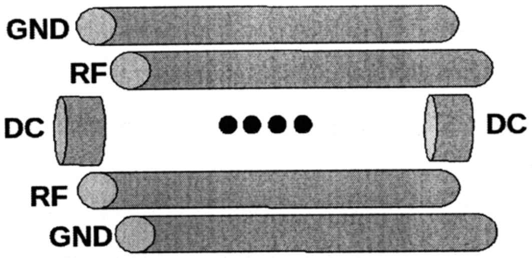

Figure 6-1: Schematic of a linear ion trap. Of four rods, two diagonally opposed rods carry an rf voltage, while the other two are grounded. Confinement along the trap axis is provided by two endcaps that carry a dc voltage. If confinement along the axis is weaker than that along the other two directions, then a linear chain of ions (depicted as blue circles) may be trapped.

the ions align in a linear chain along $\hat{z}$ at the minimum of the pseudopotential. Quantum operations take advantage of the fact that the ions share a common vibrational mode along $\hat{z}$. The linear electrodes most frequently have been cylindrically-shaped. An alternative design uses "knife-edge" electrodes; these have the advantage of minimizing the exposure of trapped ions to conducting surfaces. This can lead to a reduction in the motional heating rates of the trapped ions.

Despite the numerous achievements made with conventional linear ion traps, they are evidently not scalable, due to the finite number (at most tens) of ions that may be confined along the trap axis. Scaling to larger numbers requires a different approach. As we discussed in Ch. 4, the rate at which quantum gates may be performed is limited by the motional frequency. This frequency is known to scale broadly as the inverse of the trap scale. Thus, a microfabricated trap would enable both a higher density of ions in space and overall higher interaction rates, provided that the ions reside in the same trap region during the interactions. In the case of a digital quantum simulator, microfabricated surface-electrode traps are also conducive to ion shuttling operations between different trap regions. For both analog and digital types, obtaining a higher ion density and coupling rate is advantageous.

There are two basic approaches to creating microfabricated ion traps, three-dimensional and two-dimensional (which we refer to as *surface-electrode* traps). Here we review this distinction. 3-D versions have been designed and constructed by the Wineland group at NIST Boulder [RBKD$^+$02], the Monroe group at the University of Michigan (now University of Maryland) [MHS$^+$04, SHO$^+$06], the National Physical Laboratory (NPL) of the United Kingdom [BWG$^+$05], and others. 3-D microfabricated traps have the advantage that generally the trap depth is higher for a given drive voltage and frequency than for comparably-sized 2-D traps. One disadvantage is that fabrication processes are more complicated, and that alignment of the different layers of electrodes can be more difficult. 2-D traps, by contrast, contain all trapping electrodes in a single plane. We refer to these traps as *surface-electrode* ion traps. This idea was first proposed by the Wineland group

[CBB^+05]. Surface-electrode traps are easier to fabricate than their 3-D counterparts, but have a lower trap depth. Because there exist methods that are capable of loading traps with depths on the order of 100 meV, which is considerably less than conventional macroscopic ion traps, we have chosen to exploit the simpler fabrication processes required for surface-electrode traps.

Following Chiaverini's proposal, a number of surface-electrode traps were demonstrated. The first such trap came from the Wineland group in a paper by S. Seidelin *et al.* [SCR^+06]. This trap was made of gold electrodes patterned on quartz. They demonstrated confirmation of the trapping potentials, ion crystallization, and a heating rate of 5000 quanta/s. This is the world record low for electric field noise in a room-temperature ion trap (scaled to ion-electrode distance and trap frequency). Heating rates as low as 5 quanta/s were subsequently demonstrated by Labaziewicz *et al.* in traps that were cryogenically cooled to 6 K [LGA^+08]. This work built on a previous study from the Monroe group that showed dramatic suppression of heating rates when trap electrodes were cooled to 150 K [DOS^+06].

Chronologically in between the Seidelin and Labaziewicz papers, our group pioneered the use of printed circuit boards (PCB's) for ion trapping. The first publication along these lines came in 2006, when the Chuang group at M.I.T. (of which the author is a member) used PCB traps to confine charged macroscopic particles and demonstrate all the basic ion movement operations in surface-electrode ion traps [PLB^+06]. Although this was a useful experiment for prototyping multiplexed surface-electrode traps, the experimental conditions were very different from those for atomic ions. To reiterate a bit from Sec. 5.5, vacuum is not required, and in fact an ambient air pressure actually increases the stability region for stable trapping. Also, a stable laser source is not needed, as the laser light scatters incoherently from the trapped particles.

Our group subsequently demonstrated the first use of PCB traps for trapping atomic ions. Our work on PCB traps has focused on methods for loading the traps, as well as confirming basic properties (e.g. motional frequencies) of the traps. With one trap, we used traditional electron gun loading combined with a helium buffer gas to trap in a PCB trap, then performed micromotion compensation on a fairly large sample of ions [BCL^+07]. In the second experiment, we used laser ablation to directly load a smaller PCB ion trap [LCL^+07]. These experiments are the subject of the remainder of this chapter.

6.2 Design and construction of a planar PCB ion trap

The first PCB trap to be loaded with atomic ions, dubbed "San Quentin" by our group, was designed to be a surface-electrode version of a linear ion trap. A diagram of the trap electrodes is shown in Fig. 6-2. The trap follows a five-rod design, in which ions are trapped above a grounded center electrode which has rf electrodes on either side of it that are separated from it by a gap that is milled out of the PCB substrate. The side electrodes

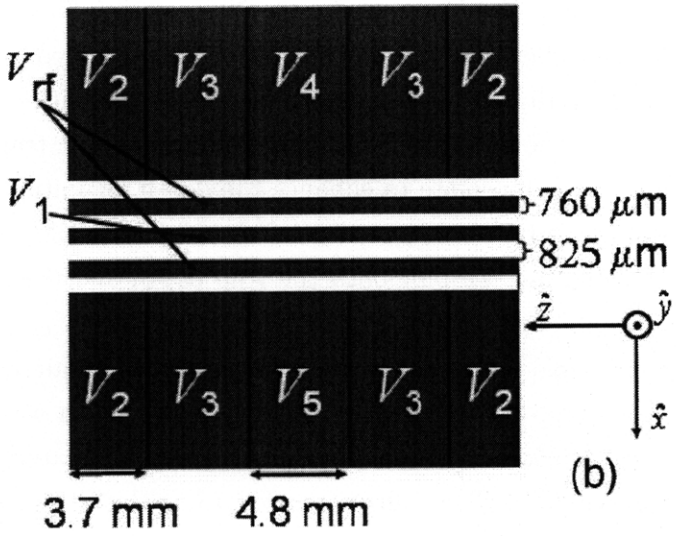

Figure 6-2: Layout of the trap electrodes for San Quentin, each labeled with the voltage applied. All voltages except V_{rf} are dc. A coordinate axis is also supplied; the vantage point in this figure is from the positive $\hat{y}$ axis, or above the trap.

are segmented and are held at carefully-chosen dc potentials. These electrodes both provide confinement along the trap axis and compensate for stray dc fields. Some compensation must be done even in the absence of stray fields, since the endcap electrodes have field components not only along $\hat{z}$, the trap axis, but also along $\hat{y}$, which is defined to be the vertical direction as noted in the figure. Also, optionally, a "top plate" is positioned above the ion trap with a hole cut for fluorescence imaging. It is often grounded but may hold a dc voltage V_{top}. Such an electrode was used in the macroion, but not the $^{88}\mathrm{Sr}^+$ ion, experiments reported in Sec. 5.5.

6.2.1 Modeling the trap

The trap is modeled using the CPO software that was discussed also in Ch. 5. The method is to calculate the static potentials that result from voltages on the rf electrodes, then apply the pseudopotential approximation (Eq. 4.8) to them. To this pseudopotential is added the potential resulting from static voltages on the dc electrodes. Typical rf voltages of V_{rf} = 500-1200 V were applied at $\Omega/(2\pi)$ = 7.6 MHz. This rf drive frequency may take a range of values; normally a suitable range of values is found from simulations and the exact frequency used depends on the rf properties of the combined resonator-trap system, which is difficult to exactly predict ahead of time. Other typical voltages were V_2 = 110 V, V_3 = 50 V, and $V_4 = V_5 = 0$.

Surface-electrode traps have the unique property compared to 3-D Paul traps that the trap depth can be increased by applying a voltage V_{top} to the top plate. With this increase in trap depth, however, comes decompensation of the trap. This fact is demonstrated by plotting cross sections of the pseudopotential for two different top plate voltages in Fig. 6-3. With V_{top} = -25.4 V, we predict that the trap should be compensated, with a trap depth of 1.0 eV. By contrast, V_{top} = 15 V leads to a decompensated trap with a depth of 5.4 eV. A typical strategy, at least in the early period of surface-electrode ion trapping in our group, was to apply a voltage to the top plate to enhance the depth for initial trapping, and then gradually tune the compensation voltages and laser positions while reducing V_{top} to the compensated value. In Fig. 6-4, we plot both the trap depth and the displacement of the trap center from the rf null as a function of the top plate voltage V_{top}.

We have seen the principle illustrated in Fig. 6-4 used in Ch. 5 already, in the macroion experiment, when a high trap depth was useful, but compensation was not critical to the measurements. In the atomic ion experiment of that chapter, fortunately, applying a voltage to the top plate was not required. The main caveat regarding this theoretical work is that the real compensated values may be quite different from the prediction due to stray fields. In the next section we will actually measure the stray fields and find quite different compensation voltages. However, it is still useful to have an idea of how the trap will behave if there are no stray fields; hopefully, they are but a perturbation on the controlled fields.

6.2.2 Constructing and mounting the trap

The trap was manufactured by Hughes Circuits in San Diego, CA. The electrodes are copper deposited on a fiberglass epoxy substrate, Rogers 4350B, which features a small rf loss tangent and UHV-compatibility. The thickness of the copper is about 25 μm. The minimum feature size is about 75 μm, which obviously limits the extension of the technology to microfabricated traps. In addition, the slot size was set at 850 μm since this was the smallest standard slot size. To reduce the accumulation of stray charges, the dielectric material in between rf electrodes was milled out by Hughes, and the sides plated with copper.

The electrodes were polished using a multi-step diamond grid process. This process involves putting diamond grit paste containing diamond pieces of a given average size, together with a lubricating oil, onto a paper disk that is mechanically rotated. Polishing is done by moving the rotating disk across a trap that is mounted securely on a countertop. Following each polishing step, the trap is thoroughly cleaned with acetone and isopropanol and then a smaller-caliber grit paste is applied to a new disk for the next step. Diamond sizes ranging from 15 μm to 1 μm were used. Following this process, the trap was cleaned using the multi-step vacuum cleaning process described in Sec. 5.3.1. Fig. 6-5 is a photograph of the trap after the polishing and cleaning processes.

Following the cleaning, the trap was mounted in the vacuum chamber using a breadboard-style component from Kimball Physics that is secured to the "grabber grooves" that are a part of the spherical octagon vacuum chamber. The top plate, consisting for this experi-

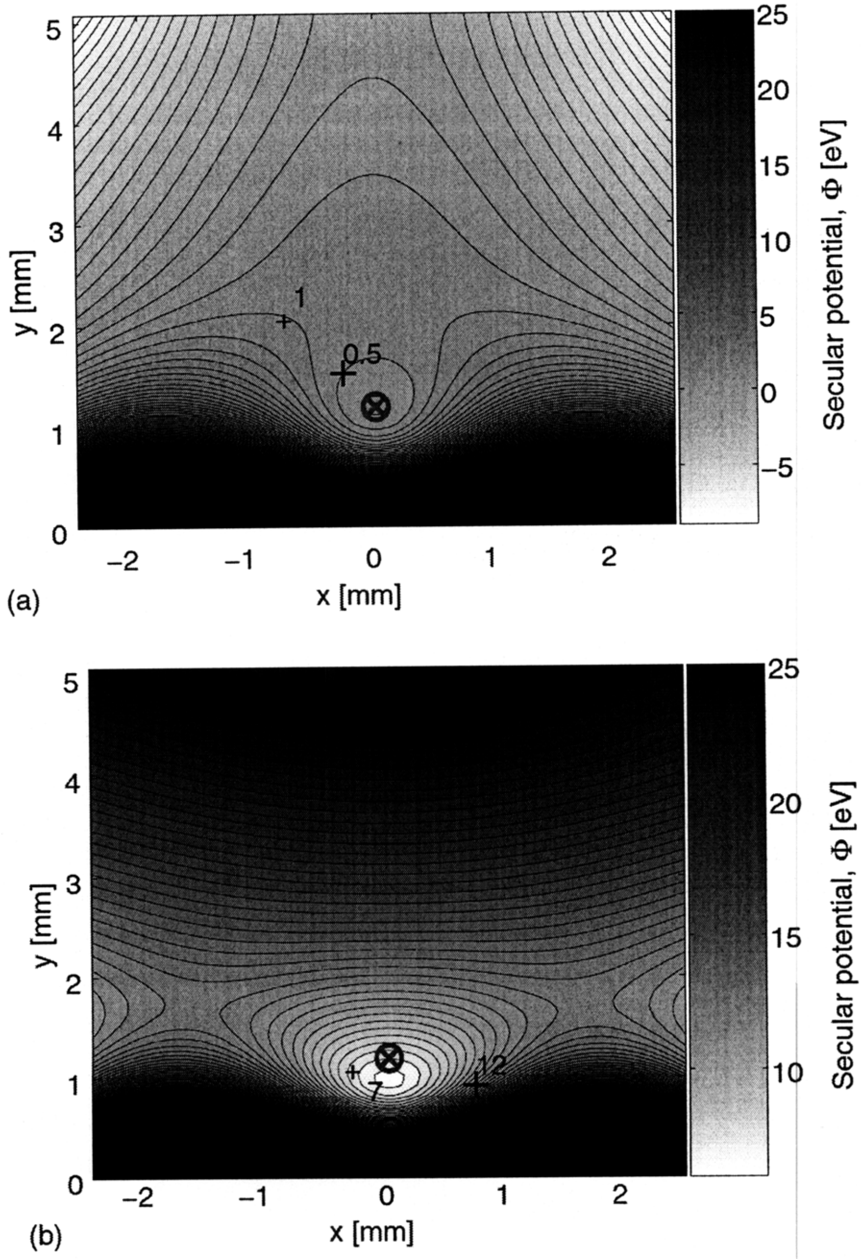

Figure 6-3: Above are the cross sections of two pseudopotentials of San Quentin which were relevant to our work. The rf voltage used was $V_{rf} = 1260$ V at $\omega/(2\pi) = 7.6$ MHz, $V_2 = 110$ V, and $V_3 = 50$ V. The two figures (a) and (b) correspond to V_{top} voltages of 25.4 and 15 V, respectively. Micromotion compensation is expected in the 25.4 V case, but with a depth of only 1 eV, while the uncompensated 15 V case has an expected depth of 5.4 eV. The position of the rf null is indicated in each plot by an "⊗".

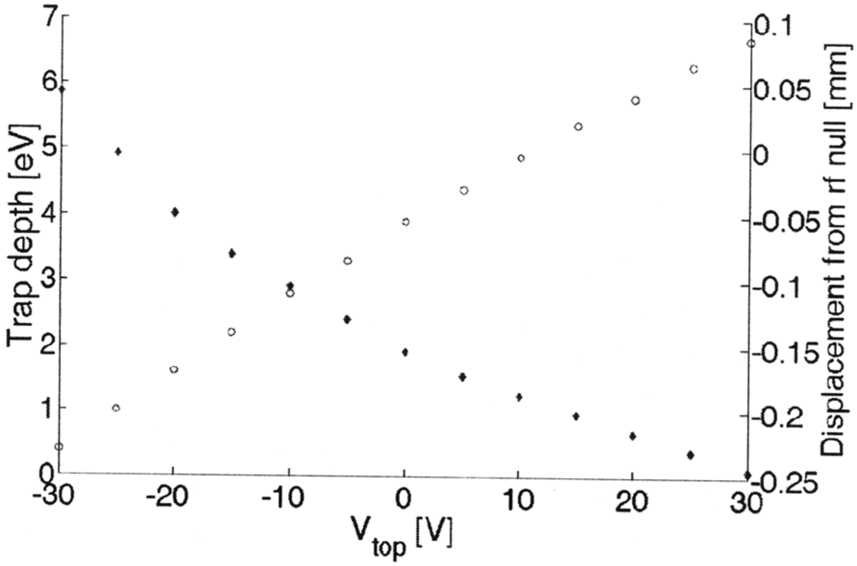

Figure 6-4: Calculated values of trap depth (hollow circles) and ion displacement from the rf null (solid diamonds) as V_{top} is varied. As trap depth is increased, the displacement of the ion cloud from the rf null leads to increased micromotion.

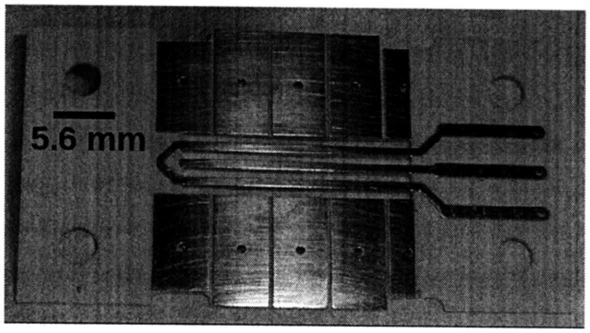

Figure 6-5: Photograph of San Quentin after polishing and cleaning. Width of the dc electrodes along the trap axis is about 5 mm.

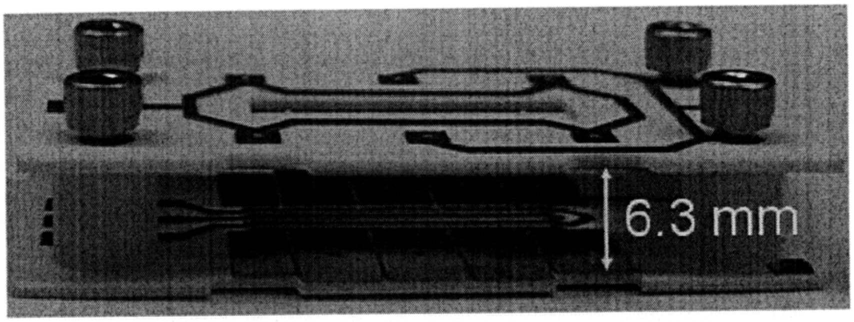

Figure 6-6: Photograph of the trap with the top plate mounted 6.3 above. A slit is cut in the top plate for ion fluorescence detection.

ment of a copper-plated PCB, was mounted above the trap using standoffs (as shown in Fig. 6-6). Connections to the trap were made by soldering Kapton-coated wires, connected to the electrical feedthrough, to the trap using 80/20 Au/Sn solder, applied with an ultrasonic soldering iron. The other components of the experiment, the vacuum chamber, imaging optics, and laser system, will not be discussed here, since they are very similar to those used in Ch. 5, excepting that a titanium sublimation pump was not yet part of the setup, but that a leak valve for introducing a helium buffer gas was.

6.3 Buffer gas loading and micromotion compensation in a PCB ion trap

6.3.1 Experimental setup and ion loading

San Quentin was loaded using the most conventional method for loading ion traps, electron impact ionization. In this method, a resistive oven containing solid metal pieces of the element to be ionized and trapped (c.f. Sec. 5.3.1) is aligned, across the trap, to a filament, which in our case is made of thoriated tungsten. This filament is called an electron gun, or *e-gun*. Current is flowed through both the oven and the e-gun. The current through the e-gun causes emission of electrons, which can be enhanced by applying a (negative) bias voltage to the filament. The electrons strike neutral atoms evaporated from the oven within the trap region, with some probability removing an electron from the neutral atoms and leaving the newly-minted ion with a sufficiently small kinetic energy to remain in the trapping region. If the ion is immediately Doppler-cooled by lasers that pass through the trapping region, this can increase the loading rate, but only works if the lasers are already well-aligned to the trap center.

The electron impact ionization process is quite reliable, and it serves to ionize almost any species. This fact can be viewed in both a positive and a negative light: one can load ions without having a frequency-stabilized set of lasers, as is required for photoionization

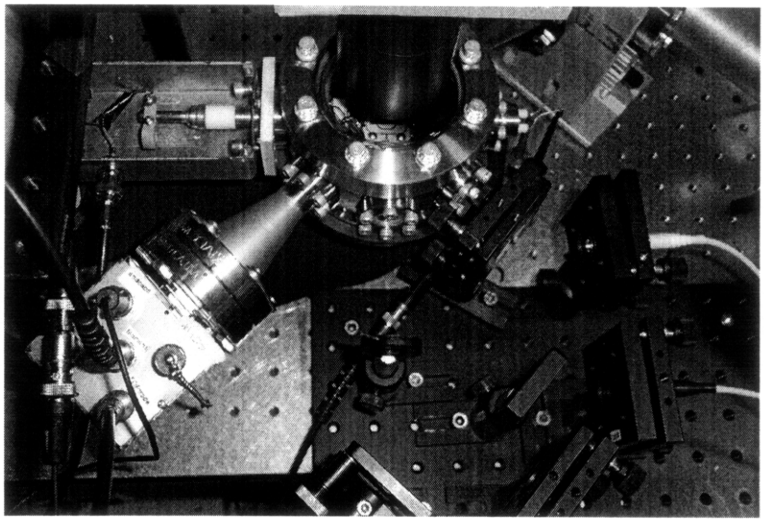

Figure 6-7: Photograph of the experimental setup for measurements on the San Quentin trap. The spherical octagon vacuum chamber with 4 1/2 in. CF viewport is visible top center, and the top plate PCB is seen within it. Above it is the 2 in. diameter lens tube. Connection of the rf signal is top left, while connections to the dc electrodes and the e-gun are on the small box (bottom right). Connection to the oven is top right. The 422 and 1092 nm lasers are collimated by Thorlabs collimation packages, are coaligned on a dichroic mirror, and are then sent through the 1 1/3 in. CF viewport to the trap. Vacuum pumps and the leak valve are outside the frame of this photograph.

(PI) loading, but at the same time species-specific loading is not possible, and "dark ions," particles other than the desired one that are trapped but do not fluoresce, are quite common. The key disadvantage of the technique for surface-electrode traps became evident in our work; the e-gun deposits a stray electric charge on the exposed dielectric that is an unavoidable part of the PCB trap. The stray fields resulting from this trapped charge can become high enough to prevent any trapping in UHV conditions.

Our vacuum system includes a leak valve for introducing helium buffer gas. The collisional cooling provided by the helium allows large samples (100's of ions) to be trapped and cooled even without stray field compensation or optimal alignment of the cooling lasers. In this trap, a current in the oven of 8 A and a voltage across the filament of about 3.5 V was used. The filament was also biased at -20 V with respect to ground to increase the flux of emitted electrons. A photograph of our experimental setup is shown in Fig. 6-7.

Trapped ions were detected using both an electron-multiplying CCD camera (Princeton Instruments PhotonMax) and a photomultiplier tube (Hamamatsu H6780-04). The 422 nm and 1092 nm lasers used for inducing fluorescence were locked to low-finesse cavities. Typical laser powers in this experiment were 1.2 mW of 1092 and 20-50 μW of 422. The width of the 1092 was about 1 mm, so that the entire trap region would be illuminated by it, while the 422 was focused to a 60 μm spot. The smaller spot size is useful in our measurement of the position of the ion cloud. Ions were loaded prior to nulling the stray electric fields

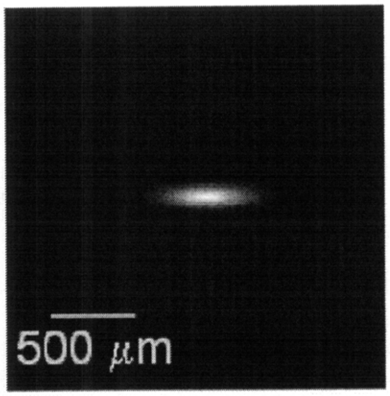

Figure 6-8: CCD image of a cloud of trapped $^{88}\mathrm{Sr}^+$ ions in San Quentin. The ions are immersed in 1.0×10^{-5} torr helium gas pressure.

at a 1.0×10^{-5} torr pressure of ultra-high-purity helium (99.9999% purity). The ion getter pump was switched off prior to filling. Fig. 6-8 is a CCD image of a cloud of ions trapped in San Quentin.

6.3.2 Measurement of stray fields

We now turn to the measurement of the stray fields in this trap. This is done by measuring the change in cloud position as the pseudopotential depth is varied [BMB+98]. An accurate value of the stray dc electric field can be calculated from the following model. The electric field along a coordinate x, at the rf null position, is well approximated by $E(x) = E_0 + E_1 x$. For an rf pseudopotential of frequency ω, the ions obey the equation of motion $m\ddot{x} + m\omega^2 x + e_c E(x) = 0$, which results in a new secular frequency $\omega_1 = \sqrt{(\omega^2 + e_c E_1/m)}$, and a new cloud center position $x_0 = e_c E_0/(m\omega_1^2)$. By measuring both x_0 and ω_1, E_0 may be determined.

The measurement is done by translating the 422 nm laser in the $\hat{x}$-$\hat{y}$ plane and fitting the fluorescence signal, as measured by the photomultiplier tube, to a Gaussian with center (x_0,y_0). The trap frequency $\omega_{\hat{n},1}$ along each direction $\hat{n}$ is measured by applying a 250 mV oscillating voltage to the electrode labeled V_5. This electrode can stimulate both $\hat{x}$ and $\hat{y}$ motion because electric fields due to voltages on this electrode have components along both directions. Resonant excitation of the ion motion causes dips in the fluorescence at $\omega_{\hat{n},1}$. These measurements are repeated at 10 different rf voltages, and a linear fit of the cloud center positions x_0 and y_0 to $1/\omega_{\hat{x},1}^2$ and $1/\omega_{\hat{y},1}^2$, respectively, gives the stray fields $E_{\hat{x}0}$ and $E_{\hat{y}0}$. The stray field component along $\hat{z}$ is not measured or compensated because, in principle, confinement along this axis is due entirely to dc voltages. Therefore, stray fields along $\hat{z}$ do not lead to micromotion. In practice, there are rf field components along $\hat{z}$, but they are much smaller than those along $\hat{x}$ and $\hat{y}$.

Our experimental results are presented in Fig. 6-9. This composite figure illustrates several results. First, in (a), it shows that the cloud fluorescence intensity closely matches a Gaussian fit, allowing measurement of the cloud center to within ± 0.5 μm. This translates into a precision of electric field measurement of about 10 V/m at zero field. The remainder of this figure shows our measurements of the $\hat{x}$ and $\hat{y}$ electric fields as a function of V_{top}. This enables us to determine the required compensation voltages, $V_{top} = 1.0 \pm 0.1$ V and $V_5 = 1.3 \pm 0.3$ V. Either V_4 or V_5 could be used for compensating $\hat{x}$. It was convenient to use V_5, since V_4 was already used for the secular frequency measurement. The estimated residual displacement of a single ion at these voltages is 0.2 μm. The nonlinear dependence of $E_{\hat{y}}$ on V_{top} is due to the anharmonicity of the trap along $\hat{y}$, unaccounted for in the above simple model.

6.3.3 Discussion

Our measurements demonstrate that the compensation voltages for the trap do not agree well with the prediction of theory. At the theoretical compensation voltages $V_5 = 0$ V and $V_{top} = -24.5$ V, both $E_{\hat{x}}$ and $E_{\hat{y}}$ should be zero. We can determine the stray fields by measuring the actual values of $E_{\hat{x}}$ and $E_{\hat{y}}$ at these settings. At $V_5 = 0$ V and with $E_{\hat{y}} = 0$ (done by setting V_{top} to 1 V), $E_{\hat{x}}$ was measured to be 30 V/m. Unfortunately, the trap was unstable at the ideal V_{top} voltage. Instead of measuring $E_{\hat{y}}$ at this point, we extrapolate from Fig. 6-9, subfigure (c), that $E_{\hat{y}} \approx 2000$ V/m. This is in order-of-magnitude agreement with a parallel plate model, $E_{\hat{y}} = (V_{expt} - V_{ideal} - V_1)/d = 4200$ V/m, where V_{expt} is the measured compensation voltage ($V_{top} = 1.0$ V), V_{ideal} is the ideal compensation value ($V_{top} = -24.5$ V), and d is the distance between the top plate and the trap electrodes ($d = 6.3$ mm). Of course, these results depend on the agreement between our measured and predicted secular frequencies. They agree on a 5-10% level, with greater differences along $\hat{y}$, presumably due to the larger stray fields in that direction. These errors increase the uncertainty in our measurements a bit, but do not change the basic conclusions.

The stray field along $\hat{x}$ is comparable to those reported for 3-D ion traps [BMB+98]. However, that along $\hat{y}$ is on the order of 10 times larger. This suggests significant charging on either the dielectric on the ion trap, the top plate, or the observation window. This is clearly a problem when using PCB ion traps. Indeed, these stray fields all but prevented direct loading at UHV pressures, necessitating the use of the helium buffer gas. This is mainly because the stray field degrades the trap depth, although it also can cause excessive rf heating. This is due to the fact that, in the cloud state, driven micromotion couples to the secular motion. Before compensation, the UHV cloud lifetime was less than 10 s. Following compensation, ion cloud lifetimes of 10 minutes at 10^{-9} torr were observed. This pressure was limited by residual buffer-gas pressure. As stated above, Rogers 4350B is a UHV-compatible material after bakeout. Subsequent PCB traps in vacuum have attained pressures in the 10^{-11} torr range.

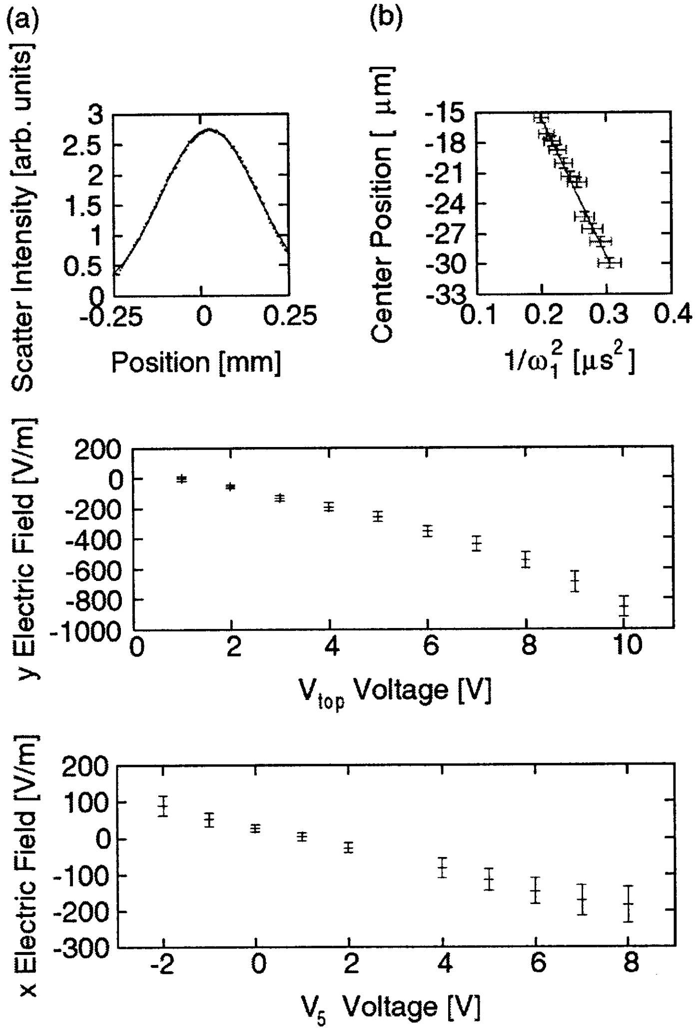

Figure 6-9: Measurement results showing compensation of micromotion in the trap at a helium buffer gas pressure of 1.0×10^{-5} torr. (a) Cloud intensity profile along the $\hat{y}$ axis, fit to a Gaussian, for a representative value of the $\hat{y}$ compensation voltage V_{top}. (b) Linear fit of the cloud center position y_0 versus $1/\omega_{\hat{y},1}^2$. Measurements in (a) and (b) permit measurement of the electric field $E_{\hat{y}}$ for a specific value of V_{top}. (c) Plot of the $\hat{y}$ electric field as a function of the V_{top} voltage, showing that the stray field is minimized at $V_{top} = 1.0$ V. (d) Plot of the $\hat{x}$ electric field as a function of the middle electrode voltage V_5, showing compensation at $V_5 = 1.3$ V.

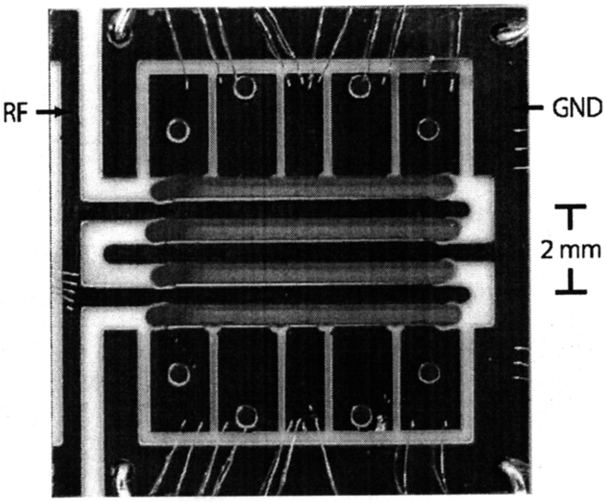

Figure 6-10: Photograph of the surface-electrode PCB trap, known as "Bastille," used for ablation loading experiments. The rf electrodes are spaced by 2 mm center to center, leading to an ion height above the surface of 0.8 mm, as predicted by numerical modeling. The long center electrode is held at rf ground, but may have a dc offset applied to it. The segmented electrodes on the sides carry dc potentials for confinement along the long axis of the trap, as well as elimination of stray electric fields. The wirebonds visible on the edge of the electrodes connect them to gold pads on the CPGA chip carrier.

To summarize this section, a PCB ion trap was loaded with the aid of buffer gas using electron impact ionization. The buffer gas allows sufficient ion signal and lifetimes to perform compensation measurements before loading in UHV with reasonable lifetimes ($\mathcal{O}$(minutes)) is achieved. There are two primary lessons from this work: the first is that exposure to dielectric must be minimized to limit the surface area that can trap charges that act on the ions; the second is that methods for loading ions must be found that lead to less accumulation of charge. Buffer-gas loading was a useful expedient in this work, but is not ideal as a long-term solution, since it results in a much higher UHV pressure than is possible without it.

We therefore turn to a different ion trap setup and study ablation loading of surface-electrode traps.

6.4 The second-generation PCB ion trap

Follwing successful trapping in San Quentin, we produced a new surface-electrode PCB trap. This trap, known as "Bastille," has become a real "workhorse" to us, since it traps so reliably that it may be used first in a new apparatus to verify that everything else is working before a new trap is tested. In this section we present the design of this trap, a photograph of which is shown in Fig. 6-10.

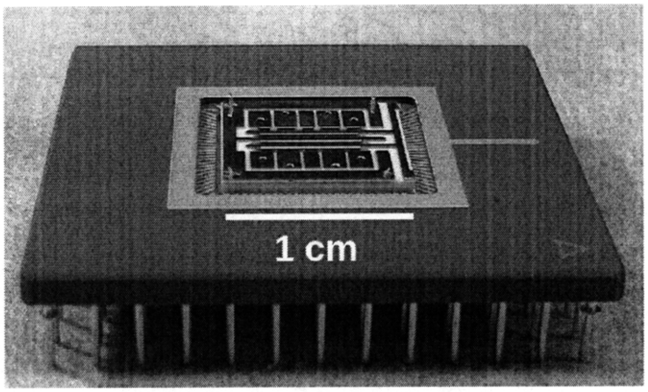

Figure 6-11: Bastille mounted in the CPGA.

The noteworthy features of this trap compared to San Quentin are as follows. The gaps between rf and dc electrodes are 0.5 mm, compared to 0.83 mm. This is the minimum width machinable by our manufacturer, Hughes Circuits. The ground electrode extends all the way around the segmented dc electrodes. This can help prevent neutral atom flux from the oven from shorting the dc electrodes together; atoms primarily come from the side ($\hat{x}$ direction), but with this feature, only atoms with a velocity component along the $\hat{y}$ direction can cause shorting. Aside from that, the whole trap is somewhat smaller in scale.

The trap is polished using a process similar to that of San Quentin, but the mounting process is quite different. The trap is mounted in a ceramic pin grid array (CPGA) chip carrier, like that used in Ch. 5. The trap is held above the center gold pad of the CPGA by 1 mm thick glass slides; UHV-compatible epoxy (EpoTek 353ND) holds it together. Wirebonds connect the trap electrodes to gold pads on the CPGA, which connect to pins on the underside of the chip carrier. These fit in a socket that connects to the electrical feedthrough. A photograph of the trap mounted in the CPGA is given in Fig. 6-11.

6.5 Ablation loading of planar PCB ion traps

In this section we present our work on loading ion traps using laser ablation. Ablation is a process in which a high-energy pulsed laser is used to eject high-energy material, including neutral atoms, ions, electrons, and molecules, from the surface of a solid. It has found wide usage in the physical chemistry community for producing molecules to be studied with laser spectroscopy or mass spectrometry [Phi07], and has had some limited usage in the ion trapping community.

Laser ablation of a solid target has been used to load ion traps as early as 1981 [KGF$^+$90]. In contrast to other methods of loading ion traps, atoms are not ionized once already inside the trap region. Instead, a pulse of high-energy electrons from the ablation plume reaches the trap first, shorting it out for a time of $\mathcal{O}(10\,\mu\text{s})$. While the trapping potentials are thus

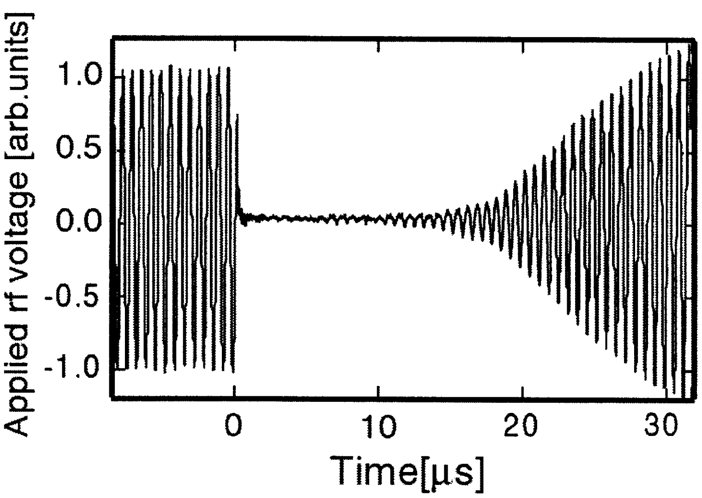

Figure 6-12: Measured pickup from the rf electrode during laser ablation. The rf begins recovering after about 15 μs, and during this time ions are trapped. Figure reproduced from Ref. [HMO$^+$06].

lowered, some ions enter the trap, which returns to full strength with some ions already inside it. This was first observed by Hashimoto *et al.* [HMO$^+$06], and the relevant plot from that paper is presented in Fig. 6-12. The loading of ions into a conservative trap potential requires a nonconservative step; normally, it is the conversion of neutral atoms into ions within the trap, but with ablation loading it is an induced time-dependence of the trapping potentials themselves. We note also that lower-energy ablation pulses have been used in lieu of an oven to produce neutral atoms that are then photoionized within the trap [HGH$^+$07].

Laser ablation has a number of possible advantages. For one, it requires only a single laser, and the process is not sensitive to its frequency. For instance, if one wished to load simultaneously atomic and molecular ions, an ablation pulse (or set of synchronized ablation pulses) might do the trick. As with e-gun loading, however, the lack of isotopic selection could potentially lead to unwanted trapped species. Second, it is very fast: carefully-calibrated ablation loading could thus be very useful for loading the many ions needed in a scalable quantum simulator. If an ion was lost during a simulation, one could envision a classical subroutine that pauses execution of the algorithm and then reloads an ion in the correct spot using a single ablation pulse. The ion could be trapped and re-cooled in much less than one second. Third, ablation loading does not create a large heat load. In a cryogenic environment, the heat generated by a resistive oven could be conducted to the trap electrodes, increasing decoherence rates. In our later work, we solve this problem by placing the oven in contact with the 40 K radiation shield, which has enough cooling power to handle the heat load. In the future, however, it may be advantageous to have very site-specific loading, as in the scenario described above. In this case, ablation loading may be a superb option.

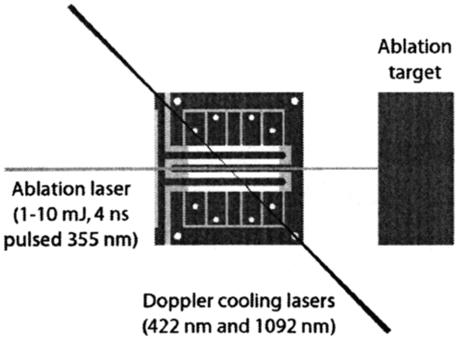

Figure 6-13: A diagram of the setup showing the position and orientation of the ablation target relative to the ion trap. The surface of the ablation target is approximately 25 mm from the trap center and is orthogonal to the direction to the ion trap. Not to scale.

Attractive as laser ablation loading is, there is much that is not well-understood about it, especially on a practical level. This motivates the following research questions:

1. How shallow a trap may be loaded with direct laser ablation, and how does that value compare to other techniques, including electron impact ionization and photoionization?
2. How does the loading efficiency depend upon the composition of the material that is ablated, and upon the ablation laser power?
3. How does the number of ions loaded depend on the ablation laser power?
4. Is the buildup of stray charge an issue when using this method, especially with a surface-electrode trap?

In the remainder of this section we present an experimental study of the ablation loading of ion traps, focusing on our experimental setup and results, with a goal of evaluating the utility of the technique for loading ion traps in view of the above questions.

6.5.1 Experimental setup

The trap is driven with an rf voltage with amplitude 200-600 V at 8 MHz. The dc voltages, not discussed here in detail, are chosen to provide sufficient $\hat{z}$ confinement (with depth at least equal to that in the $\hat{x}$ and $\hat{y}$ directions) and rough compensation. The ablation laser is a frequency-tripled pulsed Nd:YAG laser (Continuum Minilite) at 355 nm. It produces pulses from 1-10 mJ at a duration of 4 ns. The 422 nm and 1092 nm lasers are directed in a direction along the $\hat{z}$ and $\hat{x}$ directions, while the ablation laser is along $\hat{z}$; this is depicted in Fig. 6-13. As in the last section, a CCD camera and PMT are used for ion detection.

The base pressure of the vacuum chamber was 2×10^{-9} torr, but rose to 3×10^{-9} torr when the ablation laser was fired 10 times in 10 seconds. This rise is less than the typical value when one is first using an oven, but somewhat larger than the pressure rise due to an oven after a long period of use.

A number of different ablation targets were tested. These include Sr metal (99% pure random pieces from Sigma-Aldrich), Sr/Al alloy (10% Sr, 90% Al by mass from KB Alloys), single crystal $SrTiO_3$ ($\langle 100\rangle$ crystal orientation from Sigma-Aldrich), and $SrTiO_3$ powder in an epoxy resin (5 μm $SrTiO_3$ powder from Sigma-Aldrich mixed with Loctite 5 min epoxy). Of all the targets only Sr metal oxidizes in air, so although it's the most obvious choice of material, it may not be best. Results obtained with each of these targets are presented below.

6.5.2 Experimental results

We now present data to answer each of the above research questions. We begin with studying the effects of the composition of the target material. The goal is to measure both the efficiency of the loading process and the number of times a single spot on the target may be ablated before the efficiency begins to decrease. This is known to happen due to a profile being formed in the material that modifies the ablation process [CH94]. This process is not a fundamental limitation, however, since the spot being ablated can be varied from shot to shot.

We study this question by ablating a given spot on each target a number of times, and measuring the ion signal in each load. Since the electrons that short the trap during ablation remove the ions already in the trap, we measure after each shot only the number of ions loaded during that shot. We find that there is some variance in the number of ions loaded per pulse, which is not ideal. More is said on this later. The data for each target is presented in Fig. 6-14.

In all, we find that the $SrTiO_3$ crystal is the "best" target choice. It produces, overall much more consistent ion numbers than the other targets, and has the longest lifetime, as well. The overall lower number of ions loaded is not a problem, since we are interested mainly in loading small numbers of ions. It is somewhat odd that the ion loads from the alloy peak after around 100 loads, but it is possible that impurities on the surface must be removed before loading efficiency can reach its maximum potential.

Next, we turn to the question of loading into low trap depths. As in all our other traps, the depth is calculated using CPO and the pseudopotential approximation. Here, ions are loaded into the trap at a series of decreasing rf voltages which correspond to decreasing trap depths. We use an ablation laser pulse energy of 1.1 mJ and a spot size of 680 μm for this experiment; these values were chosen to maximize the ion signal at low trap depth. Our results are presented in Fig. 6-15. We found that ions could be loaded into a minimum trap depth of 40 meV, comparable to the shallowest depths loaded with photoionizaton of

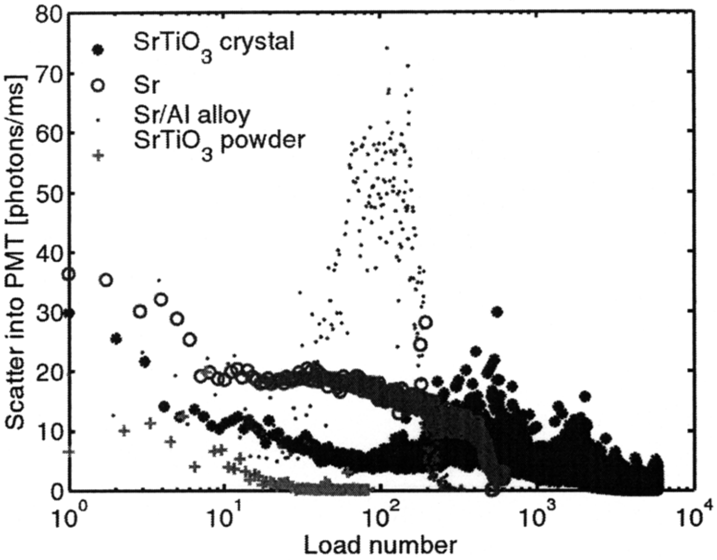

Figure 6-14: A plot of the trapped ion signal as a function of the number of ablation pulses fired on a single spot of each of several targets. Each point represents the signal due to a single ablation pulse of energy 8 mJ. The ablation laser was focused to a spot size of 300 μm for this experiment. For reference, a single ion scatters roughly 0.2 photons/ms into the PMT in this setup.

a thermal atomic beam [SHO$^+$06]. The same trap loaded with electron impact ionization of a thermal beam had a minimum loading depth of 470 meV.

Next, we wish to address the possibility of loading single ions on demand. As stated above, the number of ions loaded per pulse varies greatly. Is it possible to tune the laser power to obtain a single ion at a time? The study of ablation targets in Fig. 6-14 involved loading hundreds of ions per shot. For this experiment, the pulse power was set at 2 mJ and the width of the spot at 0.5 mm. We present in Fig. 6-16 a plot of the probability of loading a certain number of ions with this set of parameters.

The experimental probability distribution fits well to a Poisson distribution with a mean ion number of 0.16. With these parameters, it takes on average seven pulses to load and the probability of loading more than one ion is 8%. This is a satisfactory result, as these ions can simply be removed and the trap reloaded if only one ion is desired. The probability of loading more than two ions could also be lowered by further reducing the pulse intensity.

Finally, we turn to a somewhat more qualitative discussion of the final question above, that is, the buildup of stray charge and other material during the loading process. Indeed, this is an issue that is more unique to surface-electrode traps, compared to macroscopic 3-D traps. Not only can charged material alter the trap potentials, but even additional neutral metal deposited is thought to alter the heating rate of trapped ions by changing the the makeup of the surfaces to which the ions are exposed [DK02, RBKD$^+$02, TKK$^+$99].

After 5000 ablation pulses, we do not see any qualitative change in trap behavior. This

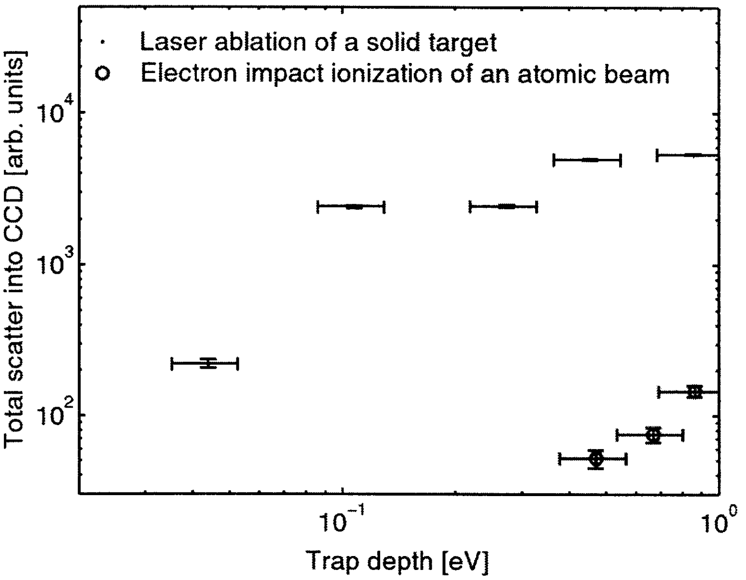

Figure 6-15: A plot of the trapped ion signal as a function of the computed trap depth for both ablation and electron impact ionization loading. An ablation pulse energy of 1.1 mJ was used with a spot size of 680 μm. Each point is the ion signal obtained from a single pulse of the ablation laser or from loading using electron impact ionization until the ion signal stops increasing.

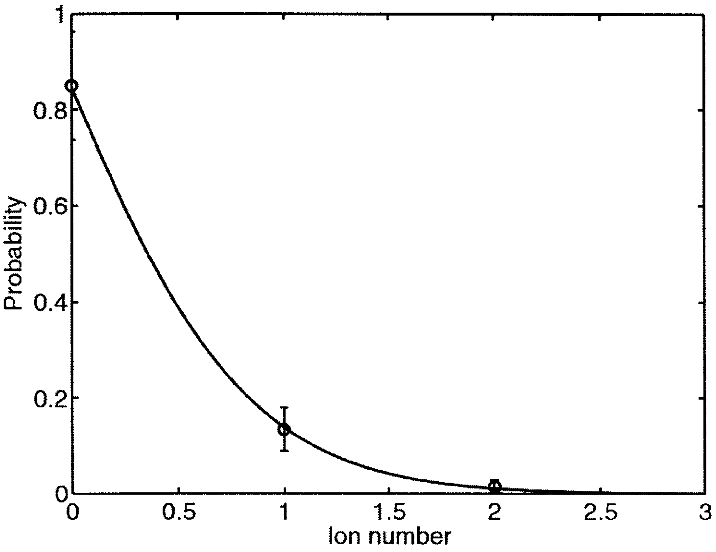

Figure 6-16: Probability distribution for the number of ions loaded with a single ablation laser pulse. The circles are experimental data and the line is a Poisson fit with a mean ion number of 0.16.

allows us to upper-bound the amount of material deposited at one monolayer, as this amount or more would electrically short the trap electrodes and radically alter the pseudopotential. However, the stray fields created by ablation do seem to be on the same order of magnitude as those from electron impact loading (although not at the extreme level seen above with San Quentin). In principle, it should be possible to reduce the amount of charging caused by ablation loading by using ion optics to remove the electrons from from the ablation plume and focus the ions. Alternatively, the approach in Ref. [HGH$^+$07] could be followed, requiring a photoionization laser.

6.6 Conclusions

In this chapter, we have presented the design and testing of printed circuit board ion traps, loaded using both electron impact ionization and ablation loading. We have found that by almost any measure (except cost) the ablation method is to be preferred. However, neither is better for our specific purposes than photoionization loading, and thus we will return to that method in the next chapter.

We also have seen that the stray fields near PCB ion traps can be quite large, up to ten times larger than those that normally exist in 3-D linear ion traps. Fortunately, the buffer gas technique enabled us to load and characterize the San Quentin trap even in the presence of such fields. We found that the e-gun loading method renders the trap particularly susceptible to the accumulation of stray charge.

The traps presented here were surface-electrode versions of linear ion traps, which have application most especially to digital-type quantum simulations. Such traps could form a basis for the CCD-style architectures, which were briefly discussed in Ch. 1. However, if ions are meant to be kept in static positions, or interlinked by photons or electrical currents, it is not strictly necessary for the trap to have this structure. For instance, the trap in Ch. 5 was specifically designed to have a set of ions in a fixed configuration in space. A surface-electrode analogue of the lattice trap of Ch. 5 could in fact be made from PCB technology.

We conclude both that PCB ion traps are suitable for the rapid development of ion trap designs, and that photoionization loading is preferable, as compared to electron impact or ablation, for the investigation of trap designs for analog quantum simulation. These conclusions may be applied to the design, construction, and evaluation of ion trap designs for quantum simulation, a task that is described in Ch. 7.

Chapter 7

Quantum simulation in surface-electrode elliptical ion traps

As discussed at length in this thesis, two-dimensional arrays of trapped ions have great potential for a number of types of quantum simulations, most particularly for the simulation of spin frustration. We report in Ch. 5 that an array of individual microtraps, although appealing for its ability to generate an evenly-spaced array of ions, suffers major drawbacks in the interaction rate between neighboring trapped ions, whether considering motional coupling or the simulated spin-spin interaction rate. This motivates our present study of ion-ion interactions between ions in the same potential well that form a 2-D array through mutual Coulomb repulsion. In this case, the motional coupling rate is on the same order of magnitude as that in a linear ion trap with the same ion-ion spacing.

In this chapter, we explore one example of an trap that creates a 2-D array of ions: a surface-electrode elliptical Paul trap. We choose the Paul trap approach in order to avoid the large Zeeman shifts and crystal rotation associated with Penning traps, as we did in Ch. 5. The surface-electrode geometry, as in Ch. 6, is beneficial for simplicity of microfabrication and eventual scaling down to microscopic sizes, if required. Prior to this work, the only 2-D ion crystal prepared in a Paul trap had been in a linear trap. An added benefit of our elliptical trap approach is the ability, in principle, to apply magnetic field gradients to wires that reside in the plane of the trap electrodes, creating magnetic field gradients that can effect state-dependent forces in a manner similar to that proposed in Ref. [CW08], but with theoretically much stronger interaction rates. This is another advantage of the surface-electrode elliptical trap over other methods for generating a 2-D array of ions in the same potential well.

A sensible objection to this technique is the existence of micromotion that cannot be compensated away and that affects every ion in the trap. The reason for this is that the rf null in such a trap exists only at the center of the trap, which is the minimum of the potential in three dimensions. Thus, only one ion may be confined without excess micromotion. One of the principal questions discussed in this chapter is the effect, in theory, that this micromotion has on an example quantum simulation. The structure of large 2-D crystals, as well as the impact of rf heating and background gas collisions, was discussed in Ref. [BKGH08]. However, the question of micromotion had not previously been adequately addressed.

We also construct and demonstrate a test elliptical trap, to verify a portion of the above theoretical work. Since it is crucial to reduce motional decoherence (anomalous heating) in such a trap, we construct a new closed-cycle cryostat apparatus for the testing of these traps, in order to provide an electrical noise environment in which progress toward quantum simulation can be made. We then test our predictions of the crystal structure and motional frequencies of ions in this trap. We come to the conclusion that quantum simulations with at least a few ions should be possible in this trap.

The chapter is organized as follows. In Sec. 7.1, we introduce the basic model of the elliptical trap, and present calculations of the structure of ion crystals therein. In Sec. 7.2, we discuss the effects of micromotion on the fidelity of a quantum simulation, by numerically simulating the quantum dynamics with a time-dependent potential resulting from the micromotion. The expected coupling rates due to laser pushing forces are also calculated. In Sec. 7.3, we study the origin of the state-dependent forces, looking at optical forces, and also at magnetic field gradients. In Sec. 7.4, we discuss the closed-cycle cryostat apparatus used for testing the elliptical traps. We put our theoretical predictions to the test in Sec. 7.5, measuring the motional frequencies and structure of crystals in the elliptical test trap. Finally, we evaluate the suitability of the elliptical trap design for quantum simulation in Sec. 7.6, and then conclude in Sec. 7.7.

7.1 Elliptical ion trap theory

In this chapter, we explore the idea of using elliptical ion traps to perform quantum simulation in 2-D. Elliptical traps were proposed and demonstrated by DeVoe [DeV98] with the aim of producing a miniature linear ion trap with relatively simple fabrication and fairly favorable amounts of micromotion. Here, we study instead 2-D ion crystals in such a trap.

To obtain an ordered lattice of ions in a single plane, it is desirable to have a trap with approximate cylindrical symmetry. However, in such traps (the ring trap included), the two "radial" vibrational modes are degenerate; hence, there is no preferred axis along which the ion crystal may align. This undesirable condition can be rectified by introducing an asymmetry in these two directions. In such a trap, ions will align in a 2-D array until a critical ion number is reached, at which point the crystal may minimize its energy by transitioning to a 3-D shape. This is the primary motivation for making the trap elliptical.

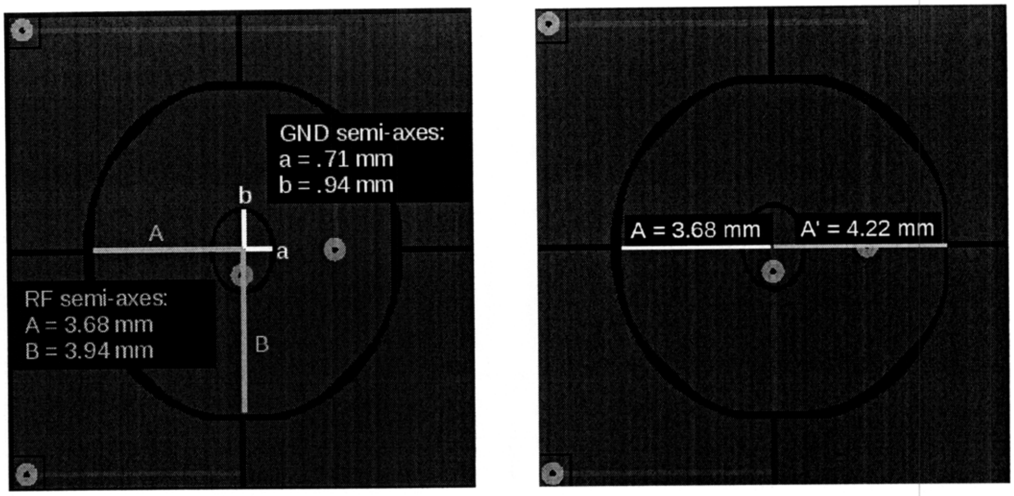

Figure 7-1: Left: Uraniborg 1, as rendered by the EAGLE scripting language. The lengths of the rf semimajor and semiminor axes are shown as dimensions A and B, while the ground semimajor and semiminor axes are shown as a and b. Four dc electrodes surround the rf electrode to provide dc compensation voltages, and the ground ellipse can be controlled as well. A gap of ≈ 0.1 mm is present between all electrodes due to fabrication constraints. Right: Uraniborg 2. The trap is identical to Uraniborg 1, except that the rf semiminor axis is different on the two sides of the ground ellipse.

Our project in this section is to calculate this crystal geometry and transition point for a model trap geometry.

Our model elliptical trap consists of two electrodes in a single plane. There is an elliptical rf ring electrode surrounding a grounded electrode (also elliptical). Four numbers are required to specify the semimajor and semiminor axes of the ground and rf ellipses, but in this model we will assume that the rf ellipse is similar to the ground ellipse, and thus three numbers are used to specify the trap electrodes: the dimensions of the grounded ellipse and a scaling factor that specifies the size of the outer ellipse.

Calculations are presented in this section for the traps that we tested, which are named "Uraniborg."[1] Secular frequencies for traps of a different scale may be estimated by scaling the curvature of the potentials appropriately with the trap size. There are two different elliptical traps presented here; in the first, Uraniborg 1, there is a single semiminor axis length for the rf ellipse, while in the second, Uraniborg 2, one side is made longer than the other in an effort to tilt the vertical principal axis and thereby increase the Doppler cooling efficiency. Diagrams of these traps are presented in Fig. 7-1.

An appropriate rf voltage V_{rf} is applied to the ring electrode, while the center ellipse is grounded. These voltages result in a trap region characterized by secular frequencies $\omega_{\hat{n}}$, where $\omega_{\hat{z}} = \omega_{\hat{x}} + \omega_{\hat{y}}$. This relation should always hold for the elliptical trap, as long as the confinement is due entirely to rf fields. Below we present the calculation of the trap depth

---

[1] After the observatory where Tycho Brahe made his measurements of planetary orbits, enabling Johannes Kepler to discover that the orbits were actually ellipses.

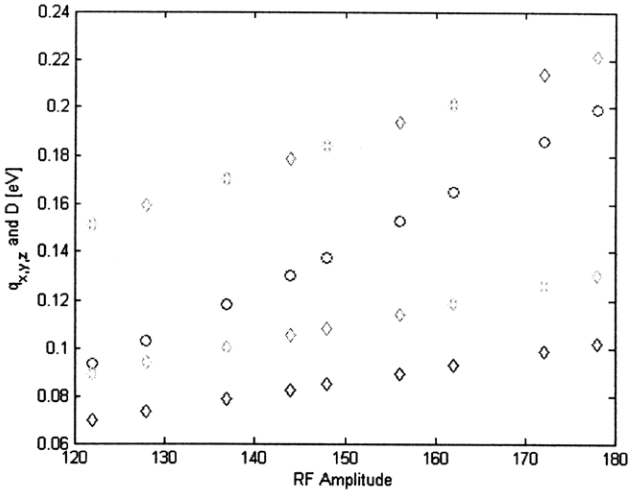

Figure 7-2: Calculated q parameters and trap depths for a series of rf drive voltages and an rf frequency of 3.5 MHz. The q parameters are blue, cyan, and green for x, y, and z respectively, with $q_{\hat{z}} > q_{\hat{x}} > q_{\hat{y}}$. The trap depths are plotted in red and measured in eV. The trap is stable along all three directions and also deep enough to trap for this parameter set.

and secular frequencies, along with the ion crystal structure in the trap.

7.1.1 Secular frequencies and trap depth

The secular frequencies and trap depth are calculated numerically, using the CPO numerical modeling software (as in Chs. 5 and 6), for a given set of trap dimensions and rf signal. We present this calculation here for Uraniborg 2. The trap geometry that was an input to CPO was generated by parametrically drawing the ellipses using a Matlab program. The rf drive frequency was $\Omega/(2\pi) = 3.5$ MHz, which is suitable for a trap of this size. In Fig. 7-2 and Fig. 7-3, we plot the simulation results. In Fig. 7-2, we plot the trap depth and Mathieu q parameters as a function of rf drive voltages, and in Fig. 7-3, we plot the three secular frequencies as a function of the same. All dc voltages were assumed to be zero.

It is only necessary to compute the secular frequencies for a single trap size, since scaling to smaller traps may be done by changing the unit size in the electrostatic computation. We expect that the secular frequencies will scale as $1/r_0$, where r_0 is a characteristic length of the trap. In practice, this quantity is numerically calculated and does not correspond to some specific distance. The height of a single trapped ion above the plane of the electrodes does, however, obey the same scaling law. We plot in Fig. 7-4 the secular frequencies as a function of the ion height. A caveat is that even if the dimensions of the electrodes remain the same, there will be some minimum spacing between electrodes that is given by the fabrication process used. For microfabricated traps, this is typically a few microns. For

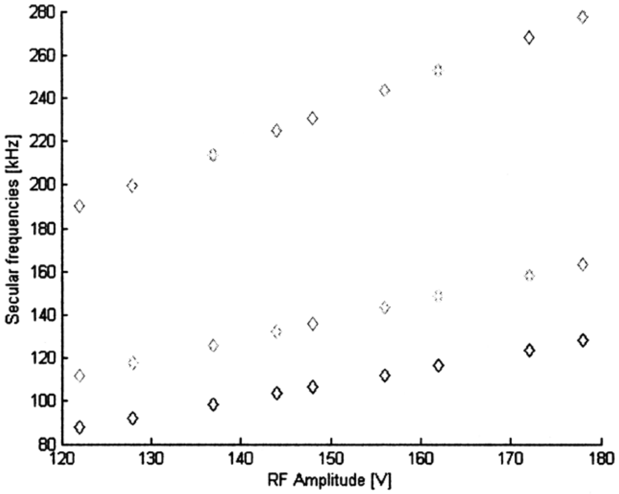

Figure 7-3: Calculated secular frequencies for the trap at 3.5 MHz and a series of rf amplitudes. The frequencies are blue, cyan, and green for x, y, and z respectively, with $\omega_{\hat{z}} > \omega_{\hat{x}} > \omega_{\hat{y}}$

PCB traps, it is on the order of 100 μm.

7.1.2 Ion crystal structure

The structure of ion crystals is computed by numerically minimizing the potential energy of a given number N of trapped ions. We intuitively expect the crystals to align in the $\hat{x}$-$\hat{y}$ plane. As the number of ions increases, the potential energy can be lowered by the ion crystal extending itself along $\hat{z}$. However, we expect that since the vertical confining fields are still roughly twice as strong as the horizontal fields, the extent along $\hat{x}$ and $\hat{y}$ should still be larger than that along $\hat{z}$, so that perhaps the ion crystal will still be approximately planar.

We calculate the ion crystal structure using the Mathematica notebook included in Appendix B. We first check this program against the analytical value for the separation of only two ions, which is simple to compute by balancing the Coulomb and trap forces (see Eq. 7.2). The ions are expected to align along the direction of weakest secular frequency, which is $\hat{y}$. The analytical value for $\omega_{\hat{y}}/(2\pi) = 151$ kHz is 16.12 μm. From the Mathematica code, the value is 16.16 μm. This gives an idea of the inaccuracy level of the numerical calculation; it is quite close to the analytical value.

In the calculations below, we assume the motional frequencies calculated above for V_{rf} = 150 V. We first study the structure of 2-D crystals, and then observe (in theory at least) the expansion of the crystal into the vertical direction as the number of ions is increased. Fig. 7-5 shows the structure of 2-D and 3-D ion crystals for four, seven, and 15 ions. Fig. 7-6 is the same for 30 and 60 ions.

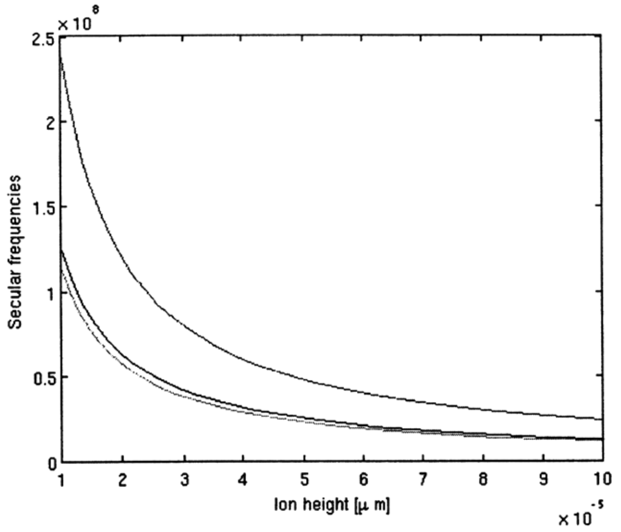

Figure 7-4: Scaling of the three secular frequencies in an elliptical trap as a function of ion height (trap scale). The $1/r_0$ scaling is assumed. Frequencies are angular, in units of 2π s^{-1}. Blue corresponds to $\omega_{\hat{y}}$, green to $\omega_{\hat{x}}$, and red to $\omega_{\hat{z}}$.

We note, with the addition of ions, that the crystal transitions from an almost perfectly 2-D shape to a 3-D shape whose extent along $\hat{z}$ is still considerably less than that along $\hat{x}$ and $\hat{y}$. We would now like to study how the extent into the vertical direction changes with ion number. To impart a sense of this, the order of magnitude of vertical extent of the crystal is plotted vs. ion number in Fig. 7-7.

The results of this calculation are interesting: for small ion numbers, the crystal is almost perfectly planar, in that the extent along $\hat{z}$ is orders of magnitude less than that along $\hat{x}$ and $\hat{y}$, which is essentially zero. At 26 ions, the crystal transitions into a 3-D shape, for which the $\hat{z}$ extent is about a tenth of the others. It alternates between this and the planar shape as additional ions are added, until above 30 ions it remains in the approximately planar 3-D state.

Another important note is that this elliptical trap was made with a higher eccentricity than is probably required for breaking the degeneracy. For testing purposes, we decided to err on the side of caution. With this eccentricity, however, the crystal is less regular than it would be with a higher degree of symmetry. This situation has been studied by authors including those of Ref. [BKGH08]. In fact, it may be possible to create more-regular planar crystals for larger number of ions by increasing the $\hat{z}$ motional frequency through the addition of a dc quadrupole field. In Ref. [BH09], it is noted that the condition for planar crystals in an ion trap is given by the following condition:

$$\frac{\omega_{\hat{z}}^2}{\omega_{\hat{x}}^2} > \left(\frac{70N}{\pi^3}\right)^{1/2}, \tag{7.1}$$

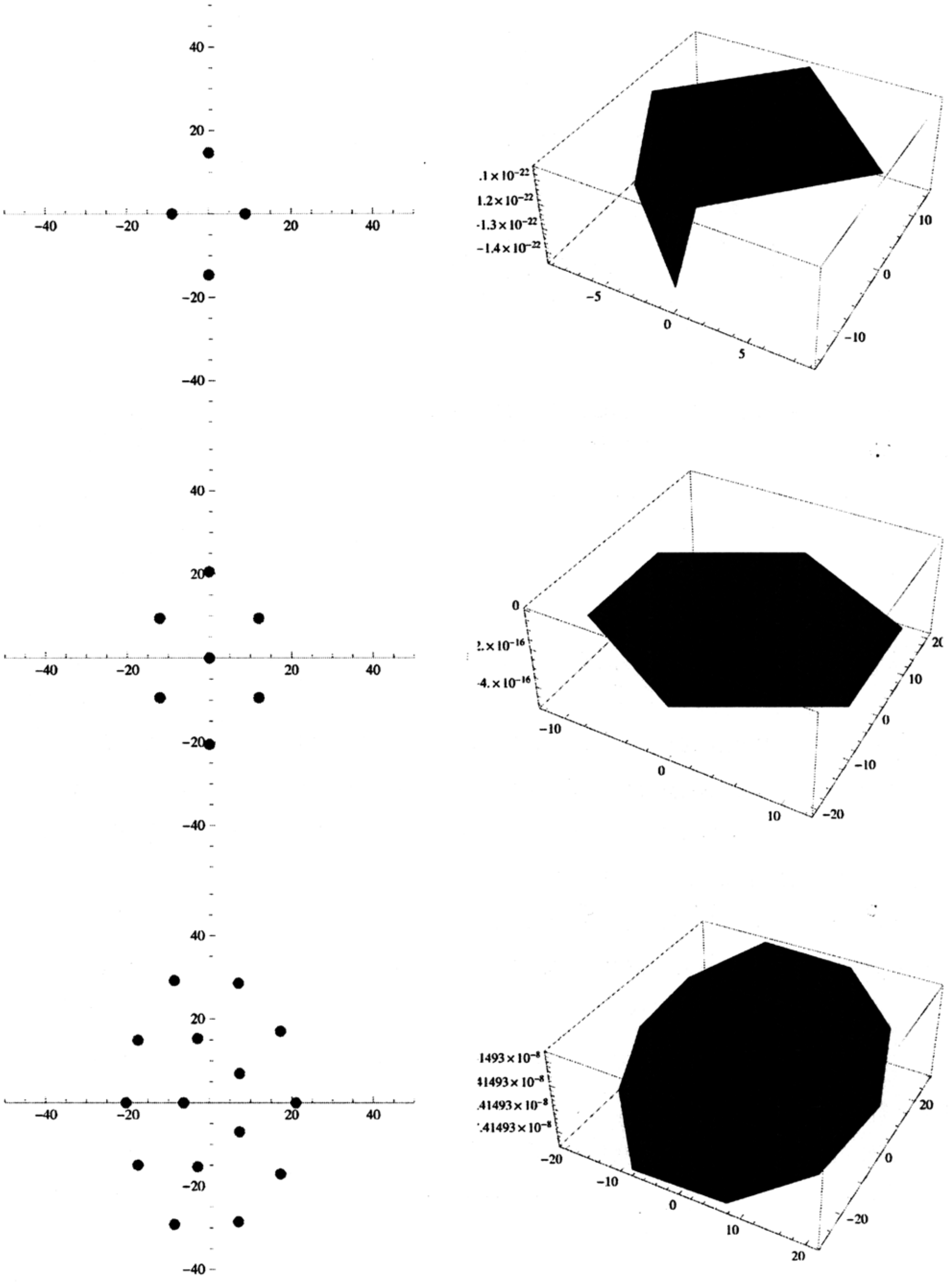

Figure 7-5: Left: Structure of 2-D crystals of four, seven, and 15 ions. Right: 3-D rendering of the ion positions. Trapping parameters are those specified in the text, and axes are in μm.

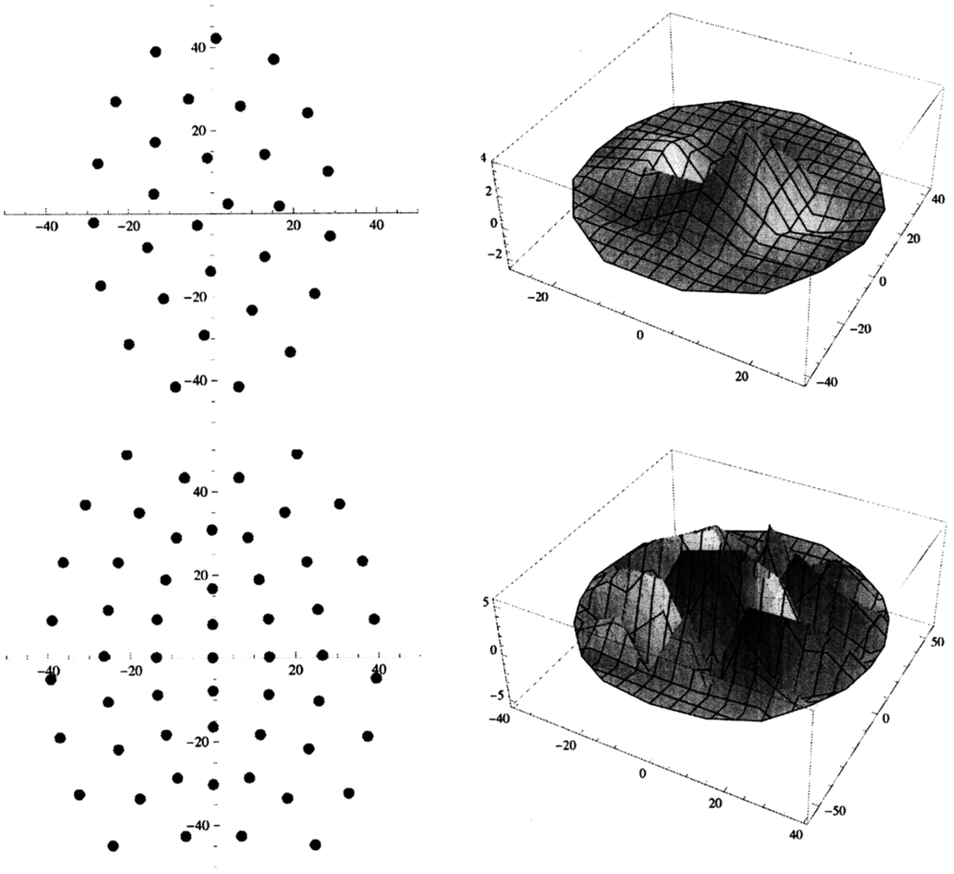

Figure 7-6: Left: 2-D projection of the crystal structure of 30 and 60 ions. Right: 3-D rendering of the positions of 30 and 60 ions. Trapping parameters are those specified in the text, and axes are in μm.

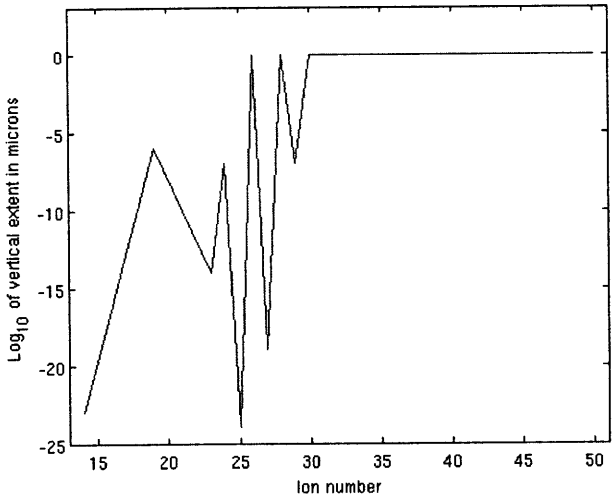

Figure 7-7: Scaling of the order of magnitude of the vertical extent of the ion crystal as a function of the number of ions. Trapping parameters are those specified in the text. A transition from an almost-perfectly planar crystal to an approximately planar crystal is seen.

where $\omega_{\hat{x}} = \omega_{\hat{y}}$ and N is the ion number. The fourth-root dependence on N implies that modest increases in $\omega_{\hat{z}}$ will lead to planar crystals for larger numbers of ions.

As an example, we calculate the crystal structure for 120 ions. According to Eq. 7.1, and for a radial frequency of $\omega_{\hat{x}} = \omega_{\hat{y}} = 2\pi \times 150 \text{ s}^{-1}$, the condition for a planar crystal is $\omega_{\hat{z}} > 2\pi \times 608 \text{ s}^{-1}$. For a frequency of $\omega_{\hat{z}} = 2\pi \times 500 \text{ s}^{-1}$, according to our algorithm, the crystal is planar, while for $\omega_{\hat{z}} > 2\pi \times 608 \text{ s}^{-1}$ it is not. We plot the 2-D projections of the crystal structure in Fig. 7-8. Near the center of the crystal, the ions form a nice regular hexagonal lattice.

While it may be possible to produce the above secular frequencies using a top plate voltage (as in Ch. 6) together with the center electrode, numerical simulations have shown that it is not possible to create such a trapping region using only the electrodes present on the surface-electrode elliptical trap. We calculate that the maximum number of ions for a planar crystal in such a trap is 35, which would still be a very interesting situation for quantum simulation. In addition, it may be possible to implement quantum simulations using ion crystals that are only approximately planar, such as those depicted in Fig. 7-6.

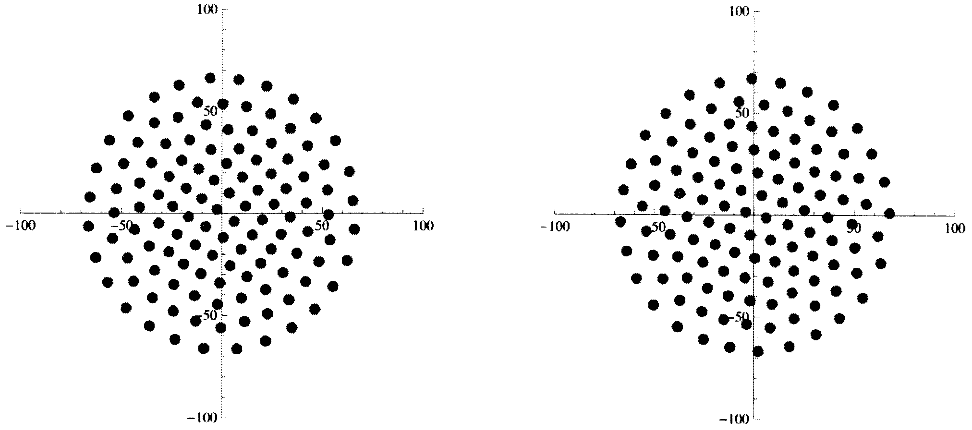

Figure 7-8: Crystal structures for 120 ions with $\omega_{\hat{x}} = \omega_{\hat{y}} = 2\pi \times 150\ \mathrm{s}^{-1}$. Left: 2-D projection of the 3-D ion crystal that results for a vertical frequency of $\omega_z = 2\pi \times 500\ \mathrm{s}^{-1}$. Right: 2-D ion crystal structure for $\omega_{\hat{z}} = 2\pi \times 650\ \mathrm{s}^{-1}$, greater than the critical frequency for crystal planarity (according to Eq. 7.1) of $\omega_{\hat{z}} = 2\pi \times 608\ \mathrm{s}^{-1}$.

7.2 Micromotion scaling and its effect on quantum simulation

7.2.1 Scaling of the micromotion amplitude

We now turn to the calculation of the micromotion amplitude for the ions in the elliptical trap, as well as the effect that it has on quantum simulation. The micromotion amplitude A_μ along $\hat{x}$ is given to first order by $A_\mu = \frac{1}{2} q_{\hat{x}} \Delta x$, where $q_{\hat{x}}$ is the Mathieu parameter along the direction $\hat{x}$ and Δx is the displacement of the ion from the rf null along $\hat{x}$. Similar relations apply for the other directions. Given a numerical solution for the trapping potential along with the ion geometry calculation presented in the last section, we can calculate this numerically as well.

The scaling of the micromotion amplitude for two ions is straightforward. Suppose two ions align along the $\hat{y}$ axis of an elliptical trap. Then, by balancing the Coulomb and trapping forces, the ion-ion distance is

$$d = \left(\frac{e_c^2}{2\pi\epsilon_0 m \omega_{\hat{y}}^2} \right)^{1/3}, \tag{7.2}$$

and the displacement from the rf null is just $\Delta y = d/2$. Since the frequency $\omega_{\hat{y}}$ scales as $1/r_0$, the basic scaling law for micromotion is $A \propto r_0^{2/3}$, therefore it decreases as the overall size of the trap is reduced. This is one motivation for decreasing the overall size of the trap.

The micromotion amplitudes of ions in larger 2-D crystals may be estimated from the ratio of displacements of ions given above in the ion crystal structure calculations. Interactions between neighboring ions are impacted only by the *relative* motion of the ions involved. Because ions near the center of the trap experience oscillating electric fields in opposite directions, their relative motion may be higher than ions further from the trap center, even though each individual ion experiences greater micromotion.

7.2.2 Effect of micromotion on quantum simulations

The calculation of micromotion amplitudes is important, but the much more interesting (and hotly debated) question is what effect this micromotion has on the fidelity of quantum simulation. We now endeavor to answer this question. We will limit our study here to a specific Hamiltonian, the transverse Ising model, which is one example of a Hamiltonian under which spin frustration may occur. In a typical experiment, antiferromagnetism is produced by using the "radial" modes [PC04b], which in the parlance of Porras and Cirac means the modes perpendicular to the line segment that connects the two ions and perpendicular also to the plane of the trap, i.e. the vertical ($\hat{z}$) direction. In this case, the interaction is a short-range dipolar one, with the coupling constant $J \propto 1/d^3$, where d is the ion-ion distance. We are accordingly concerned with short-range, pairwise interactions. Therefore, most of the calculations study the effect of micromotion on two ions.

The question we ask is this: for a given Hamiltonian, simulation time, and set of trap parameters (including micromotion amplitude), what is the fidelity of the quantum simulation as compared to the simulation in the absence of micromotion? We want to study the behavior of the system for a number of cases that we believe to be relevant for future experiments:

- Constant F in space and time.
- F constant in space, but adiabatically ramped up.
- F varying in space, and following constant or adiabatic time dependence.

The approximation that F is constant in space is good if F varies weakly across the region of space occupied by a given ion, which, in the presence of micromotion, may be up to a few hundred nanometers. If a standing-wave optical force is used, then the spatial extent of the ion trajectory is comparable to the gradient of the force, and the spatial dependence must be accounted for.

Methods

The Hamiltonian that we consider is the transverse Ising model. We define the $\hat{z}$, $\hat{x}$, and $\hat{y}$ axes as being the principal axes of the elliptical trap in order of decreasing secular frequency, while Z, X, and Y are the Pauli operators for the ionic internal states along each of these directions. We shall simulate

$$H_{TI} = -\hbar \sum_{i,j=i+1} J_{i,j} Z_i Z_j + \hbar \sum_i B X_i \tag{7.3}$$

using the approach outlined in Sec. 4.2. Noting that we make use of the vertical modes, leading to $\beta_{\hat{z}} \ll 1$, the coupling constant $J_{\hat{z}}$ along $\hat{z}$ is given by

$$\hbar J_{\hat{z}} = \frac{c_{\hat{z}} e_c^2 F_{\hat{z}}^2}{4\pi\epsilon_0 m^2 \omega_{\hat{z}}^4 d^3}, \tag{7.4}$$

where $\omega_{\hat{z}}$ is the trap frequency along $\hat{z}$, $F_{\hat{z}}$ is the component of the state-dependent force along $\hat{z}$, and d is the distance between the ions. In this situation, the constant $c_{\hat{z}} = -2$. The state-dependent force also adds a magnetic field along the $\hat{z}$ direction:

$$\mu_{\hat{\alpha}} B'_{\hat{z}} = \mu_{\hat{\alpha}} B_{\hat{z}} + \frac{4F_{\hat{z}}}{3m\omega_{\hat{z}}^2}, \tag{7.5}$$

The above expressions describe the simulated coupling between two two ions; this is adequate for our purposes since in the $\beta \ll 1$ limit, the interactions are approximately nearest-neighbor. This effective magnetic field is in addition to the transverse magnetic field $B\hat{x}$ that appears (as just B) in Eq. 7.3. Note that within this section, we will now drop the directional superscripts, i.e. $F \equiv F_{\hat{z}}$.

With nonzero micromotion, the ion-ion spacing d is no longer constant in time. This means that the normal mode frequencies ω_n also change in time, and as a consequence, J becomes time dependent. This dependence is apparent by writing

$$d(t) = d\left(1 + 2A_\mu \cos\left(\Omega t + \phi\right)\right) , \tag{7.6}$$

where Ω and ϕ are the rf drive frequency and phase. The micromotion amplitude A_μ given here is relative to the ion-ion distance d. That is, if A is the actual micromotion amplitude, $A_\mu = A/d$. The time dependence of J renders the equations of motion difficult to analytically integrate; therefore, we use numerical methods exclusively.

To begin the simulations, we pick a constant amount of evolution time, equal to approximately $10J$, and pick an initial state. We propagate the system forward in time, adjusting the Hamiltonian at each time step. This requires a time step τ that satisfies $\tau \ll 2\pi/\Omega$. We then measure some expectation value $\langle M(t, A_\mu)\rangle$ at each time step, and compare these values to that which is obtained in the absence of micromotion. The error between the two is calculated simply as the difference between $\langle M(t, A \neq 0)\rangle$ and $\langle M(t, A = 0)\rangle$ Following this, we increase the simulation time. Unless otherwise stated, we choose the initial state $|\Psi_0\rangle = |\uparrow\uparrow\rangle$ (in the z basis) and measure $M = Z_1 + Z_2$. The Matlab codes to do the simulations presented here are included in Appendix A.

Results

Before presenting the numerical results, let us offer an intuitive view of the effect of micromotion on the evolution of the two-ion system. Micromotion is a driven oscillation at the rf drive frequency Ω. This causes the two ions that are undergoing an effective spin-spin interaction to have a time-dependent spacing d, as noted above. Since the J-coupling depends upon d approximately as $J \propto 1/d^3$, the effective J-coupling rapidly oscillates during a simulation. The ions, being driven by the rf, will spend as much time closer to each other as they spend further apart. However, due to the $1/d^3$ dependence of J, the time-averaged interaction rate will be *higher* than it would be if the ions were stationary. We also expect that since $\Omega \gg J$, the varying J due to micromotion may be treated as a value that is time-averaged over many periods of $2\pi/J$. Another way of stating this is that the only term in the Hamiltonian which effects a spin-spin interaction is JZ_1Z_2, and therefore the fastest interaction rate is set by J, even if J oscillates at a frequency Ω.

This picture is confirmed by our numerical simulations. As an example, we compute the evolution of the initial state $|\uparrow\uparrow\rangle$ under the Hamiltonian written in Eq. 7.3. The parameters for this calculation are $J = -10^3$ s^{-1}, $\Omega = 10^6$ s^{-1}, and B = -J. The relative micromotion amplitude was assumed to be $A_\mu = 0.1$, a sensible value for many experiments. We numerically integrate the equations of motion for the two-spin state both with and without micromotion, and calculate the time-dependent error as the difference between the $A_\mu = 0$ and $A_\mu = 0.1$ time-dependent expectation values for the observable $Z_1 + Z_2$. We find that over a time of several periods of J, the error quickly grows to a maximum value of 0.5, to be compared to the maximum possible expectation value of 2.[2] This result is plotted in Fig. 7-9.

This calculation permits us to calculate the time-averaged J-coupling constant if the ions are undergoing micromotion; for the above parameters, this is equal to $J_{av} = 1.036 \times 10^3$ s^{-1}. As expected, this value is slightly higher than the J for $A_\mu = 0$. When the simulation is performed with $A_\mu = 0.1$ and the calculated value for J_{av}, the error falls strikingly, by about three orders of magnitude. This result is also presented in Fig. 7-9.

Although the intuitive picture of the effects of micromotion is confirmed, at least in theory, there are important further questions. Generally, one may wish to prepare an arbitrary state of the two ions, then apply the simulated interaction. In addition, position dependence of the state-dependent force will also alter J_{av}; we must show that a similar averaging technique works in this case as well. Further, the applied potentials may have time-dependence, for example in the event that one wished to adiabatically apply a spin-spin interaction in order to observe a phase transition.

We now treat each of these situations in turn, beginning with the operations on arbitrary states. We note that in practice the two-qubit states used will not be truly arbitrary,

---

[2] This scale is arbitrary; to convert into actual angular momentum values for spin-1/2 particles, multiplication by $\hbar/2$ is required.

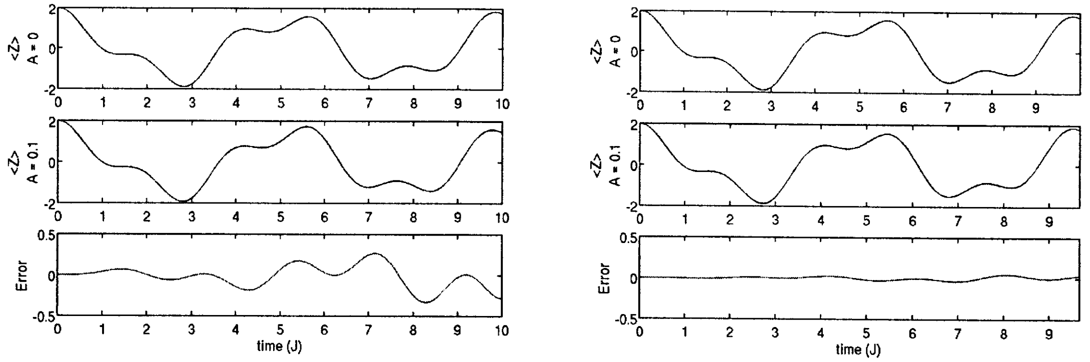

Figure 7-9: Calculation results for a simulated Ising model for two ion-qubits with a spatially and temporally constant force. Left: The trajectory of the observable $\langle Z \rangle \equiv \langle Z_1 + Z_2 \rangle$ as a function of time in the absence of micromotion is plotted on top. Below this, the trajectory with a micromotion amplitude of $A_\mu = 0.1$ is plotted. The difference between the two is plotted on the bottom. Without micromotion, $J = 10^3$ s^{-1}. Right: The same plots as on the left, but with the correct average value $J_{av} = 1.0305 \times 10^3$ s^{-1} used for the $A_\mu = 0$ case. When this is done, the error drops by three orders of magnitude.

but will consist of the tensor product of two arbitrary single-qubit states. Entanglement between the qubits will not form until after the application of the J-coupling, but the set of arbitrary two-qubit states states subsumes this special case. We follow the above approach, but with random, complex amplitudes for each basis state (normalized to 1). We find that for random states, the error is reduced using the same average coupling as before ($J_{av} = 1.036 \times 10^3$ s^{-1}). The average error during the course of each simulation, regardless of the initial state, is 1.42×10^{-5}.

The effects of a position-dependent force, i.e. $F(x)$, may be considered by applying a linear gradient at the position of each ion. The maximal gradient likely to occur in an experiment is that due to an optical standing wave. We take, for the sake of argument, 400 nm to be the lower-wavelength limit of such a wave. In considering the most extreme cases, we will also assume a maximum relative micromotion amplitude of $A_\mu = 0.1$. The reason for this is as follows. Suppose that two ions are on opposite sides of the rf null; then their displacement from the rf null is equal to $d/2$, and the micromotion amplitude of each is $A = \frac{q}{2}\Delta x = \frac{q}{2}\frac{d}{2}$, yielding $A_\mu \approx 0.08$ for $q = 0.3$.

We proceed by computing the J_{av} for a set of force gradients, then confirming that the error indeed vanishes. A set of gradients F_r from 0 to 1, relative to the micromotion amplitude, as used. This means that for $F_r = 0$, the force is constant in space, while for $F_r = 1$, the force falls to zero when the ion is located at the position $x = A$. As expected, the uncorrected error due to micromotion rises as the force is allowed to vary in space, but nevertheless these errors may be corrected by using J_{av} rather than J, and are quenched by three orders of magnitude. Fig. 7-10 contains plots of J_{av} and the uncorrected error as a function of the relative force gradient.

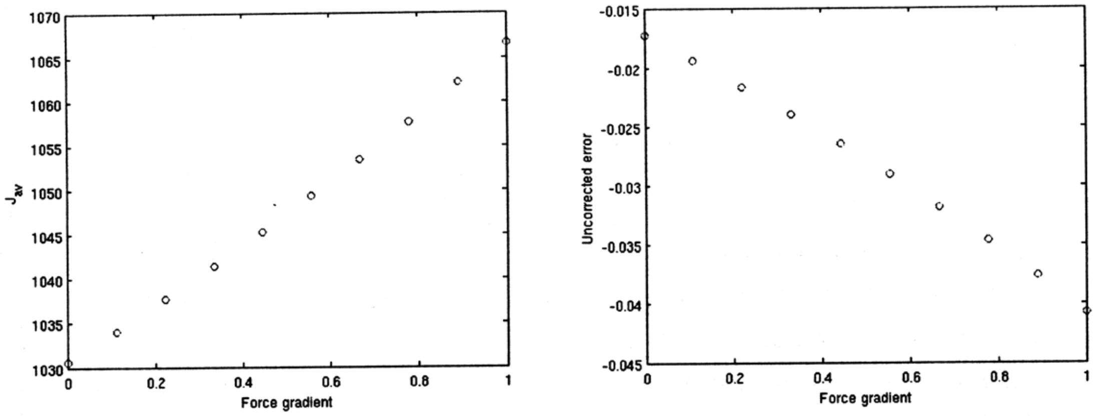

Figure 7-10: Calculation results for a simulated Ising model for two ion-qubits with a position-dependent force. Left: The time-averaged coupling J_{av} as a function of the relative force gradient as defined in the text. Without micromotion, $J = 10^3$ s^{-1}. Right: The average uncorrected error as a function of the relative force gradient. When using the correct average value J_{av}, the error drops by three orders of magnitude.

The final problem we treat in this section is the calculation of the simulation error when the applied force $F(t)$ is time-dependent. We use a linear variation in time of the force F, rising from 0 at $t = 0$ to F at the final time ($t = 10/J$). In this case, we evaluate the time-averaged force for both the $A_\mu = 0$ and $A_\mu = 0.1$ cases, and then multiply the $A_\mu = 0.1$ value by the ratio between the two. This is demonstrated numerically to dramatically reduce the error. Fig. 7-11 plots these results.

Discussion

For a number of important cases, it has been shown that the effect of micromotion is to systematically shift the J-coupling rate under which the internal states of two ions evolve. This is an interesting result, but it raises questions about how a simulation might actually be put into practice with a 2-D array of ions. There are two cases that will be relevant: "global" forces that impact each ion equally, and "local" forces which may be applied pairwise between ions.

In the latter case, the effects of micromotion may be nulled by adjusting the state-dependent force according to the site in the array being addressed. Although this requires a substantial amount of control, there is no fundamental reason why it could not work. In the former case, one will find a "spread" of J_{av} values across the ion crystal. Although this will reduce the fidelity of the simulation, it may still be possible to observe interesting quantum phases.

We would also like to note that there are important cases that have not been addressed in this work. We believe that the examples presented here, however, shed light on the cases that are still unaddressed. Three such cases are a "hard pulse," in which $F = 0$ for some time,

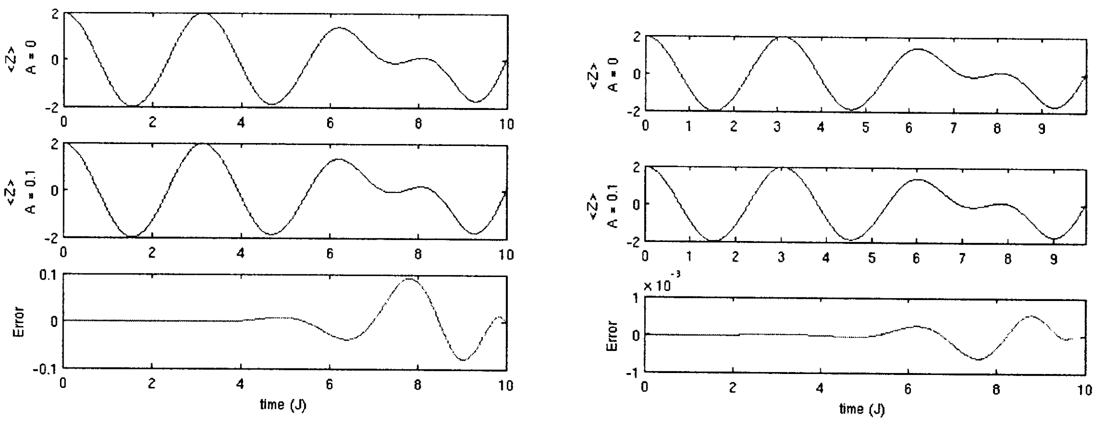

Figure 7-11: Calculation results for a simulated Ising model for two ion-qubits with a time-dependent force. Left: The $A_\mu = 0$ (top) and $A_\mu = 0.1$ (center) plots show significant deviations in the measured expectation value as the state-dependent force becomes large late in the simulation. Right: The error in the simulation is virtually removed by multiplying J for the $A_\mu = 0.1$ case by the ratio of average J couplings for the $A_\mu = 0$ and $A_\mu = 0.1$ cases.

then $F \neq 0$ for some time, and then $F = 0$ again; a nonlinear time dependence of F; and a nonlinear spatial gradient. With respect to the first, we note that our current simulations already treat a hard pulse. They begin with a random state (that could well be considered to be the result of evolution with $F = 0$), and then evolve under the Hamiltonian with $F \neq 0$. After this, F could be set again to zero and the states freely evolve until measured. In the second case, we note that any smooth and continuous force F may be approximated by a number of linear segments; for each segment then, an appropriate effective J could be applied. For the third case, we again invoke the idea that for small displacements, any force function may be approximated as a series of linear gradients, and the appropriate J_{av} calculated and applied. Therefore, it appears that for two ions, the effects of micromotion may be nulled for a great number of cases, provided sufficient control is available.

In this section, we have focused on the effect of micromotion on the spin-spin evolution under which the internal states of ions evolve. However, this is not the only effect of micromotion. The most notable other effect is the broadening of the spectral lines through the Doppler effect, which increases the Doppler cooling limit. Therefore, even when effective controls are present to implement the correct J_{av} values, it is still desirable to minimize the micromotion amplitudes. One way in which this can be done is by reducing the overall dimensions of the trap; recalling the relation $A = \frac{1}{2}q\Delta x$, the micromotion amplitude A may be reduced by keeping q constant and decreasing the ions' displacement from the rf null Δx. In contrast to methods based on 3-D linear ion traps, the surface electrode trap is amenable to microfabrication.

7.3 Magnetic gradient forces

Now that we have seen that in many cases quantum simulations may be performed in an elliptical trap (or other trap with nonzero micromotion), we are ready to discuss the actual source of the state-dependent forces F. Optical forces have been discussed at length in Ref. [PC04b], and in the thesis of Ziliang Lin [Lin08]. We focus in this section, rather, on fields of a magnetic origin. This has been treated in Ref. [CW08], but for the case of an array of microtraps, similar to the trap design studied in Ch. 5. The weakness of interactions between ions contained in different trapping regions motivates our work here on ions in the same trap. Two questions drive this work:

1. What types of forces may be created using wires in the ground plane of the elliptical trap?
2. How does the magnitude of this force and the magnitude of the J coupling rate scale with the trap size?

A state-dependent force based on magnetic fields requires a field gradient in space, giving rise to a force $\vec{F} = -\nabla(\vec{m} \cdot \vec{B})$, where $\vec{m}$ is the magnetic moment of the atom. For the present work, we will consider the Zeeman-split sublevels of the ground S state in a $^{40}\text{Ca}^+$ or $^{88}\text{Sr}^+$-like ion. The absolute value of the magnetic moment is then $m = g_J \mu_B m_J$, where μ_B is the Bohr magneton and m_J is the magnetic quantum number for the projection on the $\hat{z}$ axis of the total angular momentum J. This choice is made to facilitate straightforward estimates for the types of ions discussed in this thesis, and indeed, coherence times of several seconds have been observed for such qubits encoded in decoherence-free subspaces [HSKH+05]. However, hyperfine levels may prove to be a better choice because of their excellent coherence times even without such encoding.

The state-dependent force thus depends on the alignment of the atom's magnetic moment in space, which follows the orientation of the local magnetic field. This force, for example along direction $\hat{y}$, is given by

$$F_{\hat{y}} = g_J \mu_B \left(m_{\hat{x}} \frac{\partial B_{\hat{x}}}{\partial y} + m_{\hat{y}} \frac{\partial B_{\hat{y}}}{\partial y} + m_{\hat{z}} \frac{\partial B_{\hat{z}}}{\partial y} \right). \tag{7.7}$$

7.3.1 Calculation of the gradients and interaction strengths

The calculation of the fields and field gradients can be done by direct numerical integration of the applied surface currents. Methods used are similar to those employed by Wang *et al.* [WLG+09] in their design of magnetic gradients for individual ion addressing. We assume that the wires are infinitesimally narrow; this becomes less accurate as the trap scale is decreased, and more sophisticated methods must be employed. Also, we limit the current through a given wire to 1 A, comparable to the maximal currents employed in neutral atom traps [HHHR01]. The fact that eventually, to reduce heating rates, these traps will need to

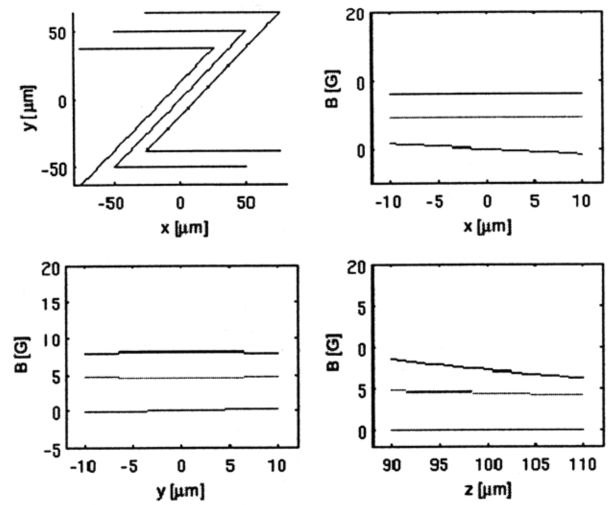

Figure 7-12: The triple-Z wire configuration and resulting magnetic fields. The wire configuration is top left; each wire carries 1A of current in the same direction. Each other the other plots gives the magnetic field components along a given direction. In all figures, $B_{\hat{x}}$ is in blue, $B_{\hat{y}}$ is in green, and $B_{\hat{z}}$ is in red. Note that the field gradients are quite constant across the volume occupied by the ions. Nonzero fields at the trap center must be cancelled by additional pairs of Helmholtz coils to avoid unwanted Zeeman shifts, electron alignments, and even ion crystal rotation.

be operated at cryogenic temperatures suggests that superconducting wires could be used, mitigating resistive heating [REL$^+$08].

We focus on two different wire configurations to give a flavor of the possibilities for simulated Hamiltonians. The first is a "Z" shape, the classic shape of the gradients coils used in chip-based atom traps. This shape is repeated three times, in order to further strengthen the field gradients. The second configuration is a set of three concentric square rings, that produce a different set of gradients.

Results from the Z shape are given in Fig. 7-12. These are based on an elliptical trap that gives an ion height of 100 μm. We see that the gradient is of the approximate form $\frac{\partial \vec{B}}{\partial x_i} = \frac{\partial B_{\hat{z}}}{\partial x}\hat{z} + \frac{\partial B_{\hat{z}}}{\partial y}\hat{y} + \frac{\partial B_{\hat{x}}}{\partial z}\hat{z} + \frac{\partial B_{\hat{y}}}{\partial z}\hat{z}$. Depending on the projection of the atomic dipole, as set by the external bias fields, this yields the possibility of an Ising of Heisenberg interaction. The specific interaction induced depends upon the direction along which F acts.

We now wish to calculate the actual interaction strengths and how they scale with the trap size. What do we expect? First, we recall from Ch. 5 that for constant trap depth the secular frequencies scale as $1/r_0$, where r_0 is some characteristic length scale of the trap (usually defined as the distance from the ion to the rf electrode). At the same time, the distance between ions d is given by $d^3 = e_c^2/(4\pi\epsilon_0 m\omega^2)$, as calculated by balancing the Coulomb and trapping forces. The magnetic field strengths scale as $1/r_0^2$, and plugging that all into the formula for J ($J \propto F^2/(\omega^4 d^3)$), we expect that J will scale as $1/r_0^2$.

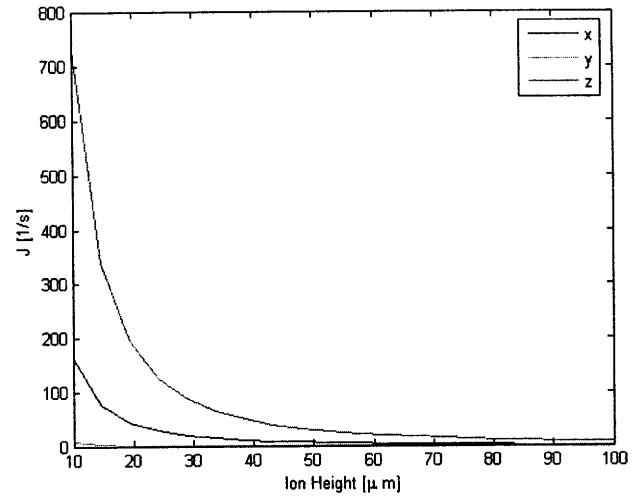

Figure 7-13: Scaling of the J-coupling rates for all three directions as a function of the ion height in an elliptical trap, for the three concentric square rings wire configuration. The value for each direction will only hold if the projection of the electron spin is entirely along that direction; this would give an Ising-type interaction.

Numerically, this is nicely verified. We apply the above scaling law to the secular frequencies, compute the mean ion-ion distance, and calculate the J coupling as a function of h, the height of the ion above the trap surface (calculation with respect to r_0 would yield the same scaling). The highest coupling rate plotted here is 700 s^{-1}, which will be observable if the dominant decoherence rates are significantly lower than that.

By contrast, the fields due to the rings produce a field gradient at the location of the ions with the form $\frac{\partial \vec{B}}{\partial x_i} = \frac{\partial B_{\hat{x}}}{\partial x}\hat{x} + \frac{\partial B_{\hat{y}}}{\partial y}\hat{y} + \frac{\partial B_{\hat{z}}}{\partial z}\hat{z}$. We expect basically the same scaling law for the rings as for the triple-Z, due to the above arguments. However, the total interaction rates are different (and higher, overall). This is plotted in Fig. 7-15.

7.3.2 Discussion

The above results are but a small sample of the interactions that may be created with magnetic field gradients. Indeed, one appealing thing about this approach is the sheer variety of forces that may be created. The source of this freedom is the fact that the wires that create the gradients are separated from the source of the trapping potentials. Thus, the tight integration of wires and trapping electrodes proposed in Ref. [CW08] is not required. However, this greater flexibility in the global potentials does not come without a cost; individually switching interactions between individual pairs of ions is not possible.

The methods presented in the section will apply the same state-dependent force to every ion in a 2-D crystal in an elliptical trap. These translate into Ising or Heisenberg Hamiltonians, depending on the experimenter's choice. There remain two major questions:

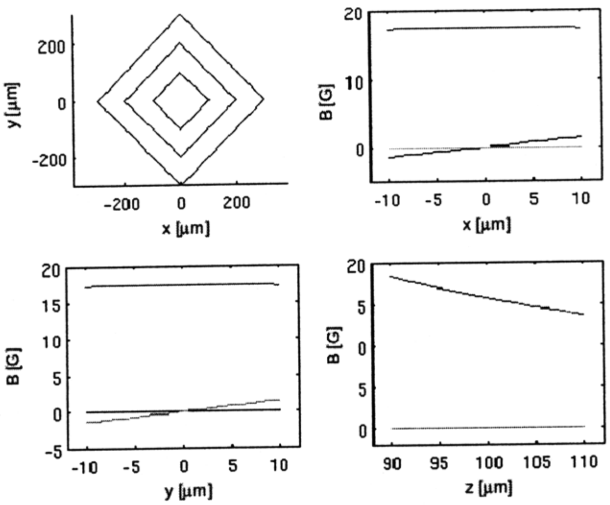

Figure 7-14: The concentric rings wire configuration and resulting magnetic fields. The wire configuration is top left; each wire carries 1A of current in the same direction. Each other the other plots gives the magnetic field components along a given direction. In all figures, $B_{\hat{x}}$ is in blue, $B_{\hat{y}}$ is in green, and $B_{\hat{z}}s$ is in red. Note that the field gradients are quite constant across the volume occupied by the ions. Nonzero fields at the trap center must be cancelled by additional pairs of Helmholtz coils to avoid unwanted Zeeman shifts, electron alignments, and even ion crystal rotation.

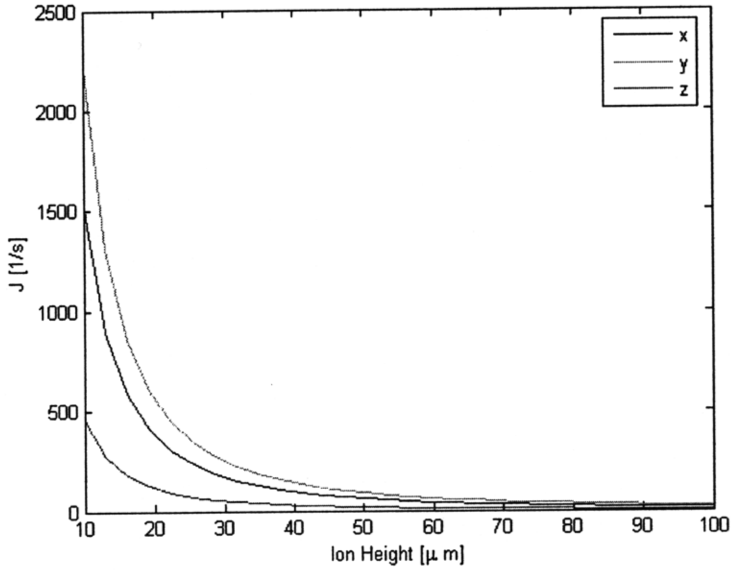

Figure 7-15: Scaling of the J-coupling rates for all three directions as a function of the ion height in an elliptical trap, for the three concentric square rings wire configuration. The value for each direction will only hold if the projection of the electron spin is entirely along that direction; this would give an Ising-type interaction.

how are single-ion operations to be applied, and what is the effect of the unequal ion-ion distance in a crystal containing more than two ions?

There exist a number of ways of implementing single-ion operations. The first is simply to address the ions with a tightly-focused laser. This seems impractical, however, for the surface-electrode elliptical trap, since the laser would need to be aimed directly toward the ground electrode. Although it could be applied at an angle, it is unlikely that scatter off this electrode would not interfere with the states of neighboring ions. A much more appealing idea would be to do the addressing using rf or microwaves, tuned to the Zeeman or hyperfine transition being used. The gradient wires used for implementing the state-dependent force could be turned on to produce a small gradient that can be used for discriminating the transitions of the individual ions in frequency space. This approach has been successfully pioneered by our group with laser addressing of ions [WLG$^+$09], and has been demonstrated by the Wunderlich group with hyperfine qubits [JBT$^+$08].

With respect to the unequal ion-ion spacing, we make a few points. The first is that despite coupling rates that are not perfectly constant across all ion pairs, there is nevertheless the possibility of observing interesting physics such as phase transitions. For instance, the transition from a paramagnetic to an antiferromagnetic state is caused by competition between a static magnetic field and the ion-ion interaction. A J-coupling rate that varies in space would add to the uncertainty in measuring the transition point, but this might still be a useful measurement. The second point is that optical potentials could be used to regulate the position of ions, as was suggested in Ref. [PC04b]. Furthermore, initial trapping of ions in an elliptical trap could facilitate loading into a fully optical potential, as discussed in Ref. [SRM$^+$08]. In the case of an elliptical trap, additional state-dependent forces may be added by the magnetic gradient coils, in addition to any forces already present from the optical potential. Finally, we note that the same level of control required to compensate for the effects of micromotion could be used to compensate for the unequal ion-ion spacing: if one can compensate for one effect, then one can compensate for the other.

A final note of caution is that the ultimate number of wires, their geometry, and their width is limited by the minimum feature size of the fabrication process used. This will in turn limit the minimum size of the trap and gradient wire structure, limiting the interaction rates achievable.

7.4 The cryostat and vacuum apparatus

Given the need for reducing heating rates, and the desirability of rapid pumpdown to UHV pressures, a 4 K closed-cycle cryostat was set up to carry out the trap testing. We use an Advanced Research Systems (ARS) DE-210 system with a DMX-20 anti-vibration interface. The system is very similar to the closed-cycle system presented in Ref. [ASA$^+$09]. The cryostat operates by repeated expansion of high-pressure (250 psi) helium gas into

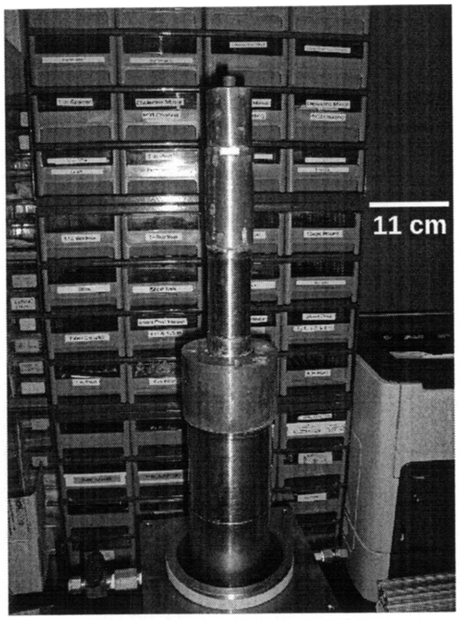

Figure 7-16: Photograph of the expander. This unit had been removed due to a helium leak. Some corrosion is visible, which may be due to the presence of liquid water if the bellows had not been adequately flushed with helium.

a low-pressure (20 psi) return line, in a process called the Gifford-McMahon refrigeration cycle. Two stages are present on the cold head, one that cools to 40 K with a cooling power of 35 W, and one that cools to 4.2 K, with a cooling power at that temperature of 0.8 W. The three key components of the cryostat presented here are the expander, the compressor, and the vibration isolation mechanism. In this section, we discuss these components, then present the vacuum chamber housing and the mounting of the entire system.

7.4.1 The cryostat

The expander is the part of the cryostat in which high-pressure helium is allowed to expand into a low-pressure return line and thereby fall in temperature. The low-pressure gas is then returned to the compressor to be pressurized again. The expander contains a valve that is operated by electrical power sent from the compressor, which opens to allow the high-pressure helium to expand at a rate of about 2 Hz. Inside the lower portion of the assembly is a displacer assembly, with first and second stage displacer units, the second being of a smaller diameter. The function of the displacer units is to capture a small amount of the helium that has been cooled by expansion, and then bring the cold head to that temperature by the use of heat exchanging elements. The displacers open and close according to the pressure above them. A photograph of the expander is shown in Fig. 7-16.

The compressor is the part of the cryostat that provides the necessary high- and low-pressure helium gas flow to and from the expander. It holds a static helium pressure of

250 psi, which increases to around 310 psi in the high-pressure line when the compressor is running. It is water-cooled with a chilled water supply with a flow rate of about 1.5 gal/min.

The DMX-20 anti-vibration interface thermally connects the cold head to the experiment without mechanical contact. A reservoir is filled with ultra-high-purity (99.9999%) helium gas at a pressure of about 1 psi. The reservoir is closed with a rubber bellows that does not transmit vibration from the expander to the experiment. Heat is exchanged by a pair of copper coils, one attached to the cold head and the other to the DMX-20 interface, between which helium gas is present.

When being operated, the expander is anchored to the ceiling with an 80/20 aluminum framework, while the experiment remains fixed to the table. If alignment of the cold head is not correct, then vibrations can be felt by hand on the experiment and the cold head position readjusted.

7.4.2 Vacuum chamber and optical access

The experimental assembly was mounted on an optical breadboard using an 80/20 aluminum framework. The breadboard was converted into a table using four 3 in. wide 80/20 pieces, with rubber feet on the bottom of each and some supports across the legs for stability. When the cryostat is not running, standoffs hold the expander in place within the DMX-20. The vacuum chamber is mounted on a pivot so that it can be rotated up 90° and opened. The vacuum chamber is made of con-flat parts for maximum isolation from atmosphere. The DMX-20 unit is encased in a 8 in. flanged nipple. On the bottom, a 4 1/2 in. CF viewport, AR coated for 422 nm and 1092 nm, is mounted on an 8 in. flange. When the cryostat is opened, this flange is removed. A photograph of the exterior setup is presented in Fig. 7-17.

Cryogenic vacuum setups differ in two main ways from room-temperature ones. On one hand, the choice of materials is broader than in a room-temperature setup. Materials that outgas too much at room temperature, such as plastic and lead solder, are acceptable at 4 K, making the experimental design somewhat simpler. On the other hand, obtaining this low outgassing, as well as minimizing the electrode temperatures, requires good thermal isolation from 300 K. Thermal "shorts" can be caused by conduction or radiation.

A radiation shield is constructed and anchored to the 40 K stage. This is composed of a 4 1/2 in. CF spherical octagon from Kimball physics, on top of which is a copper plate that holds the imaging lens assembly. Viewports are installed on two sides of the octagon to permit the lasers to access the trap, while other ports of the octagon are covered with copper baffles. Wiring from the external feedthroughs goes around these baffles. Fig. 7-18 shows the 4K baseplate with electrical connections for dc and rf. The 40K shield is also visible around this.

Preventing thermal shorts due to conduction is achieved by a combination of good wire

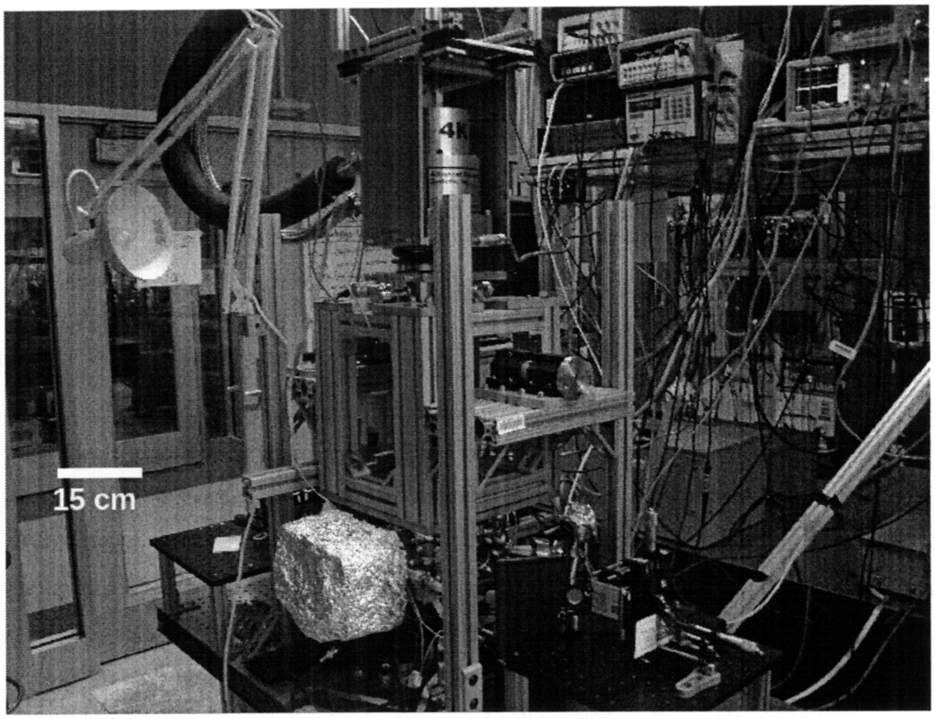

Figure 7-17: Photograph of the exterior of the vacuum chamber. The 80/20 framework is seen; the cryostat is currently in the configuration to be cooled down, with aluminum plates mounting the expander to the overhead framework. The box-shaped object covered in aluminum foil is the ion pump, mounted directly to the outer spherical octagon.

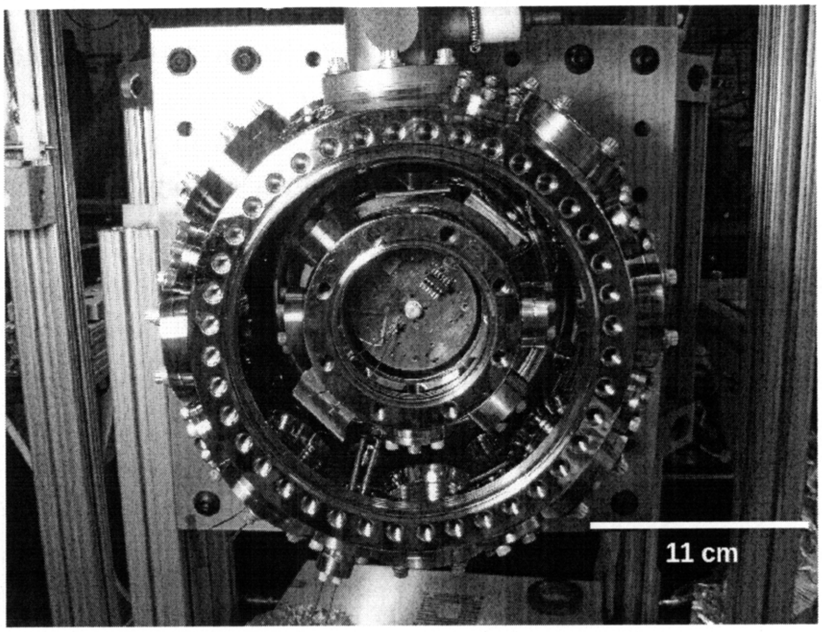

Figure 7-18: At the center of this photograph is the 4 K baseplate. The center screw attaches the baseplate to the DMX-20. The baseplate may be freely rotated before this screw is tightened. A series of tapped holes in the baseplate are used for mounting. Two sets of connectors have been glued onto the 4 K baseplate; on the right is the dc connector, and rf is on the left. The internal octagon which is attached to the 40 K stage surrounds the baseplate. The four 1 1/3 in. CF viewports may be seen, as well as the copper baffles for covering open ports. The feedthrough on the bottom is for sending current to the 40 K charcoal getters, and clockwise from that is the rf feedthrough. The oven goes in the empty 1 1/3 in. CF port on top, while the ion pump connects at the very top.

choices and heat sinking. The wire used for the dc connections and a portion of the rf line is a 36-gauge phosphor bronze wire, LakeShore Part No. WSL-36-500. The constant of thermal conductivity is 48 W/(K·m). For a temperature gradient of 294 K across a wire length of 10 cm, the thermal conductivity is 2 mW. Since this is much less than the cooling power at 4 K and 40 K (0.8 W and 35 W, respectively), heat gain due to conduction should be negligible. Actually, the figure is better than this, since the dc wires were wrapped repeatedly around the 40 K shield (increasing the length and heat-sinking) before being taped down to the 40 K baffle and then heat-sunk to the 4 K shield using StyCast thermally-conductive epoxy.

The rf wiring was purposefully made shorter than the dc wires to reduce stray capacitance. From the exterior feedthrough, a thin wire (to break thermal conductivity) was taped to the 40 K baffle, then attached to a thicker wire (to increase electrical conductivity), before being soldered to a thin wire which was heat-sunk with StyCast to the 4 K baseplate and routed to the trap. This combination was designed to provide as much electrical conductivity as possible while still breaking the thermal connections.

Upon finishing work inside the cryostat, the system was put under turbo pump vacuum, leading to ultimate pressure in the high 10^{-6} torr range. A 50 Ω heater is installed on the cold head, and this was engaged to bring the system to a temperature of 380 K for around 24 hours, allowing some oils, water, and other residues to bake off and be removed from the system. This is done partially to improve the ultimate pressure, and partially to remove substances which might freeze onto the trap electrodes at 4 K. A pair of charcoal getters were also installed on the 40 K shield, and were discharged during this time with a wire whose resistance totaled 150 Ω. A current of 0.06 A through the getters was used.

Finally, a 20 l/s ion pump was installed directly on the outer octagon. This was turned on before cooldown. There are two main advantages to this. The first is that the system is completely closed from the "outside world" during cooldown. This prevents cryopumping from actually pumping material from the turbo pump line into the cryostat. Furthermore, in case of a malfunction of the turbo or roughing pumps, it prevents oils from being cryopumped into the system. The other advantage is that reading the ion pump current enables one to upper-bound the pressure inside. Since the ion pump is connected directly to room temperature, we expect the pressure inside the radiation shield to be considerably less than that measured on the ion pump. It was impressive that the pressure reading on the ion pump, when the system was fully cooled, read 0.0×10^{-9} torr.

The system was equipped with two diode temperature sensors. Each requires a 10 μA current, and the temperature is inferred from the voltage across the diode. One is anchored to the cold head, and is called the control sensor. The other can be placed anywhere else, and is called the free sensor. We chose to place the free sensor directly on the 4 K baseplate, anchored with StyCast. The free sensor came to a temperature of 4-5 K normally, while the control sensor was at 11-13 K. It is not known why the temperature was not lower;

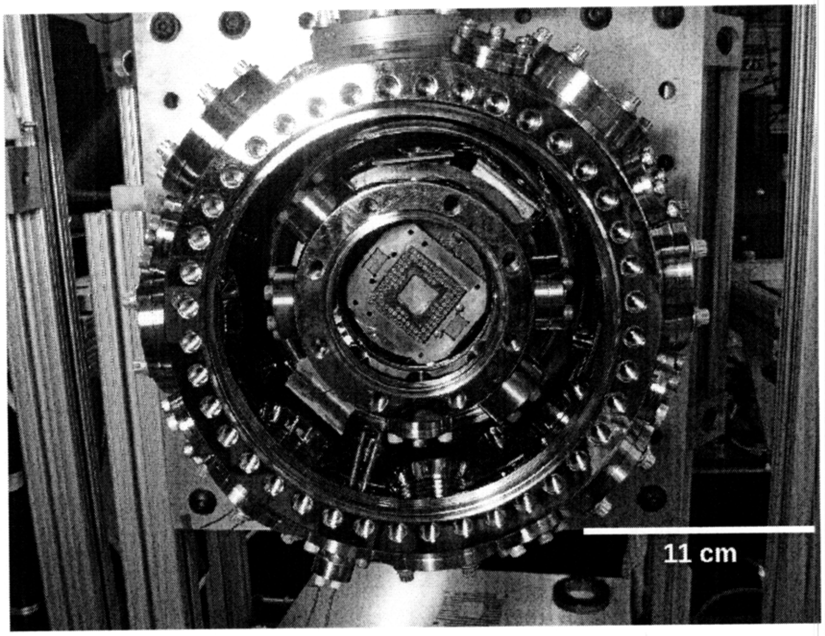

Figure 7-19: The plastic socket that holds the cpga mounted above the 4 K baseplate (at center of photograph). Electrical connections are made to each pin receptacle from below.

probably switching to a fully-copper 40 K shield would help, as copper is a much better thermal conductor than the stainless steel that the octagon is made of.

Some supplementary information concerning practical aspects of operating the cryogenic experiment may be found in Appendix C.

7.5 Experimental study of the elliptical trap

In this section we present an experimental investigation of the elliptical traps discussed in Sec. 7.1, focusing on verifying the secular frequency and ion crystal structure calculations. We begin by discussing the experimental setup, then report verification of our theoretical calculations.

7.5.1 Experimental setup

Trap mounting, oven, connections

The trap is held above the 4 K copper baseplate by copper standoffs, onto which screws a copper plate which holds a plastic socket into which the cpga is inserted. The electrical connections are plugged into the bottom side of this socket, making reconfiguration of the pinout relatively simple.

The socket mounted above the 4 K baseplate, surrounded by the 40 K shield, is depicted in Fig. 7-19. Fig. 7-20 contains two photographs: first, a labeled photograph of Uraniborg

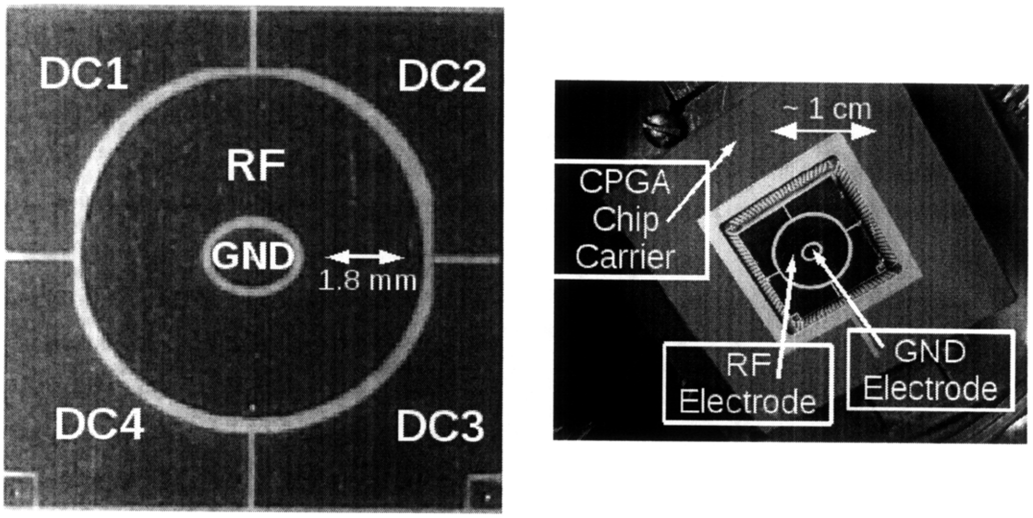

Figure 7-20: Left: Photograph of Uraniborg 2. The electrodes are labeled with the voltage applied to each, as referenced in the text. Right: Photograph of Uraniborg 1 mounted in a CPGA. The width of the PCB trap is ~ 1 cm.

2, indicating the labels given to each electrode, and second, the trap (Uraniborg 1 rather than 2) mounted in a CPGA chip carrier for installation into the cryostat. A copper braid (solder wick) was soldered to one of the dc electrodes, with the other end screwed into the 4 K baseplate, in an effort to heat sink the trap to 4 K.

The strontium oven for trap loading was mounted on a 1 1/3 in. CF feedthrough which was mounted on the exterior octagon. The end of the oven was placed in a hole in one of the copper baffles. The hole was drilled at the approximate height of the trap. This particular oven was made of a thin stainless steel tube. Steel wires spot-welded to the feedthrough were spot-welded to strips of tantalum foil, which were then spot-welded to the steel tube, which was filled with strontium metal. The tantalum, which has a high electrical resistivity, serves to heat the oven with a lower level of current than would otherwise be needed. As it was, 2.0 A was sufficient for loading the trap, the lowest value of any oven the author has made.

Imaging optics

Optical breadboards were mounted at a proper level to address the ions, with lasers propagating roughly parallel to the plane of the trap electrodes. The 422 nm and 1092 nm lasers were set up on one side of the cryostat. Each passes through a series of collimating and focusing lenses before being coaligned on a dichroic mirror. The initial coalignment was done by eye. Their beam waists were minimized and the coalignment of the beams was fine-tuned using a ThorLabs beam profiler. On the other side of the cryostat, the 460 nm and 405 nm photoionization beams were brought to a focus at the trap center using a fast achromat from ThorLabs.

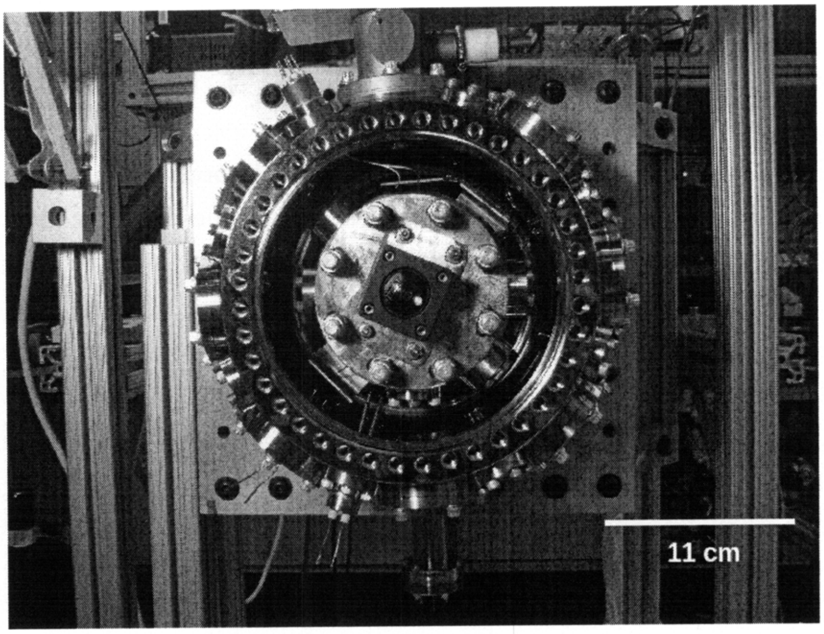

Figure 7-21: The two internal lenses mounted on the 40 K shield, above an ion trap. The top of the 40 K shield is mounted in the octagon, and may rotate by small amounts. The lenses are also mounted on a separate copper plate that can move freely, for centering the lenses. The lenses are mounted on a cage system, so that the focus to the trap can be adjusted.

The detection and PI beams were made to counter-propagate across the trap. This setup has certain advantages and disadvantages. Counter-aligning was more practical given the geometry of the experimental setup and the space available on the optical table. Also, aligning was fairly easy. Normally, neutral strontium atoms would be observed using the 460 nm light. The beam of neutrals was centered on the trap, and then the height of the beam was adjusted to the height computed by CPO (about 1.3 mm). The detection lasers were then counter-aligned to this beam. Typically only small adjustments in the laser positions were then required to detect trapped ions. The disadvantage is mainly that back-reflections from the PI optics caused additional 422 nm scatter, which was reduced when the PI lasers were blocked after loading.

Detection of ions was done on an Santa Barbara Instruments Group (SBIG) ST-3200ME CCD camera with a 422 nm interference filter in place (as in Ch. 5). The imaging optics are as follows. Inside the cryostat, two lenses were mounted on the 40 K shield, a 20 mm aspheric lens and a 150 mm achromat. The focusing light emerging from the cryostat was reflected off a silver mirror into another 150 mm achromat, which collimated the light and served as the focusing lens. A final 150 mm achromat focused the image onto the CCD. Fig. 7-21 shows the lens assembly, including the internal 20 mm asphere and 150 mm achromat, mounted above an ion trap.

Electronics

The electronics for this experiment were similar to those used in previous ones (Chs. 5 and 6). Briefly, dc voltages were supplied to four of the dc electrodes on the trap using an eight-channel voltage source that interfaces to the computer. The dc signals were filtered by standard R-C low-pass filters with a cutoff frequency of about 100 kHz. This was chosen to provide an rf short to ground for the dc electrodes at the drive frequency (3.5 MHz) while still allowing the lower-frequency voltages used for secular frequency measurement to pass through.

An rf signal was produced by an Agilent 33250 function generator and sent directly to the helical resonator. To produce the proper voltages, no additional rf amplifier was required. The resonator was mounted to the table and connected to the chamber with an rf feedthrough. Grounding straps connected the rf input with the function generator, the cryostat hoses, and earth ground, and also provided the rf ground for the dc filters.

7.5.2 Secular frequency measurements

Secular frequencies were measured by using a low-amplitude voltage applied to the electrode DC2. The amplitude required varied a great deal between the different motional frequencies.

Prior to this, basic compensation of the trap was done by setting the dc voltages such that the ion cloud did not move when the rf amplitude was changed. There was actually a significant movement of the ion cloud (tens of microns) with a change in V_c of only 0.1 V; therefore, the vertical direction could be roughly compensated by setting V_c such that the cloud did not move out of the laser when the rf was changed. The final set of dc voltages were V_1 = -3.90 V, V_2 = 1.56 V, $V_3 = V_4$ = 0 V, and V_c = -2.62 V. Fig. 7-22 is a plot of one data set taken at a sequence of RF voltages with these dc voltages. The secular frequencies were measured by exciting the ions at their motional frequencies and observing drops in their fluorescence, as discussed in Sec. 5.4.

The CPO-computed frequencies for this voltage set are plotted below, in Fig. 7-23. One sees that the agreement is not very good. Why is this? For one thing, note that the theoretical frequencies have changed a great deal from those with only rf confinement (cf. Fig. 7-3). Therefore, the dc voltages do not merely move the position of the ions; they change the curvature of the trap itself. A portion of the dc voltages here merely nulls stray fields that existed in the first place. Some portion, however, also contributes to altering the trap curvature. Another clue is provided by the fact that although $\omega_{\hat{x}} + \omega_{\hat{y}} = \omega_{\hat{z}}$ to fairly good agreement in the simulation, this relation does not hold for the experimental data, indicating that dc voltages have a contributing effect.

Another possible source of error is that the rf voltage measured on the exterior of the cryostat does not necessarily equal the voltage on the trap. The degree to which it does depends greatly on the specific experimental setup. The wire extending from the feedthrough is quite long in order to reach the 4 K area and be properly heat-sunk on the

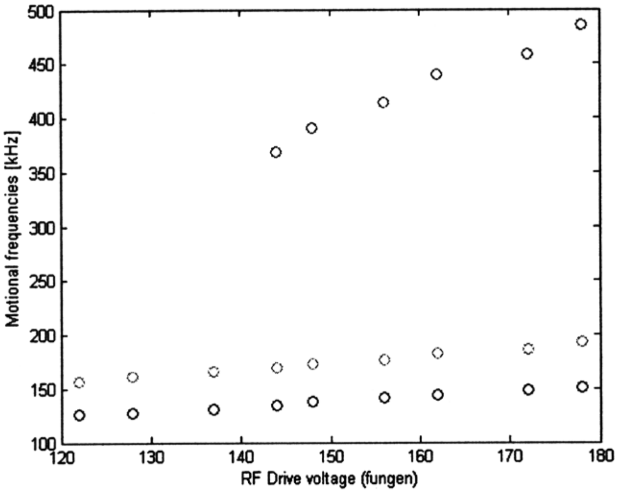

Figure 7-22: Measured secular frequencies as a function of rf voltage amplitude for the three motional modes of Uraniborg 2. $\omega_{\hat{x}}$ is blue, $\omega_{\hat{y}}$ is green, $\omega_{\hat{z}}$ is red, and $\omega_{\hat{z}} > \omega_{\hat{x}} > \omega_{\hat{y}}$ for all rf voltages. Errors on each frequency measurement are ±2 kHz.

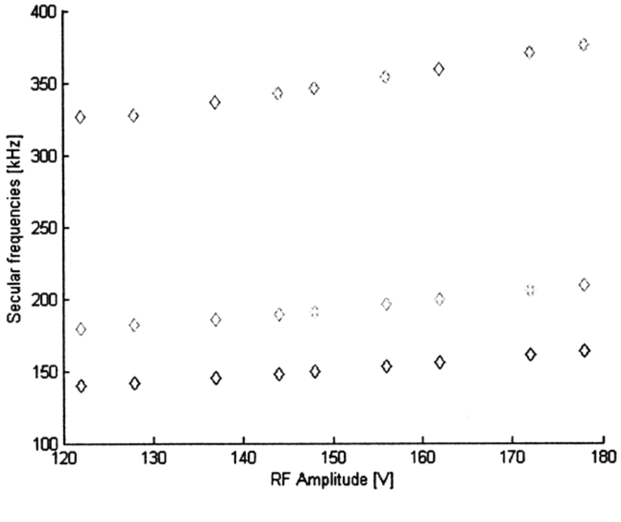

Figure 7-23: Calculated secular frequencies for the trap at 3.5 MHz and a series of rf amplitudes. The frequencies are blue, cyan, and green for $\omega_{\hat{x}}$, $\omega_{\hat{y}}$, and $\omega_{\hat{z}}$, respectively, with $\omega_{\hat{z}} > \omega_{\hat{x}} > \omega_{\hat{y}}$.

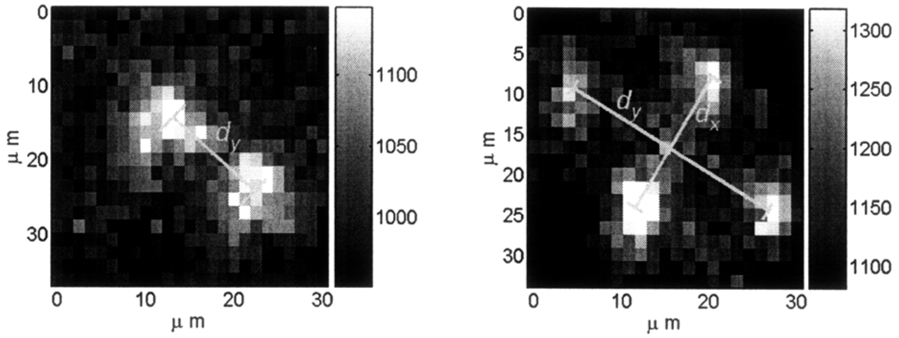

Figure 7-24: Images of ion crystals of two and four ions in Uraniborg 2. The principal axes $\hat{x}$ and $\hat{y}$ of the trap are shown by depicting the corresponding ion-ion spacings d_x and d_y in each figure.

way, and this wire forms a part of the resonant circuit that drives the trap. Therefore, some voltage differential is expected. In some papers, the rf voltage is treated as a fit parameter since it is difficult to directly measure [SCR$^+$06, CLBC09]. However, in this case the frequencies are not off by a constant factor, so this is not a completely satisfactory explanation. It is possible that some combination of the two effects explains the discrepancy: the dc fields at the ion location are unknown, as is the magnitude of the rf field.

A more interesting question is how well the ion crystal structures match the theory for the measured frequencies, which we explore next.

7.5.3 Ion crystal structure

Ion crystals consisting of between one and four ions were observed in Uraniborg 2. To obtain these images, it was necessary to readjust the imaging optics repeatedly to reduce aberrations, to set the dc voltages carefully, and to carefully coalign and focus the detection lasers. Without these conditions being met, somewhat misshapen crystals of two ions (but no more) were observed. Unfortunately, it was difficult to cool more than four ions into a crystalline state in this trap.

Although ion crystals were observed, the signal was fairly weak and long exposure times of up to 5 s were required, using the HIGH resolution of the SBIG camera, in which each individual pixel is displayed (no binning). Images of crystals are plotted in Fig. 7-24.

Images were analyzed as follows: the centers of each ion were determined from a Gaussian fit of the intensity. The magnification was calibrated to the spacing of two ions. The image of four ions was processed in the same way, using this magnification. Errors on the spacing of ions were determined from the standard deviation on the centers of the ions. For two ions, the calculated spacing is 16.5 μm, and the spacing between ions is 11±3 pixels, giving a magnification of 4.5, or 1.5 μm per pixel.

For four ions, we calculate the spacing between the ions along the $\hat{x}$ and $\hat{y}$ directions.

Along $\hat{y}$, the spacing is $d_{\hat{y}} = 28\pm3$ μm, while along $\hat{x}$ it is $d_{\hat{x}} = 17\pm3$ μm. These values are consistent with the theoretical values of $d_{\hat{y}} = 29.6$ μm and $d_{\hat{x}} = 17.1\mu$m.

Again, it was not possible to crystallize larger numbers of ions, and therefore confirmation of the crystal structure for higher numbers of ions was not done. However, we do now have some confidence that the crystal structure in elliptical traps may be accurately computed. There are a number of possible reasons for the low ion number. Among them are the stability of the lasers used, the fact that crystals were only observed at relatively low trap depths (0.3 eV), and the possibility of heating from the rf electrode rendering larger crystals unstable. Indeed, the lifetime of a single ion in the absence of cooling light was at most a few seconds, indicating that heating may indeed be a problem.

7.6 Discussion: connection to quantum simulation

We have now presented the design and testing of a new method for preparing a 2-D Coulomb crystal in a Paul trap: the surface-electrode elliptical trap. The next step is to evaluate the usefulness of this trap for quantum simulation, focusing again on the challenging problem of spin frustration. We frame this discussion in terms of the requirements posed in Sec. 4.3. There, we note that a viable trap design must:

1. Provide a regular array of stationary qubits in at least two spatial dimensions.
2. Enable sufficient control over each qubit to implement the desired simulation.
3. Possess, in principle, a low enough decoherence rate to perform meaningful simulations given certain coupling rates.

We address these criteria one-by-one.

7.6.1 Regular array of stationary qubits

We have calculated crystal structures for the elliptical trap presented in this chapter, but it is seen from these that a truly *regular* array of ions is not produced. The reason for this is that the test trap was designed with more difference between the radial frequencies $\omega_{\hat{x}}$ and $\omega_{\hat{y}}$ than is strictly necessary to support a 2-D crystal with fixed ion positions.

Recent calculations [BKGH08, BH09] have suggested that in a 2-D ion crystal regular lattice structures near the center of the lattice may be observed. We expect that, in our trap, as $\omega_{\hat{x}} \rightarrow \omega_{\hat{y}}$, that such regular structures will also appear. The calculations of Sec. 7.1.2 support this hypothesis.

7.6.2 Sufficient controls

We have outlined in this chapter two methods for implementing the state-dependent forces required for quantum simulation of spin models: optical forces and magnetic field gradients.

A major contrast between these approaches is that the magnetic gradient approach is well-suited to applying global effective Hamiltonians to the system, while the optical forces may be applied either globally or pairwise between ions. Regardless of the method used, we would like to remind the reader that the simulated coupling rates in the elliptical trap are of the same order of magnitude that they would be in a "linear" ion trap (the applied force F and ion-ion spacing d being the same for both). In Sec. 5.6, we compared the interaction rates between lattice traps and traps in which ions are confined in the same potential well. Both the motional coupling rates and simulated coupling rates are therefore as high as they would be in a linear ion trap, except that they can act along multiple directions.

Despite high interaction rates, the elliptical trap has certain control errors that do not occur in lattice-style traps, most especially those due to micromotion. The unequal micromotion amplitudes across the crystal mean that the effective (time-averaged) J-coupling varies across the ion crystal. If ions on the periphery of the crystal are used, such that the ion-ion distance varies from site to site, this adds an additional control error that exacerbates the one due to micromotion. Although it is arguably easier to apply magnetic gradients to create a global force, and although this approach removes errors due to spontaneous scattering, pairwise interactions with an optical force have the potential to correct the systematic errors. Adjusting the controls in such a manner is tractable, since the ion positions and relative micromotion amplitudes are efficient to calculate. The limited system size of about 100 ions further limits the computational resources required to do this. At the same time, doing such implementations in practice will require excellent control (with precision of $\mathcal{O}(\sim 1-10\mu\text{m})$) of the pushing laser position. Similar control would be required to optically perform single-qubit operations in such a trap.

In summary, the question of magnetic vs. optical forces presents a tradeoff between control and simplicity. The point remains that there is no fundamental limitation to doing high-fidelity quantum operations in an elliptical trap. We note further that the results of this chapter regarding control errors due to micromotion apply generally to 2-D ion crystals in Paul traps, and are not limited to the elliptical traps that were the focus of this chapter.

7.6.3 Decoherence rates

Although not the primary subject of this chapter, decoherence rates will ultimately determine the feasibility of quantum simulation in elliptical traps (or other traps that generate 2-D ion arrays). Given the cryogenic temperature and relatively large (mm-scale) size of the Uraniborg traps, it is possible that the motional heating rate could be well below the interaction rate J, which may be on the order of kHz. Heating can also occur due to background gas collisions, but here the cryostat provides an excellent vacuum environment, on par with or superior to the best room-temperature UHV systems. Since conventional ionization gauges do not function at cryogenic temperatures, other methods must be used to measure the pressure. Ref. [ASA$^+$09] uses ion lifetimes to upper-bound the partial pressure of O_2 to 2×10^{-12} torr.

Decoherence of the internal states depends on many factors, including fluctuations of the parameters (amplitude, phase, etc.) that describe the control pulses, fluctuations in ambient magnetic fields, and processes intrinsic to the atom such as spontaneous emission. The last of these can result in decoherence even for qubits that have very small spontaneous emission rates, such as hyperfine qubits, since spontaneous scattering during the Raman pulses that are used can decohere the states. Although we don't specifically treat these decoherence processes in this thesis, we may legitimately hope that internal state coherence times of several seconds may be obtained, in the event that hyperfine states are used.

7.7 Conclusions and future work

In this chapter we have explored the possibility of using surface-electrode elliptical ion traps for analog quantum simulation, particularly simulation of quantum spin models. We have presented calculations of the structure of 2-D and approximately 2-D crystals within such a trap. These predictions were confirmed experimentally for a small number of ions. We have also studied, in theory, how micromotion affects the fidelity of a quantum simulation, and have seen that studies of quantum spin phases are probably possible even in the presence of micromotion. In addition, magnetic field gradient coils embedded in the ground electrode of the elliptical trap might prove an excellent way to produce global state-dependent forces for implementing a variety of spin models.

On the theoretical side, this work is a starting point. For instance, other types of quantum simulations to which ions may be well-suited have not been considered. It would be an interesting problem to study the possibility of observing Bose-Hubbard physics in this system. Furthermore, although we have calculated the effects of micromotion for small numbers of ions, the work should be extended to larger numbers. Small errors in the pairwise interactions will propagate across the system as global correlations are created, and it will be an interesting (but computationally intensive) task to examine how the global fidelity of the simulation is altered. We note, however, that such errors may be corrected for, provided adequate controls are available.

Experimentally, a natural first step is attempting to form larger ion crystals in the elliptical trap. Although the source of the relatively low lifetimes of crystals is unknown, the heating rates in this system should be measured. If anomalously high heating rates are a problem, even at 4 K, materials other than copper such as silver or gold, which exhibit lower heating rates, may be used for trap fabrication. Naturally, we would someday like to see experimentally if methods based on magnetic field gradients are viable for this purpose, and whether the effects of micromotion for small ion numbers are as we predict.

In all, the elliptical trap appears to be a much more promising system than arrays of microtraps for analog quantum simulations with a few tens of ions. The ability to maintain trap depth and to keep ions in the same trap region as secular frequencies increase means that the coupling rate of the motional state will remain on the same order of magnitude as the secular frequency. This is equivalent to having a β parameter on the order of 0.1, as opposed to orders of magnitude lower, and may be crucial for observing these interactions.

Part III

Toward ion-ion coupling over a wire

Chapter 8

Motivation for and theory of ion-ion coupling over a wire

In the first two parts of the thesis, we explored digital and analog quantum simulation using two different quantum technologies: nuclear magnetic resonance and trapped ions. We also saw that both NMR and the types of ion traps studied in Part II have only a limited scalability, up to at most perhaps tens of interacting particles. This provides the motivation for studying a way to scale up quantum simulation to truly arbitrary numbers of interacting particles.

We now turn to the third and final part of the thesis. The main goal of the research presented here is the coupling of two trapped ions over a conducting wire. This little-studied system could potentially be used to scale up ion trap quantum simulation, linking ions in separate trap regions through the image charges induced in the wire by the motion of the ions. Application to both digital and analog quantum simulation is conceivable, and in contrast to the trap designs of Chs. 5 and 7, such coupling is, in principle, electronically switchable, and there is no apparent limit to the number of ions that may be networked in this way.

In this chapter, we present a theoretical treatment of the coupling of two ions over a wire. We explain that the system has the form of two coupled oscillators, with the coupling mediated by the image charges in the wire rather than by free-space Coulomb coupling, which is the most common case with ion trap quantum simulation. We also present a calculation of this coupling rate, showing how it depends on the experimental parameters such as the ion-wire distance, the trap frequencies, and the capacitance of the wire. This calculation permits us to set bounds on these parameters for an experimental demonstration of the coupling, and also to estimate the rates of certain decoherence processes in the system. These results are included in Ref. [DLC$^+$09b].

The chapter is organized as follows. In Sec. 8.1, we motivate the study of ion-ion coupling over a wire. In Sec. 8.2, we present the theory of ion-ion coupling over a wire and calculate the relevant coupling rates, and then in Sec. 8.3 proceed to estimate the pertinent decoherence rates. These calculations lead to the brief section on experimental considerations (Sec. 8.4), which explains some aspects of the experimental setup in the next chapter. Finally, in Sec. 8.5, we summarize the results of this chapter.

8.1 Motivation

Communication between trapped ions is a critical aspect of building a scalable quantum simulator or computer. There are, to date, three proposed methods for doing this:

1. Move the ions between different zones of a trap to enable them to interact with each other.
2. Connect ions using photons that travel between different traps.
3. Connect ions electronically, using conducting wires.

These methods are discussed in Sec. 1.4.3; here, we summarize their advantages and disadvantages. Method 1 is attractive because it does not require precise (and probably expensive) optical components at each ion site as in method 2, and does not rely on technology that is as underdeveloped as method 3. Method 2, by contrast, seems very attractive if the optical components, for example fiber optics and cavity mirrors, can be mass-produced in a reliable and cost-effective way, and if sufficient coupling between the ion and the light mode can be achieved. Method 3, if proven to work, may be the simplest of all; fabrication of the wires that connect the ions can be done presumably using existing technologies, and the couplings between ions are, in principle, electronically switchable.

The third method, linking ions over wires, is the subject of this part of the thesis. There have been interesting ideas for the use of such technology that go beyond linking atomic ions for a quantum simulator. One example is the proposal of Ref. [SGA$^+$05] to link electrons in individual Penning traps to act as a quantum processor. In another example, it is proposed to connect an atomic ion electronically to a superconductor as a means of scaling up quantum computation [TBZ05].

As exciting as the applications seem, there are important and unanswered questions. For instance, what are the expected coupling rates in a realistic experimental system? What are the expected decoherence rates? How does the wire used for coupling affect the potentials of the ion traps? These are the questions pursued in this part of the thesis.

8.2 Theory of ion-ion coupling over a wire

We now discuss the theoretical calculation of the coupling rate between two ions, mediated by a conducting wire. We define the coupling rate ω_{ex} as follows. For two ions, $t_{ex} = 2\pi/\omega_{ex}$

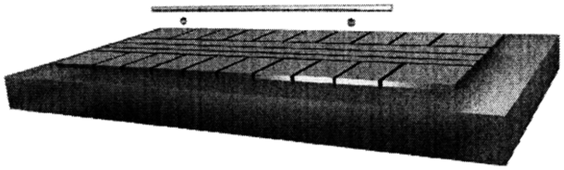

Figure 8-1: Schematic of the experimental setup. The two ions are trapped in different potential wells, set by the segmented dc electrodes. Distances are approximately to scale for our experiments; actual values are presented below.

is the time required for the two ions to completely exchange motional states. Normally, the $1/d^3$ scaling of the interaction rate ω_{ex} means that this coupling quickly becomes negligible as the ions are moved apart. Here, we will focus on the case where free-space coupling may be ignored, and the only observable coupling is due to the wire.

Fig. 8-1 depicts a schematic of the experimental setup. A single wire is positioned close to two trapped ions, which are confined in a linear surface-electrode ion trap and are set far enough apart so that coupling due to their shared normal mode is negligible. The creation of two different trap regions is possible by adjusting the segmented dc electrodes; fine adjustment of these voltages can also aid in setting the secular frequencies of the two ions to be equal, a resonance condition which is important for optimal coupling.

In what follows we will follow two approaches to describe the dynamics of this system. In the first, we solve the dynamics directly from electrostatic calculations. In the second, we use an effective circuit model, a useful approach when studying the effects of decoherence in the next section. This approach was followed by Heinzen and Wineland in a paper that first treated the coupling of ions over a wire, among other related situations [HW90]. The new contribution here is the solution of the dynamics directly from electrostatics, presented in Sec. 8.2.1 which was undertaken mostly by the author's collaborator Nikos Daniilidis, and provides a more rigorous justification of the circuit model for our experimental situation.

8.2.1 Electrostatic solution

In order to solve for the behavior of the above system, we need to make some simplifying (but reasonable) assumptions. We consider a wire of radius a and length L, positioned a height H above an infinite conducting plane, and parallel to this plane. Treating this plane (which is, in reality, the trap) as infinite in extent and a continuous conductor is the first assumption. The two ions are situated at heights h_1 and h_2 (h_1, $h_2 < H$) above the trap, and are some distance d apart. We assume also that h_1, h_2, $H \ll d < L$. The ions are treated as point charges, a very reasonable assumption. We depict this situation in Fig. 8-2.

Considering both ions to have a charge e_c, and the wire to have zero net charge, it can be shown using Green's function techniques that the electrostatic potential of the wire with

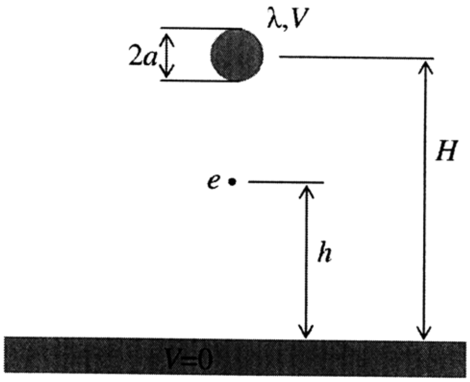

Figure 8-2: Diagram of the model used in our calculations.

respect to ground is

$$V = \frac{e_c}{4\pi\epsilon_0}\left[\ln\left(\frac{H+h_1}{H-h_1}\right) + \ln\left(\frac{H+h_2}{H-h_2}\right)\right]. \tag{8.1}$$

To obtain the coupling rate, we need to know how the induced charges in the wire due to one ion affect the electric potential seen by the other ion. We write down the potential energy of each ion due to the induced charge in the wire as

$$U_i = \frac{e_c V}{\alpha}\ln\left(\frac{H+h_i}{H-h_i}\right), \tag{8.2}$$

where $i = 1,2$ indexes the ions and the geometric constant $\alpha = \ln\left[(2H-a)/a\right]$.

Equipped with this potential energy, we can calculate the coupling constant from its second derivative. First, we switch to a more convenient coordinate system, in which the height of the ion h_i is equal to its equilibrium height h_{0i} added to its displacement from equilibrium z_i. The coupling constant is given by

$$\gamma \equiv \frac{\partial^2(U_1+U_2)}{\partial z_1 \partial z_2} = \frac{2e_c^2 H^2}{\pi\epsilon_0 \alpha L(H^2-h_1^2)(H^2-h_2^2)}. \tag{8.3}$$

Given the fact that each ion is in a separate harmonic trap, we can write the full system Hamiltonian:

$$H = \frac{p_1^2}{2m} + \frac{1}{2}m\omega^2 z_1^2 + \frac{p_2^2}{2m} + \frac{1}{2}m\omega^2 z_2^2 + \gamma z_1 z_2\,, \tag{8.4}$$

where $\gamma z_1 z_2$ is the lowest-order interaction term between the two ions.

The solution to this equation is quite well known in the classical case. For higher temperatures, this approach would be approximately correct. However, in the quantum-mechanical case the solution is a bit more difficult. Ref. [EKN68] considers both the resonant case ($\omega_1 = \omega_2$) exactly, as well as in the rotating wave approximation. These two approaches are in close agreement in the case of small coupling constants ($\gamma/\left(m\omega^2\right) \ll 1$). A more recent solution has shown that complete exchange of motional states can only occur on resonance ($\omega_1 = \omega_2$) and for specific initial motional states [PRDB08].

The exchange rate, also known as the coupling rate ω_{ex}, is given by

$$\frac{\omega_{ex}}{2\pi} = \frac{\gamma}{\pi\omega m}, \tag{8.5}$$

where γ and α were defined above and $\omega = \omega_1 = \omega_2$ (the resonant case). Incidentally, it is also equal to the classical expression!

Referring to Eq. 8.3, the above formula for ω_{ex} allows us to evaluate the sensitivity of the coupling rate to the various parameters of our model system. For instance, the length of the wire and ion-wire distances enter as $1/\left[L(H - h_1)(H - h_2)\right]$, a strong dependence, while the dependence on the wire radius a is only logarithmic (it is contained in α). Overall, we see that a shrinking of the entire system size leads to increased coupling, as the ions induce more charge when closer to the wire; also, a shorter wire length leads to a higher overall charge density on the wire. The inverse dependence on the secular frequency ω is an expected feature of coupled harmonic oscillators; we have seen similar physics at work in the lattice traps of Ch. 5. Physically, tighter confinement (higher ω) reduces the effective "dipole moment" of each ion, which scales as $1/\sqrt{\omega}$.

8.2.2 Circuit model solution

The above model leads to a physical picture of the physics of our system. In this section, we explore a different approach, which is based on a circuit model of the system, in which each component is treated as a lumped element: an inductor, capacitor, or resistor. This can have two key advantages: one is that the above physical model is based on assumptions that are not strictly true, but are good approximations. To take an example, the capacitance between the wire and ground will differ from that computed for an infinite ground plane, especially since the length of the wire is not much less than the width of the trap in our experiment. A circuit model allows one to quickly plug in more reasonable estimates of this capacitance. The second, and more compelling, reason to use a circuit model is that it makes the treatment of decoherence simpler. This is because the main decoherence sources are electrical in nature; dissipation of currents in the wire and Johnson noise heating are the two prime examples. This approach was presented in Refs. [WD75] and [HW90], and we follow it here.

We begin with the equations of motion for the ions:

$$\frac{e_c}{m}E_i = \ddot{z}_i + \omega_i^2 z_i, \tag{8.6}$$

where the electric field E_i is due to the voltage in the wire induced by the other ion. We wish to write this field in terms of quantities in the above model, and the result is

$$E_i = V \frac{2H}{(H^2 - h_i^2) \ln\left(\frac{2H-a}{a}\right)}. \tag{8.7}$$

The details of this derivation are found in Ref. [DLC$^+$09b]. We now invoke a result of Shockley [Sho38] to find that the charge induced in the wire by a single ion may be written as

$$q_{ind} = -\frac{e_c}{\alpha} \ln\left(\frac{H+h}{H-h}\right). \tag{8.8}$$

Noting that the current I in the wire is proportional to $q_{ind}\dot{z}$, the above result enables us to write the mechanical equation of motion as an electrodynamic one involving currents and voltages:

$$U_i = L_i \frac{dI}{dt} + \frac{1}{C_i} \int I dt, \tag{8.9}$$

where the effective inductance L_i and capacitance C_i of a single trapped ion are given as

$$L_i = \frac{1}{\xi_i^2} \frac{mH^2}{e_c^2} \tag{8.10}$$

and

$$C_i = \frac{1}{\omega_i^2 L_i}, \tag{8.11}$$

and the geometric factor ξ_i given by

$$\xi_i = \frac{2H^2}{\alpha(H^2 - h_i^2)}. \tag{8.12}$$

These formulas enable us to answer a very interesting question: what are the effective inductance and capacitance of a single trapped ion? The answer is that the inductance is very large, while the capacitance is very small. Let us assume some feasible values for this experiment: $H = 200\ \mu\text{m}$, $h_{1,2} = 150\ \mu\text{m}$, $L = 10$ mm, $a = 12.5\ \mu\text{m}$, and $\omega/(2\pi) = 1$ MHz. For these values, $L_{1,2} = 3.7 \times 10^4$ H and $C_{1,2} = 6.9 \times 10^{-19}$ F. This explains why trapped ions are such excellent resonators; the usual Q factor for an electrical circuit is given by $Q = \sqrt{L/R^2 C_i}$, and is on the order of 10^{11} for our trapped ions.

The motional coupling rate ω_{ex} in terms of these quantities is given by

$$\omega_{ex} = \frac{1}{2\omega LC}, \tag{8.13}$$

where C is the capacitance of the wire to ground, as detailed in Ref. [HW90]. We may now calculate the expected coupling rate. Using the above parameters and a wire capacitance of $C = 2 \times 10^{-15}$ F, it is $\omega_{ex} = 10^3\ \text{s}^{-1}$.

8.2.3 Simulated coupling rates

We now address how the calculated motional coupling rates above may be translated into a simulated coupling rate. As in Part II, we restrict our discussion to the simulated J-coupling rate in a spin model simulation using the methods outlined in Ref. [PC04b]. We will assume that a state-dependent force of magnitude F is applied to each of two ions, although they may reside in different trap regions.

The J-coupling rate may be calculated by separating the motional coupling rate (parametrized by β) from the part of J that is due to the state-dependent force. Recalling the results of Sec. 4.2.2 and taking the $\beta \ll 1$ limit, we find that J for a given direction may be written as

$$\hbar J = \frac{2c\beta F^2}{m\omega^2} \tag{8.14}$$

where ω is the secular frequency along a given direction, m is the ion's mass, and c is a constant of order unity that depends on the direction of the state-dependent force. Here, we set $c = 1$ since we are mainly concerned with an order of magnitude for the coupling rate. Recalling that β is the motional coupling rate per secular vibrational period, we write it as

$$\beta = \frac{\omega_{ex}}{\omega}. \tag{8.15}$$

For the parameters used in Sec. 8.2.2, we find that $\beta \approx 10^{-3}$. Taking our value from Ch. 5 of $F = 2.7 \times 10^{-21}$ N, and using the mass of $^{40}\text{Ca}^+$, we find that $J \approx 100$ s^{-1}. Although this seems like a poor figure, we note that the same scaling laws that apply to the lattice ion traps (Ch. 5) do not apply to the present situation. For instance, it may be possible to decrease the secular frequency, even with a small ion-wire distance. Part of the reason for this becomes apparent when we discover the effect that the wire has on the trap potentials (Ch. 9): it may be easier with wire-mediated coupling to preserve trap depth while lowering the secular frequency.

Naturally, there are other possible avenues to increasing J, such as applying a stronger force. For now, we regard the simulated coupling as observable in principle, under favorable but realistic decoherence rates.

8.3 Decoherence

We now turn to estimating the rates of decoherence in the above system. The decoherence processes are important to understand for the obvious reason: they may tell us if coherent information transfer is possible over a wire at all, even if the coupling rate seems adequate, and may also help us to answer questions such as the requisite temperature and resistivity of the wire. Because these decoherence sources are electrical in nature, we will find the

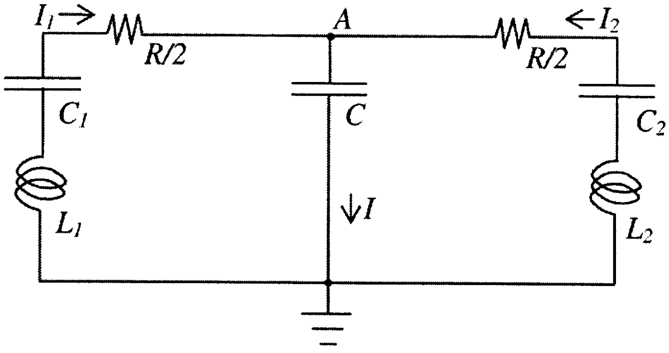

Figure 8-3: Equivalent circuit of two ions, each with inductance L_i and capacitance C_i, defined as in the text. They are coupled by a wire with ohmic resistance R and a capacitance of C to ground. The currents I_i are determined by the velocity of each ion, according to Eq. 8.8.

circuit model to be of great utility. In Fig. 8-3, we have drawn a schematic of the equivalent circuit that describes two ions and the wire.

The primary types of decoherence we will treat here are dissipation (Joule heating of the wire), Johnson noise, and anomalous heating.

8.3.1 Dissipation

To treat dissipation, we need to calculate the current in the wire due to the motion of the ions. Again invoking Eq. 8.8, this current is given by

$$I = \frac{e_c \dot{z} \xi}{H} \approx \frac{e_c \xi \sqrt{\hbar\omega/m}}{H} . \tag{8.16}$$

For the above parameter set, this current amounts to 0.1 fA, for a wire resistance of 0.6 Ω; thus 2 $\times 10^5$ s would be required to dissipate only one quantum of vibrational energy. Given the very small current and the I^2 dependence of the heating law, this is not surprising. Therefore, the dissipation of the induced currents will not pose a problem.

8.3.2 Electric field noise

Johnson noise and anomalous heating are two manifestations of the uncontrolled fluctuations in electric field (electric field noise) that acts upon an ion. These processes can result in the ion gaining kinetic energy in an uncontrolled way, and therefore decohering the motional state of the ion.

Johnson noise

We begin our discussion of Johnson noise by writing down the Johnson noise heating power P_J:

$$P_J = k_B T \Delta\nu, \tag{8.17}$$

where, as usual, k_B is Boltzmann's constant, T is the temperature, and $\Delta\nu$ is the frequency bandwidth in which the ion accepts the power. The latter is inversely related to the Q-factor of the ion's motion, mentioned above. To calculate the time over which one quantum of vibrational energy is absorbed from the wire by the ion, we use the formulas $E_v = h\nu$ and $Q = \nu/\Delta\nu$, and arrive at

$$\tau^{-1} = \frac{P_J}{E_v} = \frac{k_B T \Delta\nu}{h\nu} = \frac{k_B T}{hQ}. \tag{8.18}$$

An alternative, but equivalent expression for the Q parameter (c.f. Sec. 8.2.2) may be derived from the dissipated power $P_d = I^2\Re(Z)$, where I is the current due to a single ion and $\Re(Z)$ is the real part of the impedance. We find that

$$Q = \frac{E_{\text{ion}}}{P_d/\nu} = \frac{m\dot{z}^2\nu}{I^2\Re(Z)} = \frac{m\nu H^2}{e_c^2\xi^2\Re(Z)}. \tag{8.19}$$

Putting it all together, we calculate the time constant for the absorption of one quantum to be

$$\tau^{-1} = \frac{k_B T e_c^2\xi^2\Re(Z)}{h\nu m H^2}. \tag{8.20}$$

Taking $\Re(Z) = 0.6\ \Omega$ at $T = 298$ K, and using the same parameters given above, the heating time due to Johnson noise is $\tau = 0.1$ s/quantum. The corresponding rate $1/\tau$ is thus significantly smaller than the motional coupling rate ($\mathcal{O}(10^3\text{ s})$) calculated above. However, the heating rates are not expected to be dominated by Johnson noise, especially at room temperature.

Anomalous heating

Anomalous heating is a motional heating of ions with a poorly-understood origin. It scales as roughly D^{-4}, where D is the distance from the equilibrium position of the ion to the nearest trap electrode. This scaling law implies that as ion traps become smaller, the noise level can quickly lead to too much decoherence of the ions' motional state. Even a very low heating rate in a room temperature trap, such as observed in Ref. [SCR$^+$06], will add a quantum of energy to the ion's motional state in, on average, 200 μs. However, as we have reported elsewhere in this thesis, cryogenic cooling can greatly mitigate this heating. Taking our estimate of $t_{ex} = 1$ ms, along with the best-case heating rate reported in Ref. [LGA+08] in a 75 μm trap (5 quanta/s), it does seem reasonable to be able to observe the coupling without interference from heating, provided that the trap and the wire are sufficiently cooled. Even with a simulated coupling rate of $J = 100$ s^{-1}, spin models of a modest size may be simulated. Both of these estimates, however, depend upon internal state coherence times being on the same order as or greater than the motional heating time.

8.4 Experimental questions

We have now calculated, or otherwise justified, the expected coupling rates and decoherence rates for our system. However, these rates are based on a specific model, which will not hold perfectly in the lab. Can we anticipate some effects that may require adjustment to the model? Also, what are the steps that should be done before attempting a wire-mediated coupling experiment? There are three main questions that drive the experimental work of the next chapter:

1. What are the constraints on the resistance and capacitance between the wire and ground?
2. How do the rf confining fields affect the potential on the wire?
3. How do the heating rates scale as a function of ion-wire distance?

The first question will guide the setup of the experiment, while the second and third will require experimental measurements. We discuss each briefly.

8.4.1 DC and RF paths from the wire to ground

Intuitively, paths to ground, whether rf or dc, seem likely to reduce the coupling rate by allowing charge to escape from the "system" to the "environment." Here, we will briefly justify why this is the case, and put it into a more quantitative form, in order to figure out exactly *how* isolated the wire must be from ground.

We first consider the wire's resistance to ground. The wire basically is an RC circuit, with a very large resistance and very small capacitance. The figure of merit is the time constant that characterizes the leakage rate of charge on the wire to ground. Clearly, a fast time constant will result in the shorting of the current moving between the two ions to ground, reducing the coupling rate. The necessary condition will be $\tau_{leak} = RC \gg t_{ex}$. For a capacitance of a few femtofarads, we find that $R = 10^{13}\ \Omega$ will provide a leakage time greater than 1 s. Current leakage, however, is not the only consideration. Note that a changing total charge on the wire will randomly change the force exerted on the ions, leading to decoherence of their motional states. Therefore, whatever the total charge on the wire is, we require it to remain constant during an experiment. Satisfying the above condition should suffice. Note that the above resistance is also consistent with the requirement due to Johnson noise presented in Sec. 8.2.2.

Next, we consider how small the capacitance actually needs to be. Intuitively, a capacitance at rf is the same as a short, and therefore the current moving between the ions will be coupled to ground and the overall coupling between ions will be weakened. This is mathematically borne out by Eq. 8.13, which contains the capacitance between the wire and ground in the denominator. As noted in Sec. 8.2.2, the needed wire capacitance C may be calculated from a target motional coupling rate, which we take to be $\omega_{ex} = 10^3$ s^{-1}. Taking the inductance of each ion to be the calculated value of 3.7×10^4 H and the motional frequencies to be $\omega/(2\pi) = 1$ MHz, we arrive at a capacitance of 3×10^{-15} F.

We see that the wire must be electrically floating to a very high degree. This affects the choices of materials, as well as the expected potentials on the wire. For instance, a very good insulator must be used to mount the wire near the ions. This, though, leads in turn to the possibility of large amounts of stray charge existing on that piece. It is also certainly true that some unknown charge will reside on the wire as well. This affects the compensation voltages, and also raises the possibility of yet another decoherence source: the random gain or loss of electrons on the wire during an experiment. This is not a problem as long as the resistance is very, very high.

8.4.2 Potentials on the wire due to the rf trapping fields

Unknown, slowly-varying charges on the wire can lead to changing compensation voltages, as well as (possibly) to decoherence. However, the charges in the wire are also influenced by the rf trapping fields. Our model above does not include this effect, but we can expect that the wire will be polarized by these electric fields, in such a way that the fields tend to be cancelled near the wire. In this sense, we can think of the wire as an rf ground, despite our best efforts to isolate it from ground. This is due to the effect that the wire will have on the curvature of the electric field lines.

An important experiment will be to measure how exactly the secular frequencies vary as a function of the ion-wire distance. As we have seen, increasing secular frequencies are bad for the coupling rate. How do the changing frequencies then affect the scaling of the coupling rate as a function of ion-wire distance? If they adversely affect ω_{ex} too much, perhaps then we can reduce the rf trapping voltages in order to keep the ω_i low. When we do this, is the trap still stable? How does the trap depth change?

8.4.3 Heating rates vs. ion-wire distance

It has been generally observed that anomalous heating tends to have a D^{-4} dependence, where D is the distance from the ion to the nearest trap electrode. This is a general trend with a lot of scatter, however. The authors of Ref. [DOS$^+$06] did a systematic study using two rf electrodes with a variable distance from the ion, and found that the exponent is more nearly -3.5. We wish to undertake a similar experiment, but with the electrically floating wire that will be used for the coupling experiment. Heating rates as a function of the ion's distance from an electrically floating conductor have not previously been measured.

Further systematic measurements of the distance dependence of heating rates should be undertaken. These are not only germane to the eventual coupling experiment, but also are an interesting experiment in their own right, as they may yield additional insight into the origins of anomalous heating.

8.5 Summary

In this chapter, we have reviewed the motivation for and theory of the coupling of two ions over a conducting wire. It has become clear from our predicted coupling rate, together with observed heating rates at room temperature and at cryogenic temperatures, that cryogenic cooling will probably be necessary to observe coherent transfer of information across a wire. However, we have also pointed out some important questions, regarding the potential on the wire arising from the trapping potentials, together with the distance dependence of the heating rates, that can be addressed in a room-temperature apparatus.

The pursuit of the answers to these questions is presented in the next chapter. Although the primary topic of this thesis is quantum simulation, and electronic communication between ions could certainly facilitate that goal, it is a necessary first step to take a foray into the interaction between single ions and solid materials.

Chapter 9

Measuring the interaction of a single ion with a wire

We now turn to the experimental characterization of the interaction between a conducting wire and a single ion in a Paul trap. Recalling from Ch. 8 that the wire to be used in a coupling experiment must be electrically floating both at dc and rf frequencies, we expect that the rf voltage which drives the trap will induce a significant voltage on the wire, which in turn will influence the rf potential seen by the ion. In addition, the wire will carry some unknown dc charge, which cannot flow to ground because the wire is floating at dc. The primary purpose of this chapter is to measure how the secular frequencies and dc compensation voltages depend on the ion-wire distance. In addition, we investigate whether distance-dependence of the ion heating rates can be observed.

The present experiment has two main objectives. The first, in line with the overall goal of the thesis, is exploring the possibility of electrically connecting ions in different traps for scaling up quantum simulation. Understanding the effects of the capacitive connection between the wire and the trap, as well as the impact of unknown charge on the wire, is important for estimating the feasibility of the coupling experiment under the constraints enumerated in Ch. 8. The second objective is to investigate the possibility of measuring electrical properties of a macroscopic conductor using a single trapped ion as an extremely sensitive detector. Indeed, recent work in measuring heating rates in microfabricated traps not only demonstrates the suppression of heating at cryogenic temperatures [LGA$^+$08], a boon to quantum computation and simulation, but also provides a way to probe the surface physics of these conductors [LGL$^+$08]. We believe the types of measurements presented in this chapter are another step towards measuring not only noise, but also the capacitance and total charge of macroscopic objects using a single ion.

The chapter is organized as follows. In Sec. 9.1, we discuss the experimental apparatus used, which will introduce a new ion species, $^{40}\mathrm{Ca}^+$. Our experimental methodology for measuring stray dc voltages, secular frequencies, and heating rates is then presented in

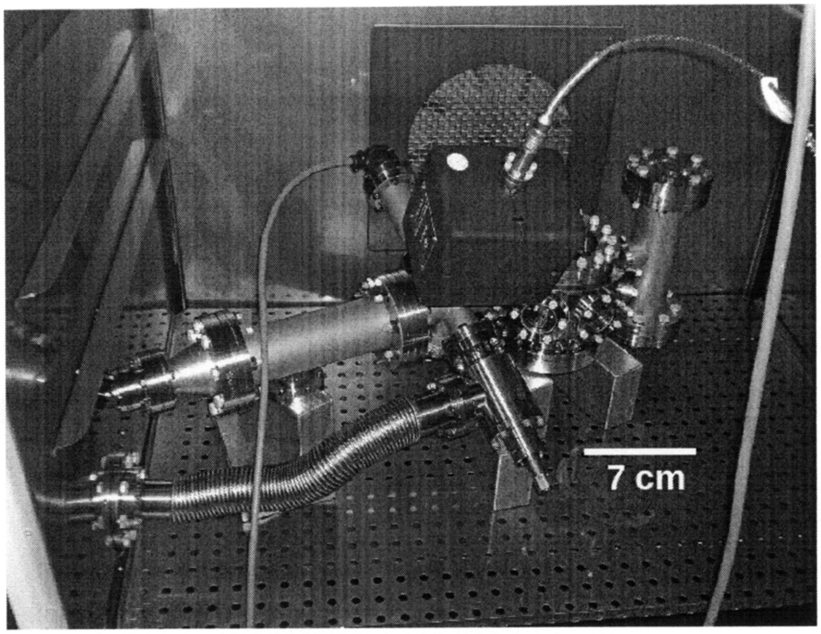

Figure 9-1: Photograph of the vacuum chamber used in Innsbruck for this ion-wire coupling experiment. The titanium sublimation pump is mounted on the left. Near the center, the ion pump, ion gauge, and main all-metal valve are mounted at an angle to the main axis of the chamber. The spherical octagon is on the right, with AR-coated CF35 (metric) viewports, roughly equivalent in diameter to 2 3/4 in. CF hardware.

Sec. 9.2. Sec. 9.3 contains the experimental results, and in Sec. 9.4, we conclude and look to future experiments.

9.1 Experimental apparatus

Much of the apparatus is similar to that used in Part II. The basic elements of a room temperature UHV system, and rf-driven Paul trap are the same as used at MIT on the strontium ion. The vacuum system is shown in Fig. 9-1.

For the rest of the section, we focus on those elements that are substantially different from the MIT setup, including the ion species, the microfabricated gold surface-electrode trap, and the moveable wire.

9.1.1 The ^{40}Ca$^+$ ion

The ^{40}Ca$^+$ ion has a level structure very similar to ^{88}Sr$^+$. The structure is presented in Fig. 9-2. The laser wavelengths for ^{40}Ca$^+$ (that we used) are $\lambda_{Dopp} = 397$ nm and $\lambda_{Rep} = 866$ nm. The spontaneous decay rate of the $P_{1/2}$ level is 23 MHz with a branching ratio of 16. Ion production is accomplished by photoionization (PI) of a neutral calcium beam in a manner analogous to that used for strontium (Chs. 5 and 7). The requisite photons,

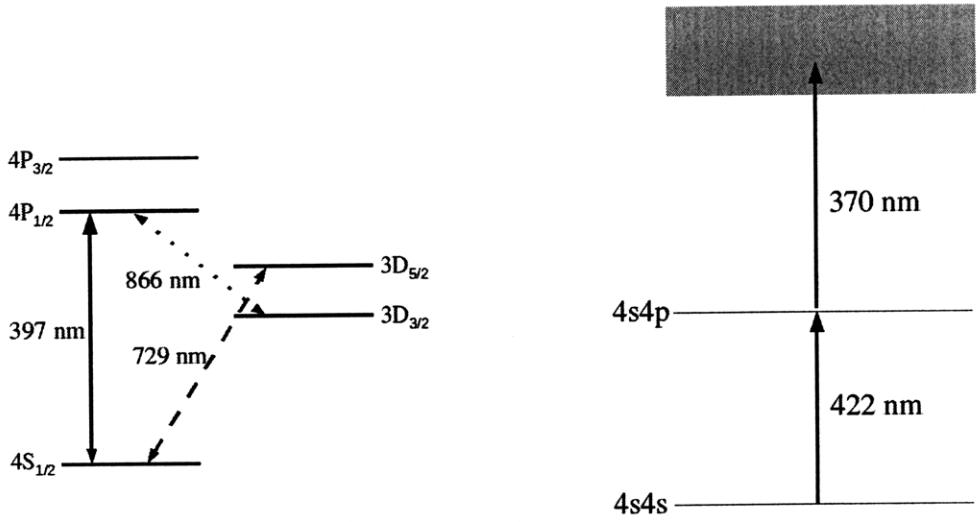

Figure 9-2: Left: Level diagram for the $^{40}\mathrm{Ca}^{+}$ ion, showing the Doppler cooling transition at 397 nm, the repumper at 866 nm, and the sideband cooling and coherent operations laser at 729 nm. The spontaneous emission rate from the $4\mathrm{P}_{1/2}$ state is 23 MHz, with the ion decaying to $3\mathrm{D}_{3/2} \approx 1/16$ of the time. The lifetime of the $3\mathrm{D}_{5/2}$ state is ≈ 1.2 s. Right: Photoionization transitions for $^{40}\mathrm{Ca}$. A 422 nm photon pumps the atom from the $4s4s$ state to the excited $4s4p$ state, then a 370 nm photon takes the atom into an autoionizing level, resulting in the loss of a single electron.

at 422 and 370 nm, are generated from extended cavity diode lasers. A schematic of the two-photon PI process is also given in Fig. 9-2.

The laser system was furnished by Toptica. The 397 nm Doppler cooling beam is produced by frequency-doubling a 794 nm laser diode, while the 866 nm radiation is produced from an extended cavity diode laser directly. Photographs of these lasers are presented in Fig. 9.1.1 and Fig. 9-4.

The lasers are locked using the Pound-Drever-Hall (P-D-H) method to a four-hole ULE cavity under vacuum, with an approximate pressure of 10^{-8} mbar.[1] The control electronics for current and temperature stabilization, as well as the P-D-H lock are furnished by Toptica. The frequencies are then monitored using a Toptica wavemeter.

9.1.2 The microfabricated trap

The trap is manufactured using standard microfabrication techniques. The credit for the design and manufacture of the traps goes to Nikos Daniilidis, a post-doc in the Innsbruck group who collaborated on this project with Andreas Wallraff at ETH Zürich. The trap

---

[1] In this chapter we shall use mbar rather than torr to describe vacuum pressures. Fortunately, 1 mbar = 0.75 torr, so that they are on the same order of magnitude.

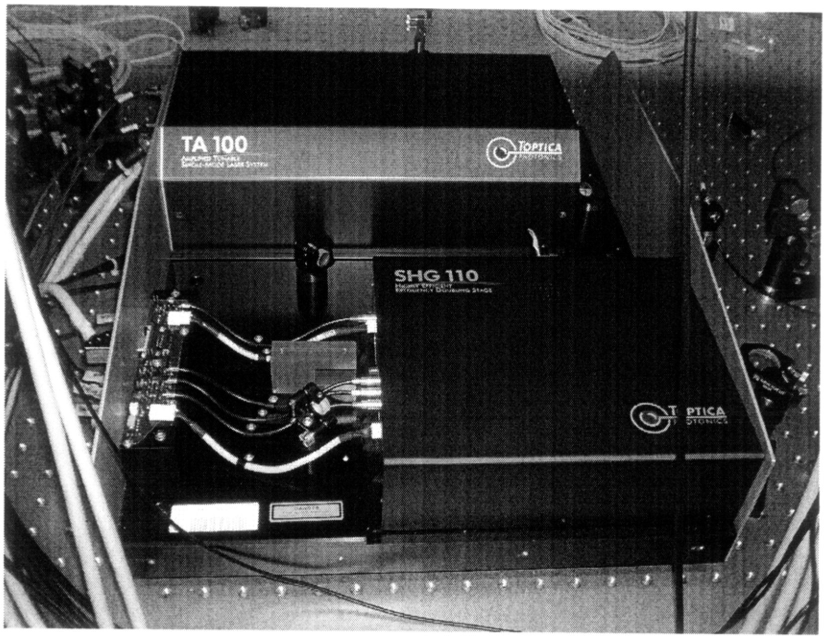

Figure 9-3: Photograph of the 397 nm laser. The main laser diode is contained within the larger box, while the doubling cavity is within the smaller. The distance between holes on the optical table is 2.5 cm.

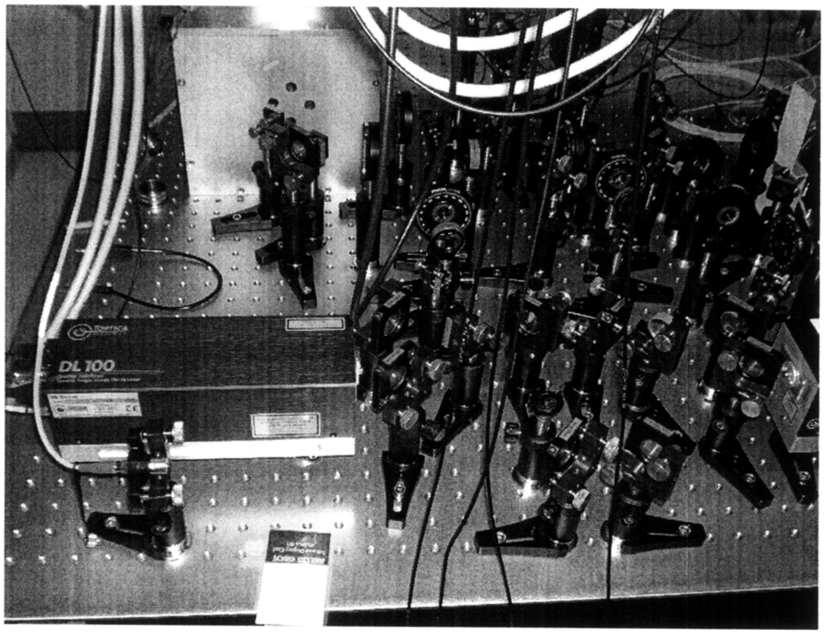

Figure 9-4: Photograph of the 866 nm laser and the outer vacuum vessel of the four-hole cavity (background). The distance between holes on the optical table is 2.5 cm.

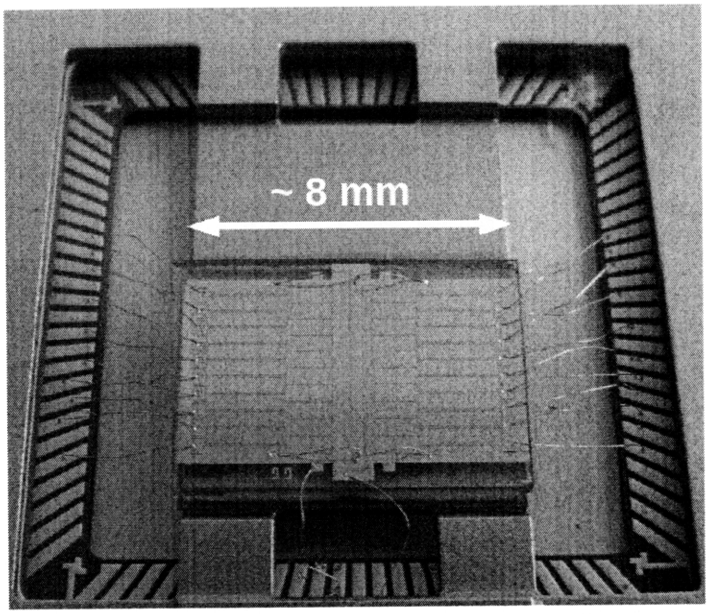

Figure 9-5: Photograph of the microfabricated trap used for ion-wire coupling experiments. The trap is mounted in a CPGA chip carrier, and wirebond connections to the gold pads are seen.

is shown in Fig. 9-5. The substrate is a sapphire wafer, used because of the low losses in the GHz range sought by superconductivity researchers. For our purposes, it did not need to be sapphire, but this works as well as other substrates for us, and the knowledge of the Wallraff group in working with this material was available to us. The metallic layers are as follows: 5 nm evaporated titanium (the adhesion layer), 100 nm evaporated gold, and finally 4-5 μm electroplated gold. The final rms surface roughness, as measured using an atomic force microscope (AFM) is 20 nm.

9.1.3 The wire

The wire used for the present experiments, and probably also for future attempts at ion-ion coupling, is a gold wire of the type used for wirebonding, with a diameter of 25 μm. It is mounted on a stainless steel "fork" with insulating ceramic inserted into the fork actually making contact with the wire. The wire is glued in place on the ceramic with UHV-compatible epoxy (EpoTek 353-ND). The fork is connected to a stack of four UHV- (and low temperature-) compatible piezoelectric actuators, furnished by AttoCube. This permits the control of four degrees of freedom: rotation of the fork about the piezo stack, translation of the wire forward and backward, vertical translation, and rotation of the wire about the axis parallel to the arms of the fork. The first and second are used to move the wire above the trap and position it slightly to one side of the trap center. The fourth is adjusted to make the wire as parallel as possible to the plane of the trap electrodes. It is the third that is used in our measurements to vary the distance between the wire and ion.

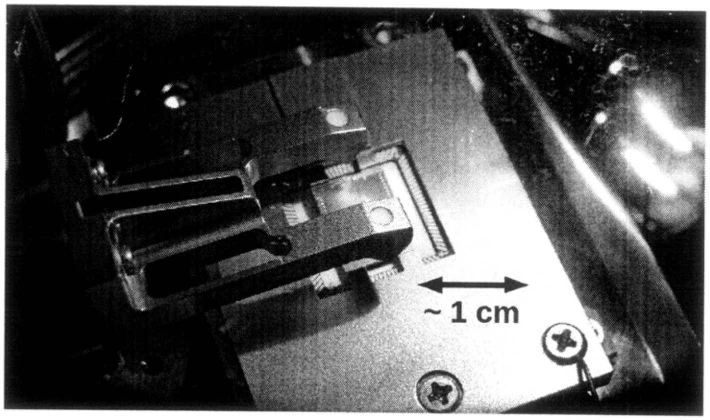

Figure 9-6: Photograph of the fork holding the wire, mounted above the trap in the vacuum chamber. The fork is machined from stainless steel, and ceramic spacers inserted into the arms of the fork provide the wire's electrical isolation. The wire, due to its 25 μm width, may be difficult to see in the picture.

A photograph of this setup is presented in Fig. 9-6.

9.2 Experimental methodology

9.2.1 Compensation and frequency measurements

The measurement of secular frequencies is done as described before (Chs. 5-7). The measurement of compensation voltages was done in an interesting way that has not been described in this thesis before. The idea is to mix in the resonant voltage at the secular frequencies directly on the rf electrodes. If the ion is at the rf null, then it will not be excited by this field; otherwise, the excitation of the secular motion can be observed. Typically, a small voltage will be required at first to excite an uncompensated ion. As compensation improves, this voltage can be increased.

9.2.2 Heating rate measurements

Heating rate measurements for higher levels of heating (many quanta/s) can be done using the method of *Doppler recooling.* This method was described theoretically in Ref. [WEL$^+$07] and then demonstrated experimentally in Ref. [ESL$^+$07]. The method consists of the following steps:

1. Doppler cool a single ion to its steady-state fluorescence level.

2. Turn off the cooling laser for a period of time.

3. Switch on the cooling laser and record the ion's fluorescence as a function of time.

A fit of the resulting curve returns the initial energy of the ion, provided that the laser detuning and intensity are well-known. The detuning and saturation parameter (related to the intensity) are plugged into the fit function, such that E_0 is the only free parameter. The derivation of this formula is presented in the theoretical paper cited above. An experiment is repeated several times to get a good curve. Since heating is a stochastic process, the ion heats up by a different amount each time, and averaging is required to get a good value for the average heating rate.

9.3 Measurements

In this section we present the data for one experimental run, bringing in the wire from a far distance ($D > 4$ mm) to $D = 0.6$ mm from the trapped ion. At each wire position, compensation was done and the vertical compensation voltage was recorded, the vertical and horizontal secular frequencies were recorded, and a heating rate measurement was performed.

For all the measurements in this section, the trap drive frequency was $\Omega/(2\pi) = 14.74$ MHz, with a drive voltage of $V_{rf} \approx 200$ V. The center of the trap was set at ground, and the voltages on the other electrodes that yielded a compensated trap were between -10 and 10 V.

Vertical compensation

Two compensation voltages, called H and V, were varied as the wire is brought in. Each is a linear combination of the voltages on several of the dc electrodes, with H changing primarily the electric field in the $\hat{x}$ direction, and V changing the field in the $\hat{y}$ direction. Of the two, only V changes appreciably, since the wire is moving vertically down onto the ion, with a small offset ($\approx$50 μm) for imaging the ion. The vertical wire positions are plotted in Fig. 9-7. We see that there is a monotonic but nonlinear dependence on the wire position. It is possible that the dc charge on the wire changes during the course of the experiment, either by discharging or by picking up stray charged particles from the (small) ambient pressure or photoelectrons induced by laser scatter.

Secular frequencies

We plot here in Fig. 9-8 the secular frequency measurements for the same set of wire positions as above. Only the horizontal ($\omega_{\hat{x}}$) and vertical ($\omega_{\hat{y}}$) frequencies are plotted.

The secular frequencies fit well to a $1/D^2$ dependence, as displayed in Fig. 9-9. The equations are $\omega_{\hat{y}}/(2\pi) = 0.124/D^2 + 1.63$ and $\omega_{\hat{x}}/(2\pi) = 0.121/D^2 + 1.44$, where $\omega_{\hat{y}}$ and $\omega_{\hat{x}}$ are the vertical and horizontal frequencies measured in 10^6 s^{-1} and d is the ion-wire distance measured in mm. 1.63 and 1.44 MHz are the values of $\omega_{\hat{y}}$ and $\omega_{\hat{x}}$, respectively, when the wire is effectively at $D = \infty$, and is not influencing the trap at all.

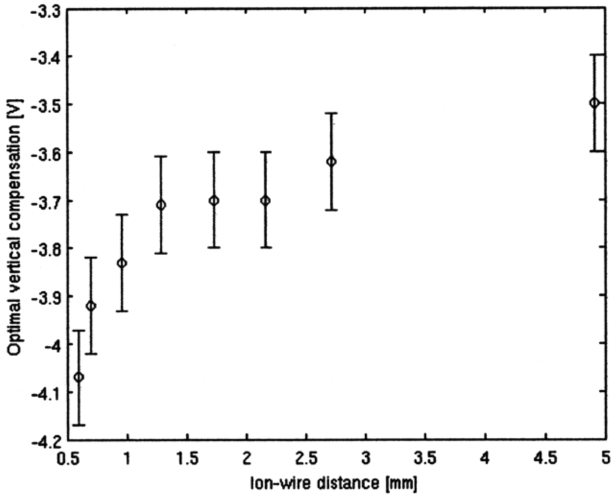

Figure 9-7: Measured dc vertical compensation values as a function of the height of the wire above the ion.

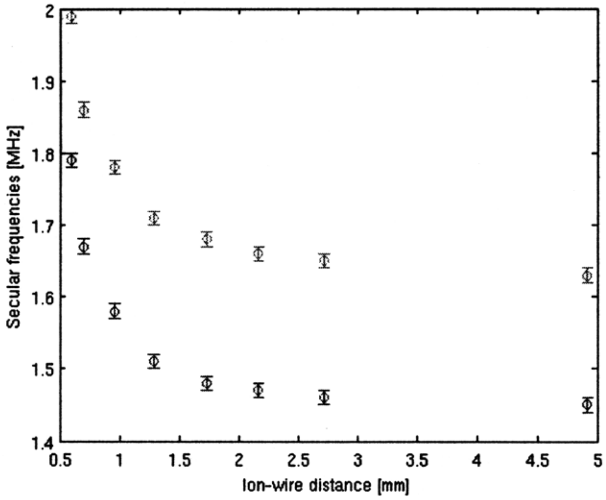

Figure 9-8: Horizontal ($\omega_{\hat{x}}$) and vertical ($\omega_{\hat{y}}$) secular frequencies as a function of the distance from the wire to the ion.

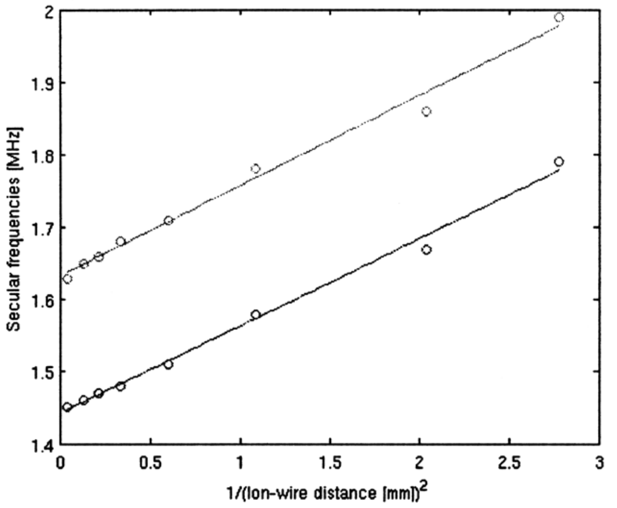

Figure 9-9: Linear fit of the $\omega_{\hat{y}}$ (green) and $\omega_{\hat{x}}$ (red) secular frequencies to $1/D^2$, where D is the ion-wire distance.

Why might this $1/D^2$ dependence appear? Our hypothesis is as follows. The rf voltage on the wire arises from a capacitive coupling from the rf electrodes to the wire. The electric field seen by the ion falls off as $1/D$, from the elementary problem in electrostatics (assuming the wire to be long). In addition, the induced voltage on the wire scales as $1/D$. This may be understood intuitively by considering the wire-trap system to be a parallel plate capacitor with one plate (the wire) much smaller than the other. Since the secular frequencies are directly proportional to the magnitude of the electric field acting on the ion, this produces a $1/D^2$ scaling.

Heating rates

We now present the heating rate measurements. These were done using the Doppler recooling method. At each wire position, the time-dependent fluorescence was recorded 200 times and added up to produce the data presented here. Fig. 9-10 shows an example plot of this data and the fit to it. The initial energy can be inferred from this plot, according to the method presented in Ref. [WEL$^+$07].

Such plots were done for each data set, and the resulting heating rate measurements are presented in Fig. 9-11 and Fig. 9-12.

Although we do not see a clear trend as a function of the ion-wire distance, this is actually a positive result. After all, the ion is closer to the trap than to the wire, and the surface area of the trap is much greater. We would expect the wire to need to get significantly closer to the ion than the trap is before heating effects due to the wire are noticeable. This bodes well for getting the wire close to the ions without inducing excess heating. Indeed, in the future, cryogenic cooling should suppress this baseline heating that

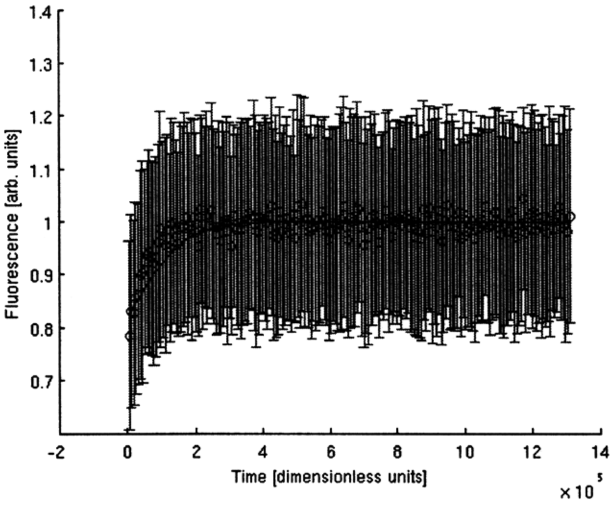

Figure 9-10: Example Doppler recooling fit. Data points are an average of 200 measurements; error bars are statistical.

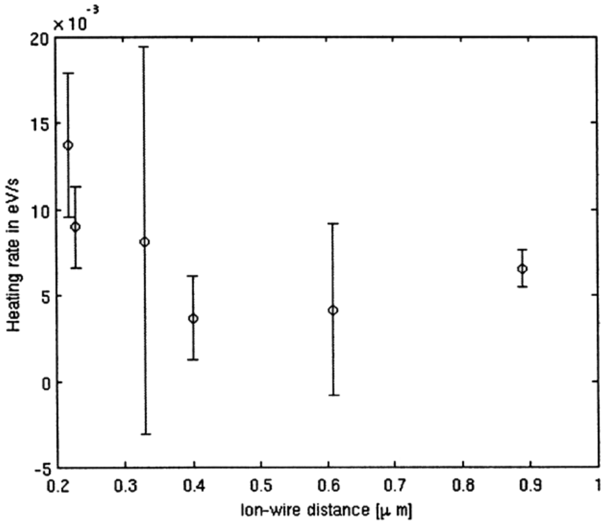

Figure 9-11: Heating rate as determined by Doppler recooling for a series of ion-wire distances. The heating rate is presented in eV/s.

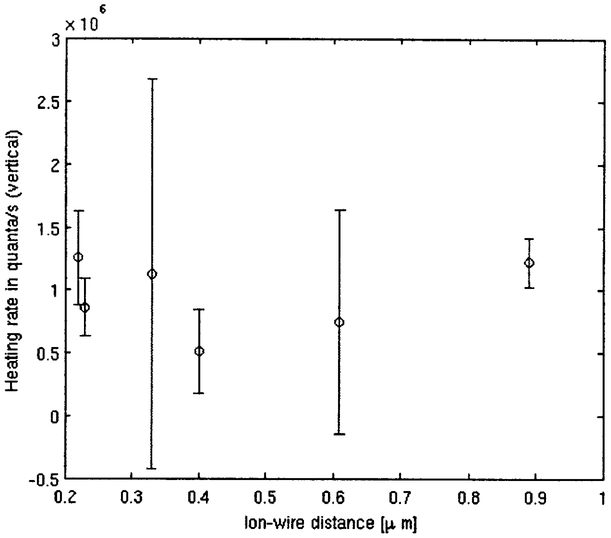

Figure 9-12: Heating rate as determined by Doppler recooling for a series of ion-wire distances. The heating rate is presented in quanta/s. Upon normalizing for the secular frequency, the heating rate is roughly constant as the wire approaches.

we see.

9.4 Conclusions

Ion-ion coupling over a wire is an intriguing possibility for quantum networking. This could find application in both quantum simulation and quantum computation. However, the necessity of the wire being electrically floating at both dc and rf frequencies poses some difficulty for this. The increase of secular frequencies as the wire approaches the ion is detrimental to the coupling rate, and could even render the trap unstable if the frequencies grow too high such that the q stability parameter approaches 0.9. In addition, stray charge on the wire that does not discharge at a sufficient rate to ground influences the dc potential seen by the ion, resulting in micromotion that must be compensated.

However, in these challenges lies an opportunity. A single trapped ion is an extremely sensitive detector of electric fields. Perhaps measurements, such as those presented in this chapter, may provide a way of measuring the capacitance of the wire, and the stray charge that it holds. Such measurements would enable a more precise estimation of the wire-mediated coupling rate, given its reciprocal dependence on the wire-ground capacitance.

The prospects for ion-ion coupling are still uncertain. It is fairly clear that the trap potentials themselves will need to be reduced in magnitude as the wire approaches, and the trap in a real sense becomes three-dimensional as opposed to surface-electrode in form. Although traps of a 50 μm scale have been demonstrated, it has not been done with an electrically floating electrode. In addition, although at the current ion-wire distance no systematic change in the heating rate was seen, the wire will need to get an order of magnitude closer before ion-ion coupling at a rate of 1 kHz may be observed. A cryogenic apparatus is now under construction in Innsbruck to deal with the future heating issue, as well as reducing the baseline heating rates we already see, and enabling more-rapid testing of traps and wires.

Chapter 10

Conclusions and outlook

This thesis presents a study of two of the most important problems facing quantum simulation: precision limitations and scalability. We have looked both at digital quantum simulation, concentrating specifically on a quantum simulation of pairing models using nuclear magnetic resonance (NMR), and at analog quantum simulation, focusing on scalable two-dimensional ion trap architectures. We have also studied, in theory, the problem of two ions interacting over a conducting wire, made experimental measurements of the effect of the wire on the trap potentials, and discussed possible application to both digital and analog quantum simulation. Here we summarize the main results of the thesis, and look ahead to the new challenges raised by this work.

In Part I, we examined one method of digital quantum simulation using a nuclear spin system. We saw that the precision of quantum simulation using Fourier transform methods faces limitations to the attainable precision arising from both intrinsic and system-dependent sources. The intrinsic sources include the sampling rate of the Fourier transform, related to the collapse of the quantum state upon measurement, as well as the natural decoherence time of the system. Further, the use of error correction increases this inefficiency due to the large number of extra gates required. The primary system-dependent limit is due to control errors, which although present in any experimental system, have been studied by us specifically for the NMR system. We conclude that for algorithms of this type, quantum simulations are not *necessarily* more efficient than classical ones with respect to the *precision* of the final result.

Despite these limits, digital quantum simulation may be of great use when no classical approximation is available, and when a limited precision is acceptable. Since a (universal) digital quantum simulator is essentially a quantum computer, the wealth of contemporary research into quantum computing technology is directly applicable to quantum simulation. However, there are to date few experimental results for digital quantum simulation using scalable technologies such as ion traps. All the digital quantum simulation experiments prior to this thesis were done in nuclear spin systems. Although the precision limitations enumerated in this thesis are independent of the quantum model system being used, more study should be undertaken of the effects of control errors in scalable quantum computing systems. Is it possible that the presence of control errors and the sensitivity of quantum simulations to them is superior in one system relative to others? Is it even possible that this system will be found not to be identical to the one that is best-suited for universal quantum computation? We do not yet know the answers to these questions, but they are, in our view, fascinating ones that must be pursued.

Moving to the subject of analog quantum simulation, we saw in Part II how an array of trapped ions could be used for simulating physics such as Ising and Heisenberg spin models, and specifically spin frustration in 2-D antiferromagnetic spin lattices. We also saw, however, that building a scalable or even semi-scalable architecture for doing such simulations in 2-D is actually quite difficult. This problem arises for arrays of microtraps from the difficulty of maintaining both low secular frequencies and high trap depths at small ion-ion distances. This is a fairly straightforward result of the physics of coupled oscillators and the equations of motion of trapped ions. Although we have not proven that quantum simulation in lattice traps is impossible, it does appear to be quite difficult.

We then looked for a different trap design for 2-D quantum simulation, and moved on to studying elliptical ion traps, calculating and measuring such properties as the motional frequencies and the structure of ion crystals in these traps. We also showed that the unavoidable micromotion is not a fundamental detriment to quantum simulation, and that interesting analog simulations, such as the search for quantum phase transitions, may be possible in such an architecture. Although other trap designs exist that create 2-D lattices of ions, elliptical traps have the advantage that they can be scaled down and microfabricated, reducing overall micromotion amplitudes and also allowing for the integration of wires that produce magnetic field gradients, which we showed can be used to provide a rich variety of simulated Hamiltonians for quantum simulation.

To date, the only realization of the spin model simulation scheme has been with two ions in a linear trap. This can and should be scaled to larger numbers of ions in a linear chain, and efforts made to understand the sources of decoherence and control errors. At the same time, prototype 2-D quantum simulators should also be built. We think that elliptical traps are a good starting point. In the future, these simulations may enable us to solve very difficult problems, such as calculating the phase diagrams of 2-D antiferromagnetic lattices, that may, in turn, shed light on the causes of high-temperature superconductivity. Other condensed-matter systems, such as the Bose-Hubbard model, may be simulable in such a trap as well. Developing a good 2-D trap design is an important step toward tackling problems that classical computers cannot efficiently solve.

Despite the possibility of exceeding the simulation power of classical computation even with 40 ions in a single trap, the 2-D architectures we proposed are not truly scalable to hundreds of ions or more. We mentioned a number of ideas for scaling ion trap quantum simulators to such large numbers of qubits, including moving ions between separate microtraps, linking ions using photons, and connecting ions electrically over a wire. The last of these framed the goals for the third part of this thesis. We built a system that includes a segmented surface-electrode ion trap and a moveable wire in vacuum. We calculated the theoretical coupling rates and decoherence rates, and set bounds on the acceptable experimental parameters, including the capacitance and resistance to ground of the wire.

The resulting stringent requirement that the wire be highly isolated from ground at both dc and rf frequencies motivated the experimental work of Part III. Here, we studied the ways in which this wire changes the electrodynamic potentials that act on a single trapped ion. Although we have not yet observed ion-ion coupling over a wire, we have joined a recently-growing effort to exploit the fact that trapped ions are extremely sensitive detectors of electric fields. Most of the work to date has focused on measuring fluctuating fields, since they affect motional heating rates. Our work is a step toward measuring electrical properties of a macroscopic conductor from non-fluctuating fields.

This experiment will progress, first into a cryogenic chamber to quell the rather high heating rates already observed, and then eventually to a point at which the wire is close enough that ion-ion coupling might be observed. Sympathetic cooling or heating of an ion in a different trap would be a good place to start. We do not yet know whether this approach will be useful to scaling up simulators, but the continued experiments will help us figure this out. If successful, the project will have bearing on other interesting approaches, such as linking a superconducting qubit (a fast processor) to a single trapped ion (a long quantum memory) over a transmission line.

In sum, then, this thesis has taken steps along three quite different approaches to quantum simulation. In the course of this work several new problems were identified, which in turn motivated new questions, which we hope will form part of the efforts of researchers worldwide well into the future. We also hope that our work hastens the day when quantum simulation is reliable and commonplace, and a part of the toolbox of every researcher who can make use of it.

Bibliography

[ADM05] Paul M. Alsing, Jonathan P. Dowling, and G. J. Milburn. Ion trap simulations of quantum fields in an expanding universe. *Phys. Rev. Lett.*, **94**, 220401, 2005.

[AGDLHG05] A. Aspuru-Guzik, A. D. Dutoi, P. J. Love, and M. Head-Gordon. Simulated quantum computation of molecular energies. *Science*, **309**, 1704, 2005.

[AJL08] D. Aharonov, V. Jones, and Z. Landau. A polynomial quantum algorithm for approximating the jones polynomial. *Algorithmica*, 2008.

[AL97] D. S. Abrams and S. Lloyd. Simulation of many-body Fermi systems on a universal quantum computer. *Phys. Rev. Lett.*, **79**, 2586, 1997.

[AL99] Daniel S. Abrams and Seth Lloyd. Quantum algorithm providing exponential speed increase for finding eigenvalues and eigenvectors. *Phys. Rev. Lett.*, **83**(24), 5162–5165, 1999.

[ALB$^+$07] M. Anderlini, P. J. Lee, B. J. Brown, J. Sebby-Strabley, W. D. Phillips, and J. V. Porto. Controlled exchange interaction between pairs of neutral atoms in an optical lattice. *Nature*, **448**, 452, 2007.

[ASA$^+$09] P. B. Antohi, D. Schuster, G. M. Akselrod, J. Labaziewicz, Y. Ge, Z. Lin, W. S. Bakr, and I. L. Chuang. Cryogenic ion trapping systems with surface-electrode traps. *Rev. Sci. Instr.*, **80**, 013103, 2009.

[BB84] C. H. Bennett and G. Brassard. Quantum cryptography: Public key distribution and coin tossing. pp. 175–179, IEEE International Conference of Computers, Systems and Signal Processing, Bangalore, India, 1984.

[BBC$^+$93] C. H. Bennett, G. Brassard, C. Crepeau, R. Josza, A.Peres, and W. Wootters. Teleporting an unknown quantum state via dual classical and EPR channels. *Phys. Rev. Lett.*, **70**, 1895–1899, 1993.

[BCC06] K. R. Brown, R. J. Clark, and I. L. Chuang. Limitations of quantum simulation examined by simulating a pairing Hamiltonian using nuclear magnetic resonance. *Phys. Rev. Lett.*, **97**, 050504, 2006.

[BCJD99] G. K. Brennen, C. M. Caves, P. S. Jessen, and I. H. Deutsch. Quantum logic gates in optical lattices. *Phys. Rev. Lett.*, **82**, 1060, 1999.

[BCL$^+$07] K. R. Brown, R. J. Clark, J. Labaziewicz, P. Richerme, D. R. Leibrandt, and I. L. Chuang. Loading and characterization of a printed-circuit-board atomic ion trap. *Phys. Rev. A*, **75**, 015401, 2007.

[BCS57] J. Bardeen, L. N. Cooper, and J. R. Schrieffer. Theory of superconductivity. *Phys. Rev.*, **108**, 1175, 1957.

[BCS$^+$04] M. D. Barrett, J. Chiaverini, T. Schaetz, J. Britton, W. M. Itano, , J. D. Jost, E. Knill, C. Langer, D. Leibfried, R. Ozeri, and D. J. Wineland. Deterministic quantum teleportation of atomic qubits. *Nature*, **429**, 737, 2004.

[BCWdW01] H. Buhrman, R. Cleve, J. Watrous, and R. de Wolf. Quantum fingerprinting. *Phys. Rev. Lett.*, **87**(16), 167902, 2001.

[BDL$^+$00] M. Block, A. Drakoudis, H. Leuthner, P. Seibert, and G. Werth. Crystalline ion structures in a Paul trap. *J. Phys. B*, **33**, L375, 2000.

[BDZ08] I. Bloch, J. Dalibard, and W. Zwerger. Many-body physics with ultracold gases. *Rev. Mod. Phys.*, **80**(3), 885, 2008.

[BH09] I. M. Buluta and S. Hasegawa. Designing an ion trap for quantum simulation. *Quant. Inf. Comp.*, **9**, 0361, 2009.

[BHC04] K. R. Brown, A. M. Harrow, and I. L. Chuang. Arbitrarily accurate composite pulses. *Phys. Rev. A*, **70**, 052318, 2004.

[BKGH08] I. M. Buluta, M. Kitaoka, S. Georgescu, and S. Hasegawa. Investigation of planar Coulomb crystals for quantum simulation and computation. *Phys. Rev. A*, **77**, 062320, 2008.

[BKRB08] J. Benhelm, G. Kirchmair, C. F. Roos, and R. Blatt. Towards fault-tolerant quantum computing with trapped ions. *Nature Physics*, **4**, 463, 2008.

[BLW$^+$07] M. Brownnutt, V. Letchumanan, G. Wilpers, R. C. Thompson, P. Gill, and A.G. Sinclair. Controlled photoionization loading of ^{88}Sr$^+$ for precision ion trap experiments. *Appl. Phys. B*, **87**, 411, 2007.

[BMB$^+$98] D. J. Berkeland, J. D. Miller, J. C. Bergquist, W. M. Itano, and D. J. Wineland. Minimization of ion micromotion in a Paul trap. *J. Appl. Phys.*, **83**, 5025, 1998.

[BW92] C. Bennett and S. J. Wiesner. Communication via one- and two-particle operators on Einstein-Podolsky-Rosen states. *Phys. Rev. Lett.*, **69**, 2881, 1992.

[BWG$^+$05] M. Brownnutt, G. Wilpers, P. Gill, R. C. Thompson, and A. G. Sinclair. Monolithic microfabricated ion trap chip design for scaleable quantum processors. *New Journal of Physics*, **8**, 232, 2005.

[CBB$^+$05] J. Chiaverini, R. B. Blakestad, J. Britton, J. D. Jost, C. Langer, D. Liebfried, R. Ozeri, and D. J. Wineland. Surface-electrode architecture for ion-trap quantum information processing. *Quant. Inf. and Comp.*, **5**, 419–439, 2005.

[CDLC09] R. J. Clark, K. S. Diab, Z. Lin, and I. L. Chuang. Surface-electrode elliptical ion traps for quantum simulation. *In preparation*, 2009.

[CFH97] D. G. Cory, A. F. Fahmy, and T. F. Havel. Ensemble quantum computing by NMR spectroscopy. *Proc. Nat. Acad. Sci. USA*, **94**, 1634, 1997.

[CGB+94] J. I. Cirac, L. J. Garay, R. Blatt, A. S. Parkins, and P. Zoller. Laser cooling of trapped ions: The influence of micromotion. *Phys. Rev. A*, **49**, 421, 1994.

[CH94] D. B. Chrissey and G. K. Hubler. *Pulsed Laser Deposition of Thin Films*, chapter 4. Wiley, 1994.

[CLBC09] R. J. Clark, T. Lin., K. R. Brown, and I. L. Chuang. A two-dimensional lattice ion trap for quantum simulation. *J. Appl. Phys.*, **105**, 013114, 2009.

[CMB+06] G. K. Campbell, J. Mun, M. Boyd, P. Medley, A. E. Leanhardt, L. G. Marcassa, D. E. Pritchard, and W. K. Ketterle. Imaging the Mott insulator shells by using atomic clock shifts. *Science*, **313**, 649, 2006.

[CPK+02] Y. Cai, W. P. Peng, S. J. Kuo, Y. T. Lee, and H. C. Chang. Single-particle mass spectrometry of polystyrene microspheres and diamond nanocrystals. *Anal. Chem.*, **74**, 232, 2002.

[CS96] A. R. Calderbank and P. W. Shor. Good quantum error correcting codes exist. *Phys. Rev. A*, **54**, 1098, 1996.

[CVZ+98] I. L. Chuang, L. M. K. Vandersypen, X. Zhou, D. W. Leung, and S. Lloyd. Experimental realization of a quantum algorithm. *Nature*, **393**, 143, 1998.

[CW08] J. Chiaverini and W. E. Lybarger, Jr. Laserless trapped-ion quantum simulations without spontaneous scattering using microtrap arrays. *Phys. Rev. A*, **77**, 022324, 2008.

[CZ95] J. I. Cirac and P. Zoller. Quantum computation with cold trapped ions. *Phys. Rev. Lett.*, **74**, 4091–4094, 1995.

[CZ00] J. I. Cirac and P. Zoller. A scalable quantum computer with ions in an array of microtraps. *Nature*, **404**, 579, 2000.

[DBIW89] F. Diedrich, J. C. Bergquist, W. M. Itano, and D. J. Wineland. Laser cooling to the zero-point energy of motion. *Phys. Rev. Lett.*, **62**, 403, 1989.

[DDL03] L.-M. Duan, E. Demler, and M. D. Lukin. Controlling spin exchange interactions of ultracold atoms in optical lattices. *Phys. Rev. Lett.*, **91**, 090402, 2003.

[DeV98] Ralph G. DeVoe. Elliptical ion traps and trap arrays for quantum computation. *Phys. Rev. A*, **58**, 910–914, 1998.

[DiV00] D. P. DiVincenzo. The physical implementation of quantum computation. *Fortschritte Der Physik - Progress of Physics*, **48**, 771, 2000.

[DK02] R. G. DeVoe and C. Kurtsiefer. Experimental study of anomalous heating and trap instabilities in a microscopic ^{137}Ba$^+$ ion trap. *Phys. Rev. A*, **65**, 063407, 2002.

[DLC+09a] N. Daniilidis, T. Lee, R. Clark, S. Narayanan, and H. Häffner. Measurement of electrical properties of a conductor with a single trapped ion. *In preparation*, 2009.

[DLC$^+$09b] N. Daniilidis, T. Lee, R. Clark, S. Narayanan, and H. Häffner. Wiring up trapped ions to study aspects of quantum information. *J. Phys. B., to appear*, 2009.

[DOS$^+$06] L. Deslauriers, S. Olmschenk, D. Stick, W. K. Hensinger, J. Sterk, and C. Monroe. Scaling and suppression of anomalous heating in ion traps. *Phys. Rev. Lett.*, **97**, 103007, 2006.

[DRS03] J. Dukelsky, J. M. Roman, and G. Sierra. Comment on "Polynomial-time simulation of pairing models on a quantum computer". *Phys. Rev. Lett.*, **90**, 249803–1, 2003.

[DS96] D. P. DiVincenzo and P. W. Shor. Fault-tolerant error correction with efficient quantum codes. *Phys. Rev. Lett.*, **77**, 3260, 1996.

[DS99] J. Dukelsky and G. Sierra. A density matrix renormalization group study of ultrasmall superconducting grains. *Phys. Rev. Lett.*, **83**, 172, 1999.

[EKN68] L. E. Estes, T. H. Keil, and L. M. Narducci. Quantum-mechanical description of two coupled harmonic oscillators. *Physical Review*, **175**, 286–299, 1968.

[ESL$^+$07] R. J. Epstein, S. Seidelin, D. Leibfried, J. H. Wesenberg, J. J. Bollinger, J. M. Amini, R. B. Blakestad, J. Britton, J. P. Home, W. M. Itano, J. D. Jost, E. Knill, C. Langer, R. Ozeri, N. Shiga, and D. J. Wineland. Simplified motional heating rate measurements of trapped ions. *Phys. Rev. A*, **76**, 033411, 2007.

[Fey82] R. Feynman. Simulating physics with computers. *Int. J. Theor. Phys.*, **21**, 467, 1982.

[Fis76] J. R. Fisk. Helical-resonator design techniques. *QST*, p. 11, 1976.

[FKW02] M. H. Freedman, A. Kitaev, and Z. Wang. Simulation of topological field theories by quantum computers. *Comm. Math. Phys.*, **227**, 587, 2002.

[FSG$^+$08] A. Friedenauer, H. Schmitz, J. Glückert, D. Porras, and T. Schätz. Simulating a quantum magnet with trapped ions. *Nature Physics*, **4**, 757, 2008.

[GC97] N. Gershenfeld and I. L. Chuang. Bulk spin-resonance quantum computation. *Science*, **275**, 350, 1997.

[GC99] D. Gottesman and I. L. Chuang. Demonstrating the viability of universal quantum computation using teleportation and single-qubit operations. *Nature*, **402**, 390, 1999.

[Gho95] P. K. Ghosh. *Ion Traps.* Oxford Science Publications, 1995.

[GKK$^+$08] D. Gavinsky, J. Kempe, I. Kerenidis, R. Raz, and R. de Wolf. Exponential separation for one-way quantum communication complexity, with applications to cryptography. *www.arxiv.org: quant-ph/0611209v3*, 2008.

[GL50] V. L. Ginzburg and L. D. Landau. *Zh. Eksperim. i Teor. Fiz.*, **20**, 1064, 1950.

[GME$^+$02] M. Greiner, O. Mandel, T. Esslinger, T. W. Hänsch, and I. Bloch. Quantum phase transition from a superfluid to a Mott insulator in a gas of ultracold atoms. *Nature*, **415**, 39–44, 2002.

[Got97] D. Gottesman. Theory of fault-tolerant quantum computation. *Phys. Rev. A*, **57**, 127, 1997.

[GP00] G. Grosso and G. P. Parravicini. *Solid State Physics.* Academic Press, 2000.

[GRL$^+$03] S. Gulde, M. Riebe, G. P. T. Lancaster, C. Becher, J. Eschner, H. Häffner, F. Schmidt-Kaler, I. L. Chuang, and R. Blatt. Implementation of the Deutsch-Josza algorithm on an ion-trap quantum computer. *Nature*, **421**, 48–50, 2003.

[Gro97] L. K. Grover. Quantum computers can search arbitrarily large databases by a single query. *Phys. Rev. Lett.*, **79**, 4709, 1997.

[GS01] B. Georgeot and D. L. Shepelyansky. Exponential gain in quantum computing of quantum chaos and localization. *Phys. Rev. Lett.*, **86**(13), 2890–2893, 2001.

[HBW98] R. Cleve H. Buhrman and A. Wigderson. Quantum vs. classical communication and complexity. In *Proceedings of the 30th Annual ACM Symposium on Theory of Computing*, p. 63, ACM, New York, NY, 1998.

[HDS$^+$08] G. Huber, T. Deuschle, W. Schnitzler, R. Reichle, K. Singer, and F. Schmidt-Kaler. Transport of ions in a segmented linear Paul trap in printed-circuit-board technology. *New Journal of Physics*, **10**, 013004, 2008.

[HGH$^+$07] R. J. Hendricks, D. M. Grant, P. F. Herskind, A. Dantan, and M. Drewsen. An all-optical ion-loading technique for scalable microtrap architectures. *Appl. Phys. B*, **88**, 507–513, 2007.

[HHHR01] W. Hänsel, P. Hommelhoff, T. W. Hänsch, and J. Reichel. Bose-Einstein condensation on a microelectronic chip. *Nature*, **413**, 498, 2001.

[HHR$^+$05] H. Häffner, W Hänsel, C. F. Roos, J. Benhelm, D. Chek-al-kar, M. Chwalla, T. Körber, U. D. Rapol, M. Riebe, P. O.Schmidt, C. Becher, O. Gühne, W. Dür, and R. Blatt. Scalable multiparticle entanglement of trapped ions. *Nature*, **438**, 643, 2005.

[HMO$^+$06] Y. Hashimoto, L. Matsuoka, H. Osaki, Y. Fukushima, and S. Hasegawa. Trapping laser ablated ^{40}Ca$^+$ ions in linear Paul trap. *Japanese Journal of Applied Physics*, **45**, 7108, 2006.

[HOS$^+$06] W. K. Hensinger, S. Olmschenk, D. Stick, D. Hucul, M. Yeo, M. Acton, L. Deslauriers, and C. Monroe. T-junction ion trap array for two-dimensional ion shuttling, storage, and manipulation. *Appl. Phys. Lett.*, **88**, 034101, 2006.

[HSG$^+$07] A. A. Houck, D. I. Schuster, J. M. Gambetta, J. A. Schreier, B. R. Johnson, J. M. Chow, L. Frunzio, J. Majer, M. H. Devoret, S. M. Girvin, and R. J. Schoelkopf. Generating single microwave photons in a circuit. *Nature*, **449**, 328–331, 2007.

[HSKH$^+$05] H. Häffner, F. Schmidt-Kaler, W. Hänsel, C. F. Roos, T. Körber, M. Chwalla, M. Riebe, J. Benhelm, U. D. Rapol, C. Becher, and R. Blatt. Robust entanglement. *Appl. Phys. B*, **81**, 151, 2005.

[HW90] D. J. Heinzen and D. J. Wineland. Quantum-limited cooling and detection of radio-frequency oscillations by laser-cooled ions. *Phys. Rev. A*, **42**(5), 2977, 1990.

[IBT$^+$98] W. M. Itano, J. J. Bollinger, J. N. Tan, B. Jelenkovic, T. B. Mitchell, and D. J. Wineland. Bragg diffraction from crystallized ion plasmas. *Science*, **279**, 686–689, 1998.

[JBT$^+$08] M. Johanning, A. Braun, N. Timoney, V. Elman, W. Neuhauser, and C. Wunderlich. Individual addressing of trapped ions and coupling of motional and spin states using rf radiation. *www.arxiv.org: quant-ph/0801.0078*, 2008.

[JOV$^+$08] J. Jordan, R. Orús, G. Vidal, F. Verstraete, and J. I. Cirac. Classical simulation of infinite-size quantum lattice systems in two spatial dimensions. *www.arxiv.org: cond-mat/0703788v4*, 2008.

[JSG$^+$08] Robert Jördens, Niels Strohmaier, Kenneth Günter, Henning Moritz, and Tilman Esslinger. A Mott insulator of fermionic atoms in an optical lattice. *Nature*, **455**, 204, 2008.

[Kas50] A. Kastler. Quelques suggestions concernant la production optique et la détection optique d'une inégalité de population des niveaux de quantifigation spatiale des atomes. application à l'expérience de stern et gerlach et à la résonance magnétique. *J. Phys. Radium*, **11**, 255, 1950.

[KBT$^+$06] F. H. L. Koppens, C. Buziert, K. J. Tielrooij, I. T. Vink, K. C. Nowack, T. Meunier, L. P. Kouwenhoven, and L. M. K. Vandersypen. Driven coherent oscillations of a single electron spin in a quantum dot. *Nature*, **442**, 766, 2006.

[KGF$^+$90] V. H. S. Kwong, T. T. Gibbons, Z. Fang, J. Jiang, H. Knocke, Y. Jiang, and B. Ruger. Experimental apparatus for production, cooling, and storing multiply charged ions for charge-transfer measurements. *Rev. Sci. Inst*, **61**, 1931, 1990.

[KJL$^+$08] I. Kassal, S. P. Jordan, P. J. Lovec, M. Mohsenia, and A. Aspuru-Guzik. Polynomial-time quantum algorithm for the simulation of chemical dynamics. *Proc. Nat. Acad. Sci. USA*, **105**(48), 18681, 2008.

[KMW02] D. Kielpinski, C. Monroe, and D. J. Wineland. Architecture of a large-scale ion trap quantum computer. *Nature*, **417**, 709, 2002.

[KSV02] A. Y. Kitaev, A. H. Shen, and M. N. Vyalyi. *Classical and Quantum Computation*, Volume 47 of *Graduate Studies in Mathematics*. American Mathematical Society, Providence, 2002.

[LBMW03] D. Leibfried, R. Blatt, C. Monroe, and D. Wineland. Quantum dynamics of single trapped ions. *Rev. Mod. Phys.*, **75**, 281–324, 2003.

[LCL+07] D. R. Leibrandt, R. J. Clark, J. Labaziewicz, P. Antohi, W. Bakr, K. R. Brown, and I. L. Chuang. Laser ablation loading of a surface-electrode ion trap. *Phys. Rev. A*, **76**, 055403, 2007.

[LD98] D. Loss and D. P. DiVincenzo. Quantum computation with quantum dots. *Phys. Rev. A*, **57**, 120, 1998.

[LDM+02] D. Leibfried, B. DeMarco, V. Meyer, M. Rowe, A. Ben-Kish, J. Britton, W. M. Itano, B. Jelenkovic, C. Langer, T. Rosenband, and D. J. Wineland. Trapped-ion quantum simulator: Experimental application to nonlinear interferometers. *Phys. Rev. Lett.*, **89**, 247901, 2002.

[LDM+03] D. Leibfried, B. DeMarco, V. Meyer, D. Lucas, M. Barrett, J. Britton, W. M. Itano, B. Jelenkovic, C. Langer, T. Rosenband, and D. J. Wineland. Experimental demonstration of a robust, high-fidelity geometric two ion-qubit phase gate. *Nature*, **422**, 412, 2003.

[Lev01] M. H. Levitt. *Spin Dynamics: Basics of Nuclear Magnetic Resonance.* John Wiley and Sons, Chichester, 2001.

[LGA+08] J. Labaziewicz, Y. Ge, P. Antohi, D. R. Leibrandt, K. R. Brown, and I. L. Chuang. Suppression of heating rates in cryogenic surface-electrode ion traps. *Phys. Rev. Lett.*, **100**, 013001, 2008.

[LGL+08] J. Labaziewicz, Y. Ge, D. Leibrandt, S. X. Wang, R. Shewmon, and I. L. Chuang. Temperature dependence of electric field noise above gold surfaces. *Phys. Rev. Lett.*, **101**, 180602, 2008.

[Lin08] Ziliang Lin. Quantum simulations with $^{88}\mathrm{Sr}^+$ ions on planar lattice traps, 2008. S.B. Thesis, Massachusetts Institute of Technology.

[LKS+05] D. Leibfried, E. Knill, S. Seidelin, J. Britton, R. B. Blakestad, J. Chiaverini, D. B. Hume, W. M. Itano, J. D. Jost, C. Langer, R. Ozeri, R. Reichle, and D. J. Wineland. Creation of a six-atom 'Schrödinger cat' state. *Nature*, **438**, 639, 2005.

[LLC+09] D. Leibrandt, J. Labaziewicz, R. J. Clark, I. L. Chuang, C.-S Pai, Y. Low, R. Frahm, and R. E. Slusher. Demonstration of a scalable, multiplexed ion trap for quantum information processing. *In preparation*, 2009.

[Llo96] S. Lloyd. Universal quantum simulators. *Science*, **273**, 1073, 1996.

[LOJ+05] C. Langer, R. Ozeri, J. D. Jost, J. Chiaverini, B. DeMarco, A. Ben-Kish, R. B. Blakestad, J. Britton, D. B. Hume, W. M. Itano, D. Leibfried, R. Reichle, T. Rosenband, T. Schaetz, P. O. Schmidt, and D. J. Wineland. Long-lived qubit memory using trapped ions. *Phys. Rev. Lett.*, **95**, 060502, 2005.

[Mah00] G. D. Mahan. *Many-Particle Physics.* Kluwer, New York, 3rd edition, 2000.

[McK96] Ross H. McKenzie. Exact results for quantum phase transitions in random XY spin chains. *Phys. Rev. Lett.*, **77**, 4804, 1996.

[MGW$^+$03] O. Mandel, M. Greiner, A. Widera, T. Rom, T. W. Hansch, and I. Bloch. Controlled collisions for multi-particle entanglement of optically trapped atoms. *Nature*, **425**, 937, 2003.

[MHS$^+$04] M. J. Madsen, W. K. Hensinger, D. Stick, J. A. Rabchuk, and C. Monroe. Planar ion trap geometry for microfabrication. *Appl. Phys. B*, **78**, 639–651, 2004.

[Mil99] G. J. Milburn. Simulating nonlinear spin models in an ion trap. *www.arxiv.org: quant-ph/9908037v1*, 1999.

[MMO$^+$07] D. L. Moehring, P. Maunz, S. Olmschenk, K. C. Younge, D. N. Matsukevich, L.-M. Duan, and C. Monroe. Entanglement of single-atom quantum bits at a distance. *Nature*, **449**, 68–71, 2007.

[MNAU02] J. M. Martinis, S. Nam, J. Aumentado, and C. Urbina. Rabi oscillations in a large Josephson-junction qubit. *Phys. Rev. Lett.*, **89**(11), 117901, 2002.

[MOL$^+$99] J. E. Mooij, T. P. Orlando, L. Levitov, L. Tian, C. H. v.d. Wal, and S. Lloyd. Josephson persistent-current qubit. *Science*, **285**, 1036, 1999.

[MS98] Klaus Mølmer and Anders Sørensen. Multiparticle entanglement of hot trapped ions. *Phys. Rev. Lett.*, **82**, 1835, 1998.

[MSW$^+$08] A. H. Myerson, D. J. Szwer, S. C. Webster, D. T. Allcock, M. J. Curtis, G. Imreh, J. A. Sherman, D. N. Stacey, A. M. Steane, and D. M. Lucas. High-fidelity readout of trapped-ion qubits. *Phys. Rev. Lett.*, **100**, 200502, 2008.

[NC00] M. Nielsen and I. Chuang. *Quantum Computation and Quantum Information.* Cambridge University Press, Cambridge, UK, 2000.

[NGB92] F. Nori, E. Gagliano, and S. Bacci. Does frustration describe doping in models for high-temperature superconductivity? *Phys. Rev. Lett.*, **68**, 240, 1992.

[NPT99] Y. Nakamura, Y. A. Pashkin, and J. S. Tsai. Coherent control of macroscopic quantum states in a single-Cooper-pair box. *Nature*, **398**, 786, 1999.

[NSO$^+$04] C. Negrevergne, R. Somma, G. Ortiz, E. Knill, and R. Laflamme. Liquid state NMR simulations of quantum many-body problems. *Phys. Rev. A*, **71**, 032344, 2004.

[OLA$^+$08] C. Ospelkaus, C. E. Langer, J. M. Amini, K. R. Brown, D. Leibfried, and D. J. Wineland. Trapped-ion quantum logic gates based on oscillating magnetic fields. *Phys. Rev. Lett.*, **101**, 090502, 2008.

[OLJ$^+$95] R. Ozeri, C. Langer, J. D. Jost, B. DeMarco, A. Ben-Kish, R. B. Blakestad, J. Britton, J. Chiaverini, W. M. Itano, D. B. Hume, D. Leibfried, T. Rosenband, P. O. Schmidt, and D. J. Wineland. Hyperfine coherence in the presence of spontaneous photon scattering. *Phys. Rev. Lett.*, **95**, 030403, 1995.

[PC04a] D. Porras and J. I. Cirac. Bose-Einstein condensation and strong-correlation behavior of phonons in ion traps. *Phys. Rev. Lett.*, **93**, 263602, 2004.

[PC04b] D. Porras and J. I. Cirac. Effective quantum spin systems with trapped ions. *Phys. Rev. Lett.*, **92**, 207901, 2004.

[PC06] D. Porras and J. I. Cirac. Quantum manipulation of trapped ions in two dimensional Coulomb crystals. *Phys. Rev. Lett.*, **96**, 250501, 2006.

[PDS04] X. Peng, J. De, and D. Suter. Quantum phase transition of ground-state entanglement in a heisenberg spin chain simulated in an NMR quantum computer. *Phys. Rev. A*, **71**, 012307, 2004.

[Pea06] Christopher E. Pearson. Theory and application of planar ion traps. Master's thesis, Massachusetts Institute of Technology Department of Physics, 2006.

[Phi07] C. R. Phipps. *Laser Ablation and Applications.* Springer, Berlin, 2007.

[PJT$^+$05] J. R. Petta, A. C. Johnson, J. M. Taylor, E. A. Laird, A. Yacoby, M. D. Lukin, C. M. Marcus, M. P. Hanson, and A. C. Gossard. Coherent manipulation of coupled electron spins in semiconductor quantum dots. *Science*, **309**, 2180–2184, 2005.

[PLB$^+$06] C. E. Pearson, D. R. Leibrandt, W. S. Bakr, W. J. Mallard, K. R. Brown, and I. L. Chuang. Experimental investigation of planar ion traps. *Phys. Rev. A*, **73**, 032307, 2006.

[PRDB08] D. Portes, Jr., H. Rodrigues, S. B. Duarte, and B. Baseia. Quantum states transfer between coupled fields. *Eur. J. Phys. D*, **48**, 145–149, 2008.

[Pre98] J. Preskill. *Proc. R. Soc. London. A*, **454**, 385–410, 1998.

[Raz99] R. Raz. Exponential separation of quantum and classical communication complexity. In *Proceedings of the 31st ACM STOC*, pp. 358–367, 1999.

[RB01] R. Raussendorf and H. J. Briegel. A one-way quantum computer. *Phys. Rev. Lett.*, **86**, 5188, 2001.

[RBKD$^+$02] M. A. Rowe, A. Ben-Kish, B. DeMarco, D. Leibfried, V. Meyer, J. Beall, J. Britton, J. Hughes, W. M. Itano, B. Jelenkovic, C. Langer, T. Rosenband, and D. J. Wineland. Transport of quantum states and separation of ions in a dual rf ion trap. *Quant. Inf. and Comp.*, **2**, 257, 2002.

[REL$^+$08] C. Roux, A. Emmert, A. Lupascu, T. Nirrengarten, G. Nogues, M. Brunel, J.-M. Raimond, and S. Haroche. Bose-Einstein condensation on a superconducting atom chip. *Europhys. Lett.*, **81**, 56004, 2008.

[RMR$^+$07] K. De Raedt, K. Michielsen, H. De Raedt, B. Trieu, G. Arnold, M. Richter, Th. Lippert, H. Watanabe, and N. Ito. Massively parallel quantum computer simulator. *Comput. Phys. Comm.*, **176**, 121, 2007.

[Sak85] J. J. Sakurai. *Modern Quantum Mechanics.* Addison Wesley, Reading, Mass., 1985.

[SCR$^+$06] S. Seidelin, J. Chiaverini, R. Reichle, J. J. Bollinger, D. Liebfried, J. Britton, J. H. Wesenberg, R. B. Blakestad, R. J. Epstein, D. B. Hume, J. D. Jost, C. Langer, R. Ozeri, N. Shiga, and D. J. Wineland. Microfabricated surface-electrode ion trap for scalable quantum information processing. *Phys. Rev. Lett.*, **96**, 253003, 2006.

[SGA$^+$05] S. Stahl, F. Galve, J. Alonso, S. Djekic, W. Quint, T. Valenzuela, J. Verdu, M. Vogel, and G. Werth. A planar Penning trap. *Eur. Phys. J. D*, **32**, 139–146, 2005.

[Sho38] W. Shockley. Currents to conductors induced by a moving point charge. *J. Appl. Phys.*, **9**, 635, 1938.

[Sho94] P. W. Shor. Algorithms for quantum computation: Discrete log and factoring. In *Proceedings of the 35th Annual Symposium on the Foundations of Computer Science*, p. 124, IEEE Computer Society Press, Los Alamitos, CA, 1994.

[Sho96] P. W. Shor. Fault-tolerant quantum computation. In *Proceedings of the 37th Symposium on Foundations of Computing*, p. 56, IEEE Computer Society Press, Los Alamitos, CA, 1996.

[SHO$^+$06] D. Stick, W. K. Hensinger, S. Olmschenk, M. J. Madsen, K. Schwab, and C. Monroe. Ion trap in a semiconductor chip. *Nature Physics*, **2**, 36, 2006.

[SRL$^+$05] P. O. Schmidt, T. Rosenband, C. Langer, W. M. Itano, J. C. Bergquist, and D. J. Wineland. Spectroscopy using quantum logic. *Science*, **309**, 749–752, 2005.

[SRM$^+$08] R. Schmied, T. Roscilde, V. Murg, D. Porras, and J. I. Cirac. Quantum phases of trapped ions in an optical lattice. *New J. Phys.*, **10**, 045017, 2008.

[SSSK08] Y.-I. Shin, C. H. Schunck, A. Schirotzek, and W. Ketterle. Phase diagram of a two-component Fermi gas with resonant interactions. *Nature*, **451**, 689, 2008.

[Ste96] A. M. Steane. Error correcting codes in quantum theory. *Phys. Rev. Lett.*, **77**, 793, 1996.

[Ste03] Matthias Steffen. *A Prototype Quantum Computer using Nuclear Spins in Liquid Solution.* Ph.D. thesis, Stanford University, 2003.

[STH$^+$98] S. Somaroo, C. H. Tseng, T. F. Havel, R. Laflamme, and D. G. Cory. Quantum simulations on a quantum computer. *Phys. Rev. Lett.*, **82**, 5381, 1998.

[Suz92] M. Suzuki. *Phys. Lett. A*, **165**, 387, 1992.

[SvDH$^+$03] M. Steffen, W. van Dam, T. Hogg, G. Breyta, and I. L. Chuang. Experimental implementation of an adiabatic quantum optimization algorithm. *Phys. Rev. Lett.*, **90**, 067903, 2003.

[SWL09] R. Schmied, J. Wesenberg, and D. Leibfried. Optimal surface-electrode trap lattices for quantum simulation with trapped ions. *www.arXiv.org: quant-ph/0902.1686v1*, 2009.

[TBZ05] L. Tian, R. Blatt, and P. Zoller. Scalable ion trap quantum computing without moving ions. *Eur. Phys. J. D*, **32**, 201–208, 2005.

[TKK+99] Q. A. Turchette, D. Kielpinski, B. E. King, D. Liebfried, D. M. Meekhof, C. J. Myatt, M. A. Rowe, C. A. Sackett, C. S. Wood, W. M. Itano, C. Monroe, and D. J. Wineland. Heating of trapped ions from the quantum mechanical ground state. *Phys. Rev. A*, **61**, 063418, 1999.

[Tro58] H. F. Trotter. Approximation of semi-groups of operators. *Pacific Journal of Math*, **8**, 887, 1958.

[TSS+00] C. H. Tseng, S. Somaroo, Y. Sharf, E. Knill, R. Laflamme, T. F. Havel, and D. G. Cory. Quantum simulation of a three-body-interaction Hamiltonian on an NMR quantum computer. *Phys. Rev. A*, **61**, 012302, 2000.

[TW05] M. Troyer and U.-J. Wiese. Computational conplexity and fundamental limitations to fermionic quantum monte carlo simulations. *Phys. Rev. Lett.*, **94**, 170201, 2005.

[Van01] Lieven M. K. Vandersypen. *Experimental Quantum Computation with Nuclear Spins in Liquid Solution.* Ph.D. thesis, Stanford University, 2001.

[VC05] L. M. K. Vandersypen and I. L. Chuang. NMR techniques for quantum control and computation. *Rev. Mod. Phys.*, **76**, 1037, 2005.

[VC08] F. Verstraete and J. I. Cirac. Renormalization algorithms for quantum many-body systems in two and higher dimensions. *www.arxiv.org: cond-mat/0407066v1*, 2008.

[Vid04] G. Vidal. Efficient simulation of one-dimensional quantum many-body systems. *Phys. Rev. Lett.*, **93**, 040502, 2004.

[Vid07] G. Vidal. Classical simulation of infinite-size quantum lattice systems in one spatial dimension. *Phys. Rev. Lett.*, **98**, 070201, 2007.

[VMC08] F. Verstraete, V. Murg, and J. I. Cirac. Matrix product states, projected entangled pair states, and variational renormalization group methods for quantum spin systems. *Advances in Physics*, **57**, 143–224, 2008.

[VSB+01] L. M. K. Vandersypen, M. Steffen, G. Breyta, C. S. Yannoni, M. H. Sherwood, and I. L. Chuang. Experimental realization of Shor's quantum factoring algorithm using nuclear magnetic resonance. *Nature*, **414**, 883–887, 2001.

[VSS+99] L. M. K. Vandersypen, M. Steffen, M. H. Sherwood, C. S. Yannoni, G. Breyta, and I. L. Chuang. Implementation of a three-quantum bit search algorithm. *Appl. Phys. Lett.*, **76**, 646–648, 1999.

[WBL02] L. A. Wu, M. S. Byrd, and D. A. Lidar. Polynomial-time simulation of pairing models on a quantum computer. *Phys. Rev. Lett.*, **82**(5), 057904, 2002.

[WD75] D. J. Wineland and H. G. Dehmelt. Principles of the stored ion calorimeter. *J. Appl. Phys.*, **46**, 919, 1975.

[WDW78] D. J. Wineland, R. E. Drullinger, and F. L. Walls. Radiation-pressure cooling of bound resonant absorbers. *Phys. Rev. Lett.*, **40**, 1639, 1978.

[WEL$^+$07] J. H. Wesenberg, R. J. Epstein, D. Leibfried, R. B. Blakestad, J. Britton, J. P. Home, W. M. Itano, J. D. Jost, E. Knill, C. Langer, R. Ozeri, S. Seidelin, and D. J. Wineland. Fluorescence during doppler cooling of a single trapped atom. *Phys. Rev. A*, **76**, 053416, 2007.

[Whi04] S. R. White. Density matrix formulation for quantum renormalization groups. *Phys. Rev. Lett.*, **93**, 040502, 2004.

[Wil75] K. G. Wilson. The renormalization group: Critical phenomena and the Kondo problem. *Rev. Mod. Phys.*, **47**, 773–840, 1975.

[WLG$^+$09] S. X. Wang, J. Labaziewicz, Y. Ge, R. Shewmon, and I. L. Chuang. Individual addressing of ions using magnetic field gradients in a surface-electrode ion trap. *Appl. Phys. Lett.*, **94**, 094103, 2009.

[WO91] H. Winter and H. W. Ortjohann. Simple demonstration of storing macroscopic particles in a "Paul trap". *Am. J. Phys.*, **59**, 807, 1991.

Appendix A

Matlab code for Ising model simulations

This appendix contains the Matlab code for simulating the Ising model for two ions including the effects of micromotion.

A.1 Simulation with constant force in space and time

```
% File: ising_small_randomstate.m
% Author: Rob Clark
% Simulates Ising model with and without micromotion, beginning with a
% random two-qubit state.

% Basis generated by {spin space of ion 1} \otimes {spin space of ion 2}

% STAGE 1: simple calculation, ising, no vibration

clear;
close all;

J = 1.0306e3;
B = -J;
A = .1;
Omega = 1.0e6;
t = 0:1/(2*Omega):10/J;

sx = [0 1; 1 0];
sz = [1 0; 0 -1];
sztot1 = kron(eye([2 2]),sz) + kron(sz,eye([2 2]));

H1 = J*kron(sz,sz) + B*(kron(eye([2 2]), sx) + kron(sx,eye([2 2])));

% Randomize initial state
amps = [rand(1),rand(1),rand(1),rand(1)] + i*[rand(1),rand(1),rand(1),rand(1)];
```

```
init1 = amps/norm(amps); init1 = init1';
expsz1 = [init1'*sztot1*init1];
for k = 2:length(t)
    curr = expm(-i*H1*t(k))*init1;
    expsz1 = [expsz1 curr'*sztot1*curr];
end

figure(1);
hold on;
subplot(3,1,1);
ylabel('Magnetization');
plot(t*J,expsz1)
axis([min(t*J),max(t*J),-2,2]);

% Now do the simulation with micromotion

expsz2 = [init1'*sztot1*init1];
tstep=t(2)-t(1);
curr = init1;
J = 1.0e3;
Jt(1) = J;
Bt(1) = B;

for kk = 2:length(t)
    Jt(kk) = J*(1+A*sin(Omega*t(kk)+pi/2))^(-3);
    Bt(kk) = B;
    Ht = Jt(kk)*kron(sz,sz)+ B*(kron(eye([2 2]), sx) + kron(sx,eye([2 2])));
    curr = expm(-i*Ht*tstep)*curr;
    expsz2 = [expsz2, curr'*sztot1*curr];
end

Jm = mean(Jt);

figure(1);
hold on;
subplot(3,1,2);
plot(t*J,expsz2);
axis([min(t*J),max(t*J),-2,2]);

theerr = expsz2-expsz1;

figure(1);
hold on;
subplot(3,1,3);
ylabel('Error');
plot(t*J,expsz2-expsz1,'r-');
xlabel('time (J)');
axis([min(t*J),max(t*J),-0.5,0.5]);
```

```
err_result = mean(theerr)
```

A.2 Simulation with a linear force gradient in space

The following is a function that computes the average J value, as well as the simulation error for a given gradient of F.

```
% File: ising_small_rs_fn.m
% Author: Rob Clark
% Simulates Ising model with and without micromotion,
% beginning with a random two-qubit state.
% A linear gradient in space is used.
% This is a function that returns the average J value when the ion undergoes
% micromotion and also the error, calculated as the deviation from the
% micromotion-free simulation.

% Basis generated by {spin space of ion 1} \otimes {spin space of ion 2}

% STAGE 1: simple calculation, ising, no vibration

function [Jm,err_result] = isrf(J0,Jav,A,grad)

% J = -10000;
% B = -J;
% J = 1.0306e3;
J = Jav;
B = -J;
% A = .1;
Omega = 1.0e6;
t = 0:1/(2*Omega):10/J;

sx = [0 1; 1 0];
sz = [1 0; 0 -1];
sztot1 = kron(eye([2 2]),sz) + kron(sz,eye([2 2]));

H1 = J*kron(sz,sz) + B*(kron(eye([2 2]), sx) + kron(sx,eye([2 2])));

% Randomize initial state
amps = [rand(1),rand(1),rand(1),rand(1)] + i*[rand(1),rand(1),rand(1),rand(1)];
init1 = amps/norm(amps); init1 = init1';
expsz1 = [init1'*sztot1*init1];
for k = 2:length(t)
    curr = expm(-i*H1*t(k))*init1;
    expsz1 = [expsz1 curr'*sztot1*curr];
end

expsz2 = [init1'*sztot1*init1];
tstep=t(2)-t(1);
curr = init1;
```

```
J = J0;
Jt(1) = J;
Bt(1) = B;

for kk = 2:length(t)
    Fr = 1-A*grad*sin(Omega*t(kk)+pi/2);
    Jt(kk) = J*Fr^2*(1+A*sin(Omega*t(kk)+pi/2))^(-3);
    Bt(kk) = B;
    Ht = Jt(kk)*kron(sz,sz)+ B*(kron(eye([2 2]), sx) + kron(sx,eye([2 2])));
    curr = expm(-i*Ht*tstep)*curr;
    expsz2 = [expsz2, curr'*sztot1*curr];
end

Jm = mean(Jt);

theerr = expsz2-expsz1;
err_result = mean(theerr);
```

This is the script that calls the above function, used for studying the effective J value as a function of the gradient in the state-dependent force.

```
% ising_small_rs_script.m
% Rob Clark
% 27 March 2009

clear;
close all;

J = 1e3;
B = -J;
A = 0.1;
grads = linspace(0,1,10); % Gradient is relative to A.

for ii = 1:length(grads)
  % Calculate average J for a given grad
  Jav = J;
  [Jm(ii),bigerrs(ii)] = ising_small_rs_fn(J,Jav,A,grads(ii));
  % Calculate error with new average J
  [Jcr,smallerrs(ii)] = ising_small_rs_fn(J,Jm(ii),A,grads(ii));
end

figure(101);
plot(grads,Jm,'ro');
xlabel('Force gradient');
ylabel('J_{av}');

figure(102);
plot(grads,bigerrs,'ro');
xlabel('Force gradient');
ylabel('Uncorrected error');

figure(103);
plot(grads,smallerrs,'ro');
xlabel('Force gradient');
ylabel('Corrected error');
```

A.3 Simulation with constant force in space and linear variation in time

```
% File: ising_small_tdep.m
% Author: Rob Clark
% Simulates Ising model with and without micromotion,
% beginning with a random two-qubit state.
% The state-dependent force increases linearly in time.

% Basis generated by {spin space of ion 1} \otimes {spin space of ion 2}

% STAGE 1: simple calculation, ising, no vibration

clear;
close all;

%  J = 1.000e3;
J = 1000; %*343.6/333.34;
B = -J;
A = .1;
Omega = 1.0e6;
t = 0:1/(2*Omega):10/J;
Fr1 = t/max(t);
tstep = t(2)-t(1);

sx = [0 1; 1 0];
sz = [1 0; 0 -1];
sztot1 = kron(eye([2 2]),sz) + kron(sz,eye([2 2]));

H1 = J*kron(sz,sz) + B*(kron(eye([2 2]), sx) + kron(sx,eye([2 2])));

% Randomize initial state
amps = [rand(1),rand(1),rand(1),rand(1)] + i*[rand(1),rand(1),rand(1),rand(1)];
init1 = amps/norm(amps); init1 = init1';
% init1 = [1;0;0;0];
curr = init1;
expsz1 = [init1'*sztot1*init1];
for k = 2:length(t)
    H1 = Fr1(k)^2*J*kron(sz,sz) + B*(kron(eye([2 2]), sx) + kron(sx,eye([2 2])));
    curr = expm(-i*H1*tstep)*curr;
    expsz1 = [expsz1 curr'*sztot1*curr];
end

figure(1);
hold on;
subplot(3,1,1);
```

```
plot(t*J,expsz1)
axis([min(t*J),max(t*J),-2,2]);
ylabel('<Z> A = 0');

expsz2 = [init1'*sztot1*init1];
tstep=t(2)-t(1);
curr = init1;
J = 1000;
Jt(1) = J;
Bt(1) = B;
Fr(1) = 0;

for kk = 2:length(t)
    Fr(kk) = t(kk)/max(t);
    Jt(kk) = Fr(kk)^2*J*(1+A*sin(Omega*t(kk)+pi/2))^(-3);
    Bt(kk) = B;
    Ht = Jt(kk)*kron(sz,sz)+ B*(kron(eye([2 2]), sx) + kron(sx,eye([2 2])));
    curr = expm(-i*Ht*tstep)*curr;
    expsz2 = [expsz2, curr'*sztot1*curr];
end

Jm = mean(Jt);

theerr = expsz2-expsz1;
err_result = mean(theerr)

figure(1);
hold on;
subplot(3,1,2);
plot(t*J,expsz2);
axis([min(t*J),max(t*J),-2,2]);
ylabel('<Z> A = 0.1');

figure(1);
hold on;
subplot(3,1,3);
plot(t*J,expsz2-expsz1,'r-');
xlabel('time (J)');
ylabel('Error');
```

Appendix B

Mathematica code for ion crystal structure

This appendix contains the Mathematica notebook for the ion crystal structure calculations. Although it was used in the thesis for the elliptical ion trap, it works for any trap for which the three principal motional frequencies are known.

```
In[1]:= (*
File: crystal_shape_6uraniborg.nb
  Author: Kenan Diab
    Calculates the structure of ion
    crystals in a trap using the three secular frequencies wx,
wy, and wz and the number of ions n as inputs. The variables z3coeff
 and z4coeff are optional anharmonicity terms.
*)

(* everything is done is cgs units.  to simplify the coulomb
 contribution to the energy, we divide everything by e^2, introducing
 the factor of 0.00131 to the harmonic part. *)

wx = 2 * Pi * (.150) * 10 ^ 6;
wy = 2 * Pi * (.150) * 10 ^ 6;
wz = 2 * Pi * (1.3) * 10 ^ 6;
z3coeff = 0; (*6.78372*10^10; *)
z4coeff = 0; (*6.52396*10^11; *)
n = 13; (* number of ions *)

(* r is the array of ion coordinates.  r[3i+1], r[3i+2],
r[3i+3] are the x,y,z coordinates of the i'th ion. *)
r = Array[Subscript[a, #1] &, {3 n}];

(* mathematica uses a (relatively) efficient simplex method *)
ans = NMinimize[0.0006306 * 0.5 * (wx ^ 2 * Sum[r[[3 i + 1]] ^ 2, {i, 0, n - 1}] +
      wy ^ 2 * Sum[r[[3 i + 2]] ^ 2, {i, 0, n - 1}] + wz ^ 2 * Sum[r[[3 i + 3]] ^ 2, {i, 0, n - 1}]) -
   z3coeff * Sum[r[[3 i + 3]] ^ 3, {i, 0, n - 1}] + z4coeff * Sum[r[[3 i + 3]] ^ 4, {i, 0, n - 1}] +
   Sum[Sqrt[1 / ((r[[3 i + 1]] - r[[3 j + 1]]) ^ 2 +
        (r[[3 i + 2]] - r[[3 j + 2]]) ^ 2 + (r[[3 i + 3]] - r[[3 j + 3]]) ^ 2)],
    {i, 0, n - 1}, {j, i + 1, n - 1}], r, WorkingPrecision → 15]


(* plot points 3D *)
s = r /. Extract[ans, {2}];
points = {};
For[i = 0, i < n, i++, points = Append[points, {s[[3 i + 1]], s[[3 i + 2]], s[[3 i + 3]]}];]
ListPlot3D[points * 10 000, AspectRatio → Automatic, AxesLabel → {"x  (μm)", "y (μm)"} ]

 (* plot points 2D, dropping z coordinate *)
s = r /. Extract[ans, {2}];
points = {};
For[i = 0, i < n, i++, points = Append[points, {s[[3 i + 1]], s[[3 i + 2]]}];]
ListPlot[points * 10 000, AspectRatio → Automatic,
 PlotStyle → {Red, Thick, PointSize[Large]},
 AxesLabel → {"x  (μm)", "y (μm)" }, PlotRange → {{-50, 50}, {-50, 50}}]

 (* calculate max distance between y vals *)
yvals = {};
For[i = 0, i < n, i++, yvals = Append[yvals, s[[3 i + 2]]];]
dist = Max[yvals] - Min[yvals]

 (* convert energy to electron volts *)
energy = ans[[1]] * 1.43965000000000000 * 10 ^ -7
```

```
Out[6]= {47640.3623492104,
  {a1 → 0.00249526329454898, a2 → -0.000195872421184956, a3 → -1.01615335007377 × 10^-11,
   a4 → 0.00189214573083234, a5 → 0.00137727911696546, a6 → 1.40594914164938 × 10^-11,
   a7 → 0.00166082992489247, a8 → -0.00162635651624383, a9 → 1.77142209690527 × 10^-12,
   a10 → -0.0000126775934318443, a11 → -0.00101272197346297, a12 → 1.46250732157699 × 10^-11,
   a13 → -0.00235752128707685, a14 → -0.000687539338317872, a15 → -2.76406689457980 × 10^-12,
   a16 → 0.000633404194797575, a17 → 0.00238881774381363, a18 → -7.62723689218269 × 10^-12,
   a19 → -0.00134322589463185, a20 → -0.00193218179314517, a21 → -2.17485783903952 × 10^-12,
   a22 → -0.00101011014777204, a23 → 0.0000133934171442451, a24 → -6.04502971918647 × 10^-12,
   a25 → 0.0000164747226301317, a26 → 0.00101068514357131, a27 → 1.49702922674624 × 10^-11,
   a28 → 0.000259410079001472, a29 → -0.00248369053655865, a30 → -1.60920502290904 × 10^-11,
   a31 → -0.00218716833903424, a32 → 0.00101829532993938, a33 → -7.79342304810769 × 10^-12,
   a34 → 0.00101331072935728, a35 → -0.0000157843643466466, a36 → 9.04047848325618 × 10^-12,
   a37 → -0.00106013484503786, a38 → 0.00214567679997688, a39 → -1.16983117096333 × 10^-11}}
```

Out[10]=

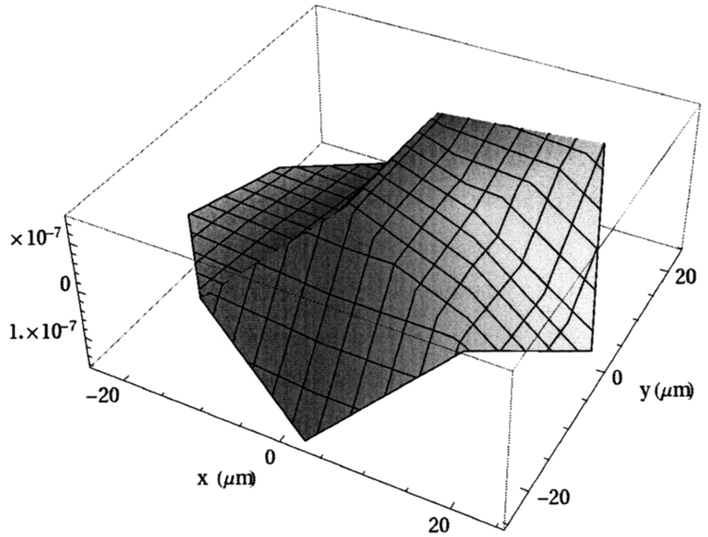

Out[14]=

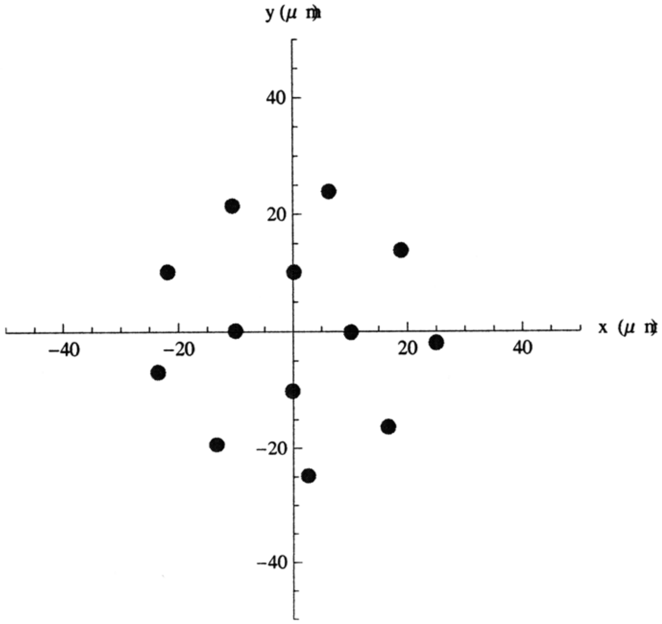

```
Out[17]= 0.00487250828037228
```

```
Out[18]= 0.00685854476560407

In[19]:= ystrengths = 0.1 * {5, 5.5, 6, 6.5, 7, 7.5, 8, 8.2, 8.3, 8.31, 8.32, 8.33, 8.335, 8.35};
         ydiffs = {0.003177, 0.002296, 0.002064, 0.001761, 0.001075, 0.0009125, 0.00070273, 0.0005642,
            0.0003123, 0.0002613, 0.0001934, 0.00006865, 3.9135 * 10^(-8), 2.048 * 10^(-10)};
         ListLogPlot[Table[{ystrengths[[i]], ydiffs[[i]]}, {i, Length[ystrengths]}],
          PlotStyle → {Red, Thick, PointSize[Large]}]

Out[21]=
```

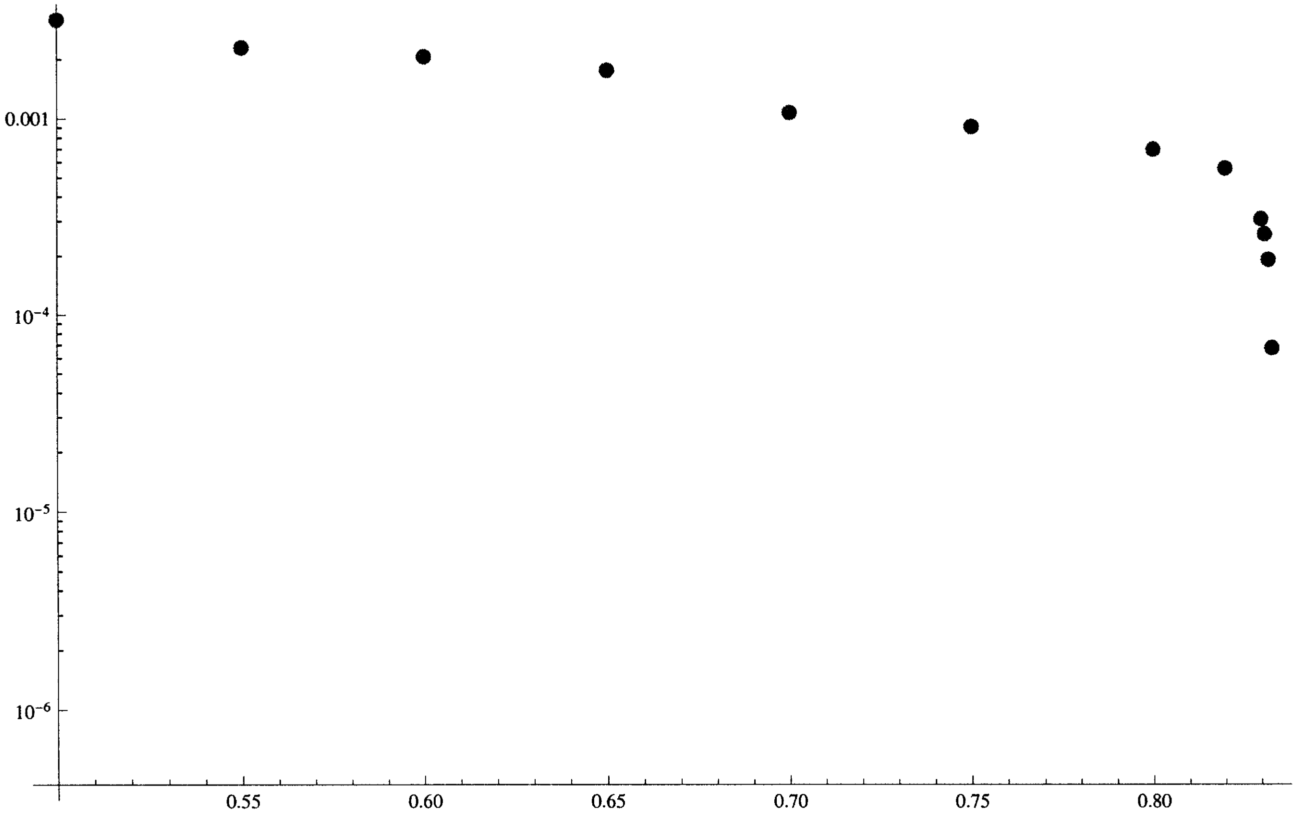

Appendix C

How to trap ions in a closed-cycle cryostat

The purpose of this appendix is to offer a practical guide to the operation of the 4 K closed-cycle cryogenic ion trap presented in Sec. 7.4. We will present the following items:

- Preparing the cryostat for cooldown.
- Turning on the compressor.
- Pressure and temperature measurement.
- Laser alignment and imaging.
- Shutdown

This appendix will be most useful after reading Sec. 7.4, which contains the basic description of the cryostat system.

C.1 Preparing the cryostat for cooldown

The cold head (expander) may be mounted in one of two configurations. In the first configuration, the cold head is held above the DMX-20 anti-vibration system using four spacers with bolts that are tightened down. In this position, the cold head is decoupled from the overhead support structure, and may be rotated up and opened. In the other configuration, the cold head is attached to the overhead structure using four aluminum plates; in this position, the cold head is vibrationally isolated from the vacuum housing of the experiment.

Before engaging the compressor, which starts the cooldown, it is important to flush and fill the bellows of the DMX-20 with ultra-high purity (UHP) helium, which is 99.9999% pure. The recommended procedure is as follows:

1. Open the safety valve on the DMX-20. This is the only manually-controllable valve on that system.
2. Start a flow of helium gas through the DMX-20. Normally, you want to hear a faint flow of gas out the valve.
3. Reduce the pressure somewhat, then slowly close the valve so that the helium begins to make the bellows expand. After the bellows expands a good deal, or stops expanding, release the pressure using the manual valve.
4. Repeat this process at least five times. The idea is simply to thoroughly flush out the DMX-20.
5. Reduce the pressure from the gas cylinder slightly, then close off the valve. The steady-state pressure should leave the bellows somewhat expanded.

As the system cools, one may observe the bellows contracting as the pressure of gas inside falls. If this happens, there is not quite sufficient pressure to the bellows. Increase, very slowly, the pressure until the bellows is slightly expanded. Also, aside from the helium used for flushing the system, there should be very little helium expended while running the cryostat. If the reading of the pressure inside the gas cylinder is visibly declining over a period of days, then either too much pressure is being supplied to the DMX-20, or there is a leak in the system. If a leak is suspected, make sure that all Swagelok connections are tight, and cannot be rotated. Leaks not only waste expensive UHP helium, but more seriously, can permit contaminants inside the DMX-20. This may permit water or nitrogen to freeze inside the bellows, creating a thermal short to the outside and destroying vibration isolation. If this occurs, the system must be warmed back up, and the bellows flushed again.

C.2 Turning on the compressor

Before turning on the compressor, the chilled water supply to and from the compressor must be opened (turn both handles at once). The compressor is turned on by insuring that the circuit breaker switch is in the "on" position (flipped up), and then flipping the green switch, which will light up when the compressor is on. Immediately, you should hear the motor begin to run, and also hear the pumping noise at about 2 Hz. The pressure gauge for the supply line will rise to ¿300 psi, and should increase periodically, in time with the pumping action.

If the motor begins running, but there is no periodic pumping (as evidenced by lack of sound and/ or pressure variation), then a blown fuse is the most likely culprit. On the front of the compressor, there are two easily accessible fuses. A fast-acting 250 V, 2 A fuse is required.

Finally, we note that the chilled water supply must be engaged whenever the cryostat is on, and must be switched off when the compressor is not running, to avoid water condensing on the hoses in places it shouldn't.

As a final caution, if the static pressure is below about 240 psi, then helium may need to be added. This should not need to happen very often, so if the pressure has fallen a good deal there may be a leak. We have, in the lab, a portable helium sniffer that can detect fairly large leaks. A mass spectrometer for vacuum systems may also be run in a sniffer mode, with higher sensitivity, if the proper attachment can be purchased or built. The author has experienced only one major helium leak, and it was located on the cold head itself (due to a manufacturing defect that has now been fixed).

C.3 Pressure and temperature measurement

The pressure inside the cryostat reaches UHV conditions in a matter of hours. However, it is not possible to directly measure the pressure near the 40 K or 4 K surfaces, since ionization gauges cannot run at cryogenic temperatures. Instead, we use the current reading on an ion pump attached to the vacuum chamber to measure the pressure outside the 4 K shield. We may reasonably assume that the pressure inside the radiation shield is significantly lower than that measured on the ion pump. For instance, if the ion pump reads 0.5×10^{-9} torr, we may expect pressure in the 10^{-11} torr range or better near the ion trap.

The temperature is measured using two Lake Shore DT-670 diodes, across each of which a 10 μA current is passed. The voltage across the diode records the temperature, and the voltage-to-temperature conversion chart is reprinted below. There are two diodes, one of which is heat-sunk directly to the 4 K cold head, and the other of which is heat-sunk to the experimental 4 K baseplate. The former typically reaches a temperature of 5 K, while the latter normally reads 9-11 K. It is not known why the temperature is not lower, but modifying the heat sinking of wires or replacing the radiation shield with an all-copper piece may help, since copper is a better thermal conductor than stainless steel.

[redacted] [redacted]

Curve DT-670

Standard Curve DT-670: Measurement Current = 10 µA ±0.05%

T (K)	Voltage (V)	dV/dT (mV/K)
1.20	1.646540	-9.87
1.40	1.644290	-12.49
1.60	1.641570	-14.79
1.80	1.638370	-17.15
2.00	1.634720	-19.30
2.20	1.630670	-21.14
2.40	1.626290	-22.61
2.60	1.621660	-23.63
2.80	1.616870	-24.16
3.00	1.612000	-24.67
3.20	1.606970	-25.63
3.40	1.601730	-26.80
3.60	1.596260	-27.91
3.80	1.590570	-28.99
4.00	1.584650	-30.21
4.20	1.578480	-31.59
4.40	1.572020	-32.91
4.60	1.565330	-33.97
4.80	1.558450	-34.74
5.00	1.551450	-35.25
5.20	1.544360	-35.60
5.40	1.537210	-35.92
5.60	1.530000	-36.22
5.80	1.522730	-36.48
6.00	1.515410	-36.71
6.50	1.496980	-36.86
7.00	1.478680	-36.21
7.50	1.460860	-35.00
8.00	1.443740	-33.42
8.50	1.427470	-31.67
9.00	1.412070	-29.95
9.50	1.397510	-28.31
10.00	1.383730	-26.84
10.50	1.370650	-25.51
11.00	1.358200	-24.31
11.50	1.346320	-23.20
12.00	1.334990	-22.15
12.50	1.324160	-21.17
13.00	1.313810	-20.25
13.50	1.303900	-19.41
14.00	1.294390	-18.63
14.50	1.285260	-17.92
15.00	1.276450	-17.31
15.50	1.267940	-16.77
16.00	1.259670	-16.31
16.50	1.251610	-15.94
17.00	1.243720	-15.64
17.50	1.235960	-15.41
18.00	1.228300	-15.25
18.50	1.220700	-15.13
19.00	1.213110	-15.20
19.50	1.205480	-15.34
20.00	1.197748	-15.63
21.00	1.181548	-16.98
22.00	1.162797	-21.11
23.00	1.140817	-20.77
24.00	1.125923	-9.42
25.00	1.119448	-4.60
26.00	1.115658	-3.19
27.00	1.112810	-2.58
28.00	1.110421	-2.25
29.00	1.108261	-2.08
30.00	1.106244	-1.96
31.00	1.104324	-1.88
32.00	1.102476	-1.82
33.00	1.100681	-1.77
34.00	1.098930	-1.73
35.00	1.097216	-1.70
36.00	1.095534	-1.67
37.00	1.093878	-1.64
38.00	1.092244	-1.62
39.00	1.090627	-1.61
40.00	1.089024	-1.60
42.00	1.085842	-1.59
44.00	1.082669	-1.59
46.00	1.079492	-1.59
48.00	1.076303	-1.60
50.00	1.073099	-1.61
52.00	1.069881	-1.61
54.00	1.066650	-1.62
56.00	1.063403	-1.63
58.00	1.060141	-1.64
60.00	1.056862	-1.64
65.00	1.048584	-1.67
70.00	1.040183	-1.69
75.00	1.031651	-1.72
77.35	1.027594	-1.73
80.00	1.022984	-1.75
85.00	1.014181	-1.77
90.00	1.005244	-1.80
95.00	0.996174	-1.83
100.00	0.986974	-1.85
105.00	0.977650	-1.88
110.00	0.968209	-1.90
115.00	0.958657	-1.92
120.00	0.949000	-1.94
125.00	0.939242	-1.96
130.00	0.929390	-1.98
135.00	0.919446	-2.00
140.00	0.909416	-2.01
145.00	0.899304	-2.03
150.00	0.889114	-2.05
155.00	0.878851	-2.06
160.00	0.868518	-2.07
165.00	0.858120	-2.09
170.00	0.847659	-2.10
175.00	0.837138	-2.11
180.00	0.826560	-2.12
185.00	0.815928	-2.13
190.00	0.805242	-2.14
195.00	0.794505	-2.15
200.00	0.783720	-2.16
210.00	0.762007	-2.18
220.00	0.740115	-2.20
230.00	0.718054	-2.21
240.00	0.695834	-2.23
250.00	0.673462	-2.24
260.00	0.650949	-2.26
270.00	0.628302	-2.27
273.15	0.621141	-2.28
280.00	0.605528	-2.28
290.00	0.582637	-2.29
300.00	0.559639	-2.30
305.00	0.548102	-2.31
310.00	0.536542	-2.31
320.00	0.513361	-2.32
330.00	0.490106	-2.33
340.00	0.466760	-2.34
350.00	0.443371	-2.34
360.00	0.419960	-2.34
370.00	0.396503	-2.35
380.00	0.373002	-2.35
390.00	0.349453	-2.36
400.00	0.325839	-2.36
410.00	0.302161	-2.37
420.00	0.278416	-2.38
430.00	0.254592	-2.39
440.00	0.230697	-2.39
450.00	0.206758	-2.39
460.00	0.182832	-2.39
470.00	0.159010	-2.37
480.00	0.135480	-2.33
490.00	0.112553	-2.25
500.00	0.090681	-2.12

C.4 Laser alignment and imaging

As discussed in the main text of the thesis, four lasers are used in the cryostat experiment. Here, I will focus on the alignment procedure.

The PI lasers are aligned first, since they are brighter to the eye than the 422 laser. The PI lasers are grazed across the center of the trap, then raised by a translation stage to the correct height above the trap surface. For Uraniborg, this height is 1.3 mm. The detection lasers are then counter-propagated against the PI lasers. This offers the advantage of very straightforward alignment, but one disadvantage is that since the optics for the PI lasers are not anti-reflection (AR) coated for 422 nm, back-reflections from the PI optics can increase the scatter on the trap. It is possible to slightly adjust the angle at which the 422 and 1092 propagate to reduce this scatter.

The detection lasers are extended cavity diode lasers, but currently lack any fast active stabilization. They may be locked to the Toptica wavemeter, which corrects drifts of $\mathcal{O}(10\,\text{MHz})$ on a timescale of 2 s. This provides enough stability for the observation of ion crystals, but would not be sufficient for experiments in which a well-defined laser detuning is required (such as Doppler recooling).

Neutral strontium ions may be detected by removing the 422 nm interference filter in front of the CCD camera, and shuttering all lasers other than the 460 nm laser. While shuttering other lasers is not strictly necessary, it helps to reduce scatter and improve the signal to noise ratio, since only 460 nm photons will carry the signal from the atomic beam. A larger current is required to observe the beam of neutrals than for loading the trap. This current may be as much as 3.5 A, compared to a loading current of 2.5 A or less. Therefore, it is important to do a good alignment beforehand, to minimize the amount of time at which the oven must be run at that high current.

C.5 What to do if you can't trap ions

This section contains the author's advice for debugging, in the event that ions cannot be quickly trapped. The assumption is that the experimentalist is moving the position of the detection lasers after each step, but not necessarily in a comprehensive fashion (covering every spot on a 2-D grid). An ion cloud in Uraniborg is of a sufficient size (estimated to be at least 200 μm) that an overlap of the laser with only part of the cloud will result in a signal. Blocking and un-blocking the IR is a good way to tell ion signal apart from other light, and switching off and back on the rf is the surest way to tell, especially if you have a high loading rate.

So here are the debugging steps:

1. Double-check basic stuff: rf resonance is where you expect, temperature and pressure are good, dc feedthrough is properly connected, etc.

2. Check that 422 and 1092 are roughly coaligned (by eye with the IR card).
3. Make sure the 405 is unblocked!!! This has caused the author to waste some time in the past.
4. If it's been a few days since someone trapped, check our wavemeter against Shannon's or against the 674 laser.
5. Look for neutrals.
6. If there are neutrals but no ions, you'll have to do some searching. Try to be systematic: map out every point on a grid with the 422/1092 lasers. If you don't find anything, you may vary the PI position as well, but at each point try to re-counteralign the 422/1092 with it.
7. Check 422/1092 coalignment on the beam profiler.
8. Lower (or raise) the rf amplitude and repeat the search pattern.
9. If that fails, adjust the dc voltages. Don't do so blindly, because that will take too long. Try another set of voltages from the group laboratory notebook blog that have worked in the past, or go to zero on all channels if you're using different values.
10. Give up. Usually if the trap is going to trap well, you find ions in a couple hours or less. There have been cases in which the author trapped nothing, then warmed up and baked the system for a day, then cooled down and realigned, and then found ions easily. Excessive charge getting trapped on the dielectric around the trap at 4K is a reasonable explanation for this.
11. Good luck!

C.6 Shutdown

In this section, we focus on the procedure for shutting down the cryostat, which is really quite simple. First flip the green switch on the compressor, shutting it down. Then, fairly soon after, close off the chilled water supply to and from the compressor. You will see the pressure reading on the ion pump begin to rise rapidly. Close off the main valve on the UHP helium cylinder. Then, for a few moments, observe the bellows. Sometimes pressure within the bellows builds up to the extent that one wishes to relieve some of the pressure manually, using the safety valve. However, this is probably not necessary.